Searches for Axion-Like Particles in Rare Higgs Boson Decays with the ATLAS Detector

UNIVERSITY OF LIVERPOOL

Thesis submitted in accordance with the requirements of the University of Liverpool for the degree of Doctor in Philosophy by

Adam James Ruby

Department of Physics
Oliver Lodge Laboratory
University of Liverpool

21st February 2023

Abstract

This thesis presents a search for the decay of the Higgs boson to a Z boson and a light, pseudoscalar axion-like particle, a, where the Z boson decays to a pair of electrons or muons and the a particle decays to a pair of photons. The search is performed using $139\,\text{fb}^{-1}$ proton-proton LHC collision data at $\sqrt{s} = 13\,\text{TeV}$ collected by the ATLAS detector between 2015 and 2018. The mass of a is assumed to be between 0.1 GeV and 10 GeV and the data are analysed in two selection categories; the merged category and the resolved category. Events are selected to the merged category if both photons from the a decay are reconstructed in the ATLAS calorimeter as a single cluster whereas resolved category events are such that they are separately reconstructed. The main background processes in this search are Z boson productions in association with photons or particle jets that are reconstructed as photons.

No excess is observed for the a mass range chosen in this analysis. The data is in agreement with Standard Model predictions with upper limits on the branching ratio $\text{BR}(h \to Za) \times \text{BR}(a \to \gamma\gamma)$ at 95 % confidence level found to vary from 0.1 % to 4 % depending on the mass value of the a particle.

Declaration

I hereby confirm this work is my own, except where other works are referenced. This work has not previously been submitted to any institute, including this one. This thesis does not exceed the relevant word count.

Adam James Ruby

Acknowledgements

The greatest thanks to my primary supervisor, Nikolaos Rompotis, for his leadership and guidance from day one. Nikos always went above and beyond to help me whenever I felt like I was struggling. I feel grateful for his patience and thank him for teaching me so much. He is an astonishing particle physicist and I have been very lucky to have him as my supervisor. I would also like to thank the rest of our small $h \to Za$ team, Cristiano, Ren-Jie and Florencia for supporting this project and working together to overcome all of the challenges. In particular to Cristiano, who always made time for me despite having many other important responsibilities. Cristiano's input to this project has been invaluable and the analysis would never have shaped in the way it has without his expertise. I would also like to thank Sergey Burdin whose guidance in my qualification task helped me learn new skills that I know will be very useful during my move to industry.

I would also like to thank CERN, ATLAS, and the wider sub-groups such as HLRS for providing our analysis with direction. Also, to all my friends and mentors in the Liverpool ATLAS group and the HEP department as a whole for being there whenever I was stuck and for keeping everything running on time.

I'd like to mention a special thank you to all of the coffee shops I visited during the writing up stage of my thesis. Most of the writing and reading was done in either Brasco Lounge on the Liverpool waterfront or Bean, the coffee shop below where I live. I thank the staff for their kindness in the times they let me stay a bit after closing to finish off a section. I'll pop in for a more relaxing drink now I'm done writing!

I could not have gotten this far, or be the person I am today, without all of the friends I've made during my PhD. The lunchtimes, the boat parties and the dancing have made the last few years definitely my most favourite. Thanks for being so

welcoming and for being there for me when I needed it most. I could not imagine this experience without my friends, especially during the COVID period. I am so fortunate to come from a city with a physics department filled with the best people to have shared this adventure with.

Most importantly, my sincere gratitude goes to my Mum and Dad. Their kindness and generosity has allowed me the time to complete this PhD. I generally don't think I could have submitted this work without their unconditional support. They make me incredibly happy and this work is solely dedicated to them both for everything they've done for me. Thank you.

Author contributions

The analysis presented in this thesis is related to the work 'Search for the decay of the Higgs boson to a Z boson and a light pseudoscalar particle decaying to two photons'. The research presented is the combined effort of 5 members of the ATLAS collaboration, each with varying roles. I, Adam Ruby, the author of this thesis, contributed to the majority of the content shown in this thesis. I contributed to the signal property studies that consequently led to the design of the categorisation criteria (Chapter 5.1), including carrying out the optimisation studies required for this. I also played a major part in producing the data sets at every selection stage.

In terms of the selection categories, I was involved with all aspects of the merged category (Chapter 7). This includes optimisation of the regions (Chapter 7.1.1), photon identification and isolation criteria studies (Chapter 7.1.2) and selection for best final discriminant (Chapter 7.1.3). I was responsible for the work that focused on fixing the Monte Carlo template in this category to sideband data (Chapters 7.1.4 and 7.1.5). This includes the work behind the normalisation of the background components as well as calculating the shape corrections and uncertainties for each. Time was also spent on the initial systematic uncertainties study including being responsible for the theoretical uncertainties for signal (Chapter 7.2.2).

Although most of my time was focused on the merged category, I also played a vital part in the resolved category, as I was the contact who produced the datasets for this selection stage. My key role in the resolved category was defining and validating the photon identification and isolation criteria (Chapter 6.2) as well as the the studies required for choosing the selection regions (Chapter 6.1). Again, similar to the merged category, I played a part in the initial studies for the systematic and theoretical uncertainties for signal (Chapter 6.7). I was also responsible for the final search interpretation to the m_a parameter space (Chapter 8.2). Contributions of other authors of the analysis are as follows:

- Cristiano Sebastiani: Analysis contact. Contributed to the resolved category in terms of background estimation (Chapter 6.5) and final fit (Chapter 6.8). In the merged category Cristiano led the post-fit studies (Chapter 7.2.3) and produced the final limit plots for the combination of both categories (Chapter 8.1). Cristiano also led the Monte Carlo requests for new signal and background samples for the majority of the time.

- Nikolaos Rompotis: Provided me with supervision throughout the entire project. Specifically Nikos contributed to the signal parametrisation of the signal for the resolved category (Chapter 6.4). Nikos was involved and helped with every stage of the analysis and generally led the decisions made throughout.

- Florencia Castillo: Led the spurious signal estimation studies (Chapter 6.6).

- Ren-Jie Wang: Present for the kick-off of the search and was responsible for the initial Monte Carlo maintenance at the early stages, before leaving ATLAS not long after.

Chapter 3.1 details the development of a visual inspection tool to eventually be used in the quality control procedure of the strip and pixel hybrids in the HL-LHC upgrade. This was the topic of my qualification task. The software in its entirety was written by myself. Scans and images of the hybrids were provided by Jon Taylor and Sven Wonsak who also work within the University of Liverpool's physics department.

The ATLAS experiment is a collaboration that involves over 3000 scientists and engineers. The search presented in this thesis could not have been studied without the efforts of the collaboration to produce the hardware and software that was required for such an analysis. In addition to the those mentioned by name, the analysis has been reviewed and also shaped by members of the editorial board and those involved in analysis sub-groups, such as those part of HLRS and Egamma who in particular helped with the validation of the photon identification and isolation criteria chosen.

Contents

List of Figures

List of Tables

Chapter 1

Theoretical Background and Motivation

The Standard Model [1, 2] is a mathematical model based on quantum field theory and gauge symmetries that describes the properties of the fundamental particles that make up the universe as well as their interactions. As of now, it has generally been successful in describing many phenomena in particle physics. Spontaneous electroweak symmetry breaking, a key feature of the Standard Model associated with generating mass for several particles, has recently been experimentally completed by the discovery of the Higgs boson at the Large Hadron Collider (LHC) [3,4]. However, despite its large success there is some phenomena the model fails to convincingly explain. For example, it does not include gravity, dark matter, dark energy and a convincing mechanism to create matter-antimatter asymmetry in the early universe. Naturalness and the hierarchy problem are also not answered. Axion-like particles (ALPs) could potentially help answer some of these questions and it's possible that they appear in the final states of rare Higgs boson decays [5].

The first part of this chapter gives an overview of the Standard Model, including what the Higgs mechanism is, and how the Higgs boson is produced at the LHC. Known issues of the model are also discussed. The second part of the chapter introduces ALPs, how they provide a potential solution to some of the features that make the Standard Model incomplete and how Run-II data from the LHC can be used to probe for such particles.

1.1 The Standard Model

The Standard Model is a quantum field theory based on gauge symmetry developed throughout the second half of the 20th century that aims to explain the fundamental interactions of particles. The elementary particles that make up the Standard Model are classified by their quantum numbers and grouped as either fermions or bosons. The most important categorisation is based on an intrinsic angular momentum property called spin, which is in units of $\hbar$, Planck's constant, with s denoting the spin quantum number. Fermions have $\frac{1}{2}$-integer spin whereas bosons have integer spin. Unlike bosons, fermions obey the *Pauli exclusion principle* which states that a single quantum state cannot be occupied by two or more identical fermions. Fermions are either categorised as leptons or quarks. Interactions between fermions are mediated by gauge bosons, by either of the three fundamental forces described in the Standard Model; the electromagnetic force, strong force and weak nuclear force. Each interaction is mediated by one or more bosons. For example, electromagnetic interactions are mediated by photons and weak interactions by $W^{\pm}$ or Z bosons [6,7].

Quarks interact with all three forces whereas leptons, such as electrons and muons, cannot interact with the strong. There are six types of quarks, known as flavours, that differ from one another based on their mass and charge. The quark flavours can be grouped into three pairs; top and bottom, charm and strange, and up and down. The 'up-type' half of the pair associates with a charge equal to $+\frac{2}{3}$ while the other 'down-type' quark has a charge of $-\frac{1}{3}$. Quarks are bound together by interacting with the strong force, according to their color quantum number, to form hadrons. *Colour confinement* explains the strong interaction at low energies in which color-charged particles such as quarks are confined together in colourless combinations [6]. Hadrons consisting of a combination of three quarks are known as baryons with those formed by a quark-antiquark pair are known a mesons. Fermions are further grouped into one of three generations, sometimes referred to as families. Fermions differ between generations based by their flavour quantum number and mass. Third generation fermions are heavier and less stable which means that after a relatively short lifetime will decay to the first generation fermion particle associated with their particular sub-type. Figure 1.1 shows a summary of the fundamental particles and which of the forces they interact with.

The three interactions in the Standard Model are described by the product of

three gauge symmetry groups:

$$SU(3)_C \otimes SU(2)_L \otimes U(1)_Y. \tag{1.1.1}$$

The notation $U(N)$ refers to unitary groups with N dimensions, with $SU(N)$ the subset in which the determinant of $U(N)$ is equal to one. The special group $SU(3)_C$ represents quantum chromodynamics (QCD) describing the strong interaction and the colour charge, C, state of the quark field. There are 8 massless vector boson generators of $SU(3)_C$ that mediate the strong interaction called gluons. $SU(2)_L$ describes the weak isospin where L indicates that the weak interaction applies only to fermions with left-handed chiral particle states, a quantum property described in Section 1.1.1. Gauge group $U(1)_Y$ is the symmetry group that describes hypercharge, where Y is the weak hypercharge quantum number. The electric charge, Q, is related to hypercharge and also to the third component of the weak isospin, I_3, by $Q = I_3 + \frac{1}{2}Y$, otherwise known as the Gell-Mann-Nishijima relation [8,9]. The weak isospin component for left-handed fermions can take the value of $I_3 = \pm\frac{1}{2}$. Right-handed fermions, and left-handed *anti*-fermions, have $I_3 = 0$ and form singlets that do not interact with $W^{\pm}$ bosons but can interact with the Z boson. The product of the two gauge symmetry groups $SU(2)_L$ and $U(1)_Y$ describes the interaction of fermions with the electroweak gauge bosons. The breaking of the electroweak symmetry is what allows fermions and bosons to gain mass and is described in more detail in Section 1.1.1.

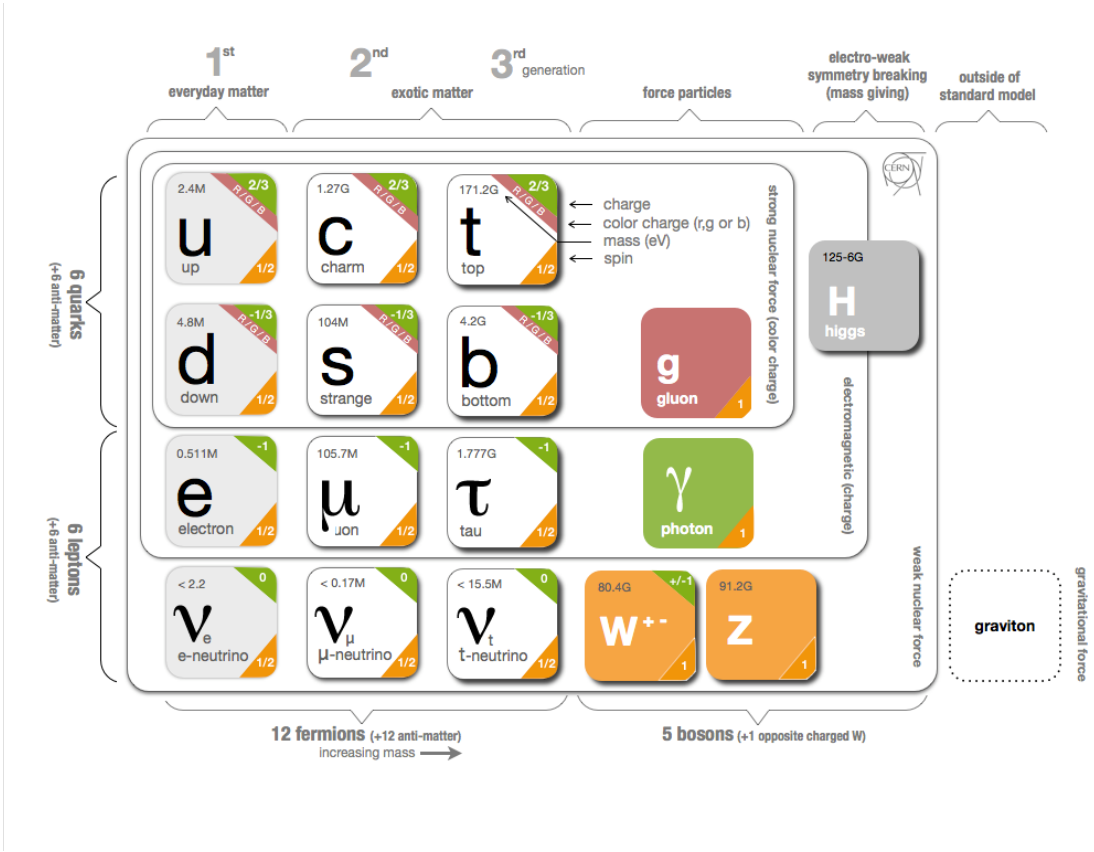

Figure 1.1: A summary of the Standard Model's elementary particles and their interactions. Reproduced from Ref. [10].

1.1.1 Electroweak interaction and the Higgs Mechanism

The relativistic quantum field theory that describes electromagnetic interactions in the Standard Model is called Quantum Electrodynamics (QED). QED is described by gauge symmetry group $U(1)$ and describes fermion-fermion interactions via the exchange of massless photons [1].

The weak interaction associates with fermions and the handedness of their chiral states. *Chirality* is a Lorentz-invariant property. A chiral fermion is such that it is an eigenstate of the chirality operator [2], γ^5. There are two chiral fermion states, one left-handed and one right-handed. There is a related quantity known as *helicity* which is not Lorentz-invariant although the eigenstates are the same as their chiral eigenstates in the limit $E >> m$, such as for massless particles [6]. Both left and right

[1] Although neutrinos are fermions, they do not interact by electromagnetic interactions but instead are only affected by the weak force.

[2] The γ^5 matrix is defined as $\gamma^5 \equiv i\gamma^0\gamma^1\gamma^2\gamma^3$ with $\gamma^0, \gamma^1, \gamma^2, \gamma^3$ representing the Dirac matrices.

handed fermions can couple to the Z boson however only those that are left-handed can undergo charged weak interactions mediated by the $W^{\pm}$ boson. The $W^{\pm}$ and Z bosons have mass with values of approximately 80 GeV and 91 GeV respectively, shown in Figure 1.1. Depending on the coupling, a consequence of having a mass of this magnitude leads to the bosons having short life-times in the order of 10^{-25} s. This means that weak interactions only occur at very short distances. The gauge symmetry group associated to the weak interaction is $SU(2)_L$.

The electromagnetic and weak interactions of quarks and leptons are combined as two aspects of the same force described by a mechanism first proposed by Glashow [11], Weinberg [12] and Salam [13] that has gauge symmetry group which is the product of $SU(2)_L$ and $U(1)_Y$ known as the electroweak interaction. The generators I_3 and Y for $SU(2)_L$ and $U(1)_Y$ respectively, described previously in Section 1.1, give rise to four non-physical massless gauge fields that mediate the interaction. These are three weak isospin W bosons $W^i_\mu (i = 1, 2, 3)$ and a weak hypercharge boson B_μ. The physical states for the $W^{\pm}$ field are linearly combined from W^1_μ and W^2_μ only whereas the physical states for the photon and Z boson come from the mixing of B_μ and W^3_μ fields. The combinations are as such:

$$\begin{aligned} W^{\pm}_\mu &= \frac{1}{\sqrt{2}}(W^1_\mu \mp W^2_\mu), \\ Z_\mu &= W^3_\mu \cos\theta_w - B_\mu \sin\theta_w \text{ and} \\ A_\mu &= W^3_\mu \sin\theta_w + B_\mu \cos\theta_w. \end{aligned} \tag{1.1.2}$$

The value of θ_W is known as the *weak-mixing angle* and quantifies the relative strengths of the weak and electromagnetic forces by

$$\tan\theta_W = \frac{g'}{g}, \tag{1.1.3}$$

where g and g' are the $SU(2)$ and $U(1)$ coupling constants respectively and has been experimentally determined as 0.23121 ± 0.00017 [14].

The theory described thus far is only gauge invariant if the particles are massless. This means that the experimentally observed massive $W^{\pm}$ and Z bosons are forbidden due to not being invariant under this gauge transformation. This contradiction motivated the formulation of a mechanism called Spontaneous Electroweak Symmetry Breaking (EWSB) proposed by Higgs [15], Brout and Englert [16], Guralnik, Hagen and Kibble [17] to solve this issue. EWSB describes the spontaneous

symmetry breaking of $SU(2)_L \otimes U(1)_Y$. A mechanism proposed to achieved this is the *Higgs mechanism*. The Higgs mechanism introduces a complex scalar doublet under $SU(2)_L$ that has a non-zero vaccum expectation value (VEV) yet still also preserves gauge symmetry. The complex scalar doublet is written as

$$\phi = \begin{pmatrix} \phi^+ \\ \phi^0 \end{pmatrix} = \frac{1}{\sqrt{2}} \begin{pmatrix} \phi_1 + i\phi_2 \\ \phi_3 + i\phi_4 \end{pmatrix}, \tag{1.1.4}$$

with ϕ_i representing a real field and the sign associated with $\phi^{+/0}$ corresponding to the electric charge. The most general renormalisable scalar potential, V, that is gauge invariant can be given as

$$V(\phi) = \mu^2(\phi^\dagger\phi) + \lambda(\phi^\dagger\phi)^2, \tag{1.1.5}$$

where μ and λ are free parameters. For spontaneous symmetry breaking to be satisfied these parameters are required to be $\lambda > 0$ and $\mu^2 < 0$. The shape of this potential in the complex imaginary plane of $V(\phi)$ and ϕ, illustrated in Figure 1.2, shows a non-zero VEV. The potential is not symmetric at this minimum.

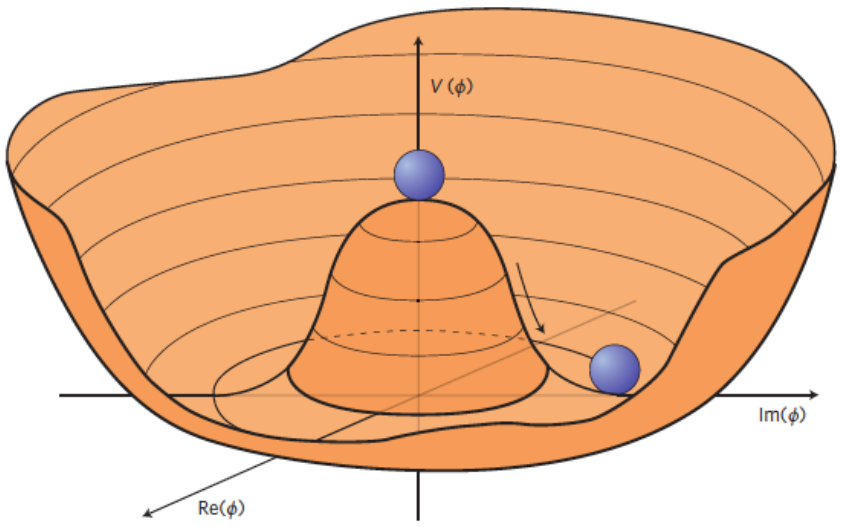

Figure 1.2: Illustration of the Higgs potential in the complex imaginary plane of $V(\phi)$ and ϕ. The movement from the central state to the bottom of the potential breaks spontaneously the rotational $U(1)$ symmetry. Reproduced from Ref. [18].

Typical values chosen for the physical vacuum of $\phi_4 = 0$ and $\phi_3 = |\phi_0|$ means

that the minimum of the potential occurs at

$$|\phi|^2 = -\frac{\mu^2}{2\lambda}, \tag{1.1.6}$$

corresponding to a VEV of

$$\nu = \sqrt{\frac{|\mu^2|}{\lambda}}. \tag{1.1.7}$$

The Lagrangian corresponding to the Higgs field is in the form of

$$\mathcal{L}_{Higgs} = (D_\mu \phi)^\dagger (D^\mu \phi) - V(\phi^\dagger \phi), \tag{1.1.8}$$

with D_μ representing the covariant derivative in terms of the electroweak gauge fields, hypercharge field, Pauli matrices $\sigma^a, a = 1, 2, 3$:

$$D_\mu = \partial_\mu - \frac{i}{2} g W_\mu^a \sigma^a - \frac{i}{2} g' B_\mu. \tag{1.1.9}$$

According to Goldstone's theorem [19], each broken continuous symmetry has an associated massless scalar field which is known as a *Goldstone boson*. As a consequence of the extra degrees of freedom from electroweak symmetry breaking the longitudinal polarisation of the gauge bosons 'absorb' the Goldstone bosons degrees of freedom. This is interpreted as the gauge bosons gaining mass. The mixing of the four generators of the electroweak symmetry results in four eigenstates; three massive $W^\pm$ and Z vector bosons corresponding to the breaking of $SU(2)_L$ symmetry and also a massless photon.

By expanding the complex doublet given by Equation 1.1.4 as a flucation around the minimum of ν, ϕ can be expressed in terms of ν and a scalar field, $h(x)$:

$$\phi = \frac{1}{\sqrt{2}} \begin{pmatrix} 0 \\ \nu + h(x) \end{pmatrix}. \tag{1.1.10}$$

The scalar field in this instance describes a physical Higgs Boson. By substituting this into the $(D_\mu \phi)^\dagger (D^\mu \phi)$ term of $\mathcal{L}_{Higgs}$ one can derive the mass relations for lowest order W and Z bosons in terms of the VEV, g and the weak mixing angle parameters as:

$$\begin{aligned} m_W &= \frac{g\nu}{2} \text{ and} \\ m_Z &= \frac{1}{2} \frac{g\nu}{\cos\theta_W}. \end{aligned} \tag{1.1.11}$$

The free parameters that form these expressions can be determined experimentally and indeed have been confirmed to be $m_W = 80.379 \pm 0.012\,\text{GeV}$ and $m_Z = 91.188 \pm 0.002\,\text{GeV}$ [14, 20, 21]. Fermions also acquire mass via interactions between the Higgs field VEV and Yukawa couplings. The Higgs mechanism predicts a scalar boson, H, with it's mass:

$$m_H = 2\lambda\nu^2, \tag{1.1.12}$$

that can be confirmed experimentally and as such is a way of verifying the mechanism. On the 4$^{\text{th}}$ July 2012, half a century after the mechanism was first proposed, the ATLAS and CMS experiments at CERN confirmed the discovery of a Higgs-like boson with a mass of approximately 125 GeV that also matched properties compatible with what was expected in the Standard Model [3, 4].

1.1.2 SM Higgs production and decay in the LHC

There are several mechanisms that contribute to Standard Model Higgs boson production in proton-proton collisions at the LHC. The most dominant is gluon-gluon fusion (ggF) which is the process that occurs when gluons from each proton in the high energy collision interact with one another. The second most common mechanism is the annihilation of the $W^{\pm}$ and Z bosons known as vector-boson fusion (VBF). The Higgs boson can be produced at the LHC also by Higgs-strahlung (VH) or t-associated production (ttH) however, although both have been observed [22, 23], are less likely to occur [24]. The lowest order Feynman diagrams and the cross-sections for $m_H = 125\,\text{GeV}$ at $\sqrt{s} = 13\,\text{TeV}$ for each Higgs production mechanism discussed are shown in Figure 1.3 and Table 1.1.

Figure 1.4 displays the branching ratio values for Higgs boson mass between 90 GeV and 200 GeV. What this figure shows is that for a Standard Model Higgs boson with a mass close to 125 GeV the decay channel $h \to bb$ is most likely to occur. The LHC however, due to the nature of how protons colliding at high energies interact, has a large multi-jet production cross-section which makes discriminating this type of signal relatively more difficult compared to others using data from the first run period. Instead, the discovery of the Higgs boson was determined by probing the $h \to \gamma\gamma$ and $h \to ZZ \to 4\ell$ channels as these signatures are easier to discriminate against backgrounds [25, 26].

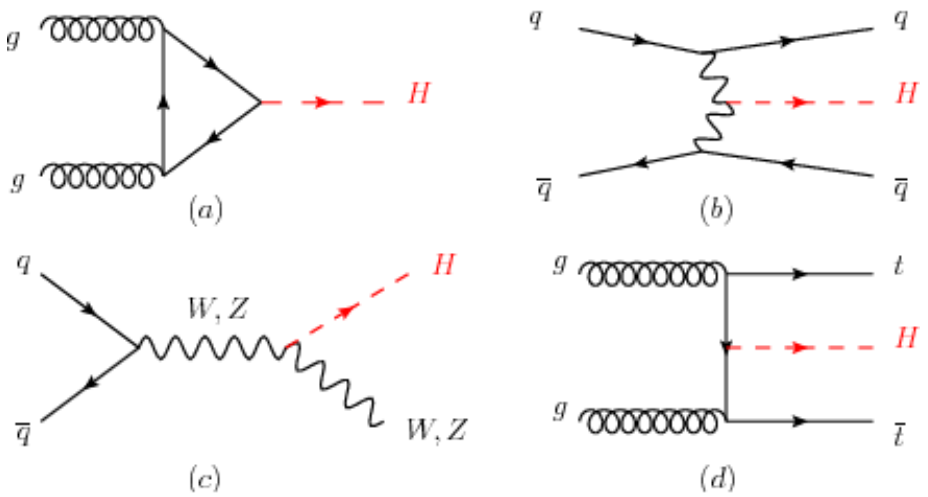

Figure 1.3: The four dominant mechanisms for Higgs production at the LHC [24]. The processes shown are (a) gluon-gluon fusion, (b) vector-boson fusion, (c) Higgs-strahlung and (d) t-associated production.

Process	σ **(pb)**	**Scale uncertainty (%)**	**PDF+α_s (%)**
ggF	48.6	$^{+4.6}_{-6.7}$	$\pm$ 3.9
VBF	3.8	$^{+0.4}_{-0.3}$	$\pm$ 2.1
WH	1.4	$^{+0.5}_{-0.7}$	$\pm$ 1.9
ZH	0.88	$^{+3.8}_{-3.1}$	$\pm$ 1.6
$t\bar{t}H$	0.51	$^{+5.8}_{-9.2}$	$\pm$ 3.6

Table 1.1: Higgs boson production cross sections for $m_H = 125\,\text{GeV}$ at $\sqrt{s} = 13\,\text{TeV}$, for which the W and Z bosons decay leptonically. Table also includes theoretical uncertainties due to renormalisation and factorisation scales and also PDF+a_s [27].

Since the announcement of the discovery in 2012, more data collected at the LHC has led to more precise measurements of the $h \to \gamma\gamma$ and $h \to ZZ \to 4\ell$ couplings and further channels predicted by the Standard Model have since been observed. For example, an observation of the $h \to \tau\tau$ channel was observed by the ATLAS and CMS collaborations in 2018 [28, 29] as was $h \to bb$ [22, 30]. Figure 1.5 summarises the Higgs boson mass value measurements in the $h \to \gamma\gamma$ and $h \to ZZ \to 4\ell$ decay channels for different data collection periods. The same figure also shows cross section measurements for various Higgs boson production mechanisms.

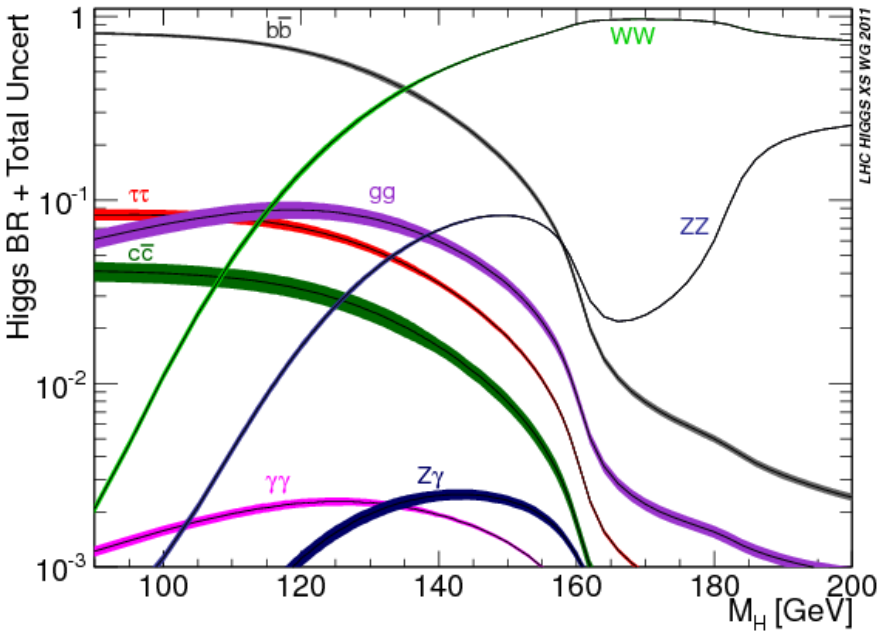

Figure 1.4: Standard Model Higgs boson decay branching ratios for m_H window 90 GeV to 200 GeV [31]. The size of each band represents the theoretical uncertainty for each decay channel.

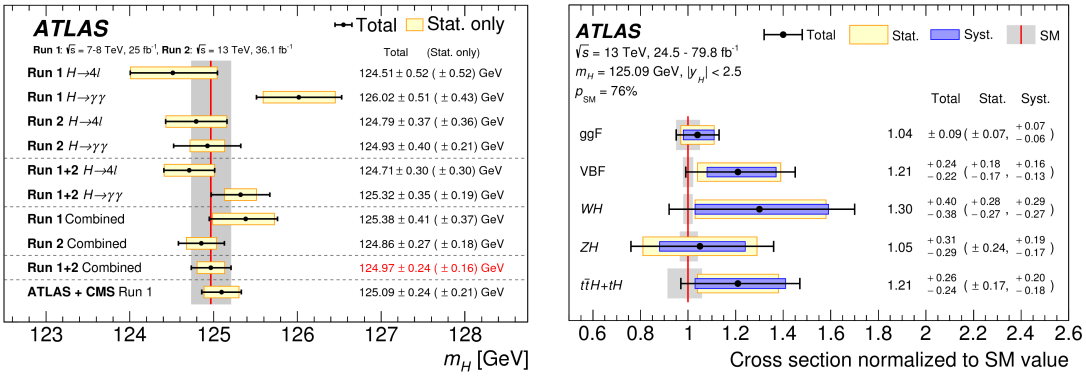

Figure 1.5: (a) A summary for Higgs boson mass measurements, in GeV, for various decay channels and run periods for individual and combined analyses and also the combined measurement for Run-I made by ATLAS and CMS. The yellow boxes represent the statistical-only uncertainty whereas the black bars are the total uncertainty. The red vertical line is the central value for the combined ATLAS Run-I and Run-II measurement with the corresponding grey shaded column being the total uncertainty [31]. (b) Measured cross sections for the ggF, VBF, WH, ZH and $t\bar{t}H + tH$ processes normalised to the Standard Model predicted values. The statistical, systematic and total uncertainties are represented by the yellow, blue and black bars respectively with the grey shaded areas corresponding to the theoretical uncertainty [32].

1.1.3 Weaknesses of the Standard Model

The Standard Model is an extremely successfully theory that has repeatedly been consistent with many experimental results over a number of decades. Particles predicted by the model have been observed at the LHC and are also in agreement with results from other collider experiments. These include experiments at the Tevatron accelerator in Fermilab [33] and SLAC [34], both located in the USA, and also the Large Electron-Positon Collider (LEP) at CERN [35].

Despite the overwhelming success of the Standard Model so far, there are fundamental issues that the model currently fails to explain, meaning that it is incomplete. An example of this is the inclusion of gravity. Despite being very well described for large systems it is difficult to describe higher order quantization of gravity with a fully consistent quantum field theory.

The asymmetry between matter and anti-matter content in the universe is also not convincingly described in the model. Electroweak baryogenesis, a mechanism to explain this asymmetry, could occur as part of the Standard Model only if what are known as the Sakharov conditions are met. However, the experimental values of quark generation mixing (Cabibbo-Kobayashi-Maskawa mixing [36]) and the Higgs boson mass imply these are unlikely to be met and therefore it is probable the model should be extended.

Other open questions of the Standard Model include what are known as the *Hierarchy Problem* and *Gauge Coupling Unification*. The hierarchy problem concerns the violation of *naturalness* in the difference between the observed Higgs boson mass and Lagrangian parameter *bare* mass due to the multiple contributions from on-loop fermionic quantum corrections coupled to the Higgs boson mass. Figure 1.6a shows an example of one-loop corrections with Higgs boson mass coupling. Gauge coupling unification on the other hand is the Standard Model prediction that the energy dependence of the coupling constants for the electromagnetic, weak and strong interactions converge at a single point. Figure 1.6b however shows that there is no point at which all three forces converge.

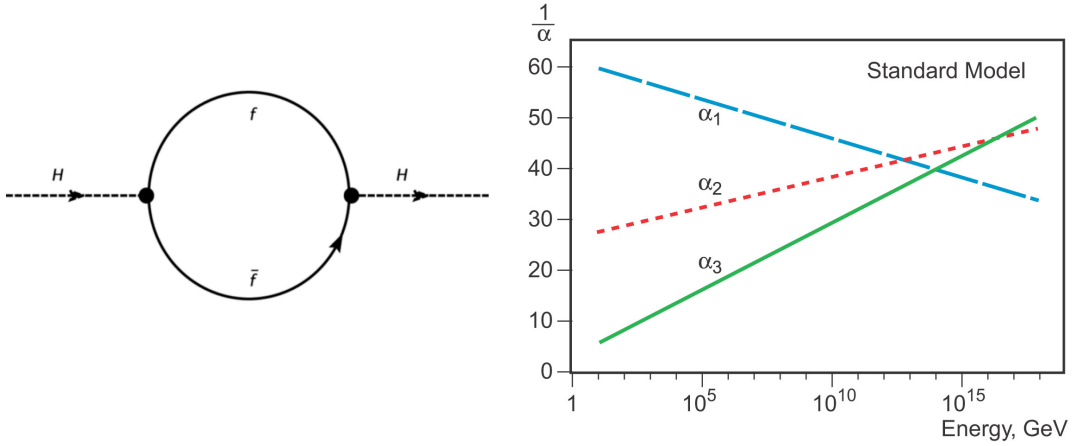

(a) (b)

Figure 1.6: (a) Feynman diagram of fermionic corrections to the Higgs boson mass at one-loop level. (b) Standard Model coupling constants as a function of energy for the electromagnetic (dashed-blue), weak interaction (dotted-red) and strong force (solid-green) [37].

Phenomena not predicted by the Standard Model that are more relevant to the focus of this thesis includes the strong CP-problem, the experimental $(g-2)_\mu$ discrepancy with theory and the existence of dark matter. The strong CP-problem is a theoretical argument that the Standard Model does not forbid the breaking of charge-parity (CP) symmetry in strong interactions. It is possible this violation could occur, however, experimentally this is suppressed. There is however a mechanism that explains this, proposed by Peccei and Quinn in 1977 [38]. This mechanism introduces a new pseudoscalar particle called an *axion*, discussed in Section 1.2, similar to the way the Higgs mechanism introduced the Higgs boson. There are also strong signs that the Standard Model's theoretical value of the anomalous magnetic moment of the muon, given by

$$a_\mu = \frac{(g-2)_\mu}{2}, \tag{1.1.13}$$

differs to what is calculated experimentally. Parameter g in this expression characterises the magnetic moment of the muon. The most recent results regarding this discrepancy come from an experiment conducted at Fermilab [39]. This result, and the result from a similar experiment conducted at the Brookhaven National Laboratory [40] average a deviation from theory of 4.2σ [39].

The Standard Model does not include the existence of dark matter, a phenomenon for which there is evidence from astronomical observation. The most direct evidence for dark matter is found by examining the *rotation curves* of galaxies [41]. Here the

galaxies circular velocity as a function of distance from the galactic center prediction only fits to data when including also dark matter (found in galactic halos). It is estimated that dark matter accounts for approximately a quarter of what makes up the universe and about 85 % of all matter. Dark matter is assumed weakly interacting matter and is therefore very difficult to detect. Currently there are no Standard Model particles suited as a dark matter candidate meaning that it is likely the model requires to be extended.

Axion-like particles (ALPs), described in detail in Section 1.2, are hypothetical bosons that feature in the decay channel focused in this thesis. They appear in common in extensions to the Standard Model as a way of addressing the stong CP-problem and sometimes as a suitable dark matter candidate. If ALPs couple to muons and photons, similarly to the process focused in this analysis, then it is also possible that the deviation seen experimentally for a_μ could also be explained [5].

1.2 Axion-like particles and $h \to Za$

As pointed out in the previous section, there are aspects of the Standard Model that are not fully described. An example that has already been mentioned is the absence of QCD CP-violation observed experimentally in strong interactions. The QCD Lagrangian contains a plausible term not forbidden by the Standard Model symmetries or renormalisability:

$$\theta \frac{g^2}{32\pi^2} G^{a\mu\nu} \tilde{G}_{a\mu\nu}, \tag{1.2.1}$$

were g is the strong coupling constant, θ the dimensionless undetermined CP-violating parameter and $G^{a\mu\nu}$ and $\tilde{G}_{a\mu\nu}$ the tensors describing the gluon field and dual field strengths respectively. In the Standard Model, this term leads to a neutron electric dipole moment [3]

$$|d_n| \approx \frac{e}{m_n} \left(\frac{m_q}{m_n} \right) |\bar{\theta}| \approx 10^{-16} \; |\bar{\theta}| \; e \text{ cm}. \tag{1.2.2}$$

Currently, the upper band of the experimental limit is $|d_n| \times 10^{-26} e\,\text{cm}$ constrain-

[3] The physical CP-violating parameter, $\bar{\theta}$, is defined such that $\bar{\theta} \equiv \theta + \arg \det M$. M is the light quark mass matrix, $(m_u, m_d, m_s) \times I$, where m_u, m_d and m_s are the up, down and strange quark masses respectively and I is the 3×3 identity matrix [42].

ing the physical violating parameter $|\bar{\theta}| \leq 10^{-10}$. The smallness of $|\bar{\theta}|$ is not respected in perturbation theory and as such is a problem of naturalness, calling for an explanation [43]. One elegant and attractive solution is one proposed by Peccei-Quinn [38]. They present θ as a $U(1)$ global symmetry that is spontaneously broken at some scale f_a predicting an associated pseudo Goldstone boson, called the axion. After the spontaneous breaking, the CP violating term in the QCD Langrangian is cancelled by the VEV of the field [44]. Potential axions with mass values associated to f_a at the electroweak scale have been ruled out [45, 46]. The Peccei-Quinn concept has been instead generalised for larger values of f_a and introduced the possible existence of axion-like particles. ALPs are included in a number of scenarios beyond the Standard Model (such as string theory). ALPs have properties similar to that of axions in that they are bosons breaking $U(1)$ symmetry however their possible mass values and couplings are not related.

The possible existence of ALPs extends the case beyond only solving the strong CP-problem. The discrepancy between the predicted and experimental values of the anomalous magnetic moment of the muon, described in Section 1.1.3, could well be explained by indirect ALP effects on lepton electromagnetic dipole moments. There is good consensus that the value of a_μ cannot be explained by hadronic loop uncertainties alone, implying new physics as a reasoning. It is postulated that an ALP with large coupling to muons and photons might be able to explain the discrepancy [47]. The decay rates of such a coupling is given by [5]

$$\Gamma(a \to \gamma\gamma) = \frac{4\pi\alpha^2 m_a^3}{\Lambda^2} C_{\gamma\gamma}^2. \tag{1.2.3}$$

Figure 1.7 shows the Feynman diagrams for ALP-induced one-loop order contributions to a_μ. ALPs are also a good dark matter candidate as they are light pseudoscalars that interact less frequently with matter.

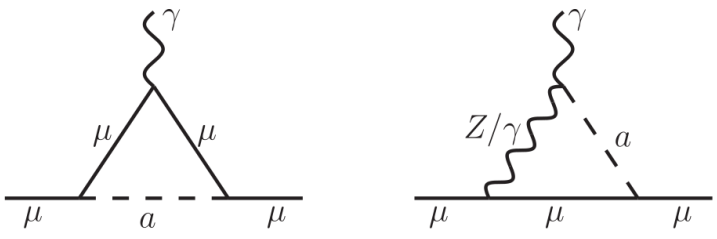

Figure 1.7: ALP-induced one-loop contribution to a_μ.

ALP-photon couplings as a function of m_a have been constrained by various particle physics experiments and cosmology. This includes analysing distortions of the cosmic microwave background spectrum [48] and measuring neutrino burst lengths from Supernova SN1987a [49]. Constraints for ALPs with $m_a < 4$ eV come from experiments such as the CERN Axion Solar Telescope [50] and also 'light-shining-through-a-wall' experiments [51]. Multiple studies exploring long-lived or invisibly decaying ALPs at the LHC have also been carried out. This includes an interesting channel probing decays involving two ALPs by the process $h \to aa$. In Ref. [52], ALPs decaying into two b-quarks reconstructed as a single jet is searched for. Here the analysis makes use of the fact the Higgs boson is produced in association with a Z-boson to allow for easier event triggering. Alternatively, searches that include at least one ALP decaying into muons allow for ten times better resolution of the ALP mass compared to ALPs with b-quark final states. In Ref. [53], $h \to 4\tau$ is studied which allows one of the tauon particles from the ALP decay to decay into a muon. Similarly, decay modes $h \to 2\tau 2\mu$ and $h \to 2b2\mu$ have also been studied [54, 55]. Another interesting strategy is to search for ALPs in photon collisions from ultra-peripheral heavy ion collisions (UPC), such as the $\gamma\gamma \to a \to \gamma\gamma$ process. This process has been analysed by both ATLAS and CMS [56,57]. Invisible ALPs, or those that are long lived and escape decaying within the detector, can be searched for in kinematically unbalanced decays associated with another detectable particle. These are referred to as *mono-X* signatures with example decay modes being $gg \to ag$ [58], $h \to aZ$ [59] and $Z \to a\gamma$ [60] though the ALP mass cannot be reconstructed in this way. No significant excess of events have been observed over the Standard Model background as of yet [61]. Though there has been much activity for ALP searches at the LHC, there has been however less activity for searches related to similar channel $h \to Za$, the Higgs boson decay which is the focus of this thesis. Suggested in Ref [5], the absence in theoretical attention for such a channel is likely due to no dimension-5 operator mediating the decay at tree-level. Despite this, they show fermion-loop graphs arising at this order and also dimension-7 tree-level contributions can induce rates similar to $h \to Z\gamma$ predicted by the Standard Model, a search already well studied at the LHC [62]. The decay relevant to the search presented in this thesis is $h \to Za \to \ell^+\ell^-\gamma\gamma$, where the Z boson decays into two leptons and the ALP to a photon pair. The yellow areas in Figure 1.8 show the ALP mass and photon coupling constraints from various experiments. The light green contour is the possible $h \to Za$ parameter region that can be probed using LHC data at 300 fb^{-1} integrated luminosity.

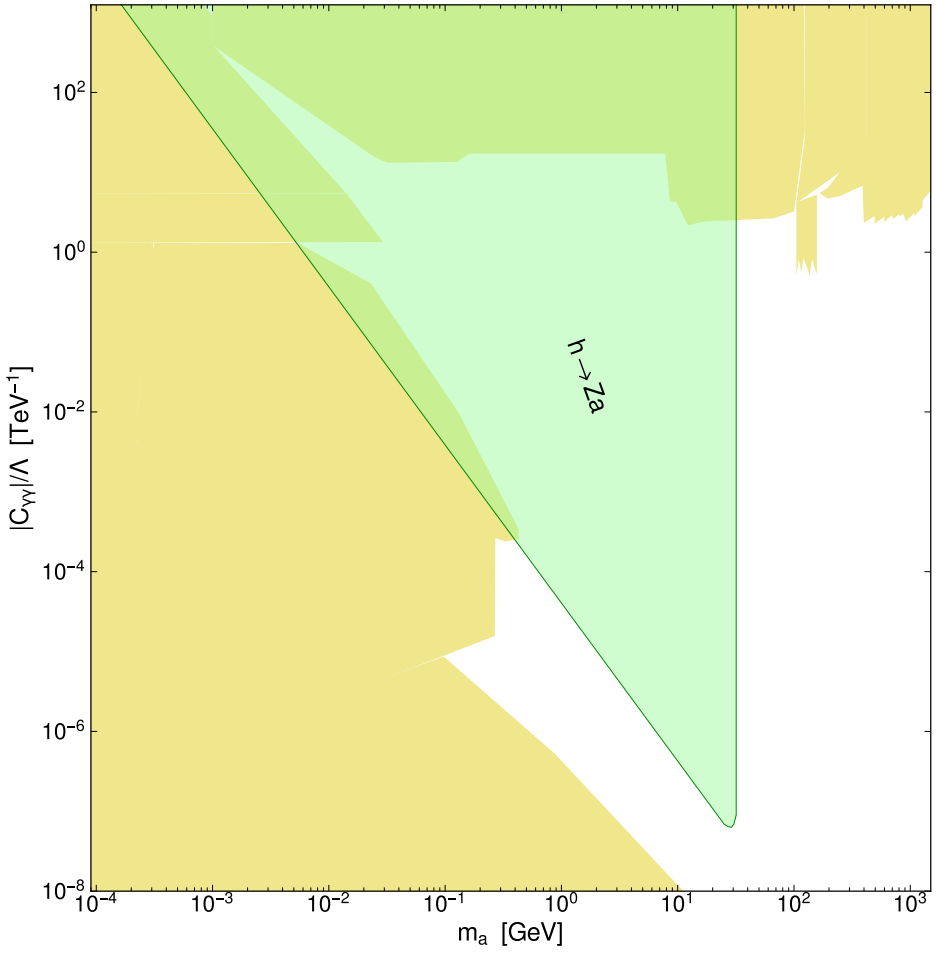

Figure 1.8: Constraints on ALP mass and photon coupling values from a number of listed experiments represented by the coloured areas. The light green contour represents the parameter region that can be probed by LHC data (for 300 fb^{-1} integrated luminosity). The lines shown on this plot are from Ref. [5].

At tree-level, the decay rate of $h \to Za$ is represented as

$$\Gamma(h \to Za) = \frac{m_h^3}{16\pi\Lambda^2} C_{Zh}^2 \lambda^{\frac{3}{2}} \left(\frac{m_Z^2}{m_h^2}, \frac{m_a^2}{m_h^2} \right), \tag{1.2.4}$$

where $\lambda(x, y) = (1 - x - y)^2 - 4xy$. From equations 1.2.3 and 1.2.4 the lifetime of the ALP decay for different photon coupling values and $h \to Za$ branching ratio as a function of ALP mass can be plotted. The branching ratio for the ALP

decay BR($a \to \gamma\gamma$) is assumed to be 100 % so that the lifetime is a function of $\Gamma(a \to \gamma\gamma)$ only. Figure 1.9a shows that stronger coupling values associate with shorter $a \to \gamma\gamma$ lifetimes and that ALPs at lower masses are more likely to live longer and perhaps decay outside of the detector. Figure 1.9b shows that stronger Zh couplings are associated with larger branching ratios although this doesn't change much with ALP mass below 10 GeV. This analysis uses monte carlo generators to simulate the $h \to Za$ decays with $C_{\gamma\gamma}/\Lambda$ and C_{Zh}/Λ values chosen to be 0.001 TeV^{-1} and 1.00 TeV^{-1} respectively. More information on the signal generation is given in Section 4.1.1.

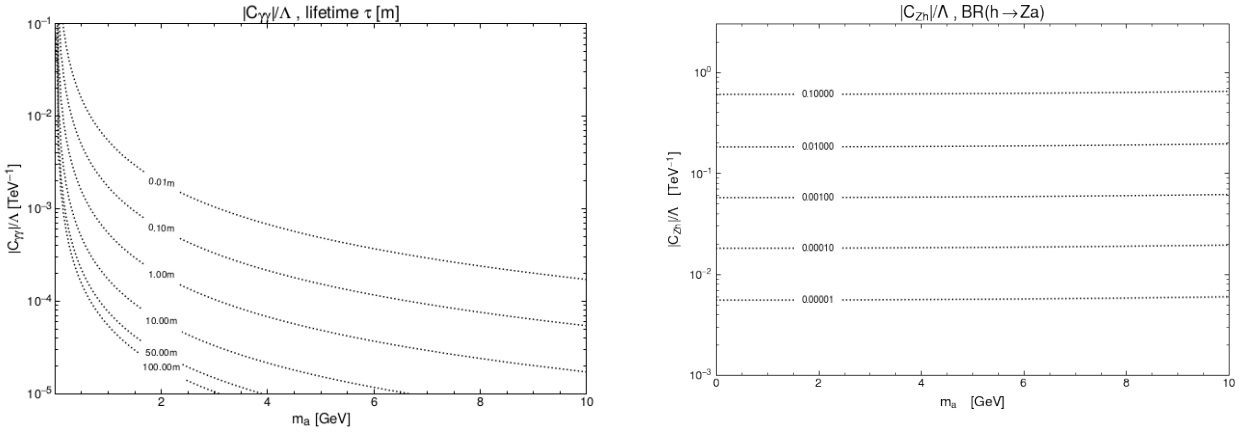

(a) (b)

Figure 1.9: Top plot shows $|C_{\gamma\gamma}|/\Lambda$ as a function of ALP mass. Contour lines correspond to the lifetime of the $a \to \gamma\gamma$ decay in meters. Bottom plot shows $|C_{Zh}|/\Lambda$ as a function of ALP mass with the contour lines corresponding to branching ratio values of $h \to Za$. BR($a \to \gamma\gamma$) = 100 % connecting $\Gamma(a \to \gamma\gamma)$ only to the lifetime.

Chapter 2

Experimental Apparatus

2.1 Experimental Apparatus

In particle physics there is a variety of different ways to collect evidence, one example is by colliding particles together. Particle collision experiments employ accelerators to accelerate particles, such as electrons or protons, to high energies with velocities close to the speed of light in opposite directions before they are brought to collide with one another. In the case of proton-proton collisions, gluons and quarks can interact and occasionally form heavier particles that decay into lighter particles with properties that can be measured by particle detectors.

The Large Hadron Collider (LHC) [63] is an example of a particle accelerator that can accelerate protons which then collide at specific interaction points where the particles produced from the collisions are measured at detectors such as the ATLAS detector. In this thesis, a search for rare beyond Standard Model Higgs boson decay $h \to Za \to \ell\ell\gamma\gamma$ is performed using collision data from the LHC and ATLAS. This chapter will describe both of these in detail including how they operate.

2.2 The Large Hadron Collider

The LHC is the world's largest particle accelerator at 27 km in circumference and is located at an average depth of 100 m crossing the border of Switzerland and France at CERN (Conseil Europeen pour la Recherche Nucleaire) near Geneva. The LHC was proposed in the early 1980's and in December 1994 the CERN council approved the idea. As a result of the successful collaboration from scientists and engineers

across the world, construction of the LHC began in 1998, using the existing tunnel of LEP [64] to accelerate hadrons instead of electrons and positrons, and was completed in 2008. The two-ring superconducting hadron accelerator is capable of accelerating protons and also heavy ions, such as lead-ions. During the years 2015 and 2018, in the data-taking period known as Run-II, the LHC operated at a center of mass energy for proton-proton collisions of 13 TeV and also accelerating heavy ions up to 2.8 TeV per nucleon.

Hadrons are injected into the LHC after firstly completing a journey through multiple acceleration stages around what is known as the acceleration complex. An overview of the entire CERN accelerator complex is shown in Figure 2.1. In proton-proton collisions, hydrogen atoms that are initially contained within a hydrogen source, are stripped of their electrons leaving only the protons. From here, the protons are initially accelerated using Linac-2, a linear accelerator firstly commissioned in 1978 [65], before reaching the Proton Synchrotron Booster (PSB) and then the 628 m in circumference Proton Synchrotron (PS) where the beam is accelerated up to 26 GeV. It is further accelerated aided by the 1,317 electromagnets and 744 dipoles of the Super Proton Synchrotron (SPS) at which point the beam eventually enters the two beam pipes of the LHC in discontinuous chains of particles known as "bunches". Proton bunches contain an order of 10^{11} protons with the spacing between each bunch set at approximately 25 ns. Beams in the LHC travel in opposite directions and are transferred around the complex where they are bent by 1,232 superconducting dipole magnets and focused by 392 quadrupoles, operating at a magnetic field strength of 8.33 T and cooled by helium to a temperature of 1.9 K. As the proton beams travel through the LHC, they are boosted and accelerated to 7 TeV by an electric field in the radio frequency cavities (RF).

There are four interaction points at different locations of the LHC ring where the particle collisions can occur. The properties of the particles produced as a result of these collisions are measured at detectors surrounding the collision points. Namely these are the ATLAS (A Toroidal LHC ApparatuS) detector [66], CMS (Compact Muon Solenoid) [67], LHCb (Large Hadron Collider beauty experiment) [68] and ALICE (A Large Ion Collider Experiment) [69]. ATLAS and CMS are both general-purpose detectors whereas LHCb is designed to focus on b-physics and ALICE to study the physics of strongly interacting matter at extreme energy densities.

Long shutdown 2 started on 10th December 2018 for the purpose of upgrading the LHC and the detectors for Run-III, which began in the summer of 2022. The upgrade will further the potential physics reach possible at the LHC, in a configuration called the High Luminosity LHC (HL-LHC). The aim is to increase the instantaneous luminosity (total number of proton-proton collisions in a unit of time) from $\mathcal{L}$=$10^{34}\,\mathrm{cm}^{-2}\mathrm{s}^{-1}$ at present by a factor of five and the total integrated luminosity (total number of collisions over a period of time) by a factor of ten. The upgrade requires new technological innovations such as the physical processes for beam collimation and 100 meter-long high-power superconducting links with negligible energy dissipation, taking several years of global research and development efforts [70].

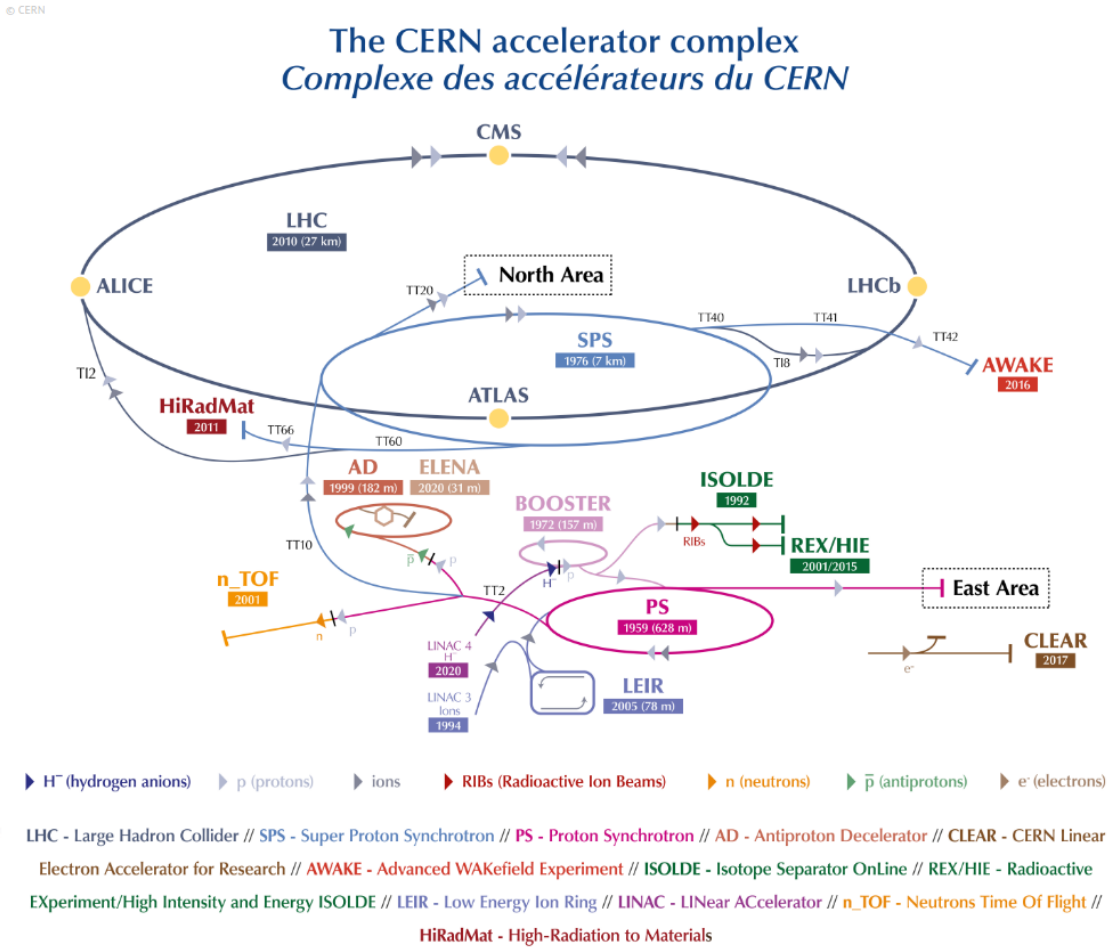

Figure 2.1: Overview of the CERN accelerator complex. Reproduced from Ref. [71].

2.2.1 Luminosity and Pile-up

Accelerating protons to high energies is important for particle collision physics however so too is the rate at which these collisions occur. In particle collision experiments, the number of collisions per unit time for a unit area is known as a quantity called luminosity. Instantaneous luminosity, $\mathcal{L}$, has units of $\text{cm}^{-2}\text{s}^{-1}$. For a Gaussian beam distribution, $\mathcal{L}$ is described as:

$$\mathcal{L} = \frac{N_b^2 n_b f_{rev} \gamma_r}{4\pi\epsilon_n \beta_*} F, \tag{2.2.1}$$

with N_b^2 being the number of protons in a bunch and n_b the number of bunches per beam. The term f_{rev} represents revolution frequency of the particles (approximately 11.2kHz for the LHC), γ_r the relativistic gamma factor and ϵ_n the normalised transverse beam emittance which is a measure of average spread of particle coordinates in position-momentum phase space. The amplitude beta function, equal to $\frac{\sigma_x \sigma_y}{\epsilon_n}$ where σ_x and σ_y are the horizontal beam sizes (approximately 2.5μm for the LHC), is denoted by β_*. The final term, F, is the geometric luminosity reduction factor due to the crossing angle at the interaction point [72]. At the LHC $\mathcal{L}$=10^{34} $\text{cm}^{-2}\text{s}^{-1}$, and at $\sqrt{s} = 13\,\text{TeV}$ means that the proton bunches collide at a rate of approximately 40 million times per second.

The total integrated luminosity, L, is related to the instantaneous luminosity by

$$L = \int \mathcal{L} dt \tag{2.2.2}$$

and as such the number of events for a particular interaction, $N_{pp\to X}$, with cross-section $\sigma_{pp\to X}$, can be calculated by

$$N_{pp\to X} = \sigma_{pp\to X} L. \tag{2.2.3}$$

This relation is paramount to the fact that the LHC must aim for greater luminosities in order to further the reach of detecting physics from rare particle decay signatures. In this regard, Figure 2.2 shows the total integrated luminosity delivered by the LHC over the entire Run-II period (2015–2018) and also that recorded by ATLAS. The proportion of total integrated luminosity recorded by ATLAS was very high, as too was the fraction suitable for physics analysis which remained at approximately 95 % throughout this time [73].

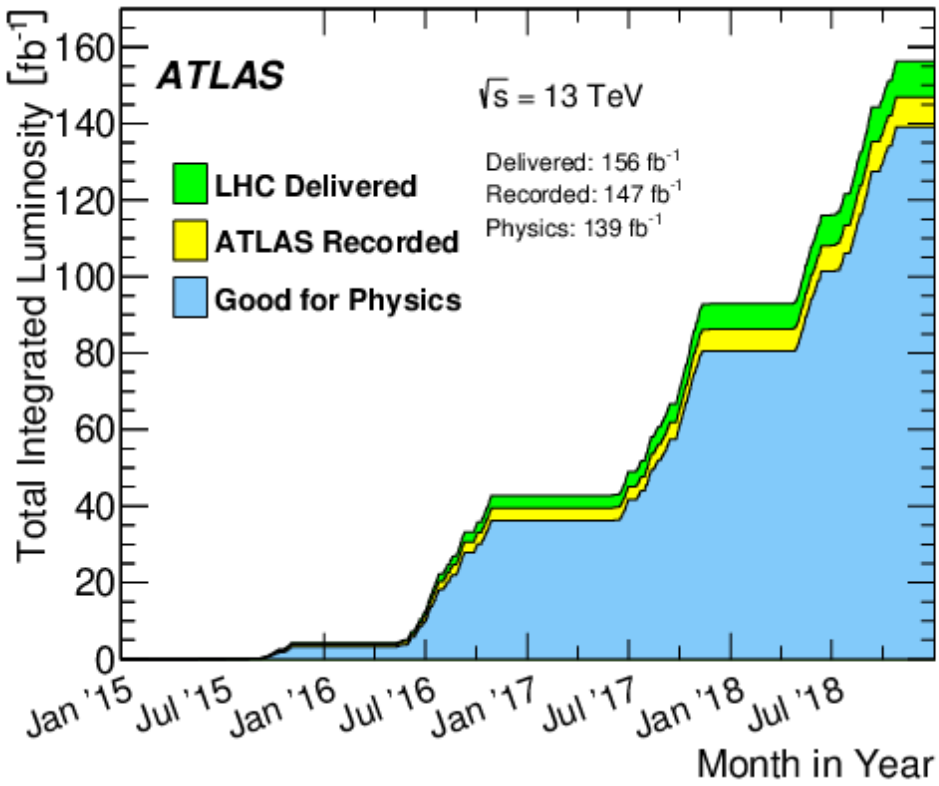

Figure 2.2: Integrated luminosity delivered to ATLAS over the entire Run-II period [73].

With a high number of collisions and large instantaneous luminosity there is a higher risk of multiple proton-proton collisions occurring within either the same bunch crossing or bunch crossings occurring around the same time as a collision containing a particle decay of interest. This is otherwise known as 'pile-up'. There are two types of pile-up relevant when discussing high rate collisions at the LHC:

1. In-time pile-up: More than one inelastic proton-proton collision occuring within the same bunch crossing as the collision of interest.

2. Out-of-time pileup: More than one inelastic proton-proton collision that occurs in bunch crossings either before or after the bunch crossing containing the collision of interest, but within the time period the detector takes to process the signal event.

At the LHC, pile-up can be quantified by the mean number of interactions per bunch crossing, $< \mu >$, and is given by:

$$< \mu >= \frac{L\sigma_{inel}}{N_{bunch} f_{LHC}}, \tag{2.2.4}$$

where σ_{inel} is the cross section of inelastic collisions. Figure 2.3 shows $< \mu >$ and the recorded luminosity at the LHC for each run year in Run-II. The average $< \mu >$ over the entire period was approximately 34. A large value of $< \mu >$ can pose a challenge for event reconstruction. The final-state observed in the detectors will not be just the products of the hard collision of interest but instead a superposition of softer collisions and this impacts negatively for instance in detector occupancy, triggers and expected physics backgrounds. In particular, this comes down to complications during the reconstruction of events. For example, jets (collimated sprays of hadrons) from hard collisions of interest might overlap with hadrons produced from pile-up and therefore bias the properties of the reconstructed jets [74].

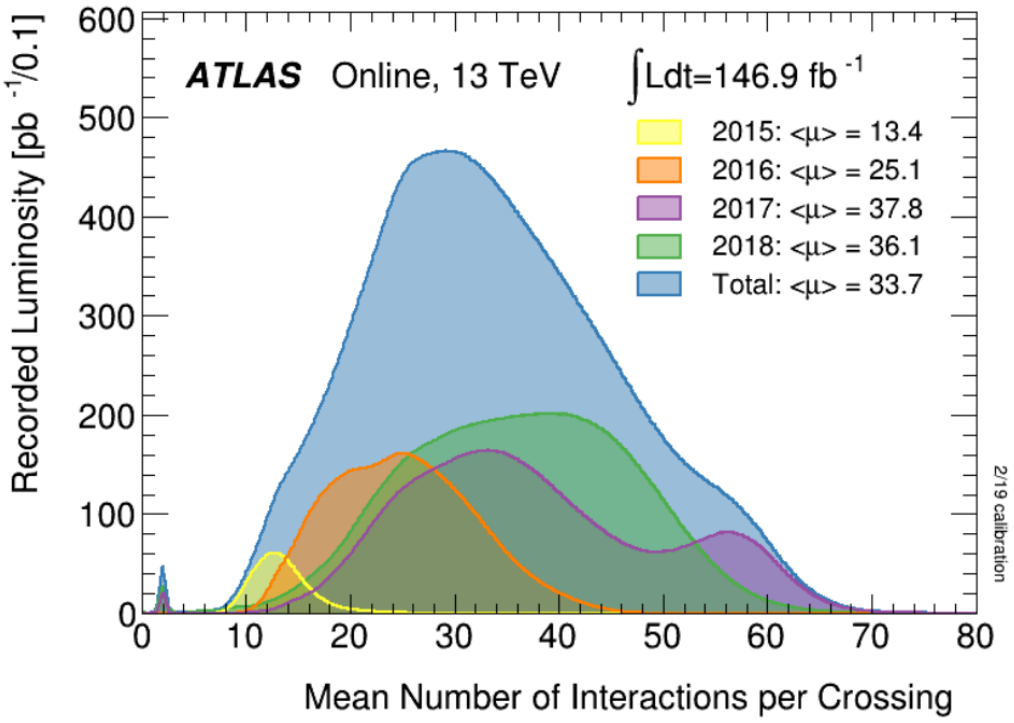

Figure 2.3: Run-II pile-up distribution for each run year [75].

2.3 The ATLAS detector

The ATLAS detector is one of four detectors located at the LHC, and is the largest of the two general purpose detectors. Installed 100 m below LHC point 1, ATLAS is 25 m in height and 44 m in length with a total weight of approximately 7,000 tonnes and is the outcome of a global collaboration from over 180 institutions across 41 countries. The detector itself measures charged and neutral particles that are produced following the high-energy particle collision interactions at the LHC and was essential in the landmark discovery of the Higgs boson achieved in 2012 [76], showing similar results to neighbouring general purpose detector CMS [77]. Results from the ATLAS experiment aim to potentially clarify some open topics in particle physics such as those surrounding supersymmetry and also measuring properties of the Higgs Boson that go beyond the Standard Model [66].

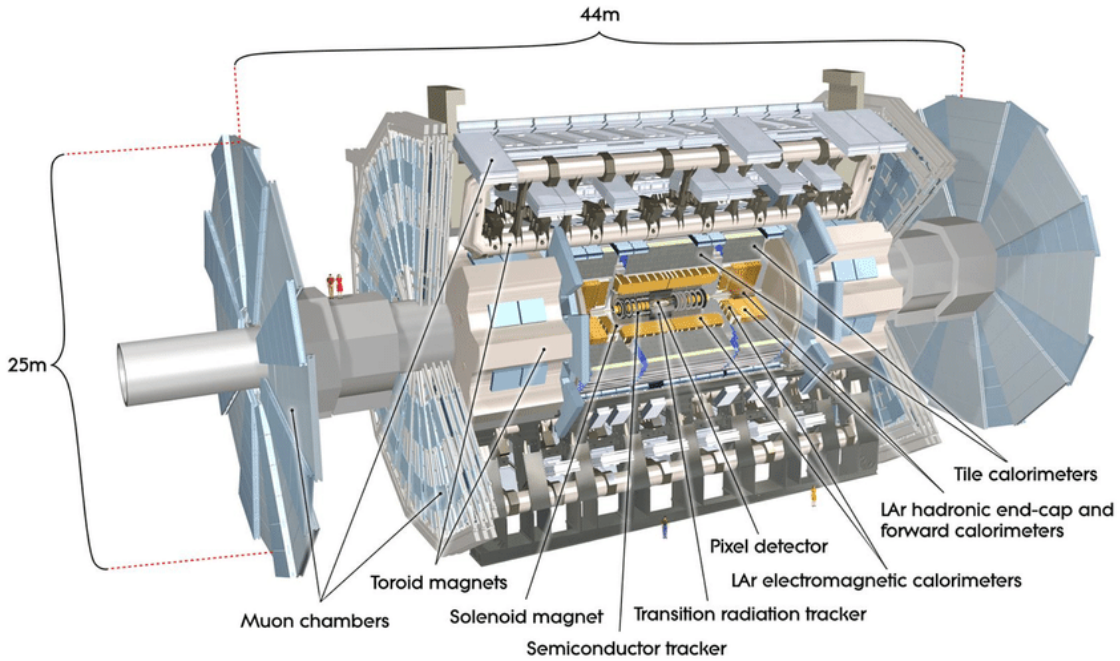

Figure 2.4: A cross-sectional view of the ATLAS detector and the sub-systems [78].

ATLAS is comprised of a number of sub-systems each containing different technologies specific to detecting distinct particles with outputs that when combined together finally image a full reconstruction of a particle collision event. Figure 2.4 shows a schematic of the detector and its sub-systems. Namely, the main sub-systems moving from the beam pipe are the Inner tracking system, the electromagnetic and

hadronic calorimeters and muon spectrometer. Immediately after particles are produced in collisions they pass through the inner detector and, if the particle is charged, electronic signals are formed which can be used to measure their path. After passing the inner detector, the particles enter the calorimeter where they are either stopped with their energy absorbed or pass through entirely to the muon spectrometer. A collision event can be fully reconstructed by analysing the particle information output by the detector. Each sub-system measures specific properties that are common to certain particles. For example, charge particles form tracks in the inner detector though non-charged particles, such as photons, do not. Muon particles penetrate the calorimetry system but their properties can be measured by the muon spectrometer. Figure 2.5 and also Table 2.1 summarise which sub-system of the ATLAS detector is responsible for detecting the common properties of different particles. At any one time, there is a very large number of collisions that occur at the LHC with the majority not containing any interesting interactions. To filter this vast amount of information and reduce wasting unnecessary disk space storage, there is a dedicated trigger system which an event must pass before it is recorded and stored to later be used in data analysis. This section discusses in detail the purpose and functionality of each of the sub-systems and how particles are detected at the ATLAS detector.

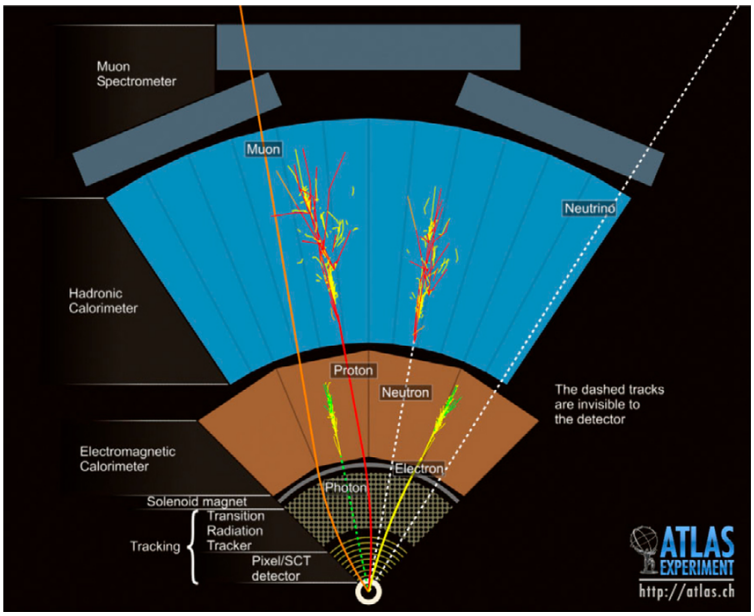

Figure 2.5: Schematic of the ATLAS detector and how different particles interact with each sub-system [78].

Particle type	Sub-system				Comments
	Inner detector & tracking	Calorimeter		Muon spectrometer	
		EM	Hadronic		
Charged (e.g e-, pi+)	✓	✓	✓		Detected in both the inner detector tracking system and calorimeters. Electrons/positrons stopped in EM calorimeter
Neutral (e.g γ, n)		✓	✓		Unconverted photons detected in EM calorimeter Neutrons detected in hadronic calorimeter
Muons	✓			✓	Muons highly penetrating and pass calorimeter detection. Their tracks are reconstructed in inner tracking and muon spectrometer only.
Neutrons					Neutrinos not detected at ATLAS as interactions with matter are rare. Neutrino information inferred from missing transverse momentum (MET)

Table 2.1: A table summarising the different types of particles detected at ATLAS and which sub-system is responsible for measuring each.

2.3.1 ATLAS Coordinate system

The coordinate system used at ATLAS is shown in Figure 2.6. At the center of Figure 2.6 is the interaction point where the proton-proton collisions occur. The z-axis is along the beam pipe. The positive x-axis points towards the center of the LHC whereas the y-axis points upwards, perpendicular to the direction of x. From the figure, ϕ is the azimuthal angle along the transverse plane, ρ the radial distance from the interaction point and polar angle θ is the angle depicting the direction between the y-axis and the beam axis, ranging between -π and +π.

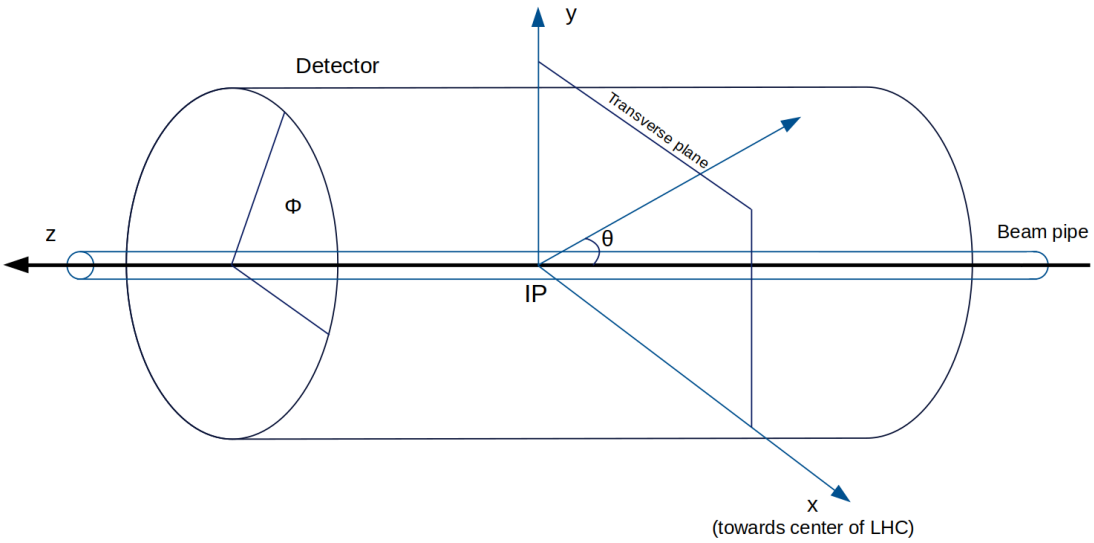

Figure 2.6: Illustration of the ATLAS coordinate system with IP being the interaction point.

In hadron collisions a quantity known as pseudorapidity, η, which is related to the polar angle in the transverse plane, is usually referred to in calculations. This is because the differences in η between two objects is invariant when moving from detector rest frame and center of mass frame.

The separation between particles in η-ϕ space, ΔR, is defined by:

$$\Delta R = \sqrt{\Delta\eta^2 + \Delta\phi^2} \tag{2.3.1}$$

with the $\Delta\eta$ and $\Delta\phi$ terms representing the difference in η and ϕ of the particle objects respectively.

Particles travel with momentum, p, relating to the energy of the particle, E, by

$$E = \sqrt{m^2 + p^2}, \tag{2.3.2}$$

with m being the particle mass. The momentum transverse to the beam line, p_T, is also a useful quantity as particles travelling in this plane are more likely associated with particle interactions occurring at the interaction point.

The terms given in this section are frequently referred to throughout this thesis to describe various aspects of the $h \to Za$ search and also how each ATLAS sub-system functions.

2.3.2 Inner detector

The Inner detector (ID) was designed to provide high quality resolution in terms of measuring particle position and momentum and is the closest sub-system to the interaction point. The ID covers the region $|\eta| < 2.5$ and is designed with a required momentum resolution of $\sigma(p_T)/p_T \leq 0.05\,\% \,\mathrm{GeV}^{-1} p_T \oplus 1\,\%$. The system has cylindrical geometry with a radius of 1150 mm relative to the beam pipe and ± 3512 mm in the z-direction. The entire system immersed within a magnetic field of 2 T from the Central Solenoid that surrounds the ID [66].

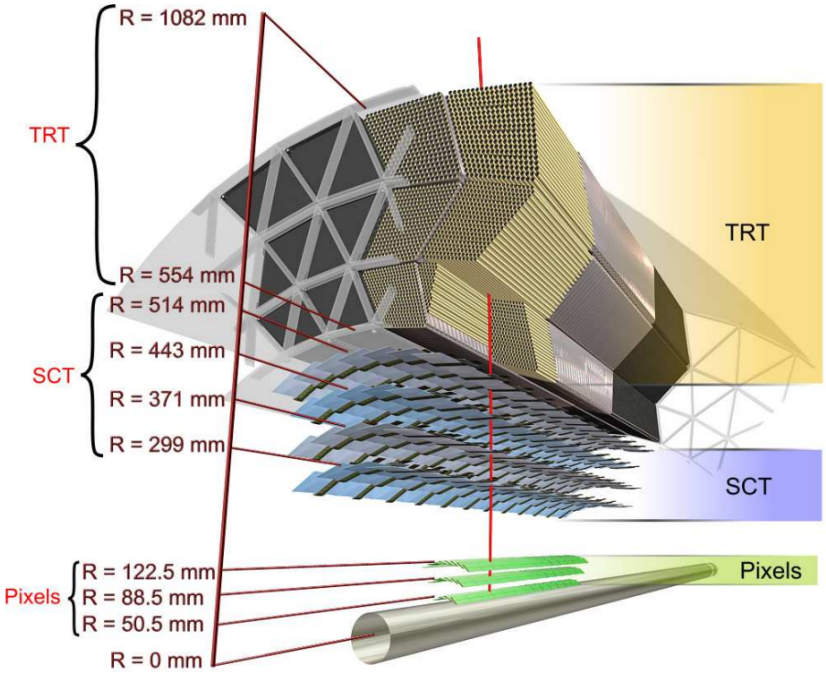

Figure 2.7: Illustration of the inner detector cross section showing each of the different detector systems. The R values on the left side represent distances from the beam line [66].

Figure 2.7 shows a schematic overview of the ID and a breakdown of the four different detector technologies that fill it. These are, in order of closest distance from the particle beam, the insertable B-layer (IBL), the Pixel detector, the semiconductor tracker (SCT) and the transition radiation Tracker (TRT). As a charged particle travels through the ID and interacts with various materials within the separate sub-detectors a track is sampled which, assisted with the information from other ATLAS sub-systems, measures the particle's properties that are required for the identification and four-vector calculations.

The Insertable B-layer

The IBL is the innermost sub-detector of the ID and as such is the first component of the detector that particles produced from high-energy collisions hit. The IBL was installed between the beam pipe and pixel detector in May 2014 during the shutdown period before the start of Run-II in order to manage the greater hit rates, radiation exposure and pileup expected of Run-II's much larger instaneous luminosity [79]. The IBL is at a radius of 33.25 mm from the beam pipe and is comprised of fourteen carbon fibre staves. The staves, shown illustrated in Figure 2.8, are each built with 32 readout chips from four 3D single chip sensors and 12 double chip sensors that are arranged cylindrically titled at an angle of 14° relative to the z-axis to cover a psuedorapidity of $|\eta| \leq 2.9$ [80].

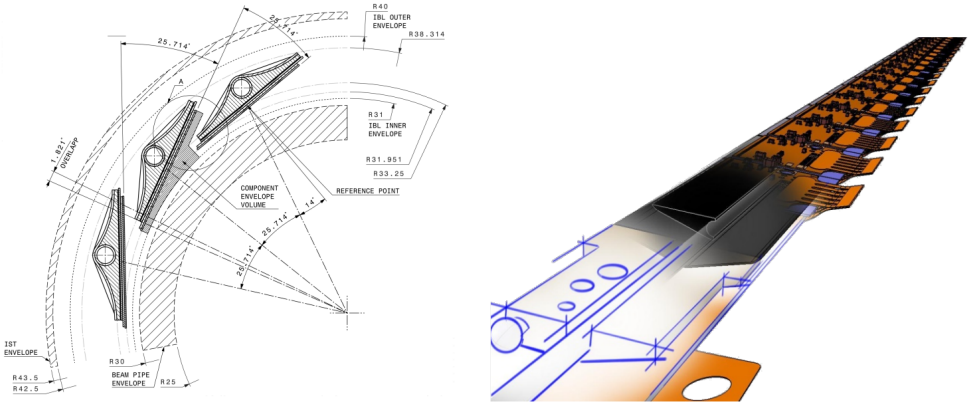

Figure 2.8: (a) Illustration of one quarter of the ATLAS IBL and (b) a drawing of one full stave [80].

The Pixel Detector

The second layer of the ID, and the layer surrounding the IBL, is the pixel detector. When charged particles from particle collisions pass through the pixel layers they leave hits meaning that particle tracks can be reconstructed. This detector is made up of 3 coaxial cylinders barrels covering the beam pipe with 3 disks attached at each end-cap. A cylinder consists of 1,744 pixel sensors that each contain 47,268 of identical pixels with size $(\rho - \phi) \times z$ 50×400 μm^2. The spatial accuracy of the pixel sensors in the cylindrical barrels is 115 μm along the z-axis and 10 μm^2 in $(\rho - \phi)$

which is also the same resolution as that specified for the disks. The pixel detector operates at a temperature of approximately $-6\,^{\circ}\mathrm{C}$ as this reduces any undesirable effects that may be caused from radiation damage.

The Semiconductor Tracker

The SCT is another sub-detector of the ID which contributes to the high resolution charge particle tracking at ATLAS. It contains four cylindrical layers of silicon sensors, which in total is comprised of 2,112 silicon modules, within the barrel and also nine disk layers, of 1,976 modules, in the end-cap regions [81]. The layers contain two silicon strips of length 6.4 cm, connected to one another and arranged so that the first is parallel to the beam direction whereas the other is offset by 40 mrad to permit for 2D coverage. This strip configuration is such that the charged particles that pass through the SCT produce 4 hits each resulting in a spatial resolution of $17\,\mu$m in the $(\rho - \phi)$ plane and $580\,\mu$m in the z-direction. The strip arrangement is the same for both the layers within the barrel and the layers in the end-cap.

The Transition Radiation Tracker

The TRT is the furthest of the four sub-detectors from the interaction point in the ID. As well as complementing the other technologies for tracking charged particles, the use of transition radiation also means that the TRT plays a key role for discriminating different types of particles from one another. The TRT is a straw tracker containing approximately 300,000 straw drift tubes, each with a diameter of 4 mm. The drift tubes are 144 cm and 37 cm in length for the barrel and end-cap regions respectively and provide directional information in the $(\rho - \phi)$ plane only. The straws are immersed in radiator material, in this case polypropylene fibres in the barrel and polypropylene foils in the end caps. The straws themselves are filled mostly of Xenon (70 %), due to this being efficient for absorbing transition radiation photons, and are operated at a voltage of 1500 V.

Transition radiation is radiation emitted when high energy charged particles travelling close to the speed of light passes through materials with varied dielectric constants and ionises the surrounding gas. The average number of hits for a charged particle track is 34 and the spatial accuracy of each straw is $130\,\mu$m, which is relatively lower than other ID sub detectors but the advantages for particle identification

of the TRT make up for this fact. For example, if an electron and a pion where subject to the same momentum, the transition radiation photons generated by the electrons would be of a much higher energy due to the lower mass of the electron. The TRT can quickly make the determination between the two particles [82]. Furthermore, the outputs from the TRT are crucial to a particle identification procedure to distinguish electron objects from other types of particles [83].

2.3.3 Calorimeter System

There are two large component calorimeters at ATLAS, the electromagnetic calorimeter (ECAL) and the hadronic calorimeter (HCAL), covering a total range of $|\eta|< 4.9$. A calorimeter is responsible for measuring the energy of incident particles. This happens when high energy particles interact with passive materials which results in a cascade of secondary lower energy particles known as a particle shower. These particles in turn produce a shower and this process repeats until all particles are stopped and their energies are fully absorbed. Electromagnetic and hadronic showers are produced in considerably different ways. For example, photons form electromagnetic showers mostly by pair production as the photons convert into electron-positron pairs that interact with other electrons in the material and substantially emit photons via the bremsstrahlung process. Hadronic showers on the other hand are dominated by multiple inelastic hadronic interactions such as nuclear decays of excited nuclei, though there is also an electromagnetic component to this due to the frequent abundance of π^0 particles that decay into photons.

Both the ECAL and HCAL are sampling calorimeters as the layer arrangement of the materials that make up the system alternate between the 'absorber' layer and 'active/sampler' layer. The active layer has a much larger radiation length compared to the absorber and is where the energy of the particles are measured and converted into an electronically readable signal.

In the ECAL, lead plates are used as the absorption material and liquid argon (LAr) the active material. The lead plates are approximately 1 mm in thickness each while the layers containing LAr are about double this. The absorption and active layers are arranged in what is known as 'accordion geometry'. The ECAL is formed by three separate detectors, the barrel calorimeter which has coverage $|\eta|< 1.475$, and two end cap calorimeters (EMEC) with $1.375 < |\eta|< 3.2$. The EM particles

produce successive showers of secondary particles as a result of hitting lead plates until the energy is below critical energy E_c. E_c is the energy at which the ionization loss per radiation length, X_0[1], is equal to the electron energy [14]. The charged particles ionize the argon in the LAr layers that produce a signal detected as energy deposits, measured in units of calorimeter cells per layer in the $\eta - \phi$ plane. The LAr calorimeter module and its cell structure is illustrated in Figure 2.9 which shows the three longitudinal layers that form it. The first layer, also known as the strip layer, has a thickness of 91 mm and a high granular structure to more accurately determine transverse shower profiles which better distinguishes photons from interesting particle decays and those originating from background π^0 decays. The middle layer is the largest with thickness 337 mm and is where the majority of the energy is deposited. Finally, the third layer is 42 mm and is responsible for measuring any energy leakage to the HCAL.

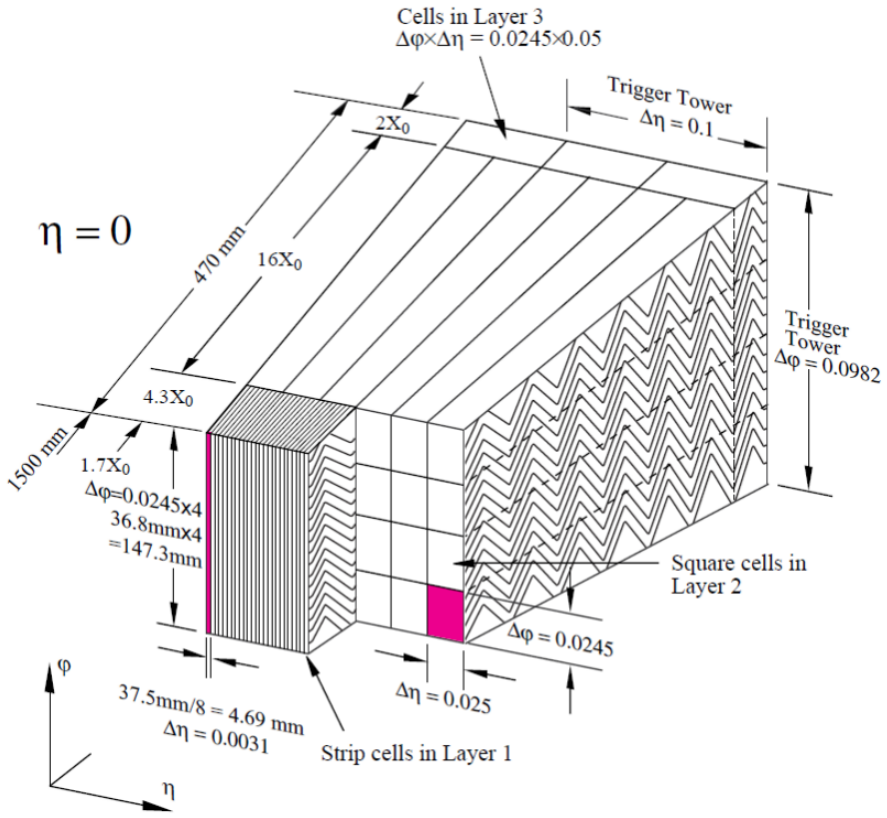

Figure 2.9: Sketch of the LAr calorimeter module and its three layers. The highlighted area shows an example of a calorimeter cell [66].

[1] X_0 is the radiation length which is equal to the distance when electrons lose on average all but $1/e$ of their initial energy.

The HCAL surrounds the ECAL as jets from hadronic decays are more penetrating than EM particles. It is made up of three calorimeters, a tile calorimeter and two liquid argon hadronic end-cap calorimeters (HEC).

The tile calorimeter consists of three layers and contains a total of 64 modules in the ϕ direction. The tile barrel has a coverage of $|\eta|< 1.0$ and is extended by two barrel containers positioned either side with coverage $0.8 < |\eta|< 1.7$. The tile calorimeter uses steel plates as the absorption material and scintillating tiles as the active medium. Charged particles passing through the scintillating tile samplers produce ultraviolet light which is subsequently converted into visible light so that a signal can be produced by a photon-multiplier.

Positioned behind the two EMEC's are two coaxial wheels which make up the HEC systems. Each wheel contains 32 copper plate modules and has a coverage of $1.5 < |\eta|< 3.2$. The HEC uses copper plates as the absorption material and LAr as the active medium.

The ATLAS calorimeter is extended to a total coverage of $|\eta|< 4.9$ due to the LAr forward calorimeter covering the region $3.1 < |\eta|< 4.9$. The forward calorimeter is positioned behind the EMEC and HEC within the same LAr cryostat and made up of 3 modules with a total thickness of $10\,X_0$. The first module uses copper as the absorption material and is responsible for measuring EM objects whereas the remaining two modules use tungsten and focus solely on hadronic decays. All three modules use LAr as the active medium.

A calorimeter energy resolution can be given as:

$$\frac{\sigma(E)}{E} = \frac{a}{\sqrt{E}} \oplus \frac{b}{E} \oplus c \tag{2.3.3}$$

with a representing the stochastic term, b the electronic noise and c a constant for the effects of detector instabilities and mis-calibration. The ECAL energy resolution is

$$\frac{\sigma(E)}{E} = \frac{2.8\%\ \sqrt{\text{GeV}}}{\sqrt{E}} \oplus \frac{0.12\ \text{GeV}}{E} \oplus 0.3\% \tag{2.3.4}$$

For the HCAL, the energy resolution is

$$\frac{\sigma(E)}{E} = \frac{52.9\% \sqrt{\text{GeV}}}{\sqrt{E}} \oplus 5.7\%, \tag{2.3.5}$$

where the electronic noise term for the HCAL is negligible [84].

The resolution for the ECAL was measured in test-beams with electrons whereas the resolution for the HCAL was calculated in test-beams for single pions.

2.3.4 Muon Spectrometer

The muon spectrometer's main purpose is to measure the momentum of charged particles that travel further than the calorimeter. Muons are charged leptons that have a substantially greater mass compared to that of an electron ($m_\mu \approx 200 m_e$) and as such are less likely to lose energy by bremsstrahlung therefore penetrating through the calorimeter layers. The charged particles that make it to the muon spectrometer are bent by super-conducting air-core magnets that have magnetic field lines concentric with the direction of the beam. The barrel toroid in the region $|\eta| < 1.4$ provides a magnetic field of 0.5 T whereas the end-cap region $1.6 < |\eta| < 2.7$ is under a magnetic field of 1 T applied by the two end-cap magnets. The trajectories of charged particles that pass through a third region known as the 'transition region' with coverage $1.4 < |\eta| < 1.6$, the space between the barrel and end-cap, are bent as a result of both the large toroid magnet and end-cap magnet with a field strength that is relatively lower. A schematic view of the muon system is shown in Figure 2.10.

The tracks of the charged particles are measured by Monitored Drift Tubes (MDT) and Cathode Strip Chambers (CSC). The MDT chambers contain drift tubes, 29.97 mm in diameter, filled with an Ar/CO_2 gas mixture (93 % Ar, 7 % CO_2) at 3 bar pressure. The cathode tubes have a 3 kV voltage difference applied between the outer tube and a Tungsten-Rhenium anode wire of 50 μm located at the center of the tube. As charged particles pass through the tubes, the Ar/CO_2 gas is ionized and produces a signal for a precise measurement of the particle track as it bends through the spectrometer. Figure 2.11 is an illustration of this process as a muon passes through the cathode tube. The chambers that contain the MDTs are arranged in three cylindrical layers parallel to the beam axis covering the majority of the de-

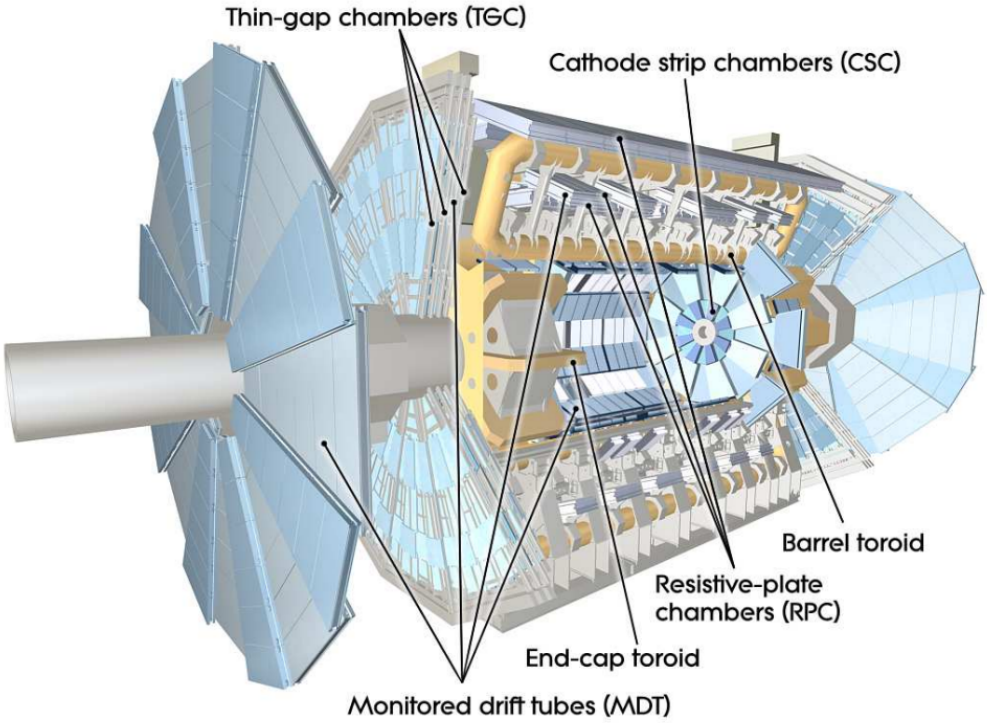

Figure 2.10: Drawing of the ATLAS detector with labels detailing only the components that make up the muon system [66].

tection range at $|\eta| < 2.0$. The maximum drift time is approximately 700 ns with a single hit resolution of 35 μm in the z-direction per tube. Tracking measurements in the end-cap layers are provided by CSCs covering the region $2.0 < |\eta| < 2.7$ and are also made up of three layers but are perpendicular to the beam axis. CSCs are multiwire proportional chambers filled also with an Ar/CO_2 gas mixture (80 % Ar, 20 % CO_2) but have a relatively lower resolution compared to the MDTs of 40 μm in the ρ direction and 5 mm in the ϕ direction, but this is compensated by a higher rate and better time resolution [66].

The tracking systems of the muon spectrometer are not limited to only tracking muons and therefore a trigger system is required. Resistive Plate Chambers (RPCs) are responsible for muon triggering in the barrel region and Thin Gap Chambers (TGCs) for the end-cap region. RPCs are two parallel electrodes separated by 2 mm with an electric field of 4.9 kV applied. The gap between the plates is filled with a unique gas-mixture that is ionised as muons pass. TGCs are multi-wire chambers that have small distances from the wire to the cathode which provides a good time

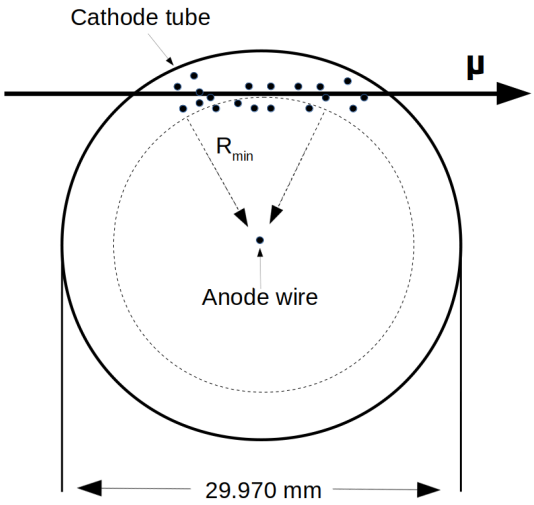

Figure 2.11: Cross-section of a MDT tube as a muon passes through. R_{min} is the radial distance from the muon track to the anode wire. Adapted from Ref [66].

resolution. RPCs measure muons in the ϕ and z directions whereas TGCs measure in ρ and ϕ.

Using $3.2\,\text{fb}^{-1}$ of proton-proton collision data at $\sqrt{s} = 13\,\text{TeV}$ in 2015, muon momentum scale and resolution was calculated for $Z \to \mu\mu$ and $J/\psi \to \mu\mu$ decays. It was found that the relative muon p_T resolution is 2.3 % and 1.7 % at low value $|\eta|$ and 2.9 % and 2.3 % in the end-caps for the Z and J/ψ decays respectively. Data and simulation agreed to >5 % for the majority of the $|\eta|$ range after momentum corrections were applied [85].

2.3.5 Trigger system

At the LHC, particle bunches cross at a designed frequency of 40 MHz. Given that the storage size of a single ATLAS event is a few MB of disk storage space, the fact that there are already bandwidth limitations and interactions from most collisions are not very interesting, it is not practical to store every event and therefore a trigger system is required. A trigger system is a set criteria which is used to decide to keep or ignore the information from each event, and to do so within a short amount of time. This means that only events that have greater potential physics interest are kept for further analysis. The ATLAS trigger consists of two main systems, a hardware based level-1 (L1) trigger and a software based Higher level trigger (HLT)

operating in that order. If an event occurs for example that contains particle objects with a high transverse momentum or is part of a potentially interesting signature, then the L1 trigger defines a Region of Interest (ROI) in the $\eta - \phi$ space of the detector where the particle objects have been observed. L1 uses only the outputs from the calorimeter and muon spectrometer to define the ROIs and does so within a time period of less than 25 ns, reducing the event rate to 100 kHz.

Once the ROIs are defined, the measured event information transfers to the software based HLT. The HLT consists of the level-2 (L2) trigger and an event filter. L2 has access to the full detector information for the ROIs and performs the fast reconstruction of particle tracks and energies. In a decision that takes approximately 40 ms, the total information for an event that passes both L1 and L2 moves offline where it is further processed by the event filter before the Data Logger stores the data to CERN permanent storage. The HLT further reduces the event rate to approximately 1-2 kHz depending on the year and run period the data is taken.

2.3.6 LHC computing grid and ATLAS offline software

LHC computing grid

The Worldwide LHC Computing Grid [86], or the *Grid* for short, stores data outputs from the detectors as well as being responsible for the processing of event simulation, object reconstruction and user analysis in a way that is decentralised with sites located across the world. The Grid is split into three separate computing site levels called Tier 0, Tier 1 and Tier 2. The first level is Tier 0 and is centralised at the CERN Data Center where all of the raw LHC data passing the trigger systems of the detectors is stored. At this level, initial reconstruction algorithms are applied to the raw data to produce purposeful object information that is stored into datasets called "AODs" (Analysis Object Data). These are distributed to second level sites, known as Tier 1, at approximately 10 GB per second. There are just over a dozen Tier 1 centers hosting this data situated in many countries. For example, in Canada the Tier 1 facility is located at TRIUMF [87] and the chosen site for the UK is GridPP [88]. Tier 1 sites are responsible for storing some fraction of the raw and reconstructed data as well as performing the majority of the AOD reprocessing into lower memory subsets of the reconstructed data called "DAODs" (derived AOD datasets). DAODs are tuned specifically so that analysis groups can run com-

putational jobs more efficiently. Also, the AOD to DAOD process is used to apply updated reconstruction algorithms. These outputs are then distributed to Tier 2 sites which are predominately universities and research institutes with facilities capable of performing adequate compulsory tasks for user analysis. There are approximately 150 Tier 2 sites located worldwide [89]. There is also a final level known as Tier 3 which include local computing resources that smaller analysis groups might use, but these resources are not formally engaged to the Grid [90].

ATLAS offline software

All levels of ATLAS data, from event simulation to reconstruction and analysis, are processed using the ATLAS software framework called Athena [91]. The Athena framework was developed based on the GAUDI framework [92], originally for LHCb, but is now used for both experiments. The design of the framework is ideal for sharing algorithms between projects, such as those required for object reconstruction, and for individual analysis software development.

Chapter 3

Pixel and Strip quality control for ATLAS upgrade

3.1 HL-LHC upgrade and the ATLAS Inner Tracker (ITk)

To further the discovery reach possible by the LHC, a major upgrade known as the High-Luminosity LHC (HL-LHC) is under construction with the aim of increasing the number of collisions by a factor of 10 compared to that achievable at the current machine. This means an instantaneous luminosity of $\mathcal{L} = 7.5 \times 10^{34}\,\mathrm{cm}^{-2}\mathrm{s}^{-1}$ which equates to a pile-up of approximately 200 inelastic proton-proton collisions per beam crossing. It is therefore possible that ATLAS accumulates an integrated luminosity of up to $4000\,\mathrm{fb}^{-1}$, which is significantly greater than the $350\,\mathrm{fb}^{-1}$ aimed to be achieved by close of Run-3 [93, 94]. Because of this ambitious target, the ATLAS tracking detector will face considerable challenges due to unparalleled radiation environments from hadron fluences of up to $2 \times 10^{16}\,\mathrm{n_{eq}/cm^2}$ and demanding data processing. These conditions would make the current ATLAS Inner Detector inoperable. In order to be able to extract good physics measurements the detector is to be upgraded during the Phase-II upgrade. Components of the present Inner Detector such as the silicon pixel, silicon strip and TRT are to be removed and replaced with an all-silicon based Inner Tracker known as the ITk [94].

The ITk comprises of two major sub-systems; a $13\,\mathrm{m}^2$ pixel detector close to the beam line and an outer $160\,\mathrm{m}^2$ strip detector enclosing it. The pixel detector consists of five layers placed between two support tubes. A Pixel Support Tube separating

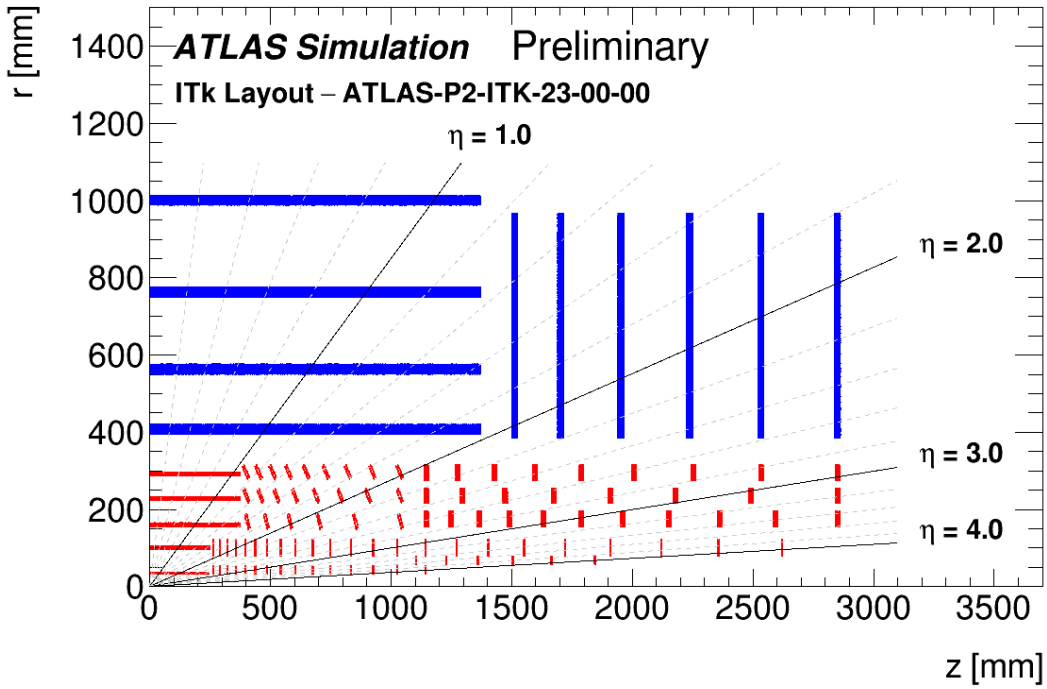

Figure 3.1: Schematic of ITk quadrant showing the pixel detector (red) and strip detector (blue) components. Horizontal axis is along beam line with the interaction point represented at (0,0). The radius from the interaction point is given as the vertical axis. Figure reproduced from Ref. [95].

the pixel and strip detectors and an Inner Support Tube placed just before the third layer to aid the replacement of the first two layers resulting from damage caused by hadron irradiation. The strip detector is made from 4 barrel layers and 6 strip disks in each end-cap [96]. The strip detector covers a pseudorapidity of $|\eta|< 2.7$ which is furthered to full coverage of η when including the pixel layer. The pixel and strip trackers will contain approximately 5 billion and 50 million readout channels respectively. A cross-section showing one quadrant of the ITk layout is shown in Figure 3.1.

3.2 ITk Visual Inspection Tool for pixel and strip hybrids

The ITk pixel and strip detectors are hybrid devices where data will be read out by ASICs with a bandwidth up to 5 Gbit/s [94]. The ITk is made up of pixel and strip hybrids and so it is paramount that these should be checked thoroughly to ensure good quality. The quality control process for the hybrids is made up of visual inspection, metrology and electrical testing. Visual inspection requires flagging any possible defects by eye, such as solder splash or misaligned/missing components, that could hinder performance. This process alone can be slow. With the number of hybrids in the order of thousands, the effort required to manually inspect the quality of each one using just an image of the hybrid alone is both tedious and time consuming. This section describes a tool which aids the visual inspection process by automatically highlighting areas of potential defects therefore guiding the user where to look and as such make decisions more efficient.

By comparing images of test hybrids to multiple images of working hybrids (also referred to in this chapter as *golden images*), using a host of image analysis software written in `Python`, the tool highlights areas of concern by automatically annotating potential defects and ranking these based on the severity. The hybrid images with their annotated counterpart are then presented clearly on an interface allowing the user to navigate the system easily. An example of the user interface (UI) for both pixel and strip hybrids is shown in Figure 3.2.

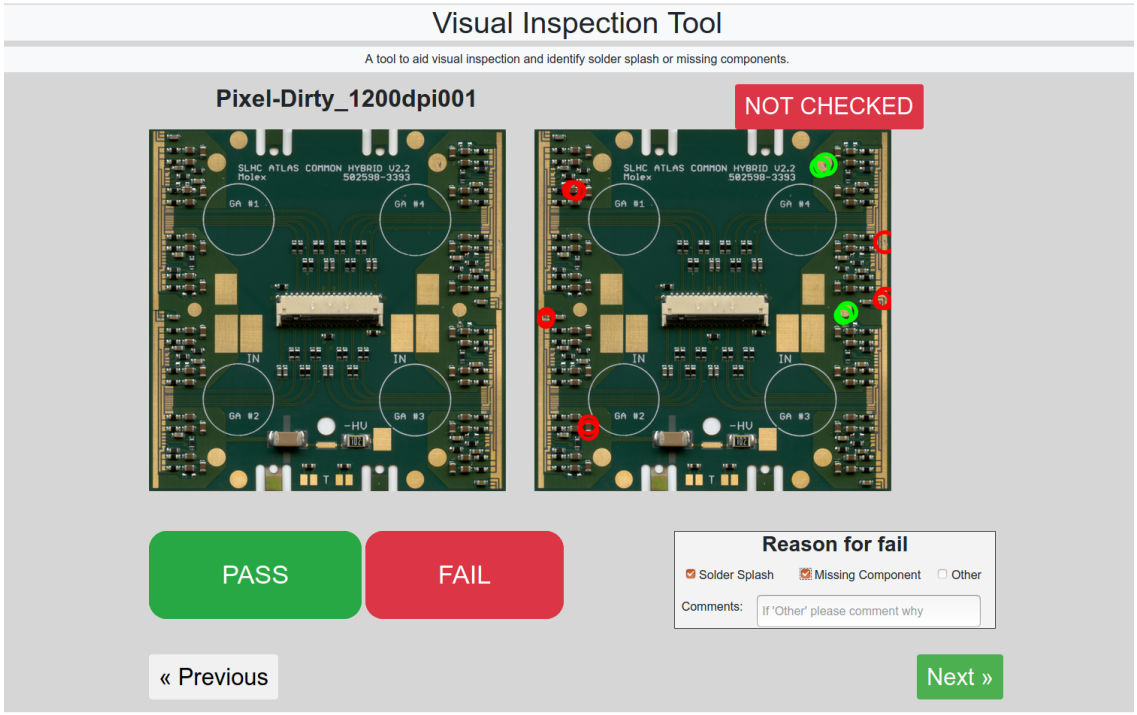

(a) Pixel hybrid example

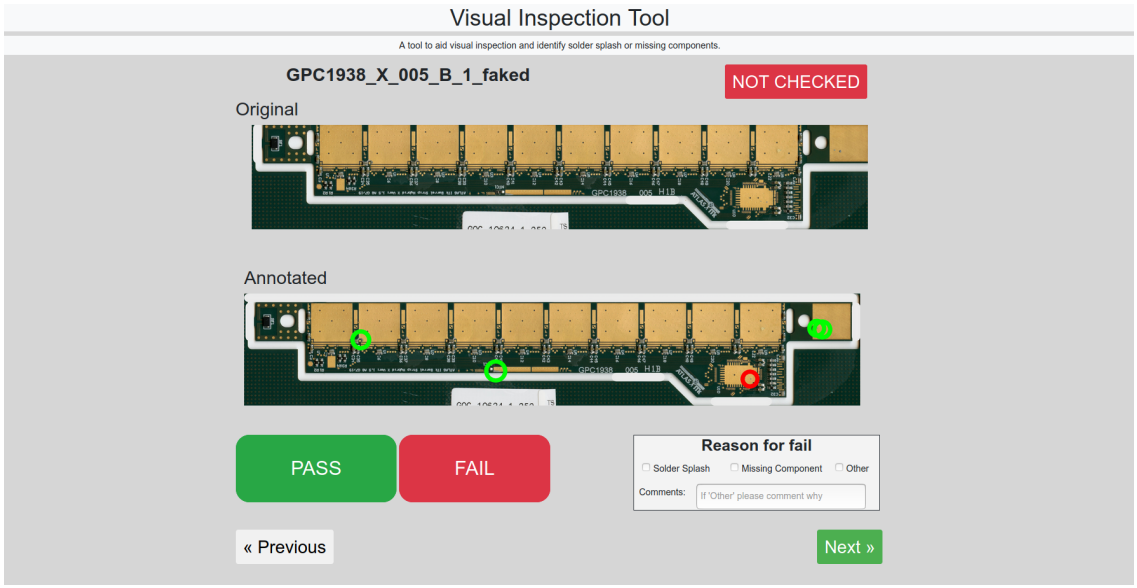

(b) Strip hybrid example

Figure 3.2: Example of the user interface view for pixel hybrids (top) and strip hybrids (bottom). The user is given the option to pass or fail the visual inspection of a hybrid with the guidance of annotations to help decide faster and more accurately. The resulting information is stored in a shared database.

The software automatically annotates the images by computing multiple stages of image analysis. The first stage is image processing which removes any side-frames that may be attached to the hybrid and leaves only the individual hybrid. The second stage is the comparison between the test image with a number of golden images that would already pass visual inspection before the software then automatically annotates the differences between them. Finally, the annotated test image is presented alongside the original image of the hybrid on a UI. An overview of these stages for a single pixel hybrid is shown in Figure 3.3. The entire process is automatic and repeated for each hybrid image. Though Figure 3.3 shows an example for a pixel hybrid only, the same process is also applied to strip hybrids even though the annotation algorithm differs slightly.

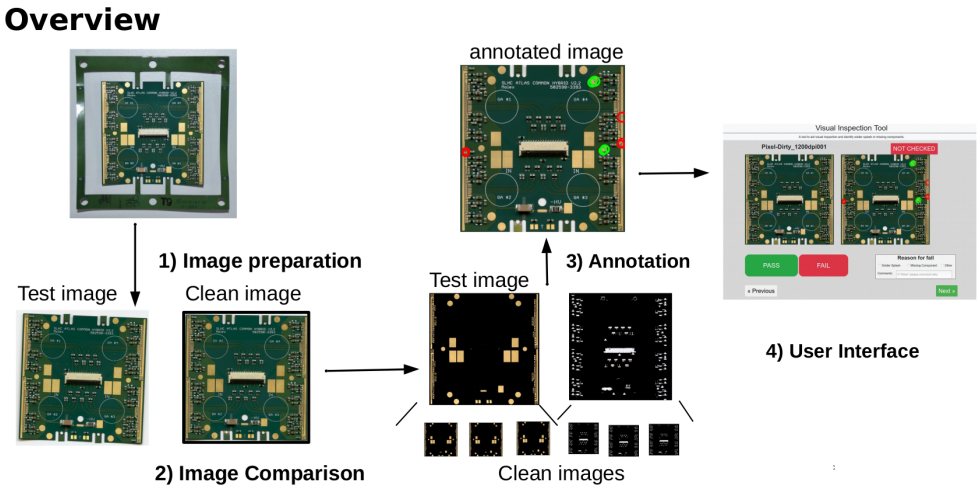

Figure 3.3: Overview of the visual inspection tool, including the annotation algorithm and user interface. All stages are computed automatically for each individual hybrid. A single pixel hybrid is used as an example for this overview but the process is the same for strip hybrids.

3.2.1 Hybrid defects

There are a number of serious hybrid defects that can be identified during visual inspection. The hybrid defects that the tool focuses on flagging, are:

- Solder splash
- Missing components
- Misaligned components

It is important to identify these issues because any contamination on the wire bonding area could affect the strength of the wire bonds and debilitate the effectiveness of remaining attached. Solder splash is generally searched for by the manufacturer, however it is occasionally missed. Misaligned components cause short-circuiting and although vendors tend to pick up "tombstone effect" [1], misalignments that cause short-circuiting are much more difficult to spot during manufacturing. Identification of such defects by visual inspection is particularly important as this issue does not seem to be flagged well during early electrical tests.

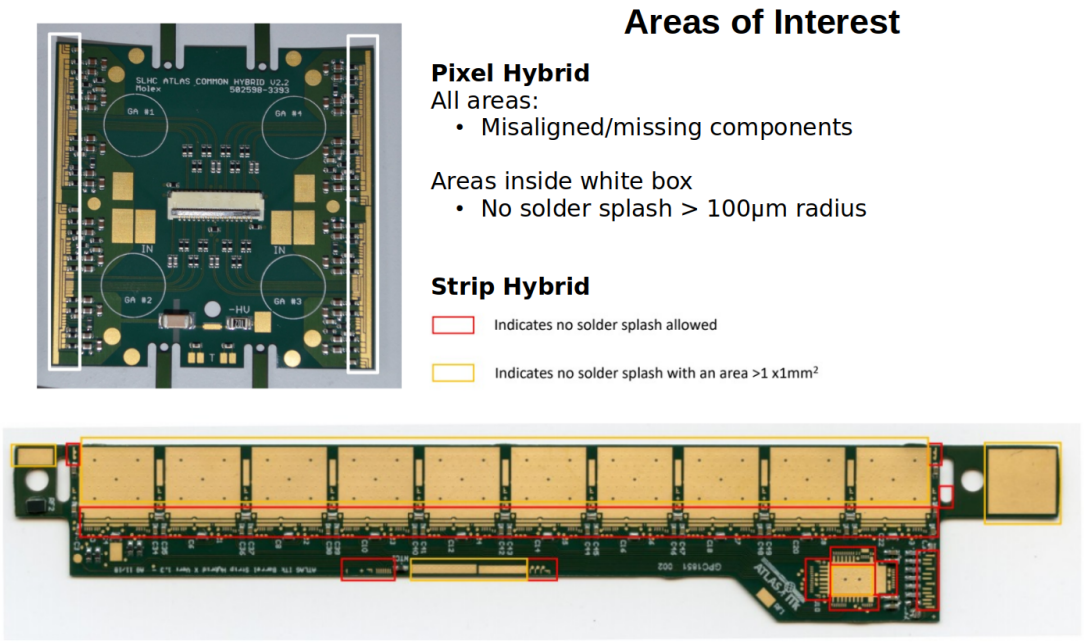

Figure 3.4: Any potential defect that falls within the areas of interest and satisfies the criteria set in Section 3.2.3 will be automatically annotated red, otherwise it will be annotated green.

Figure 3.4 summarises the areas of interest for pixel and strip hybrids that are of most concern. For example, solder splash is only deemed concerning if the droplets have a radius $> 100\,\mu$m as it might be big enough to significantly obscure a bond pad and prevent wire bonding. Despite these thresholds, the tool's algorithm works by highlighting all positions of the hybrid that could potentially be a defect and automatically classifies all areas by colour coding red or green depending on how serious each particular defect is deemed according to a set of predefined criteria, explained

[1] Tombstone effect is when one end of a component tilts from the board during the soldering process and as such is not connected properly.

in more detail in Section 3.2.3.

3.2.2 Image preparation

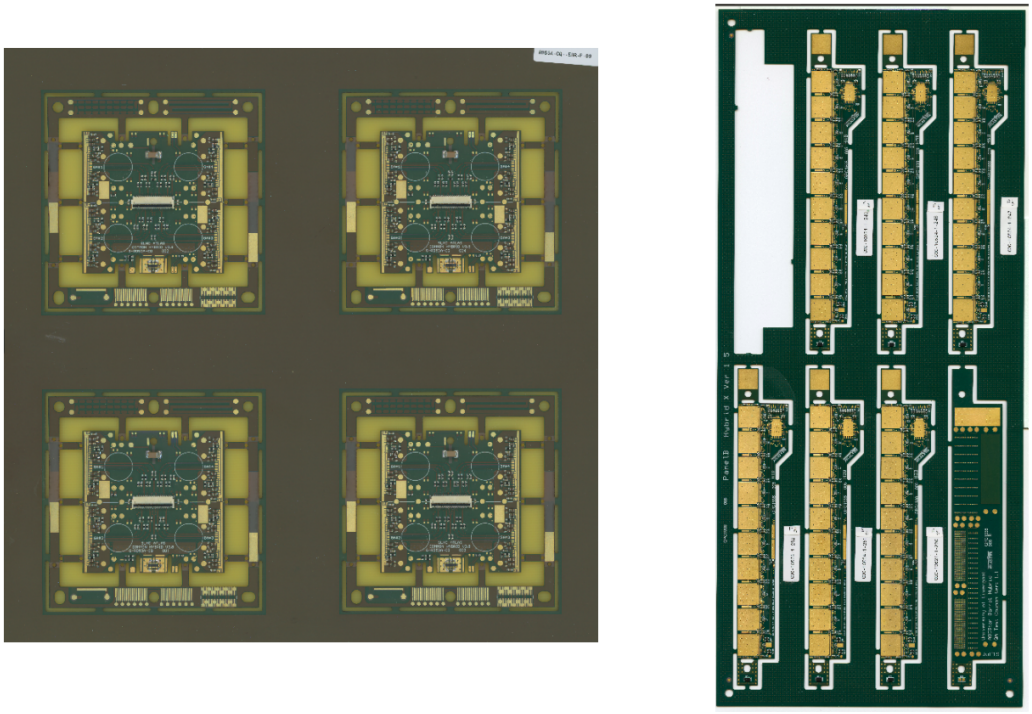

Figure 3.5: Example images of full hybrid arrays for pixels (left) and strips (right).

Images of hybrids are taken in groups, displaying the hybrids in an array of four for pixels and six for strips as shown in Figure 3.5. Commercially available scanners and cameras were tested to take the initial image of the hybrids. In terms of storage space, scanning a single strip hybrid using a resolution of 3200 dpi and 24 bit colour requires 15 MB for each image, equating approximately to a total storage of 300 GB for about 20,000 hybrids. For a single strip hybrid the scan area is 120 mm × 24 mm and for pixel hybrids 40 mm × 40 mm. Each hybrid takes about one minute to complete a single scan and because the scan area is small it is necessary for an operator to change the scan window position for each hybrid in an array. Alternatively, increasing the scan area to show the full hybrid array, like that shown in Figure 3.5, was attempted and found to be even more efficient. The storage space and time taken for each scan varied based on the resolution chosen and is summarised in Table 3.1. It was found for the purpose of identifying misaligned/missing components and solder

Scanning properties for full hybrid array		
Resolution (dpi)	**Scan time (mins)**	**Size (MB)**
2400	10	89.0
1200	2	29.7
800	1	15.7
<800	<1	<12.0

Table 3.1: Time taken and storage size for scans of full hybrid arrays with varying resolution.

splash that a resolution of 1200 dpi was most sufficient.

Images of hybrids taken by a camera and tripod setup were also tested. The camera used was a 16 megapixel DSLR camera placed inside a light box and attached to a tripod to keep the light distribution and level constant. The depth of field was set to a minimum and the light sensitivity settings (ISO) set to 100 to reduce noise by compensating more light. The shutter was operated remotely to keep vibrations on capture to a minimum. The benefit of using a camera is the increased speed and ease for which one can change the set of hybrids. However, images taken by camera were prone to light changes and problematic reflections/shine (Figure 3.6) which hindered the algorithm's effectiveness to properly crop, align and compare individual hybrids.

By using freely licensed image processing software `OpenCV` [97] written in `Python`, individual hybrids are automatically pulled from the full image and then each are aligned by homography with respect to a golden image.

The tool firstly automatically crops the individual hybrid before then aligning with a golden image. For pixels this means removing any frames that may be attached and leaving only the area within the 161 mm perimeter around the individual hybrid. For strips this is just the minimum enclosing rectangle surrounding the hybrid. The alignment of test to golden images is necessary as both images are likely to differ slightly in initial positioning when making the scan.

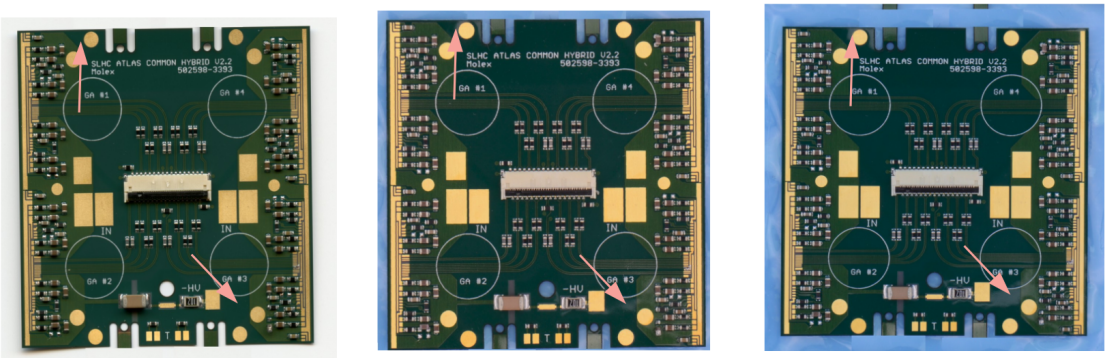

Figure 3.6: Images of pixel hybrid ID 502598-3393 taken either by scanning or from a commercially available SLR camera. The middle image is a photograph with white light and the last image is a photograph with blue light. Arrows point to same area on each image to compare reflection/shine as a result of different methods. The image produced by the scanner shows no reflection whereas both camera examples show some, with blue light the most obvious. Reflection overload can cause more noise when comparing test images to golden images therefore increasing the likelihood that the visual inspection tool in its current form is more prone to misclassifying potential defects.

3.2.3 Image comparison and Annotation

Defects are identified by comparing the visual make-up of the test and golden images and highlighting differences that are synonymous with the characteristics of a potential defect.

A computationally slow but more accurate method to do this is by extracting colours of interest and calculating the difference between the two image matrices. This is done by excluding all areas of the image that do not satisfy a particular colour range defined by cuts applied to the HSV (hue, saturation, value) model. The colours of interest, and subsequent cuts, are those associated with areas that solder splash and missing/misaligned components could occur on the hybrid. Figure 3.7 shows examples of some of these areas and the HSV value configurations set for each colour of interest. The bitwise subtraction is computed on the greyscale conversion of the image arrays that results in an output that exposes the contours for the majority of differences between the images. This process is repeated with each of the colours of interest.

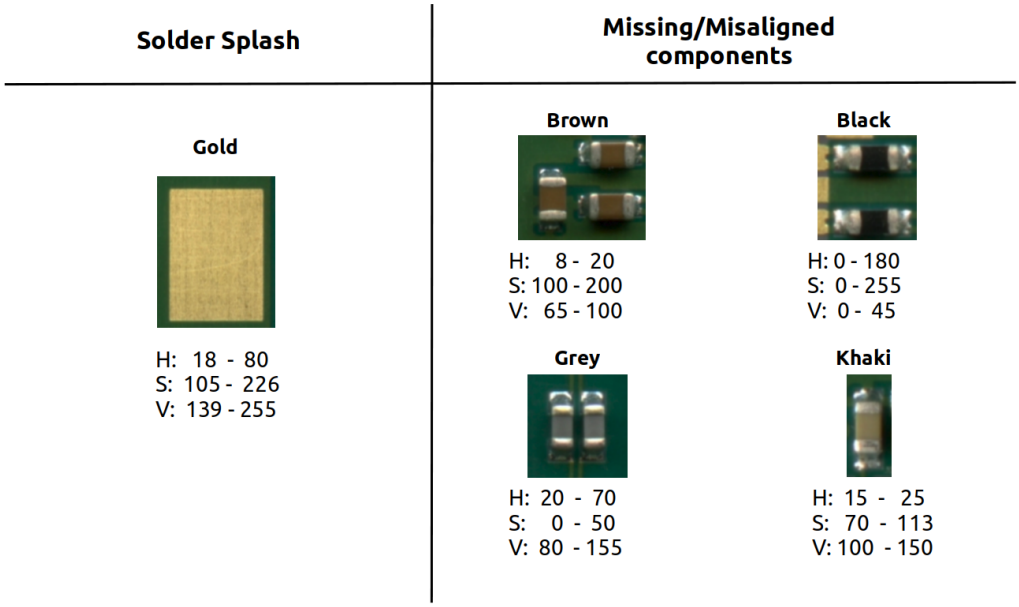

Figure 3.7: List of colours and their respective HSV value ranges required to identify solder splash and missing/misaligned components. The pictures give examples of some of the areas segmented by the chosen HSV value ranges for each colour.

For a given colour, the resulting matrix will include the positions of most concerning potential defects but does not yet exclude areas that contain differences caused by noise at this stage. Noise is a result of random variations between the test and golden images usually attributed to dust particles and slight imperfections in the automatic alignment process detailed in Section 3.2.2. Noise generally does not affect the tool from flagging misaligned/missing components, as the combined characteristics of contour shape, colour and location is such that the algorithm can spot these types of defects more easily, however solder splash is more difficult to probe. To reduce the abundance of noise reaching the final annotation stage, a stacked threshold system is applied so that only image contours with differences in intensity and shape similar to known defects are chosen by passing a particular set of criteria. The definitions of this criteria are given in Table 3.2. Examples of what some potential defects and noise might look like are shown on Figure 3.8.

Firstly, the process of finding the differences between test and golden image for a particular colour is repeated several times, comparing with multiple golden images, and averaging each output to produce a final image that is a combination of all (illustrated on Figure 3.9). Doing this allows contours that are consistently dis-

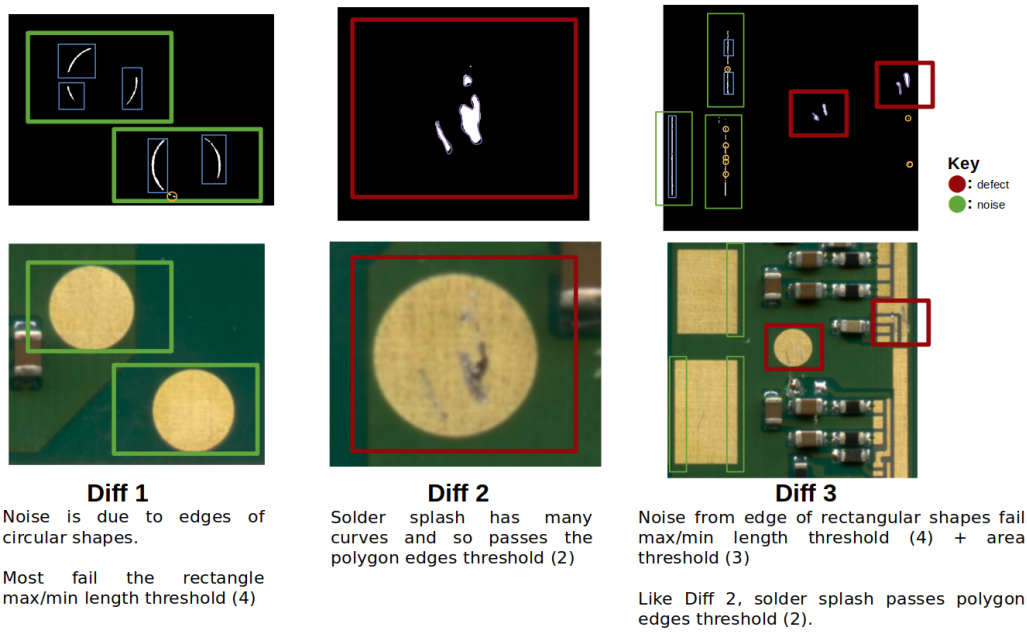

Figure 3.8: Figure showing three examples of how noise and actual defects pass and fail criteria thresholds for solder splash. The numbers in the threshold list correspond to those in Table 3.2.

similar in all comparisons, and thus more likely to represent a location of a defect, to have a greater intensity relative to minor variations. From this point, the four thresholds described in Table 3.2 are applied, reducing the probability that contours likely to be noise reach the final output image. The first threshold is a numerical cut on the intensity value of each contour applied immediately after averaging the differences from multiple golden images and removes most of the noise. The second and third thresholds remove contours that have a shape deemed irregular to what one might generally expect from solder splash large enough to be of concern. The final threshold applies a ratio cut, R_{Len}, on the height and width of the contour and removes patterned edges left over from imperfect test-golden image alignment and, characteristic to the type of hybrid in question, are usually smooth circular curves or rectangular in shape. Figure 3.8 shows some examples of both solder splash and noise, highlighting which thresholds are used and at which stage they are applied.

Any contours passing all four thresholds are categorised as a potential defect and their positions automatically annotated following the rules that define the areas of interest in Figure 3.4.

Figure 3.10 shows an example of a pixel hybrid and strip hybrid that has passed through the automatic annotation process. As brought up in Section 3.2.1, all differ-

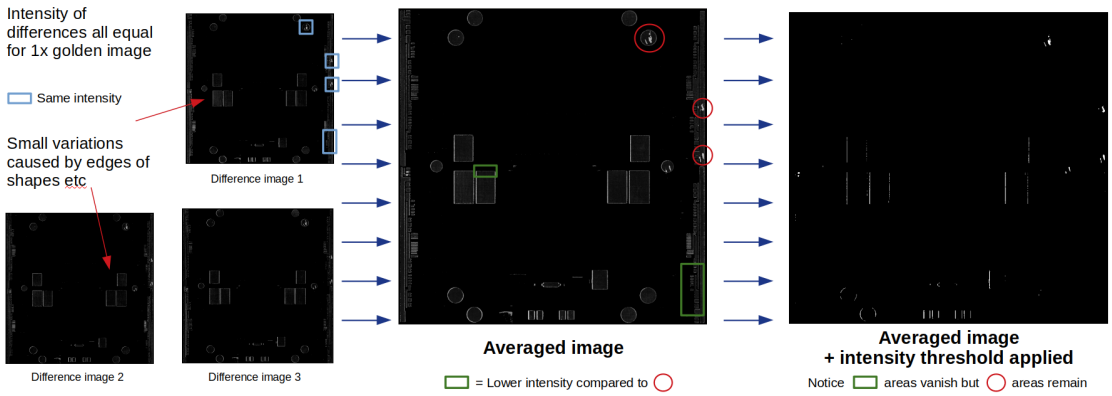

Figure 3.9: Averaging multiple images that find the difference between test and golden image exposes potential defects more clearly as the differences have a higher intensity compared to noise.

ences that are considered potential defects are annotated with circles however they are categorised by different colours based on their severity:

- Green = Noticeable potential defect but within pass boundaries.
- Red = Serious potential defect prompting the user to consider failing the visual inspection of the hybrid.

Defect criteria definitions		
	Name	**Description**
1	**Intensity threshold**	Threshold on intensity value defined by `OpenCV`.
2	**Edges/curve threshold**	Threshold on the numbers of edges (or curves) of the approximate polygon surrounding the contour
3	**Area threshold**	Threshold on the area of the contour (i.e number of pixels)
4	**Max/min length ratio threshold**	R_{Len}; Threshold on the ratio between maximum length and minimum length of the minimum enclosed rectangle around the contour

Table 3.2: Definitions of threshold criteria used for classifying those contours which are defects and those which are noise.

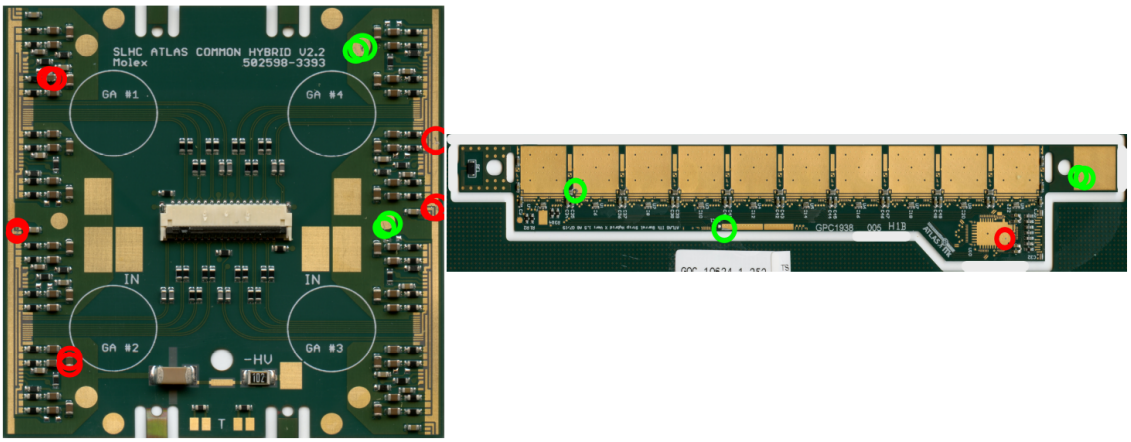

Figure 3.10: Example of pixel and strip hybrids passing the annotation algorithm. All circles are highlighting what are considered as potential defects however they are colour coded based on how severe they might be following the definitions given in Section 3.2.1 and Figure 3.4.

Defect criteria threshold values: Solder splash			
	Variable Name	**Strips**	**Pixels**
1	**Intensity threshold**	Intensity $>$ 140	Intensity $>$ 162
2	**Edges/curve threshold**	Number of edges $>$ 3.5	Number of edges $>$ 4
3	**Area threshold**	Area $>$ 20 pixels	Area $>$ 90 pixels
4	**Max/min length ratio threshold**	(rect) $R_{Len} < 6$ (circular) $R_{Len} < 2.1$	(rect) $R_{Len} < 6$ (circular) $R_{Len} < 2.1$

Table 3.3: Threshold values for the criteria that classifies pixel hybrid solder splash for variables discussed in Section 3.2.3

3.2.4 User Interface

The annotated images highlighting the areas of potential defects, alongside the original pre-annotated copies, are displayed on a user interface (UI) designed for a user to classify each individual hybrid more easily.

Hybrids that have successfully completed the automatic annotation aspect of the

tool are stored in a common database. During visual inspection, the UI presents to the user both the annotated version of the hybrid image and the original version, Figure 3.2. The annotations support the user to immediately focus on the areas of the hybrid most likely to show either solder splash or misaligned/missing components. If the user feels the defects flagged are concerning enough for the hybrid to fail quality control then they are recommended to classify the hybrid as `Failed`. Alternatively, if the user feels the hybrid poses no issues and satisfies all of the conditions of visual inspection then they are recommended to categorise the hybrid as `Passed`. A zoom functionality, Figure 3.11, can optionally be used by the user to add clarity to their decision. In addition to classification decisions alone, the user has the opportunity to write specific comments for failing visual inspection. Warning notifications have been implemented to remind the user to enter a reason for failure if they forget to do so. The information from the output is stored and updated in a shared database before the process is repeated for the next hybrid until all are completed.

3.2.5 Summary, Drawbacks and Future work

In this chapter, working examples for aiding the visual inspection process by creating a tool that automatically identifies and annotates defects in pixel and strip hybrids has been shown. In addition, a UI that displays the hybrid images was tested so that a user can choose whether a particular hybrid passes or fails the visual inspection quality control criteria and are also given the ability to leave comments for future reference before saving the information to a shared database.

Although the software works very well for the hybrid images circulating at the time, as shown in Table 3.4, the algorithm as it currently stands is not robust enough to deal with changes to design and different scanner devices or settings. For example, certain defects are searched for in specific areas of concern and a change of strip or hybrid design requires this to be updated. If there is a change of scanner device or scanner setting, the HSV values behind the solder splash and misaligned component areas needs updating. Also, because the image processing stage depends a lot on the `OpenCV` contour functions, if a scanned image does not contain the entirety of the surrounding hybrid frame then this stage may be incorrectly completed meaning that the later stages will also be invalid. If the software in its current form is to be used for the visual inspection process of the strip and pixel hybrids then there must be a standardised procedure for taking images.

Hybrid Type	Total tested	Passed Inspection	Failed Inspection
Strip	203	200	3

Table 3.4: Summary of how many strip hybrids passed or failed visual inspection using the software.

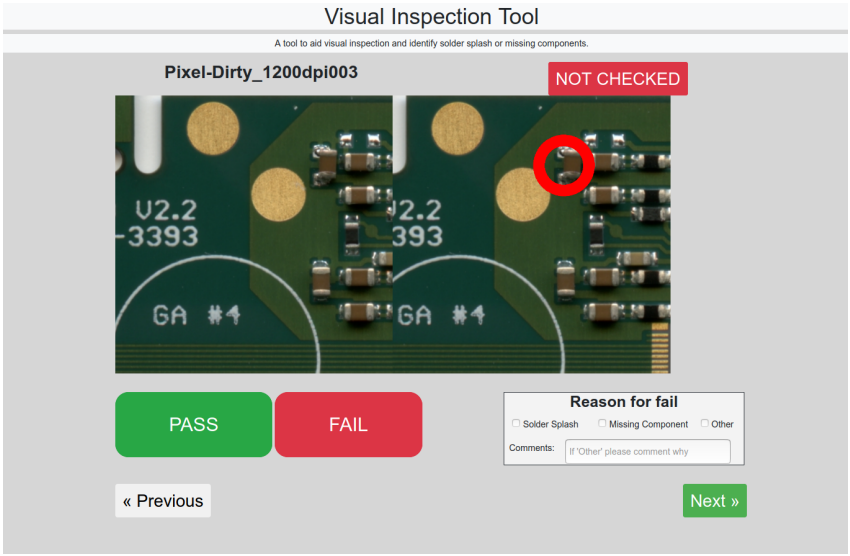

(a) Pixel hybrid example

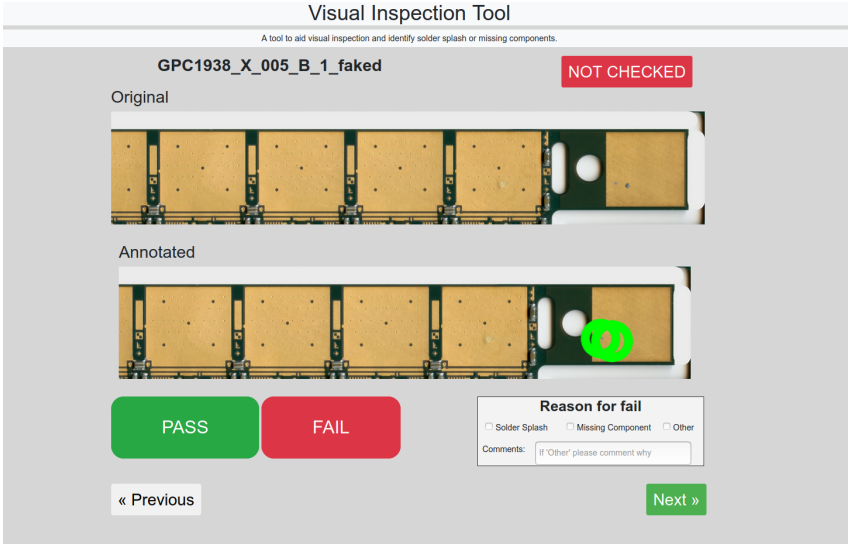

(b) Strip hybrid example

Figure 3.11: Example of UI view for pixel hybrids (top) and strip hybrids (bottom) when zooming into a specific area of the image.

Upon reflection, the current algorithm works well for solder splash recognition however the techniques used for missing/misaligned components are too sensitive and computationally expensive. An alternative approach has been initially developed that uses a convolutional neural network (CNN) for this instead by training on a collection of golden images and separating out the components for better comparison. The target is to use this setup and computer vision methods explained in this chapter as the framework for the image processing stage of the hybrid images and to identify solder splash, but to also include a CNN as a more robust technique for the classification of missing/misaligned components.

Chapter 4

Data, Simulation, Object Reconstruction and Identification

4.1 Data, Simulation, Object Reconstruction and Identification

Particle searches require analysing data events from the LHC and also those simulated by using Monte-Carlo (MC) based techniques. This analysis searches for a rare Higgs boson decay to a Z-boson and an axion-like particle, a, were $h \to Za \to \ell\ell\gamma\gamma$ is the entire signal process with the lepton and photon pairs being the final particle objects that are detected. For a particular selection, introduced properly in a later chapter, the $\ell\ell\gamma$ final state is also considered in which the two signal photons are reconstructed as one photon. Standard Model processes that contain the same final state are backgrounds. In this analysis, the processes that contribute to the majority of the background are due to Z production in association with jets ($Z+$jets) or with a photon from initial or final state radiation ($Z \to \ell\ell\gamma$).

Only the final state particles of an interaction are directly observed at the ATLAS detector. In this instance, the Higgs boson, Z and a particles are short-lived before decaying into stable leptons and photons. It is these final particles that leave various signals at the sub-systems of the ATLAS detector, as explained in Chapter 2. The resulting outputs are then fed through to a series of reconstruction and identification algorithms that determine the particle objects and their properties.

This chapter describes the data, simulated samples, and the object reconstruction

and identification of the relevant final state particles used in this analysis.

4.1.1 Data and simulated samples

This section focuses specifically on the data and the MC generated samples relevant for this analysis. The data used was recorded by ATLAS during the full Run-II period, between the years 2015 and 2018. There are multiple simulated signal $h \to Za \to \ell\ell\gamma\gamma$ MC samples for this search, each having a unique axion mass point (m_a). The background contains simulated samples for the $Z\gamma$ and $Z+$jets processes and all MC samples were passed through the full ATLAS detector simulation. The same analysis selection software was applied to both data and the simulated samples.

Data

Unless stated otherwise, the data referred to throughout this thesis corresponds to the proton-proton collision data collected by the ATLAS detector during the Run-II period between the years 2015 and 2018. During this period, the LHC was operating at a center-of-mass energy of $\sqrt{s} = 13\,\text{TeV}$.

All data events were recorded in stable beam conditions such that all of the sub-detectors at ATLAS were operating nominally.

The luminosity delivered by the LHC and recorded by ATLAS split by run year is shown in Figure 4.1. Over the Run-II period, a total integrated luminosity of $156\,\text{fb}^{-1}$ was delivered by the LHC of which $147\,\text{fb}^{-1}$ was recorded by ATLAS and $139\,\text{fb}^{-1}$ of this passed the requirements deemed good enough to be used for physics analysis. In this analysis, events passing specified lepton triggers, listed with more detail in Chapter 5, were used.

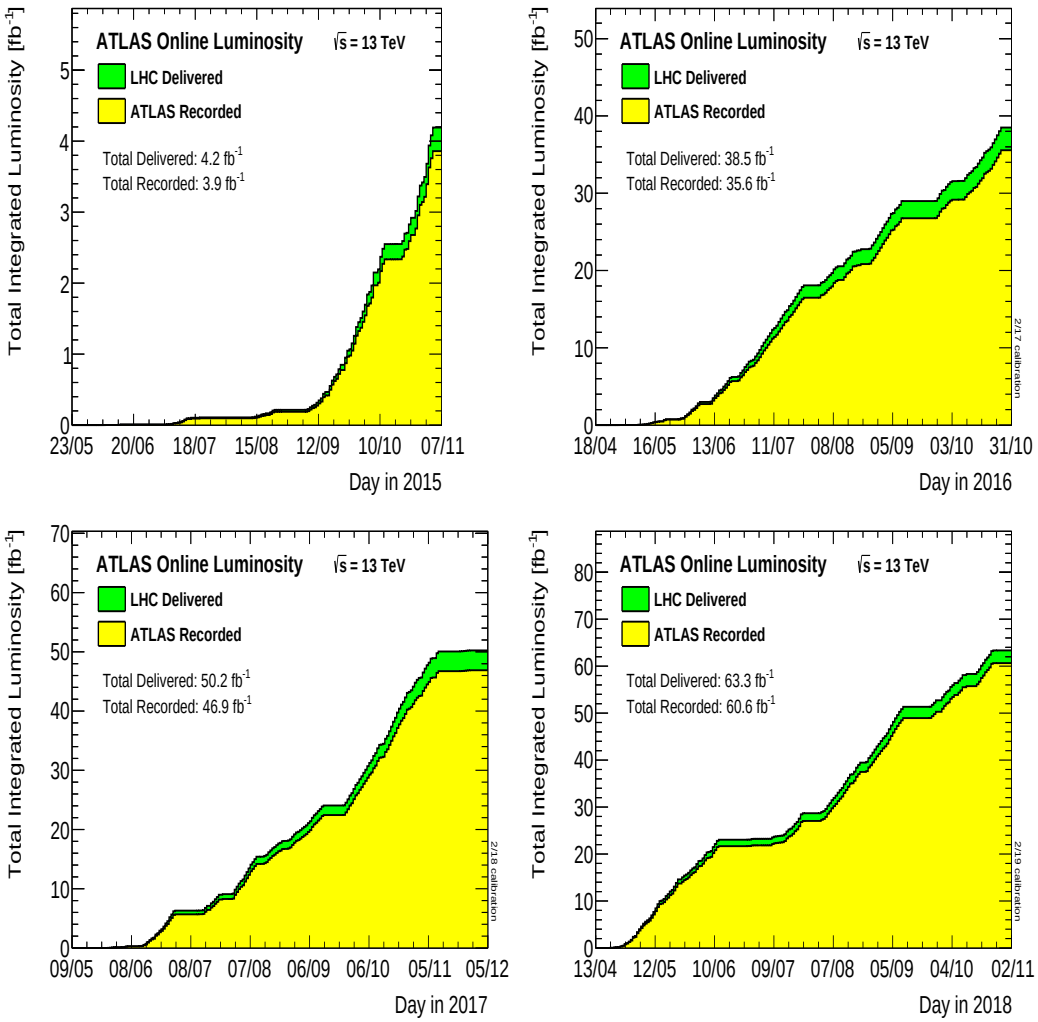

Figure 4.1: Cumulative luminosity delivered by the LHC (green) and recorded by ATLAS (yellow) for each run year [98].

Simulated Samples

Monte Carlo methods were used to produce simulations of the signal and Standard Model background processes that result from proton-proton collisions. Colliding proton beams are easier to accelerate to higher energies compared to lepton beams. A drawback however is that since the composite structure of hadrons is complex so too is the modelling of hadron collider events.

There are two important aspects to the MC simulation method; hard interactions and parton showering. Hard interactions/hard scatterings are simulated using matrix elements for leading order (LO) or next-to-leading-order (NLO) calculations from pertubation theory, with the particles decaying according to given branching

ratios. For particle MC generators this is usually calculated using the Powheg-BOX-v2 [99–101] or Madgraph [102] frameworks. Parton showers are approximations of higher-order corrections to the hard interactions and simulate coloured partons radiating into further coloured partons until the strong interaction coupling rises enough to trigger hadronisation resulting in colourless hadrons. Parton showers and hadronisation are calculated using either Pythia8 [103] or Herwig [104, 105].

The $h \to Za \to \ell\ell\gamma\gamma$ signal and $Z\gamma/Z+$jets background processes that dominate this analysis are modelled from MC methods.

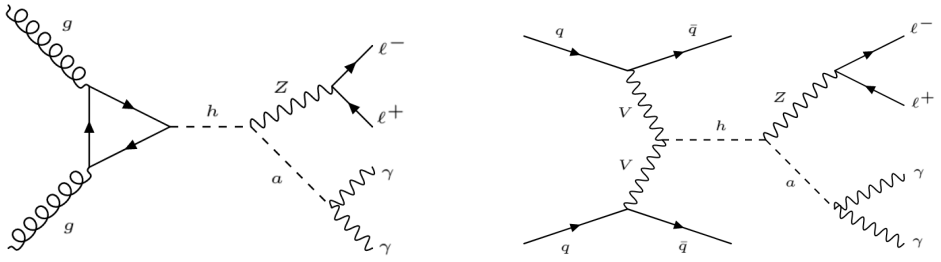

(a) ggF (b) VBF

Figure 4.2: Feynman diagrams for gluon-gluon fusion and vector-boson fusion Higgs boson production also showing the signal Higgs boson decay, $h \to Za \to \ell\ell\gamma\gamma$

$h \to Za \to \ell\ell\gamma\gamma$ signal MC

There are two Higgs boson production mechanisms considered for the signal samples. The first assumes a Standard Model Higgs boson produced through gluon-gluon fusion (ggF) and the other assuming vector-boson fusion (VBF) production. Both productions were detailed in Section 1.1.2. Figure 4.2 shows lowest order Feynman diagrams for each of the Higgs boson mechanisms. For ggF, the Higgs boson production cross section for $\sqrt{s} = 13\,\text{TeV}$, estimated at N3LO QCD and NLO EW, is $\sigma_{SM} = 48.52$ pb whereas for VBF $\sigma_{SM} = 3.79$ pb and is estimated at NNLO. The mass of the Higgs boson in both productions is set at $m_H = 125.09\,\text{GeV}$ and decays to a Z-boson and a neutral psuedo-scalar axion-like particle, $h \to Za \to \ell\ell\gamma\gamma$. The a particle is of relatively low mass and is between 0.1 GeV to 10 GeV. There are 12 signal samples for each Higgs boson production set, these are the 0.1, 0.4, 0.7, 1.0, 2.0, 2.5, 3.0, 4.0, 5.0, 6.0, 7.0, 9.0 GeV axion mass points. The analysis focuses on a particle decays that are prompt. The nominal $a \to \gamma\gamma$ final state photons at mass points $m_a < 1.0\,\text{GeV}$ were less likely to be prompt so four additional *prompt-only*

samples per production set were also generated for 0.1, 0.4, 0.7 and 1 GeV. The hard interactions for all samples are generated at NLO with Powheg-BOX-v2 using AZNLO [106] tune and the parton showering was simulated using Pythia8 with CT10/CTEQ6L1 [107, 108] PDF sets.

Background MC

The Standard Model production of $Z\gamma$ and $Z+$ jets are the main sources of background in this analysis. MC simulated samples for these background processes were used to give an idea of their behaviour under final selections. The samples are generated with Sherpa, a MC method, with the NNPDF 3.0 NNLO [109] using the same tune and PDF as used for the signal MC samples. The Standard Model Higgs boson decay to $Z\gamma$ ($h \to Z\gamma$) also considered for background though this was found to contribute only a small fraction of the total and taken as a negligible. This MC sample was generated at NNLO with Powheg and the parton shower simulated by Pythia.

Additional Standard Model processes with final states containing photons and leptons could also contribute to the background. These may come from sources such as W production in association with jets (W+jets), top pair production $t\bar{t}$, single-top-quark, WW, WZ and ZZ production and as such were also studied. The MC simulation of W+jets, WW, WZ and ZZ events are generated using Sherpa with the NNLO PDF set. The single-top-quark and $t\bar{t}$ samples are generated using Powheg and Pythia with the Perguia2012 [110] tune for parton showering and hadronisation and CT10/CTEQ6L1 PDF sets.

4.1.2 Track and vertex reconstruction

Tracks from charged particles are reconstructed from hits in the inner detector. There are four important stages to track reconstruction, in order these are cluster creation, seeding, track scoring and fitting the track.

Raw signal hits in the pixel and SCT detectors create *clusters*, using corrected component analysis, and *space points* which are the locations where the active material of the inner detector is passed by the charged particle. The average size of a cluster is approximately 2 pixels in the $\rho - \phi$ plane and 1-3 pixels in the direction

of the beam line. Clusters can be defined as *single-particle pixel clusters* or, in the case of dense environments, *merged pixel clusters*. Single-particle clusters are such that they are clusters determined by one charged particle whereas merged clusters are due to very collimated charged particles. Figure 4.3 shows example illustrations of the energy deposits for the two types of pixel clusters when particles with different trajectories pass [111].

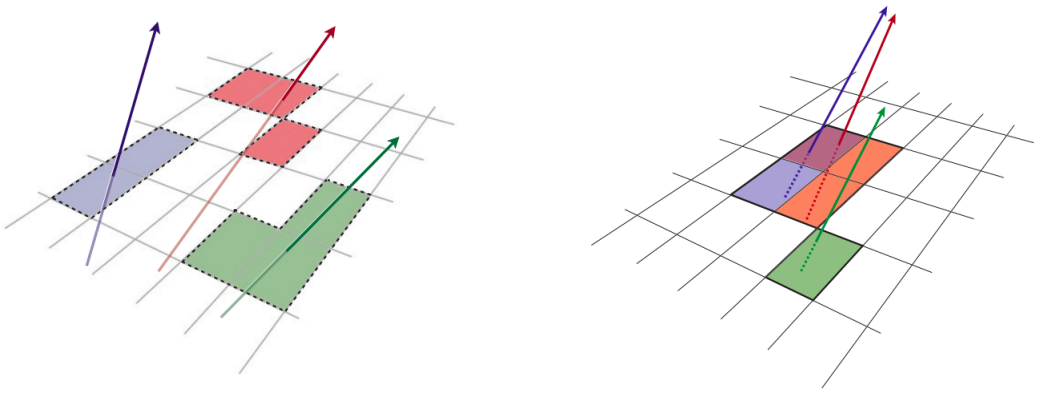

(a) Single-particle pixel cluster (b) Merged pixel cluster

Figure 4.3: Examples of single-particle pixel clusters on a pixel sensor (left) and also a merged pixel cluster from collimated charged particles (right). Each example shows three particles illustrated with different colours and their trajectories represented by the corresponding arrows [111].

Sets of three space-points form what is known as a track seed and first estimates of the momentum, trajectory and impact parameters (d_0 and z_0) are calculated for the track candidate. An impact parameter is the closest distance from the beam line to a given track. The d_0 value is the impact parameter for the transverse plane and z_0 the impact parameter longitudinally. Seeds can vary significantly in terms of purity. The purity usually depends on momentum and d_0/z_0 requirements but also can differ based on where the seed is located. For example, seeds from the SCT are considered more pure than mixed-detector seeds. Purity is improved by testing where a fourth cluster is compatible with the extended trajectory. Additional space points are added from further layers of the pixel and SCT detectors that are compatible with the preliminary trajectory which then builds a track candidate using a Kalman filter [112].

Track score is a term used to quantify the quality of the track candidates. The

track score is calculated from multiple variables such as momentum and also the χ^2 of the track fit. Track candidates are ordered by the ambiguity solver so that those with characteristics more likely to represent the charged particle trajectory, i.e those with the highest track score, are considered with greater weight. The track candidates must also pass a list of quality requirements or risk being rejected by the ambiguity solver. Some of these requirements include having a particle $p_T > 400\,\text{MeV}$, $|\eta| < 2.5$ and a maximum of either one shared pixel cluster or two shared SCT clusters on the same layer.

Finally, a high-resolution fit is performed on the remaining track candidates where the position and uncertainty of each cluster is calculated by multiple neural networks [113]. Leaving the track fit until the last stage reduces the CPU usage required when performing the track reconstruction process as a whole.

In particle interactions, vertices are the points where particles are either created or annihilated. The primary vertex is where the hard scattering occurs and is always within the interaction region. A secondary vertex might also be formed in the case where particles that decay following the primary vertex are longer lived. The reconstruction of the vertices is done using an iterative vertex finding algorithm [114] which calculates whether multiple tracks share the same crossing point and disregards those that appear incompatible.

For the selection specific to this analysis the events require to have at least one vertex. Constraints are also applied to the track where the impact parameter z_0 must be $< 10\,\text{mm}$ on lepton objects which checks whether the electrons and muons are acceptably close enough to the primary vertex.

4.1.3 Jets

Jets are groups of collimated particles that come as a result of fragmentation and hadronization of gluons and quarks. They are reconstructed from topological energy clusters inside the calorimeter. Topological clusters are formed from a *proto cluster* which are made up of cells with relatively high signal significance, ζ_{cell}^{EM}, defined as the ratio between the signal in the cell to the expected noise in the EM scale. If a cell has $\zeta_{cell}^{EM} > 4$ then this cell is chosen as the cell proto cluster seed. The significance values of neighbouring cells are also tested and if $\zeta_{cell}^{EM} > 2$ then

they too are added to the proto cluster. This process repeats until all the neighbouring cells that satisfy this criterion are added and the topological cluster formed [115].

The *anti-kt* algorithm inputs the energy deposit information from the objects and calculates two quantities, $d_{i,j}$ and d_{iB} defined as

$$d_{i,j} = \min\left(\frac{1}{p_{T,i}^2}, \frac{1}{p_{T,j}^2}\right)\frac{\Delta R_{i,j}^2}{R^2} \qquad d_{iB} = \frac{1}{p_{T,i}^2} \tag{4.1.1}$$

where i and j are energy clusters from two different objects and $\Delta R_{i,j}^2$ is the distance between them. The standard choice for the jet radius parameter R at ATLAS is 0.4. This is also the value used for the *anti-kt* algorithm used in this analysis. The two values $d_{i,j}$ and d_{iB} are compared and if $d_{i,j} < d_{iB}$ then the two energy clusters are merged together. If instead $d_{i,j} > d_{iB}$ then the energy cluster i is declared as a jet and removed from the list of clusters. This entire process is repeated until there are no more objects left [116].

An additional filter is applied to further maximise the identification of jets that originate from the hard scattering interaction and suppress those from pile-up. This is done by use of the jet vertex tagger (JVT) score. The JVT is a multivariate discriminant method, based on the k-nearest neighbour algorithm, which inputs two variables, corrJVF and R_{p_T}. corrJVF is a pile-up corrected JVF variable and R_{p_T} is a value combining calorimeter and tracking information. Both variables are defined in Ref [117].

Jet objects are selected in this analysis only if they have a $p_T > 20\,\text{GeV}$, $|\eta| < 4.4$ and satisfy a JVT score greater than 0.59, also referred to as the Medium working point. In this analysis, jets are not specifically used as final state objects but they are required during the overlap removal procedure which is detailed in Section 4.1.7.

4.1.4 Electrons

Electrons are reconstructed at ATLAS by matching tracks in the inner detector with ECAL topological energy clusters, introduced in Section 4.1.3 describing the reconstruction of jets. For electrons, only the energy in the ECAL is used to form these clusters. A track is considered matched if the conditions $|\eta| < 0.05$ and

$-0.10 < q.(\phi_{track}-\phi_{cluster}) < 0.05$ are met (with q being the charge of the track). If the number of matched tracks associated with a cluster is more than one, then tracks with hits in the pixel detector are considered with higher preference than those, for example, with signals in the SCT but not the pixel detector. If multiple tracks are matched that come from the same part of the inner detector then those with lower ΔR values with respect to the cluster are better considered (unless $\Delta R < 0.01$). The tracks that the clusters are matched to are re-fitted to take into account bremsstrahlung (a process outlined in Section 2.3.3).

Superclusters are then built by grouping together close-by clusters. Superclustering is a process described in more detail when explaining the reconstruction of photons in Section 4.1.6. For electron candidates, the cluster must satisfy a minimum transverse energy requirement greater than 1 GeV. The reconstruction of electrons is done in parallel with that of photons [118]. Generally, both are distinguished from one another when electrons are either matched to good quality tracks or if photons lack a conversion vertex. Those less distinguishable require more consideration from the analysis teams working with these objects.

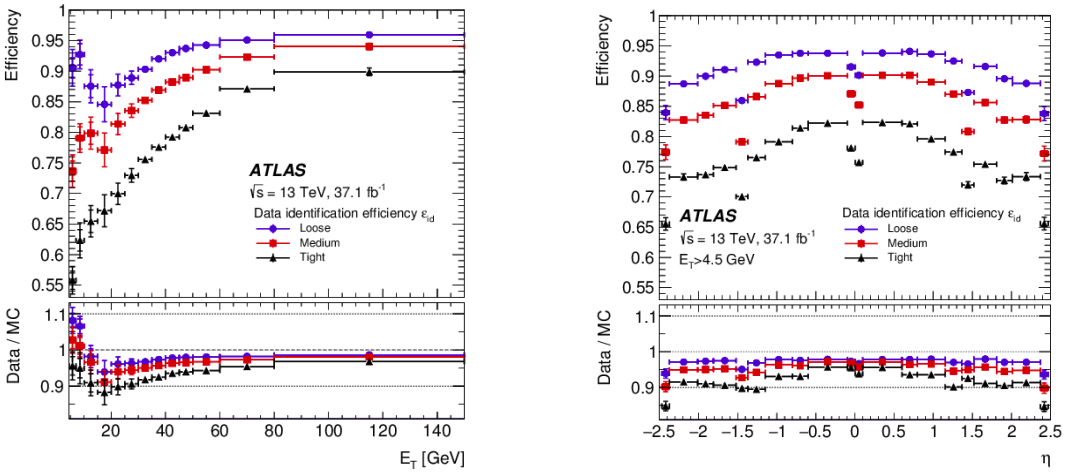

(a) (b)

Figure 4.4: Electron identification efficiencies as a function of (a) transverse energy E_T and (b) η measured in $Z \to ee$ events for all three working points; Loose (blue circle), Medium (red square) and Tight (black triangle). Inner vertical bars represent statistical uncertainties and outer bars the total uncertainty. Bottom panal shows the data to the prediction from simulation ratio for each working point [119].

After the reconstruction of an electron candidate is completed, identification criteria is also applied. There are three main levels of identification criteria for electron candidates. These are called the Loose, Medium and Tight identification working points and each represent a higher degree of background rejection at a cost of lower electron efficiencies. All electrons satisfying these criteria must have a total of 7 hits in the pixel and silicon strip detector with at least 2 hits in the pixel detector. Tight and Medium require a further hit in the first layer. Efficiency plots for each identification working point as a function of E_T and η are shown in Figure 4.4, highlighting their differences. For example, the loosest working point has an identification efficiency from 85 % at $E_T = 20\,\text{GeV}$ to 96 % at $E_T = 100\,\text{GeV}$ whereas Tight varies more from 78 % to 90 % for the same E_T range [119].

4.1.5 Muons

Muons are reconstructed generally from independent tracking information from the inner detector and the muon spectrometer. There are four types of algorithms that are used to reconstruct muons; combined muons, segment-tagged muons, calorimeter-tagged muons and extrapolated muons [120]. Combined muons are the muons mostly relevant to this analysis and these are reconstructed from matched tracks in the inner detector and muon spectrometer only. An "outside-in" algorithm extends the tracks measured in the muon spectrometer to the potential muon candidate track in the inner detector whereas an "inside-out" algorithm extrapolates the inner detector track to the muon spectrometer track.

Muon identification is applied to better classify prompt muons from W/Z decays vs muons from meson decays or jets. There are four recommended muon identification working points, Loose, Medium, Tight and High-p_T which, likewise with the electron working points, gradually reject more background but at the cost of muon efficiency. The efficiencies for each working point as a function of η are shown in Figure 4.5. In addition to identification, muon isolation is required to reject background muons such as those originating from hadrons that pass through the calorimeters and leaving tracks in the muon spectrometer using isolation variables similar to those discussed previously with electrons [121].

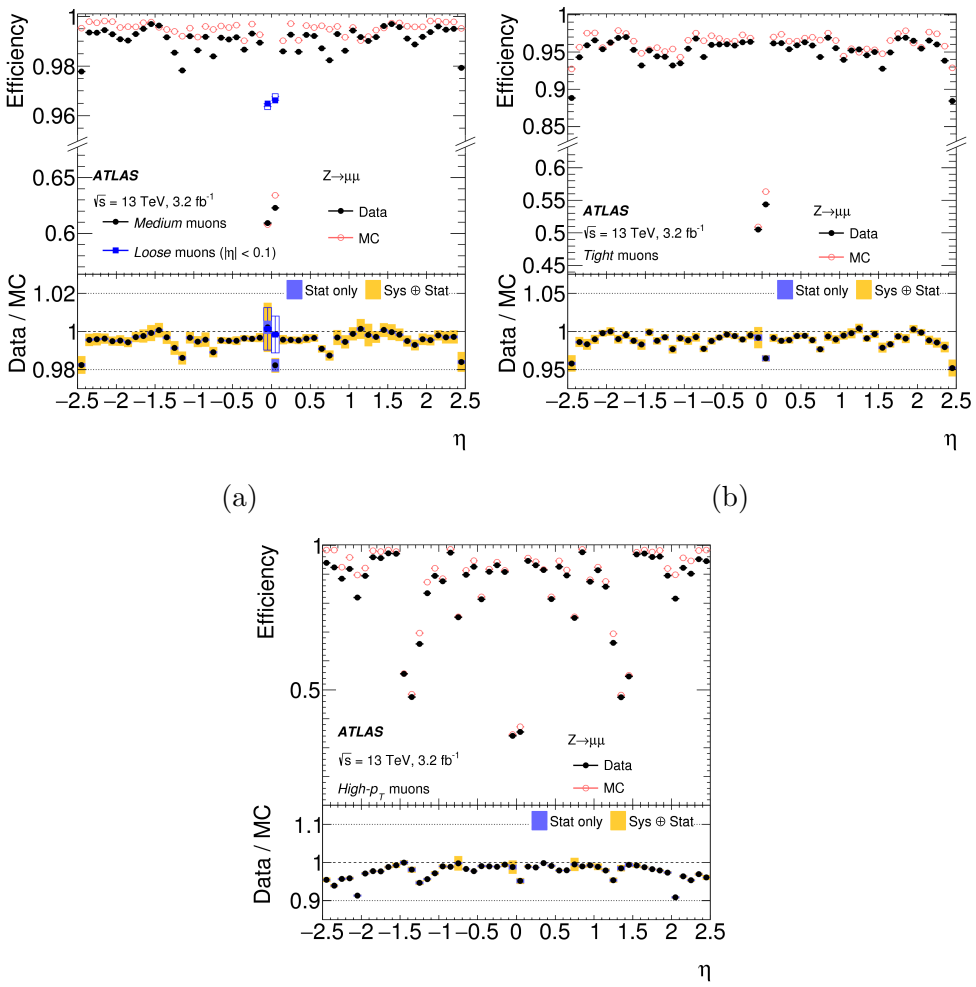

Figure 4.5: Muon reconstruction efficiency as a function of η measured in $Z \to \mu\mu$ for (a) the Loose and Medium, (b) Tight and (c) High-p_T identification working points. All muons have $p_T > 10\,\text{GeV}$. The bottom panel gives the data to the prediction from simulation ratios. Error bars in the efficiency panel are statistical uncertainties only whereas the error bars in the bottom panel contain both statistical and systematic uncertainties [121].

For the selection specific to this analysis, only muon candidates with $|\eta| < 2.5$ are considered. They must also have a $p_T > 10\,\text{GeV}$, unless they are calorimeter-tagged muons for which they require $p_T > 15\,\text{GeV}$, and also pass Medium identification. Likewise with electrons, the selected muon candidates must satisfy the Loose isolation criterion [121].

4.1.6 Photon reconstruction and performance

As discussed in Section 2.3.2 and Section 2.3.3, photons are reconstructed using information from the inner detector and calorimeters. To summarise, photons produce electromagnetic showers in the ECAL which are measured as energy clusters, similarly to how electrons are reconstructed. Occasionally these clusters might be matched to conversion vertices measured in the inner detector for photons converted via pair production ($\gamma \rightarrow e^+e^-$) in the material before the calorimeter or tracker. The output photon object is also fed through a photon identificaton procedure to better select prompt photons before being tested against photon isolation criteria which suppresses hadronic backgrounds further.

Photon reconstruction and performance

When a photon passes through the ECAL, the electromagnetic showers produced as a result of bremsstrahlung ionise the LAr active material which consequently forms drifting electrons that leave signal pulses at the Cu electrodes. It is the amplitude of this signal pulse that is used in the calculation to determine the energy deposited by the photon. The signal is sampled and is digitized for analysis. The signal distribution features, such as the gain of the output channel and calibration correction factors, are used as inputs for Equation 3.3 in Ref [122] that corrects the ionisation current into deposited energy.

Subsequently, the cells are then clustered to form topoclusters. Dynamical topological cell clustering which makes use of the cell significance values has already been introduced in Section 4.1.3 describing the reconstruction of jets. As mentioned already when describing the reconstruction of electrons in Section 4.1.4, this is the same process for photons however only energy in the ECAL is used. Once the electromagnetic topoclusters are formed, a *supercluster* is constructed from adding nearby clusters to a seed topocluster. A supercluster seed must have a transverse energy of at least 1.5 GeV. Nearby clusters are known in this context as satellite clusters. For photons these are accepted as part of the supercluster as long as they are located within a 0.075×0.125 $\Delta\eta \times \Delta\phi$ window from the barycenter of the seed, regardless of the individual cluster transverse energy. For electrons this window is 0.125×0.300 $\Delta\eta \times \Delta\phi$. Superclusters tend to represent the electromagnetic showers formed from an initial photon, with the satellite clusters emerging from

bremsstrahlung or topocluster splitting.

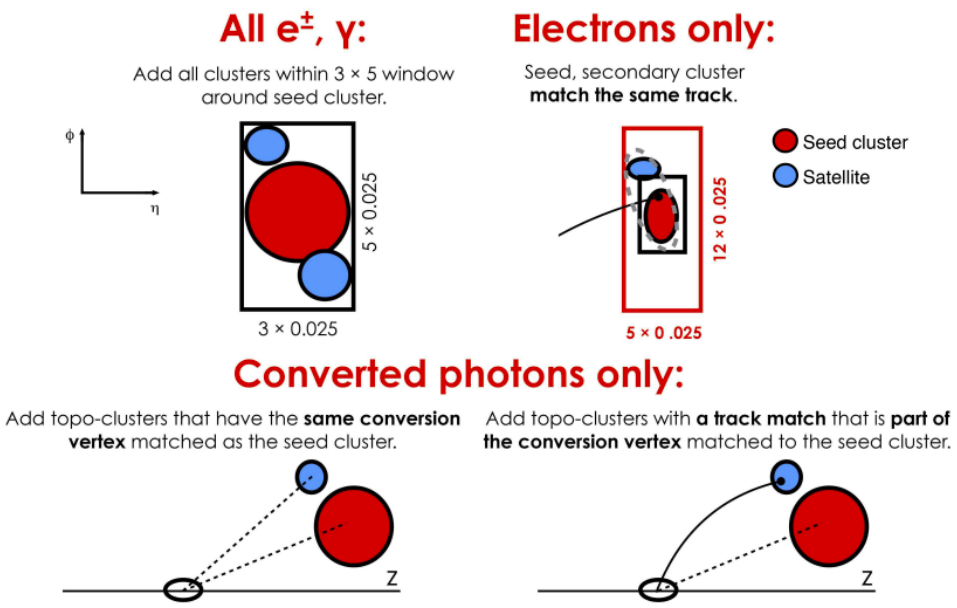

Figure 4.6: Illustration of photon and electron superclustering. Red shapes represent the seed clusters and blue shapes the satellite clusters [123].

Converted photons are reconstructed by adding topoclusters that share the same conversion vertex, or a track matched to this vertex, with the seed [123]. Figure 4.6 shows a visualisation of the superclustering for photons and electrons. Generally, electron objects are ECAL clusters matched to a track, a converted photon objects are clusters matched to a conversion vertex and unconverted photon objects are clusters not matched to either [123, 124].

After the photon energy is measured the photons are then calibrated. This is partly done by optimising the energy resolution using a multivariate (MVA) regression algorithm. Inputs to the MVA are properties of the electromagnetic shower, such as $\eta_{cluster}$ in the ATLAS frame and ratio of the energy in the pre-sampler to energy in the full accordion. The MVA is trained on simulated photon information for both converted and unconverted photons and optimises the energy resolution for each separately. Absolute energy scale is also adjusted using measurements with $Z \to ee$ decays together with pile-up uncertainties which are verified using radiative Z-boson decays, $Z \to \ell\ell\gamma$ [125].

Photon Identification

A simple cut-based selection criteria on various shower shape variables is applied to photon candidates to efficiently select prompt photons and reject backgrounds that originate from hadronic jets. This selection process is known as photon identification.

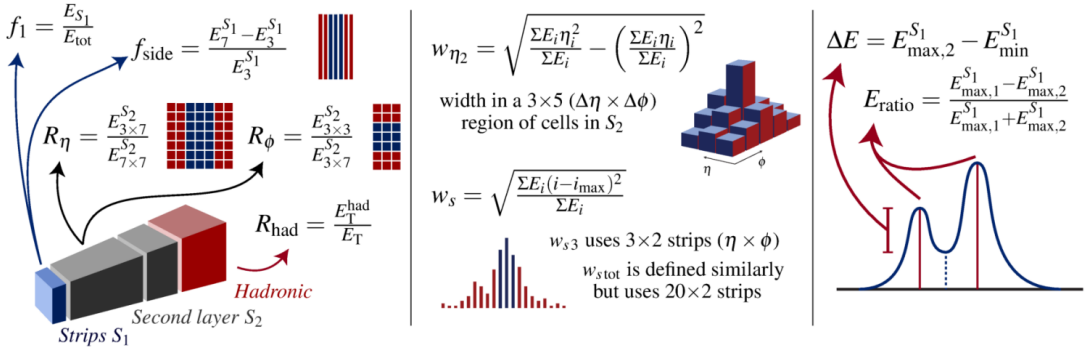

Figure 4.7: Schematic representation of the photon identification discriminating variables defined in Table 4.2. η_i denotes the psuedorapidity center and E_i the energy of cell i. $E_C^{S_N}$ is the energy measured in cluster C of ECAL longitudinal layer N [126].

There are three separate photon identification working points, each having different background rejection levels [127]. The working point of greatest background rejection is labelled Tight with the progressively less restrictive selections called Medium and Loose. The Loose selection constraints only the ECAL second layer variables R_η and $w_{\eta 2}$ and hadronic leakage transverse energy ratios R_{had} and R_{had1} that are used to describe the shower shape. This selection is included in a number of single photon and diphoton triggers. The 'Medium' selection contains the same criteria but with an additional cut on ECAL first layer shower shape variable E_{ratio}, the ratio in energy difference between the maximum and secondary energy deposits with total energy, to maintain an acceptable trigger rate for data collected from 2017. The Tight selection is the only working point to make use of the first layer discriminant variables. All working points have cuts optimised in bins of $|\eta|$ since the shower shapes are dependant on where in the calorimeter the EM shower occurs. The Tight selection criteria are also optimised in bins of transverse energy.

Table 4.2 summarises all photon identification discriminating variables with detailed descriptions, notations and whether they are included in the Loose or Tight selection sets. Figure 4.7 also shows the same details visually for the main variables. Figures 4.7-4.10 show the distributions for each variable before any identification

selection is applied for single photons with the highest p_T from $Z \to \ell\ell\gamma$ MC samples passing *pre-selection*, to be introduced in Section 5.1. This selection includes, among other criteria, the leading (sub-leading) lepton to have a $p_T > 27(20)$ GeV. Figure 4.7, Figure 4.8 and Figure 4.10 show the ECAL first layer, second layer and hadronic leakage layer photon identification variable distributions respectively.

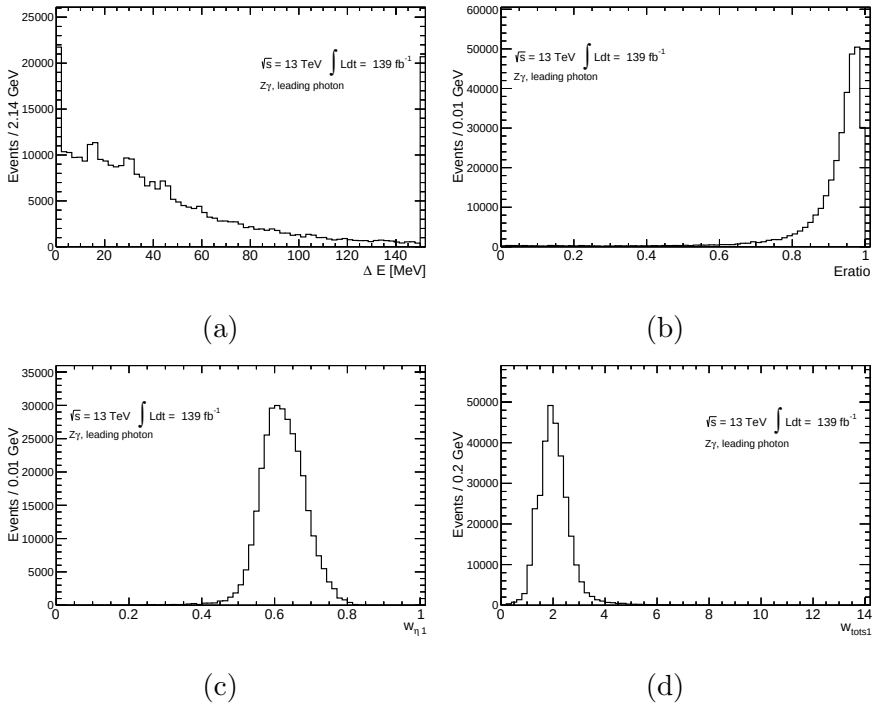

(a) (b)

(c) (d)

Figure 4.8: Photon identification discriminant distributions for ECAL first layer variables ΔE, E_{ratio}, $w_{\eta 1}$ and w_{tots1}. Photons used are from $Z \to \ell\ell\gamma$ MC simulations for events already passing pre-selection and Loose photon isolation (Section 4.1.6).

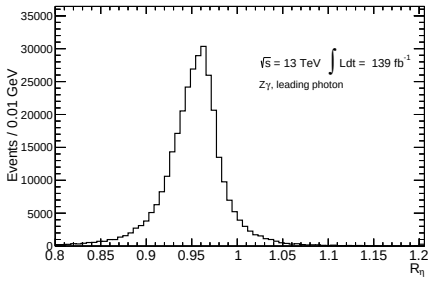

(a)

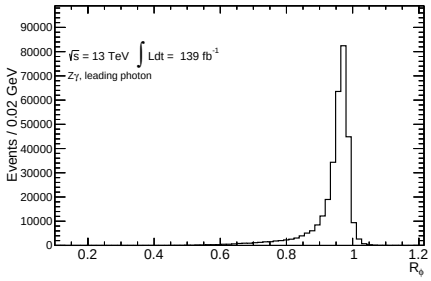

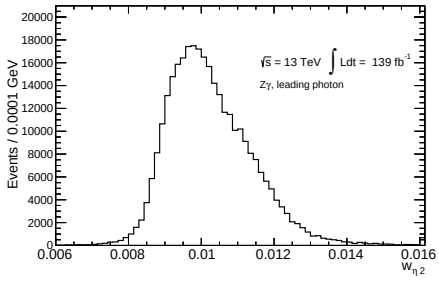

(b) (c)

Figure 4.9: Photon identification discriminant distributions for ECAL second layer variables R_η, R_ϕ and $w_{\eta 2}$. Photons used are from $Z \to \ell\ell\gamma$ MC simulations for events already passing pre-selection and Loose photon isolation (Section 4.1.6).

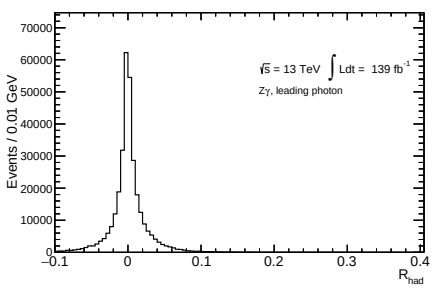

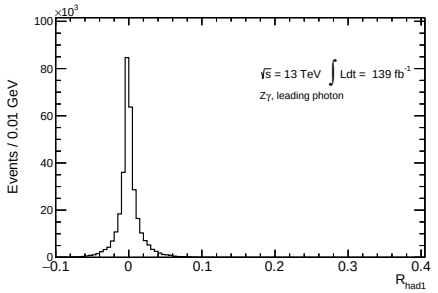

(a) (b)

Figure 4.10: Photon identification discriminant distributions for hadronic leakage variables R_{had} and R_{had1}. Photons used are from $Z \to \ell\ell\gamma$ MC simulations for events already passing pre-selection and Loose photon isolation (Section 4.1.6).

The middle layer and hadronic leakage variable cuts are optimised to reduce hadronic jet backgrounds with the first layer variable cuts for Tight identification in particular rejecting $\pi^0 \to \gamma\gamma$ decays. Tight is also optimised according to whether the photon candidate is converted or unconverted using the TMVA algorithm package [1].

The Tight photon identification performance is assessed from three separate photon efficiency measurements. These are a direct MC-data comparison using the shower shapes from $Z \to \ell\ell\gamma$ photons, a matrix-method based inclusive photon production data selection and finally an efficiency measurement using electrons from $Z \to ee$ decays with electron shower shapes modified to appear similar to those of photons. Each measurement is with respect to photons that are isolated (Section 4.1.6) and pass the Loose identification working point [125]. The final result for the photon identification efficiency is calculated as the combination of all methods and the data to MC difference taken as a MC correction factor. Figure 4.11 shows the efficiencies of each method, separating by whether the photon is converted or not.

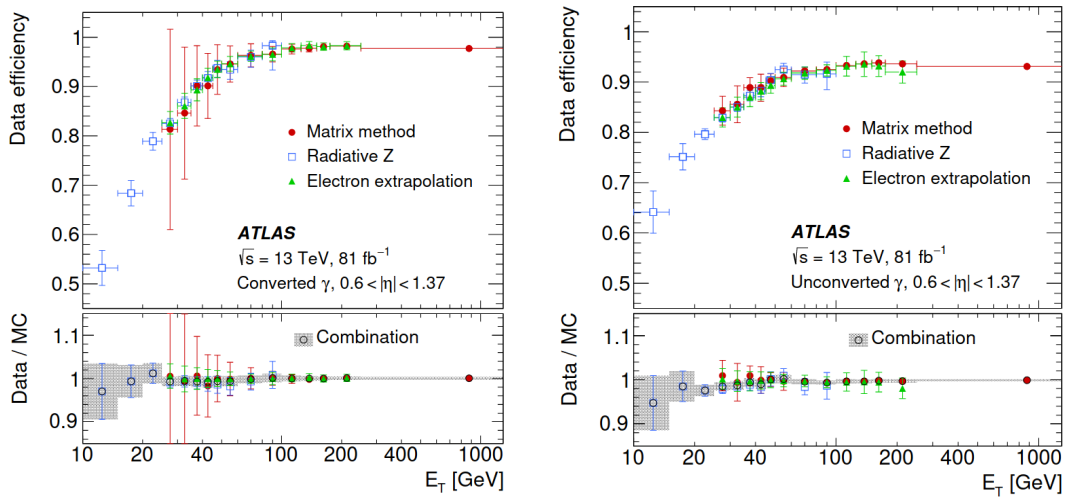

(a) (b)

Figure 4.11: Tight photon identification efficiency results for each method for (a) converted photons and (b) unconverted photons as a function of transverse energy, E_T. All photons require to have passed Loose identification and be within the region $0.6 < |\eta| < 1.37$. Bottom panel shows the combined scale factors (weighted average of all measurements) with their total uncertainties represented by the band [125].

[1] Toolkit for Multivariate Data Analysis with ROOT (TMVA) is a ROOT package which provides an interface to implement machine learning for high energy physics analyses [128].

Working point	**Calorimeter isolation criteria**	**Track isolation criteria**
Loose	`topoCone20` $<0.065 \times E_T$	`Cone20` $<0.05 \times E_T$
Tight	`topoCone40` $<0.022 \times E_T + 2.45\,\text{GeV}$	`Cone20` $<0.05 \times E_T$
TightCaloOnly	`topoCone40` $<0.022 \times E_T + 2.45\,\text{GeV}$	-

Table 4.1: Photon isolation working point definitions [129].

Photon Isolation

Prompt photons from hard scattering generally have minor energy activity in their surrounding vicinity and are considered *isolated*. Additional selection criteria can therefore take advantage of this and single out isolated photons to further reduce background contributions from hadronic jets. This kind of selection is referred to as photon isolation and depends on two isolation variables:

`topoConeX:` The sum of the topological cluster transverse energy in a cone defined with size X, excluding the area surrounding the photon candidate.

`ConeX:` The sum of the p_T from tracks in a cone defined with size X, excluding that of the photon candidate.

The X value is the size of the cone multiplied by 100. For example, X=40 represents a cone size of $\Delta R = 0.4$.

These variables have already been introduced for electrons in Section 4.1.4 and are calculated using topocluster information in a similar way. To briefly summarise, the energies of clusters with barycenters that are contained within a chosen cone are used to derive the isolation variable values excluding the 5×7 $\Delta\eta \times \Delta\phi$ cell segment centered at the photon candidate barycentre. Figure 4.12 shows a schematic example of this in the $\eta - \phi$ plane. Energy leakage from outside of the 5×7 area is corrected for as a function of transverse energy and η, as is the contribution from pile-up using the size of the chosen cone [125, 129].

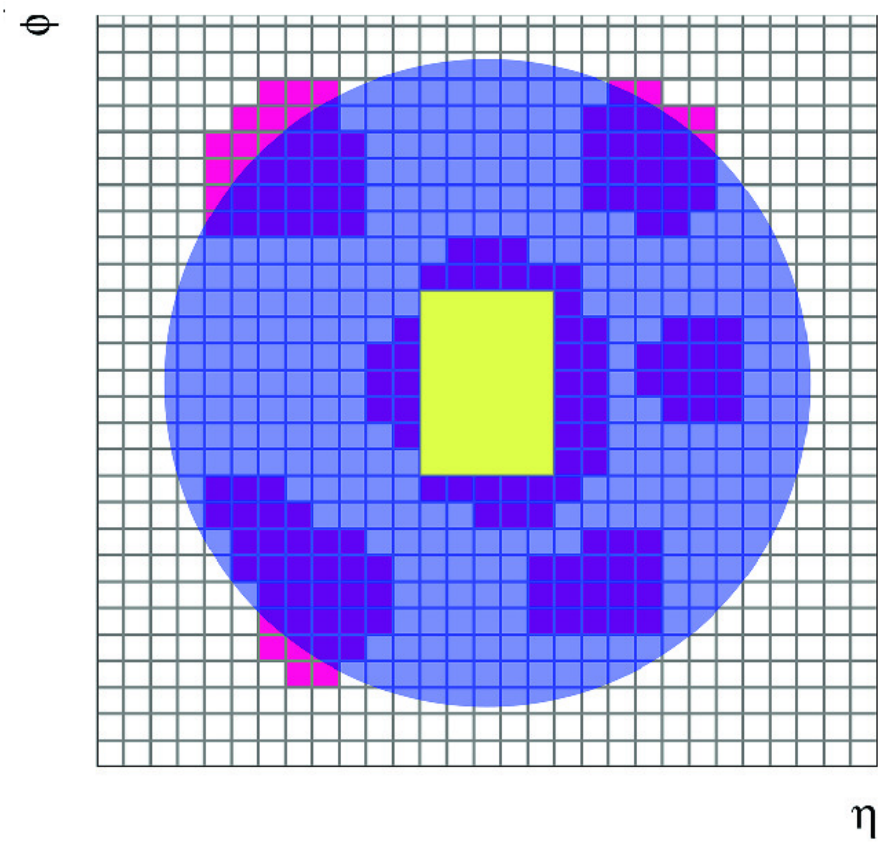

Figure 4.12: Illustrative example of calorimeter isolation in the $\eta - \phi$ plane where each unit of the grid represents calorimeter cells in the ECAL second layer. The blue circle represents the size of cone with chosen ΔR. The purple cluster of cells at the center of the cone is the photon candidate. Nearby clusters which contain barycenters that fall within the cone are included in the calculation of the isolation variable. The yellow rectangle represents the 5×7 $\eta \times \phi$ area over the photon candidate, this is the area for which information is removed from the calculation [129].

There are three photon isolation working points recommended for ATLAS searches. These working points are labelled Loose, Tight and TightCaloOnly and their definitions in terms of the cuts applied to the `topoConeX` and `ConeX` isolation variables are given in Table 4.1. The photon isolation efficiency is measured using photons radiated from leptons in $Z \to \ell\ell\gamma$ decays for transverse energy between 10 GeV and 100 GeV and also from inclusive photons between 25 GeV and 1500 GeV. Figure 4.13 gives the photon isolation efficiencies of each working point as a function of η and transverse energy for both converted and unconverted photons. These plots show that the isolation efficiencies generally increase with greater E_T. The bottom plots of Figure 4.13 show the decreasing relation in efficiency for all working points when there is greater pile-up activity [125].

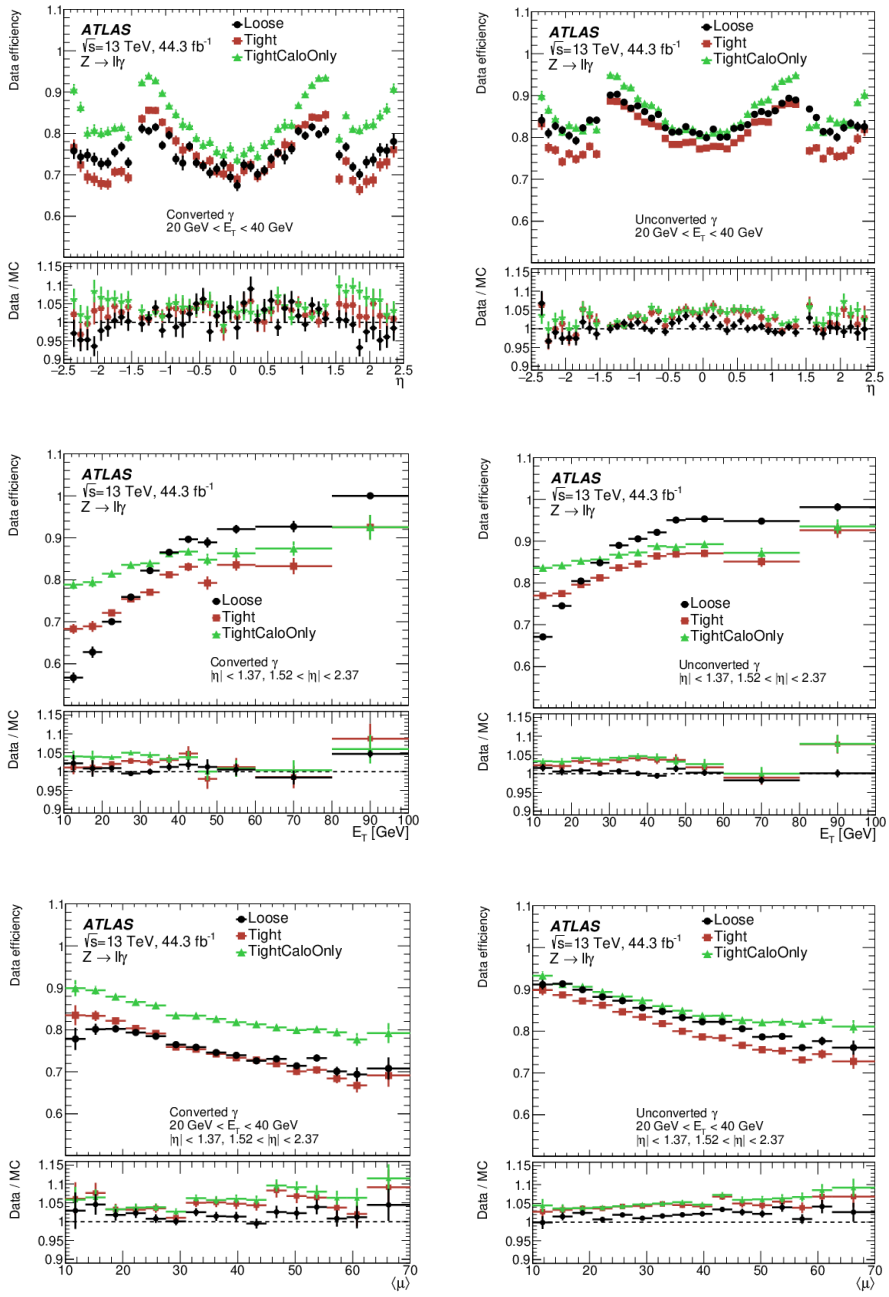

Figure 4.13: Photon isolation efficiency plots for all three working points, Loose, Tight and TightCaloOnly, measured using $Z \to \ell\ell\gamma$ events and separated by whether the photon is converted or not. Top two plots show the efficiencies as a function of η, middle plots show this as a function of E_T and bottom plots as a function of pile-up. The lower panel on each plot shows the ratio of the efficiencies between data and MC simulation. Error bars include both statistical and systematic uncertainties [125].

Photon selection for this analysis

The photons selected for this analysis require a $p_T > 10\,\text{GeV}$ and an $|\eta| < 2.37$, excluding the barrel/endcap calorimeter transition region $1.37 < |\eta| < 1.52$. All photons must pass the Loose photon identification criteria. In terms of isolation selection, this depends on which of the two selection categories in this analysis the event is selected in. These are known as the merged or resolved categories, introduced in Section 5.1. Events are categorised into the merged category if the photons from the ALP decay are reconstructed in the ATLAS calorimeter in a single cluster. Events are categorised in the resolved category if both photons are seperatly reconstructed. For resolved category events, the Loose isolation criteria is applied only if the ΔR between the two selected photons is greater than 0.22. Merged category events also pass a unique working point developed so that the Loose track isolation variable component condition of < 0.05 is kept but the calorimeter isolation variable cut is removed completely. The final isolation selections are explained in more detail in Section 6 and Section 7.

4.1.7 Overlap Removal

Objects are reconstructed independently which means that it is possible that there could be geometric overlap between objects or parts of the deposits assigned to an object that are incorrectly classified as multiple object types. To reduce this affecting the final selection, a procedure known as overlap removal is applied which removes this ambiguity and assigns objects of priority with a single object type based on the angular distance they are from each other. Distance in this context means in the $\eta - \phi$ space and is represented by the ΔR between the objects (defined in Equation 7 from Section 1.2.1).

In this analysis, the overlap removal criteria is a mix of removing photons and jets close to leptons and is as follows:

- $\gamma - e$: Removes photons within $\Delta R < 0.3$ of a nearby electron.
- $\gamma - \mu$: Removes photons within $\Delta R < 0.3$ of a nearby muon.
- jet - γ: Removes jets within $\Delta R < 0.2$ with any surviving photon.
- jet - e: Removes jets within $\Delta R < 0.2$ of a nearby electron.
- jet - μ: Removes jets within $\Delta R < 0.2$ of a nearby muon.

The order the criteria is listed is the order for which they are applied. The same overlap removal is applied to both MC simulated samples and data. Further cuts are applied to the events for better signal and background discrimination before being split into two selection categories, described from Section 5.1 onwards.

Category	Description	Symbol	*loose*	*tight*
Acceptance	$\|\eta\|< 2.37$ with $1.37 < \|\eta\|< 1.52$ excluded	-	✓	✓
Hadronic leakage	$R_{\text{had}} = \frac{E_{\text{T}}^{\text{had}}}{E_{\text{T}}}$ Ratio of the transverse energy $E_{\text{T}}^{\text{had}}$ deposited in the all cells of hadronic calorimeter whose center is in a window $\Delta\eta \times \Delta\phi = 0.24 \times 0.24$ behind the photon cluster to the total transverse energy E_{T} of the photon candidate. Used for $\|\eta\|$ region between 0.8 and 1.37	R_{had}	✓	✓
	$R_{\text{had1}} = \frac{E_{\text{T}}^{\text{had,1}}}{E_{\text{T}}}$ Ratio of the transverse energy $E_{\text{T}}^{\text{had,1}}$ deposited in the cells of hadronic calorimeter first layer whose center is in a window $\Delta\eta \times \Delta\phi = 0.24 \times 0.24$ behind the photon cluster to the total transverse energy E_{T} of the photon candidate. Used for $\|\eta\|$ region that R_{had} does not.	R_{had1}	✓	✓
EM Middle layer	$R_\eta = \frac{E_{3\times7}^{S2}}{E_{7\times7}^{S2}}$ The ratio of the sum $E_{3\times7}$ of the energies in the second layer cells of the EM calorimeter contained in a 3×7 rectangle in $\eta \times \phi$ space of cell unit 0.025×0.0245 to the sum of energies $E_{7\times7}$ in a 7×7 cell rectangle, centered around the photon cluster.	R_η	✓	✓
	$w_{\eta 2} = \sqrt{\frac{\sum E_i \eta_i^2}{\sum E_i} - \left(\frac{\sum E_i \eta_i^2}{\sum E_i}\right)^2}$ E_i is the energy deposit and η_i the position of cell i. Shower lateral width in the EM middle layer, using all cells in a window $\eta \times \phi = 3 \times 5$ in cell units	$w_{\eta 2}$	✓	✓
	$R_\phi = \frac{E_{3\times3}^{S2}}{E_{3\times7}^{S2}}$ Like R_η but in ϕ direction. Behaves differently for unconverted and converted photons since for converted the electrons and positrons bend in ϕ when immersed within a magnetic field.	R_ϕ		✓
EM Strip layer	$w_{s3} = \sqrt{\frac{\sum E_i (i - i_{\text{max}})^2}{\sum E_i}}$ Shower width in η for EM 1$^{\text{st}}$ layer using three strip cells centered on the largest energy deposit. E_i is the energy of strip cell i and i_{max} the cell ID value with the largest energy.	w_{s3}		✓
	Similar to w_{s3} but for all cells in a window $\eta \times \phi = 20 \times 2$ in cell units.	w_{stot}		✓
	$F_{side} = \frac{E(\pm3) - E(\pm1)}{E(\pm1)}$ Lateral containment of the shower along the η direction. $E(\pm n)$ is the energy $\pm n$ strip cells around cell with largest energy.	F_{side}		✓
	$\Delta E = \left[E_{2^{\text{nd}}\text{max}}^{S1} - E_{\text{min}}^{S1}\right]$ The difference between the energy of the strip with the second largest energy, $E_{2^{\text{nd}}\text{max}}^{S1}$, and the energy in the strip cell with the lowest energy between the largest and second largest energy, E_{min}^{S1}. Equal to 0 when there is no second maxima.	ΔE		✓
	$E_{\text{ratio}} = \frac{E_{1^{\text{st}}\text{max}}^{S1} - E_{2^{\text{nd}}\text{max}}^{S1}}{E_{1^{\text{st}}\text{max}}^{S1} + E_{2^{\text{nd}}\text{max}}^{S1}}$ Relative difference between energy strip cell with maximum energy, $E_{1^{\text{st}}\text{max}}^{S1}$, and strip cell with second maximum energy, $E_{2^{\text{nd}}\text{max}}^{S1}$. Equal to 1 when there is no second maxima.	E_{ratio}		✓

Table 4.2: Photon identification variable definitions categorised by detector layer and whether they are used in loose or tight photon identification [127].

Chapter 5

Event Selection and Categorisation

5.1 Event Selection and Categorisation

In this chapter, the event selection criteria that are used to distinguish signal $h \to Za$ events with final state $\ell\ell\gamma\gamma$ from background $Z\gamma$ and Z + jets is described. This chapter shows that for signals with lower m_a many of the photon pairs from the $a \to \gamma\gamma$ decay are boosted and are reconstructed as one photon object. Because of this, after events are selected using single and double lepton triggers and also other lepton requirements for background rejection, events are classified into two categories based on whether the signal photons are likely to be reconstructed as only one photon or two distinct photons. These categories are known as the "merged" category and the "resolved" category, respectively. This chapter details the studies that were done to justify the event selection and categorisation criteria.

5.2 Triggers and Event Pre-selection

Selection criteria is chosen to improve the discrimination between the signal and the background. Events are selected if they contain electron or muon objects that satisfy either single or double lepton trigger criteria, which are detailed in Table 5.1 and Table 5.2. The criteria is a combination of identification and isolation requirements as well as satisfying a p_T over a specified threshold value. The different trigger selection combinations that make up the trigger menu were chosen to maximise the efficiency of selecting specific objects, such as prompt electrons, relative to what is achievable within HLT bandwidth limitations [130]. The composition of the trigger menu is established based on the expected luminosity of each data taking period.

As the instantaneous luminosity increased with each data taking year the trigger menu was also updated. The trigger menus and their performance for each year are described in Ref. [131–134].

Data period	Single electron triggers
2017 + 2018	• At least one electron with p_T >26 GeV satisfying the Tight identification and Loose isolation criteria. • At least one electron with p_T >60 GeV satisfying the Medium identification criteria. • At least one electron with p_T >140 GeV satisfying the Loose identification criteria.
2016	• At least one electron with p_T >24 GeV or p_T >26 GeV satisfying the Tight identification and Loose isolation criteria. • At least one electron with p_T >60 GeV satisfying either the likelihood-based or cut-based Medium identification criteria. • At least one electron with p_T >140 GeV satisfying the Loose identification criteria.
2015	• At least one electron with p_T >24 GeV or p_T >60 GeV satisfying the Medium identification criteria. • At least one electron with p_T >120 GeV satisfying Loose identification criteria.

Data period	Single muon triggers
2017 + 2018 + 2016	• At least one muon with p_T >26 GeV or p_T >50 GeV satisfying the Medium isolation criteria.
2015	• At least one muon with p_T >26 GeV or p_T >50 GeV satisfying the Loose isolation criteria.

Table 5.1: Summary of the single lepton triggers used for event selection, split by data taking period for both electrons and muons.

Data period	Dielectron triggers
2017+2018	• Two electrons with p_T >17 GeV or p_T >24 GeV satisfying the very Loose identification criteria.
2016	• Two electrons with p_T >15 GeV satisfying the very Loose identification criteria.
2015	• Two electrons with p_T >12 GeV satisfying the very Loose identification criteria.

Data period	Dimuon triggers
2017 + 2018 + 2016	• Leading muon p_T >22 GeV, sub-leading muon p_T >8 GeV. Full scan at HLT.
2015	• Leading muon p_T >18 GeV, sub-leading muon p_T >8 GeV. Full scan at HLT.

Table 5.2: Summary of the double lepton triggers used for event selection, split by data taking period for both electrons and muons.

Selected events must have their leptons matched geometrically with the objects triggering the event. As mentioned in Section 4.1.4 and Section 4.1.5, the lepton objects must also pass Medium identification and Loose isolation. In addition to this, the leading lepton must have $p_T > 27$ GeV and the sub-leading lepton $p_T > 20$ GeV. Selected events also satisfy the following criteria:

- Events with more than 2 leptons are removed.
- The two leptons must have opposite electric charge.
- Mass of the two-lepton system is within a window of 81 GeV $< m_{\ell\ell} <$ 101 GeV.
- Events have a two-lepton system $p_T > 10$ GeV.

The selection criteria mentioned thus far shall be referred to throughout this thesis as "pre-selection".

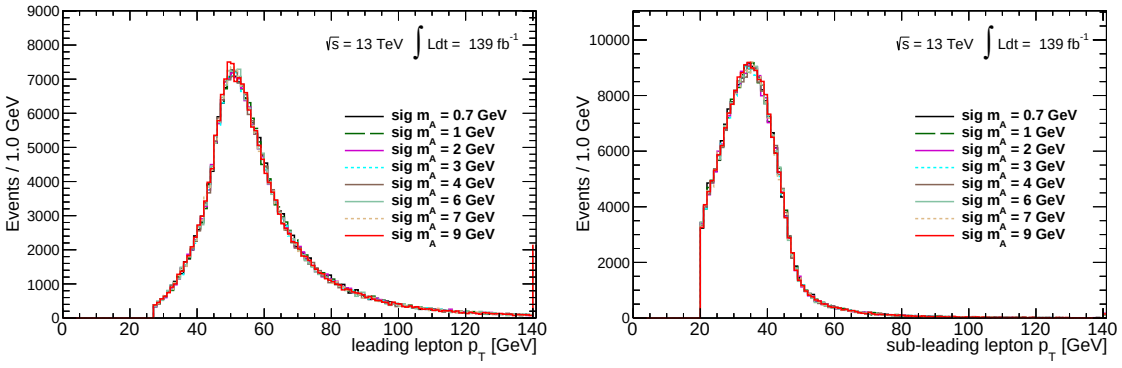

(a) (b)

Figure 5.1: (a) Reconstructed leading and (b) sub-leading lepton p_T distributions for events passing pre-selection for a range of signal samples with different axion mass values. The leading lepton is the lepton with the largest p_T of the selected pair.

The leading and sub-leading lepton p_T distributions after pre-selection are shown in Figure 5.1 for all signal samples. The leading lepton peaks at 50 GeV which is approximately 20 GeV greater than the sub-leading lepton. The $m_{\ell\ell}$ window $81\,\text{GeV} < m_{\ell\ell} < 101\,\text{GeV}$ was chosen to constrain the selection to the Z-boson mass. Other values for the $m_{\ell\ell}$ constraint were tested in an optimisation study that evaluated the significance and sensitivity comparison of each window. The full study is detailed in Appendix B. In this chapter, and the remaining chapters of this thesis, plots that show signal simulation distributions contain events from the sum of both ggF and VBF Higgs boson productions. Plots showing only one production will have either ggF or VBF specified in the legend.

The pre-selection two-lepton system p_T threshold of 10 GeV was motivated by the fact that the signal distributions all peak at higher p_T values ($\approx 30\,\text{GeV}$) compared to $Z\gamma$ and $Z+\text{jets}$ background distributions ($\approx 12\,\text{GeV}$ and $\approx 5\,\text{GeV}$ respectively) as shown in Figure 5.2. It is shown later that one of the chosen selection categories requires a correction in the two-lepton system p_T for background simulation, with $Z+\text{jets}$ being a relatively large contributor to the uncertainty. The pre-selection p_T requirement removes much of $Z+\text{jets}$ thus reducing uncertainty in this region and making the analysis more robust.

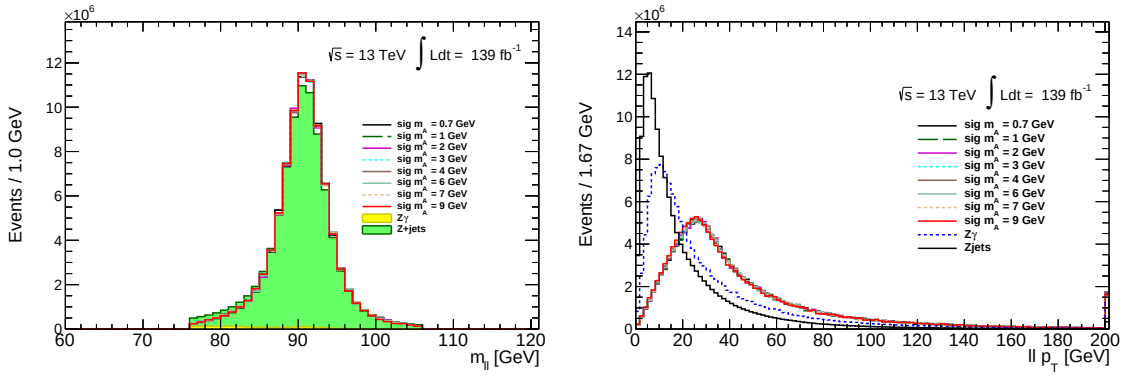

(a) (b)

Figure 5.2: (a) Reconstructed two-lepton system mass distribution in the window $76\,\text{GeV} < m_{\ell\ell} < 106\,\text{GeV}$ for signal and background MC sample events passing the pre-selection criteria. $Z\gamma$ and $Z+\text{jets}$ are stacked and the signal histograms are normalised to contain the same integral as the background for shape comparison. (b) Two-lepton system p_T distribution for events passing pre-selection but with the $\ell\ell$ p_T cut removed. Histograms for each sample are also normalised to the same integral for shape comparison.

5.3 Signal Properties

Signal events are characterised by two charged leptons from the Z-boson decay and a photon pair from the axion. The photons from the axion decay may be highly asymmetric in p_T . Figure 5.3 shows event truth-particle level quantities for signal photons at $m_a = 1\,\text{GeV}$. "Truth-particle level" means MC generator output quantities before simulated effects of the detector are applied to the simulation. Figure 5.3a demonstrates an asymmetry in photon p_T between the two photons and Figure 5.3b shows that the photons become more collimated when the photon pairs are of higher p_T . In fact, for a minimum photon p_T threshold of 10 GeV the photons have very low ΔR values that are all below 0.1 with most at approximately 0.07.

Figure 5.4 instead shows events with reconstructed photon objects *matched* to truth-level photons with the same minimum photon p_T threshold applied. "Matched" in this context means that the reconstructed photon object after detector effects are applied to the simulation is within a distance $\Delta R < 0.2$ with a truth-level photon in the $\eta - \phi$ plane. In other words, if a reconstructed photon in an event is matched to a truth-level photon this means the reconstructed photon originates from the axion decay and are not photons detected from other radiative emissions that may be

present at reconstructed level, for example initial state radiation (ISR) or final state radiation (FSR).

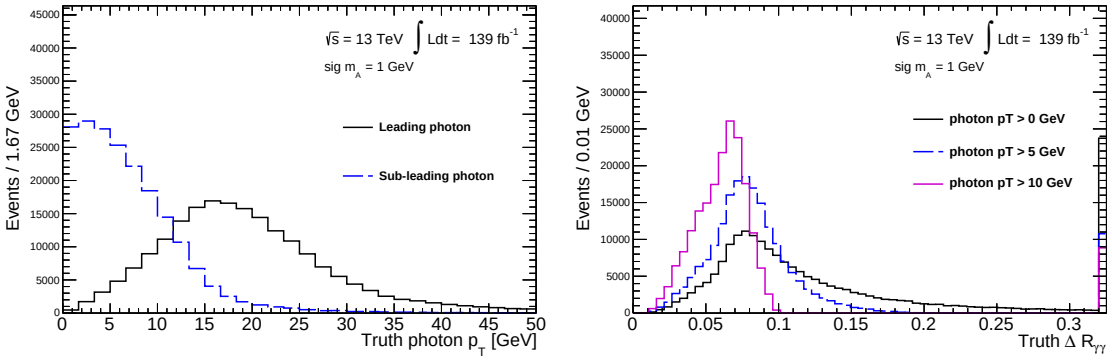

(a) (b)

Figure 5.3: (a) Leading and sub-leading photon p_T distributions at truth-level for signal $m_a = 1\,\text{GeV}$ sample. (b) ΔR between the two photons at truth-level for photon p_T thresholds at 0 GeV, 5 GeV and 10 GeV. Histograms normalised to the same integral for shape comparison.

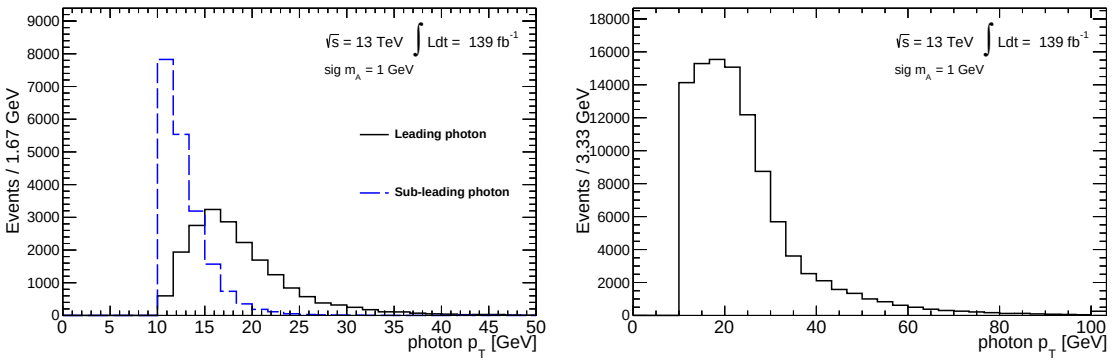

(a) (b)

Figure 5.4: Reconstructed photon p_T distributions for signal $m_a = 1\,\text{GeV}$ events satisfying pre-selection with a minimum photon $p_T > 10\,\text{GeV}$. Plot (a) shows events with at least two reconstructed photons passing these conditions and plot (b) shows events with only one. Reconstructed photon objects are matched to truth-level photons.

Figure 5.4a shows that for the same minimum p_T threshold of 10 GeV the same asymmetry in p_T is observed when there are at least two photons in an event. In many cases, the sub-leading signal photon has too low a p_T that only the leading photon is reconstructed. As well as this, as already discussed, it is possible both

signal photons are collimated and are reconstructed together as a single photon object. Figure 5.3b shows the photon p_T distribution for events where there is only one reconstructed photon, containing a mixture of both scenarios. The possibility that the photon pair from the axion decay could be reconstructed as a jet was also considered for a selection choice but it was found that, due to the JVT cut which is applied, only 30 % of events passing pre-selection were matched to the truth-level photon pair (Appendix A.1).

Figure 5.5 displays various kinematic variable distribution comparisons for the Higgs boson, Z-boson and the axion between numerous signal samples of different axion mass value. Each histogram is normalised to the same integral so that the relative shapes of the distributions can be compared more easily. The Z-boson p_T distribution for all signal mass points is similar, however the Higgs boson and axion p_T appear at larger values for higher mass points. The two lowest shown mass points, 0.7 GeV and 1 GeV, show much different distribution shapes compared to the higher mass points. In particular, this is most clearly seen by the fact that the Z-boson and axion systems are more boosted relative to each other in the ϕ plane. The $\Delta\phi$ values are lowest at higher mass points, forming a second peak, in contrast to the $m_a = 0.7\,\text{GeV}$ and $m_a = 1.0\,\text{GeV}$ simulated samples that only contain one clear maximum around the value π. The same kinematic variable distribution comparisons are again displayed in Appendix C but by also separating the signal samples by the ggF and VBF Higgs boson production processes. Figure 5.6 shows that the main difference between the two processes is the relatively higher Higgs boson p_T of VBF compared to ggF. This is due to the fact that ggF is more likely to occur at small Bjorken x [1] values whereas quark scattering, such as VBF, is more common at higher x and therefore at greater p_T values [136]. In addition to this, signal VBF mass points greater than 2 GeV peak at higher p_T values compared to the two lowest mass points, which is not the case for ggF.

[1] The fraction of the proton momentum carried by the parton [135].

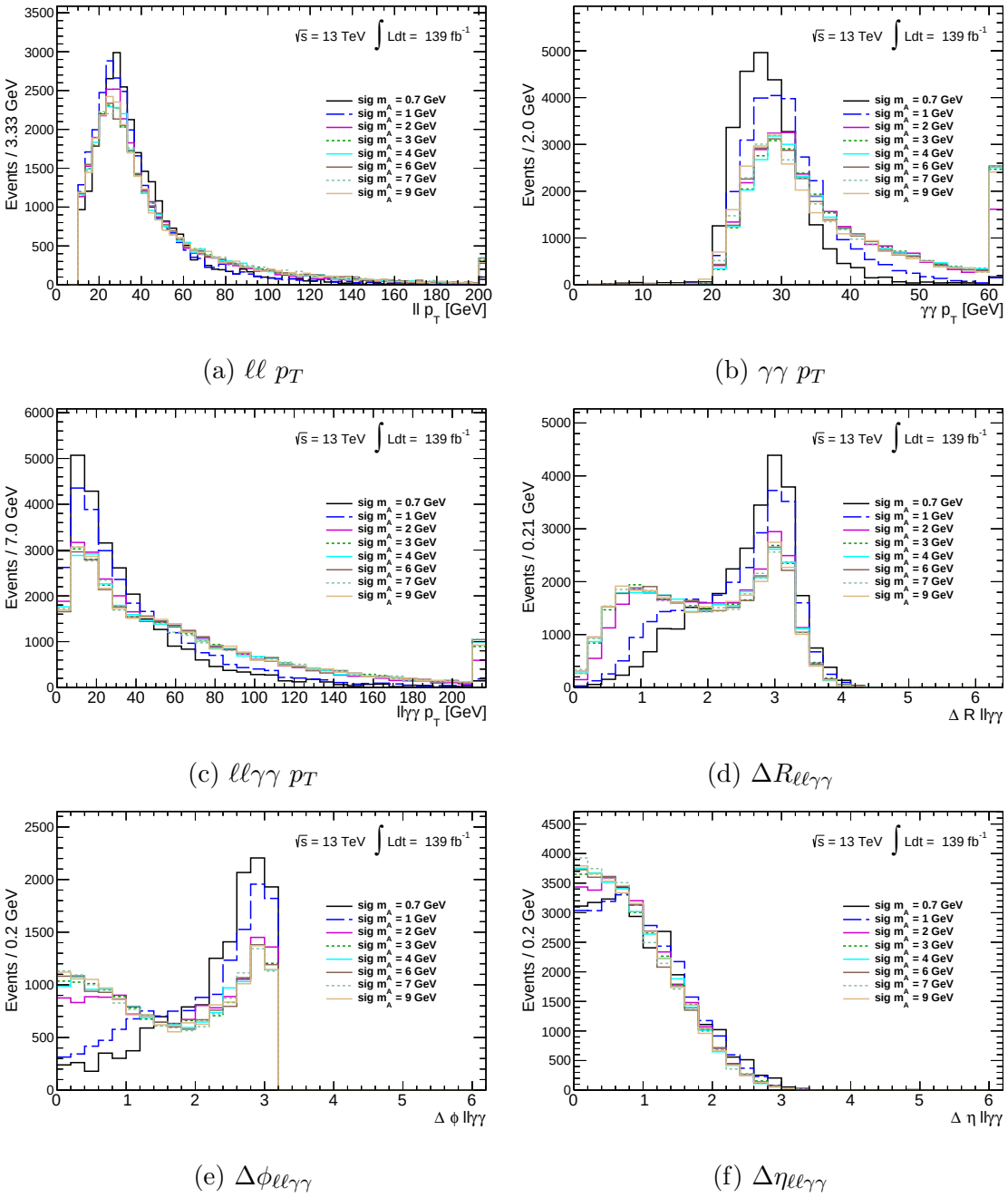

(a) $\ell\ell$ p_T

(b) $\gamma\gamma$ p_T

(c) $\ell\ell\gamma\gamma$ p_T

(d) $\Delta R_{\ell\ell\gamma\gamma}$

(e) $\Delta\phi_{\ell\ell\gamma\gamma}$

(f) $\Delta\eta_{\ell\ell\gamma\gamma}$

Figure 5.5: Various kinematic distributions for different signal sample events passing the pre-selection criteria. Histograms normalised to the same integral for shape comparison. Reconstructed photon objects are matched to truth-level photons.

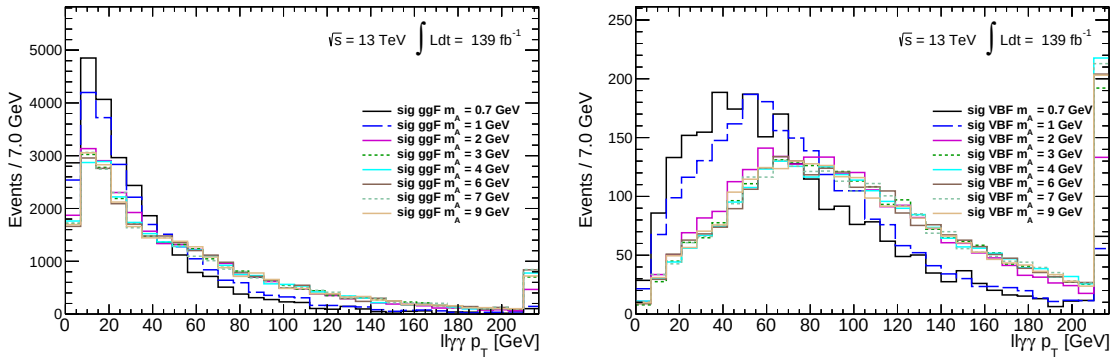

(a) ggF $\ell\ell\gamma\gamma$ p_T (b) VBF $\ell\ell\gamma\gamma$ p_T

Figure 5.6: The $\ell\ell\gamma\gamma$ system p_T for various signal axion mass points for Higgs boson processes (a) ggF and (b) VBF. Histograms normalised to the same integral for shape comparison. Reconstructed photon objects are matched to truth-level photons.

5.4 Event Categorisation

For events with two reconstructed photons, Figure 5.7 shows that for increasing m_a the angular distance between the photons is larger. The same figure also shows that photons originating from the ggF process have a mean value of $\Delta R_{\gamma\gamma}$ greater than VBF when comparing the same values of m_a. This difference comes from the generally higher Higgs boson p_T shown in Figure 5.6 for VBF compared to ggF, making the photon pair appear more boosted and more likely to decay closer together. Due to how different the $\Delta R_{\gamma\gamma}$ distributions are for each signal mass point, this variable cannot solely be used to select the two signal photon candidates. Instead, a variable denoted in this analysis as X is proposed to select the two photons. The definition of X is

$$X = \Delta R_{\gamma\gamma} \frac{p_{T_{\gamma\gamma}}}{2m_{\gamma\gamma}}, \tag{5.4.1}$$

with $\Delta R_{\gamma\gamma}$, $p_{T_{\gamma\gamma}}$ and $m_{\gamma\gamma}$ being the ΔR, transverse momentum and reconstructed mass of the two-photon system respectively. Variable X originates from the kinematic relation $\Delta R_{\gamma\gamma} \approx \frac{2m_{\gamma\gamma}}{p_{T_\gamma}}$ for a pair of particles originating from a decay of a boosted particle. Being defined in this way means that the signal two-photon system distribution has a sharp peak approximately at unity regardless of the axion mass. Figure 5.8 shows the X distributions for various signal mass points between 0.7 GeV and 9 GeV for reconstructed photons matched to the truth-level $a \to \gamma\gamma$ decay and also in the case were the photons were not matched, before any photon identification or isolation criteria was applied. ALPs with mass points of higher val-

ues are less likely to be boosted and as such the width of the distribution is larger. The difference between each matching scenario is that there is a flat tail at X values lower than 1 in the distribution with no photon matching. These events come from photons not originating from the $a \to \gamma\gamma$ decay and are generally back-to-back with broader p_T distributions. A cut at $0.96 < X < 1.2$, chosen using the truth-matched distribution in Figure 5.8, is applied in the selection to reduce the likelihood of selecting events that contain photon pairs with these properties. Background $Z\gamma$ and $Z+$jets X distributions are compared with signal in Figure 5.9 showing background events also containing a sharp peak at unity. Because of this, X is not really used as a signal-background discriminant but instead only to select the photons (although the condition $0.96 < X < 1.2$ does remove a modest number of $Z+$jets events).

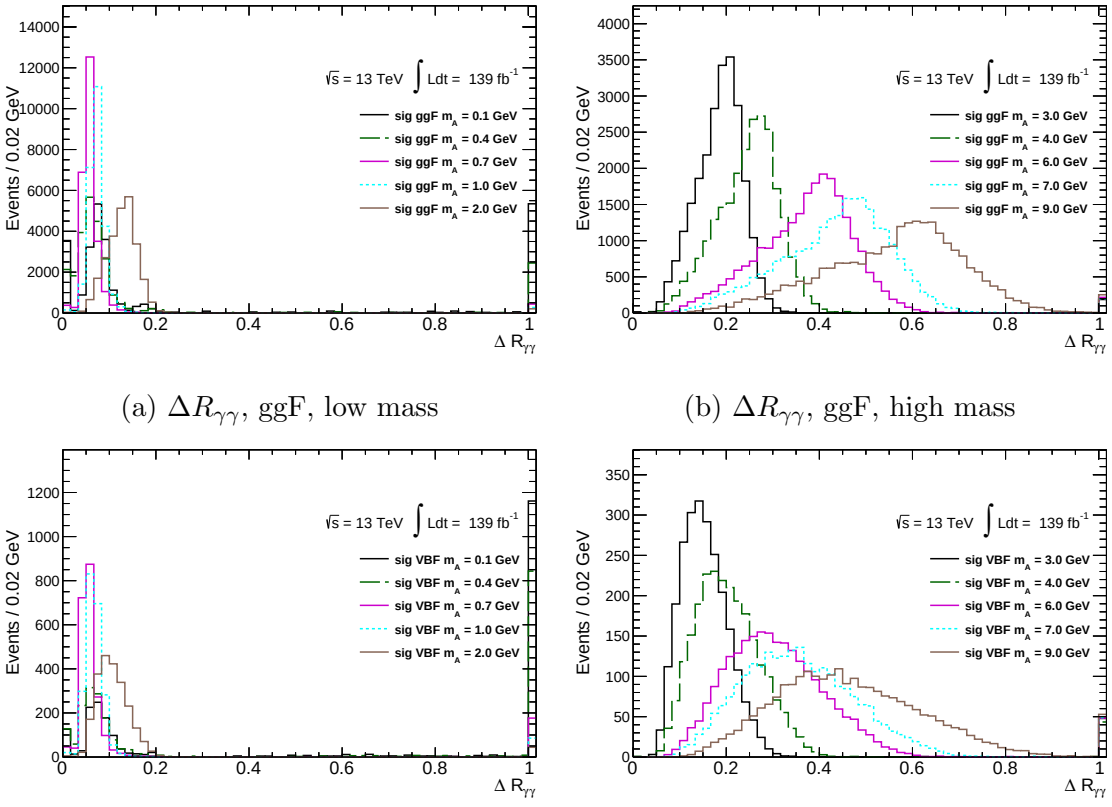

(a) $\Delta R_{\gamma\gamma}$, ggF, low mass

(b) $\Delta R_{\gamma\gamma}$, ggF, high mass

(c) $\Delta R_{\gamma\gamma}$, VBF, low mass

(d) $\Delta R_{\gamma\gamma}$, VBF, high mass

Figure 5.7: The $\Delta R_{\gamma\gamma}$ between the two leading reconstructed photons for various signal axion mass points for Higgs boson process ggF (top) and VBF (bottom) in events passing pre-selection that have at least two photons. Histograms normalised to the same integral for shape comparison. Reconstructed photon objects are matched to truth-level photons. Photons in this selection do not yet include any isolation or identification criteria.

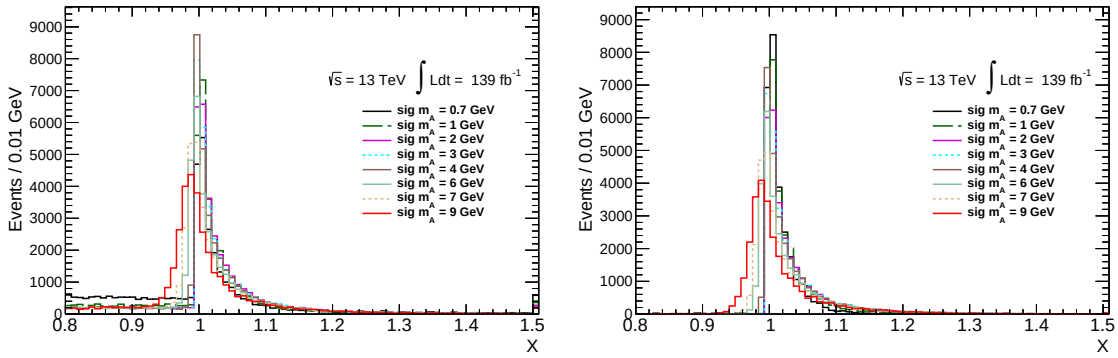

(a) no photon truth matching (b) photon truth matched

Figure 5.8: Signal X variable distributions for when (a) both reconstructed photons are not matched to $a \to \gamma\gamma$ truth-level photons and (b) when both reconstructed photons are matched to $a \to \gamma\gamma$ truth-level photons in events passing pre-selection that have at least two photons. Histograms normalised to the same integral for shape comparison. Reconstructed photon objects are matched to truth-level photons. Photons in this selection do not yet include any isolation or identification criteria.

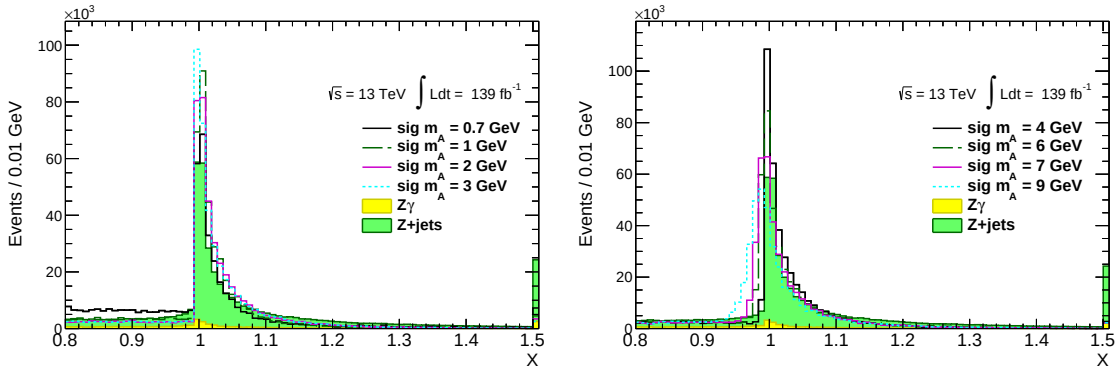

(a) signal $m_a \leq 3\,\text{GeV}$, $Z\gamma$ and $Z+\text{jets}$ (b) signal $m_a > 3\,\text{GeV}$, $Z\gamma$ and $Z+\text{jets}$

Figure 5.9: X variable distribution shape comparisons for background processes $Z\gamma$ and $Z+\text{jets}$ and (a) low signal mass points with $m_a \leq 3\,\text{GeV}$ and (b) high signal mass points with $m_a > 3\,\text{GeV}$. Both reconstructed photons are not matched to $a \to \gamma\gamma$ truth-level photons. Histograms normalised to the same integral for shape comparison. Photons in this selection do not yet include any isolation or identification criteria.

As already discussed in Section 5.3, the two photons from the axion decay may be separated enough that they are sometimes reconstructed as two reconstructed photons, however there are also many events that contain photon pairs that are highly collimated and are therefore reconstructed only as one reconstructed photon. The case in which the photons are *merged* together in this way is more likely to occur

for lower m_a signal events. Because of this, a basis selection of two categories has been examined. The first category selects for events that contain the two signal photons reconstructed as separate photon objects whereas the other category selects events were the photons are reconstructed only as one. The two categories are summarised in the following:

- Resolved category: The event includes a photon pair such that X is closest to 1 and satisfies $0.96 < X < 1.2$. Both photons must pass a minimum p_T threshold of 10 GeV and have a $\Delta R_{\gamma\gamma} < 1.5$ with respect to each other.
- Merged category: The event fails the resolved category and includes a photon with a p_T of at least 20 GeV.

After an event passes the described selection then all reconstructed photons in the event must also pass the Loose photon identification, defined in Section 4.1.6, as well as a photon isolation criteria that is different for each category (discussed in more detail in Section 6 and Section 7).

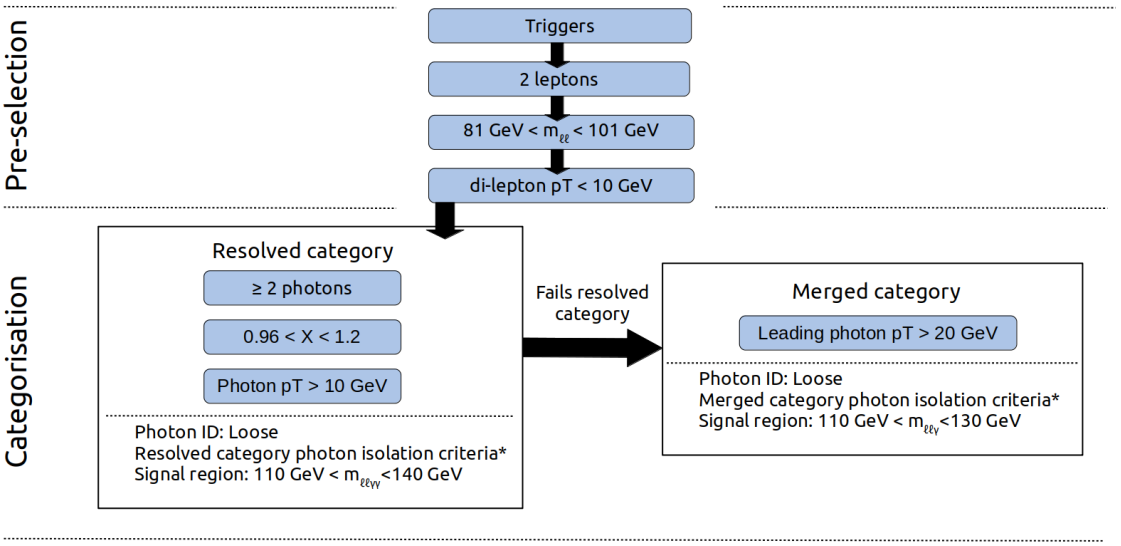

Figure 5.10: A flow-chart showing the selection process for the pre-selection and categorisation stages of the $h \to Za \to \ell\ell\gamma\gamma$ analysis. *Isolation criteria for the resolved and merged categories are detailed in Section 6 and Section 7 respectively.

The resolved category criteria are designed to select on events that contain two reconstructed photons that are potentially from the $a \to \gamma\gamma$ decay. The $\Delta R_{\gamma\gamma}$ cut at 1.5 is included since all events with photons expected to be selected in this category

should have a $\Delta R_{\gamma\gamma}$ value within this boundary, as Figure 5.7 shows. Events are considered to be categorised to the merged category only if they fail the criteria set for the resolved category first. If the event fails the resolved category but contains a high energy reconstructed photon with a p_T greater than 20 GeV then there is potential that this reconstructed photon contains both collimated photons from the axion decay. The entire selection process for pre-selection and categorisation is summarised in Figure 5.10.

Since resolved category events contain two reconstructed photons and the merged category contains only one, the Higgs boson mass which is used to define the signal and sideband regions is therefore reconstructed differently for each category. For the resolved category the Higgs boson mass is reconstructed using the four-vector addition of the two-lepton and two-photon systems, $m_{\ell\ell\gamma\gamma}$, however the merged category Higgs boson mass uses only the dilepton and single photon, $m_{\ell\ell\gamma}$. Figure 5.11 shows the reconstructed Higgs boson mass distribution shape comparisons for signal mass points 0.7 GeV, 2.0 GeV, 4.0 GeV and 9.0 GeV for the resolved and merged categories. The bottom two plots include the condition that the reconstructed photon is matched to at least one truth-level photon from the axion decay whereas the upper two plots do not include any matching. The only difference between the two matching scenarios is that the tails in the distributions are removed. There are two clear differences in distribution when comparing the reconstructed Higgs boson mass of the two categories to one another. The first is the resolution of the peak. The Full Width at Half Maximum values (FWHM) [2] of the resolved category distributions at 5 GeV are lower compared to the merged category which have FWHM values between 6 GeV and 9 GeV, depending on the signal mass point, meaning that the resolved category has a better comparable resolution. The second difference is that the mean values at which the distributions peak is shifted lower for the merged category compared to the resolved. The resolved category $m_{\ell\ell\gamma\gamma}$ contains all object information from the Higgs boson decay at reconstructed level and so peaks about the Higgs boson mass of 125 GeV. The merged category however contains only the one reconstructed photon. Although this reconstructed photon can contain all of the information from both $a \to \gamma\gamma$ photons merged together, sometimes, and especially for higher signal mass points, this is not always the case. For example, for higher signal mass points the photons are further apart and so for those categorised into the merged category then these events are actually likely to contain one large

[2] Full Width at Half Maximum is the width of a distribution at half the maximum value.

p_T reconstructed photon with the other photon too low in p_T to pass the minimum 10 GeV required for the resolved category. This is demonstrated by the fact that for the merged category the $m_{\ell\ell\gamma}$ of the 0.7 GeV mass point has a better resolution and peaks closer to 125 GeV compared to higher mass points. This is because the photons from the axion decay are more likely to be closer together with the single reconstructed photon containing the energies from both $a \to \gamma\gamma$ photons. Events shown in Figure 5.11d are for when the reconstructed photon is matched to one truth-level photon from the axion decay, not for when both photons are matched to the reconstructed photon. This means that the truth-level sub-leading photon will sometimes be ignored. Figure 5.12 shows instead a comparison between merged category events when only one truth-level photon is matched to the selected reconstructed photon and for when both truth-level photons are matched to it. As is always the case in this chapter, the truth matching uses a cone defined as $\Delta R < 0.2$. What is shown here is further evidence that the merged category favours lower signal mass points. The lowest shown signal mass point, 0.7 GeV, which contains a reconstructed photon more likely to made up of both photons from the axion decay peaks closer to 125 GeV and has a better resolution compared to the higher mass points that also appear to have mean values shifted to lower values. The highest tested signal mass point at 9 GeV has lower statistics and poorer resolution compared to all the other signal mass points that are shown. This means that there are not as many truly identified merged events for this mass point. The distributions shown in these plots confirm why the merged category is mostly useful for lower m_a whereas the resolved category is more suited for higher mass values.

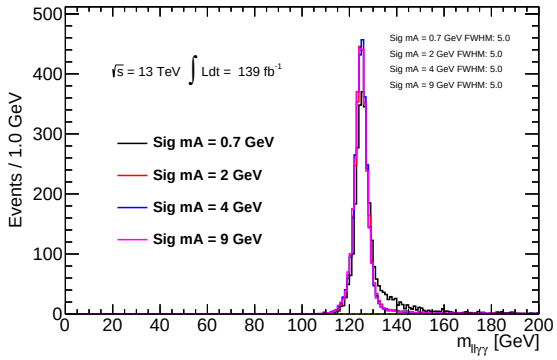

(a) Resolved category

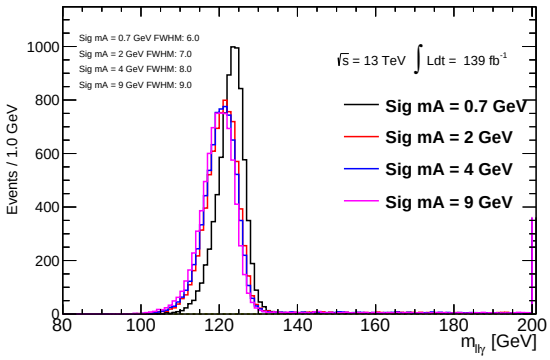

(b) Merged category

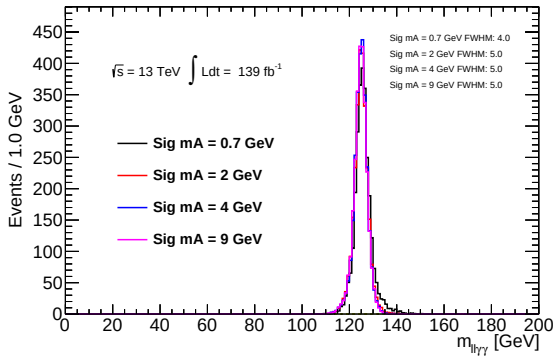

(c) Resolved category, photon truth matched

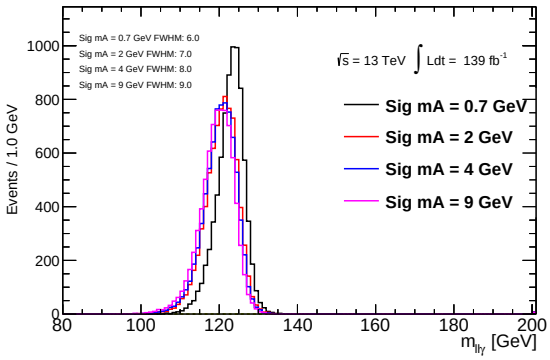

(d) Merged category, photon truth matched

Figure 5.11: The reconstructed Higgs boson mass distributions for each category selection for various signal mass points. For the resolved category the Higgs boson mass is reconstructed as $m_{\ell\ell\gamma\gamma}$ and for the merged category it is $m_{\ell\ell\gamma}$. The top two plots show events regardless of being matched to truth-level photons or not whereas the bottom two plots show the distributions after truth matching between truth-level photon(s) is applied. Selections are immediately after the categorisation selection and do not include any isolation or identification criteria applied to the photons. The resolution of the peak is quantified by the FWHM values printed on the plots. Each distribution is normalised to the same integral for better shape comparison.

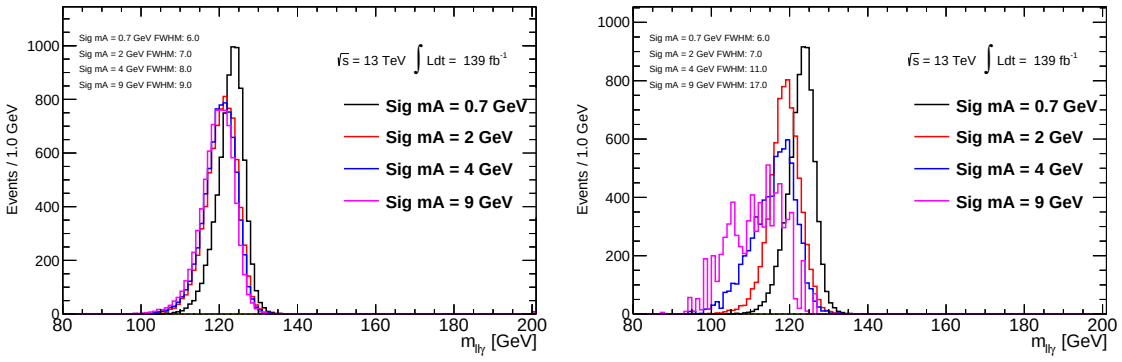

(a) one photon truth matched (b) both photons truth matched

Figure 5.12: The merged category reconstructed $m_{\ell\ell\gamma}$ distributions for various signal mass points when the reconstructed photon is truth matched to only one truth-level photon (left) and both truth-level photons (right). Selections are immediately after the categorisation selection and do not include any isolation or identification criteria applied to the photons. The resolution of the peak is quantified by the FWHM values printed on the plots. Each distribution is normalised to the same integral for better shape comparison.

The effect that the resolved category favours higher axion mass points and the merged category is more correct for lower mass points is also shown when comparing how the reconstructed photons are truth matched. Table 5.3 and Table 5.4 show the fraction of events when the selected reconstructed photon(s) are matched to either both truth-level photons from the axion decay, one truth-level photon or neither for the resolved and merged categories respectively. What is shown in the resolved category case is that generally the fraction of events with both reconstructed photons matched to the two truth-level photons is over 90 % for signal mass points greater than 1 GeV but gradually this moves to smaller values for lower mass points. Conversely, in the case of the merged category a higher fraction of both truth-level photons are matched to the selected reconstructed photon for the low mass points (85 % - 91 % for $m_a = 0.1\,\text{GeV}$ to $m_a = 0.7\,\text{GeV}$) compared to signal at substantially reduced fractions at higher mass points. For instance, the reconstructed photon for signal mass points over 6 GeV are only matched to both truth-level photons in $< 2\,\%$ of the events categorised into the merged category. Figure 5.13 shows the fraction of events for each signal mass point passing pre-selection and what category they are categorised into. For low mass points the majority of successfully categorised events are selected into the merged category showing a trend that this fraction gradually falls until plateauing at $\approx 30\,\%$ after $m_a = 2\,\text{GeV}$. For the fraction of events categorised into the resolved category the opposite is true. The fraction of events

Resolved category				
mA (GeV)	**Both photons matched (%)**	**1 photon matched (%)**	**At least 1 photon matched (%)**	**0 photons matched (%)**
0.1	69.41 ± 8.22	29.70 ± 4.64	99.11 ± 10.72	0.89 ± 0.65
0.4	78.64 ± 8.93	20.39 ± 3.60	99.03 ± 10.59	0.97 ± 0.60
0.7	88.81 ± 8.12	10.99 ± 2.07	99.80 ± 8.86	0.20 ± 0.08
1.0	94.19 ± 5.42	5.33 ± 0.92	99.51 ± 5.65	0.49 ± 0.26
2.0	97.24 ± 3.65	2.46 ± 0.41	99.70 ± 3.72	0.30 ± 0.14
3.0	97.89 ± 1.67	1.85 ± 0.16	99.74 ± 1.69	0.26 ± 0.06
4.0	97.63 ± 2.17	1.96 ± 0.21	99.59 ± 2.21	0.41 ± 0.09
6.0	96.47 ± 2.25	1.76 ± 0.21	98.23 ± 2.28	1.77 ± 0.21
7.0	96.14 ± 2.25	2.25 ± 0.24	98.38 ± 2.29	1.62 ± 0.19
9.0	96.29 ± 2.28	1.99 ± 0.22	98.28 ± 2.31	1.72 ± 0.21

Table 5.3: Truth matching reconstructed photons to truth-level photons for the resolved category. Resolved category selection is immediately after the categorisation selection and does not include any isolation or identification criteria applied to the photons.

Merged category				
mA (GeV)	**Both photons matched (%)**	**1 photon matched (%)**	**At least 1 photon matched (%)**	**0 photons matched (%)**
0.1	90.89 ± 0.54	4.59 ± 0.09	95.49 ± 0.56	4.51 ± 0.08
0.4	89.89 ± 0.55	5.31 ± 0.10	95.20 ± 0.57	4.80 ± 0.09
0.7	85.52 ± 0.59	8.18 ± 0.14	93.70 ± 0.64	6.30 ± 0.11
1.0	78.19 ± 0.61	13.78 ± 0.20	91.97 ± 0.69	8.03 ± 0.14
2.0	47.29 ± 0.46	43.22 ± 0.44	90.51 ± 0.74	9.49 ± 0.17
3.0	15.70 ± 0.16	74.95 ± 0.46	90.64 ± 0.52	9.36 ± 0.12
4.0	6.17 ± 0.13	84.22 ± 0.71	90.40 ± 0.74	9.60 ± 0.17
6.0	1.76 ± 0.07	89.38 ± 0.73	91.14 ± 0.74	8.86 ± 0.16
7.0	0.98 ± 0.05	90.13 ± 0.75	91.11 ± 0.75	8.89 ± 0.17
9.0	0.37 ± 0.03	90.76 ± 0.74	91.13 ± 0.75	8.87 ± 0.17

Table 5.4: Truth matching reconstructed photons to truth-level photons for the merged category. Merged category selection is immediately after the categorisation selection and does not include any isolation or identification criteria applied to the photons.

categorised into the resolved category gradually increases with greater values of signal mass value until, again at, $m_a = 2\,\text{GeV}$ where this trend plateaus to about 16 %. It is worth noting that Figure 5.13 shows that approximately half of events passing pre-selection level for the majority of the signal mass points are not categorised in either of the selection categories. This is due to the fact that for non-categorised events with two reconstructed photons the sub-leading photon p_T is generally below the photon p_T threshold of 10 GeV, and so cannot be categorised into the resolved category. The same is true for events with only one reconstructed photon in the sense that the photon p_T is generally less than the merged category p_T threshold of 20 GeV and therefore are not categorised either. Figure C.3 in Appendix C shows photon p_T distributions for events failing categorisation from various signal mass points.

Based on this discussion, it is chosen that the signal mass points with $m_a < 2\,\text{GeV}$ are focused for the merged category selection whereas mass points with $m_a \geq 2\,\text{GeV}$ are concentrated to the resolved.

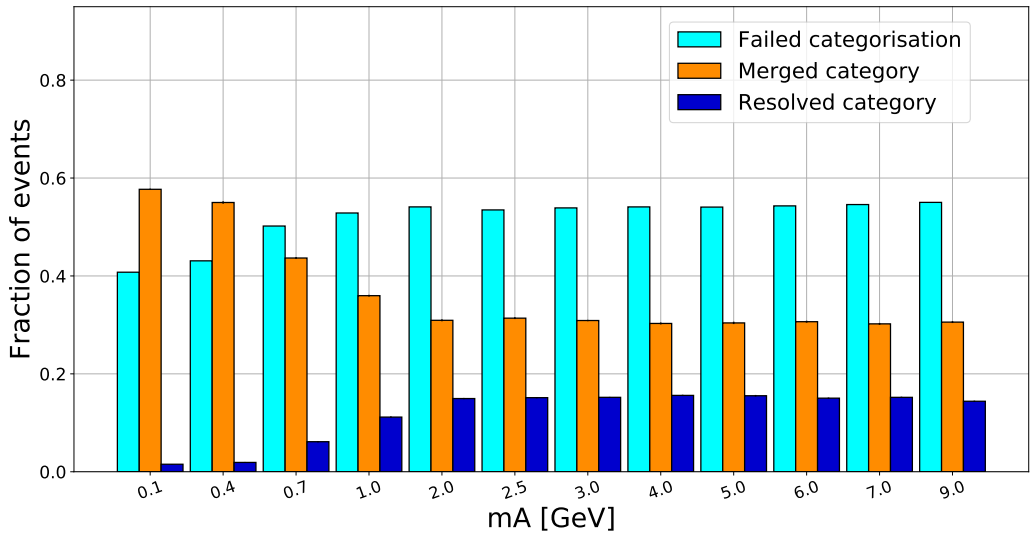

Figure 5.13: Fraction of events for each signal mass point passing pre-selection categorised into either the resolved category (dark purple), merged category (orange) or neither category (cyan).

Chapter 6

Resolved Category

Resolved Category

This chapter details the analysis for events that contain two reconstructed photons from the $a \to \gamma\gamma$ decay. This event category is known as the "resolved category". The categorisation criteria and analysis method is summarised below:

Resolved category selection: Events containing a photon pair such that X, defined in Section 5.4, is closest to the value 1 and satisfies $0.96 < X < 1.2$. Both photons must pass a p_T threshold of 10 GeV and have a $\Delta R_{\gamma\gamma} < 1.5$.
Method: The discriminating variable is the reconstructed mass of the two photon system, $m_{\gamma\gamma}$, which is expected to peak at the axion mass. The background is estimated using a simultaneous fit with data.

This chapter starts by describing the resolved category signal and sideband regions as well as the photon identification and isolation criteria required by the two photons. The $m_{\gamma\gamma}$ distributions of signal and background processes are discussed as are the origins of the photons that are selected. The signal $m_{\gamma\gamma}$ distributions are modelled with a double sided crystal ball function which covers a $m_{\gamma\gamma}$ range of 2 – 10 GeV. The data-driven methods which are used for the background and spurious signal estimations are also discussed before ending the section with the details of the systematic uncertainties and finally the results.

6.1 Selection regions

Resolved category events fall either within the signal region (SR) or sideband region (SB). A signal region is chosen using the reconstructed Higgs boson mass distribution window, $m_{\ell\ell\gamma\gamma}$, that contains signal and where data was blinded. Figure 6.1 shows the $m_{\ell\ell\gamma\gamma}$ distributon for the resolved category MC signal samples from 2 GeV to 9 GeV for both the case where the signal samples are split by the ggF and VBF processes and in the case where they are not. The signal region was chosen to be $110\,\text{GeV} < m_{\ell\ell\gamma\gamma} < 140\,\text{GeV}$. This window was optimised based on comparing significance and receiver operating characteristic curves for different $m_{\ell\ell\gamma\gamma}$ ranges and contains 97 % of signal events (study shown in Section D.1 of Appendix D). All signal samples contain a similar peak at the Higgs Boson mass, regardless of whether the process is ggF or VBF.

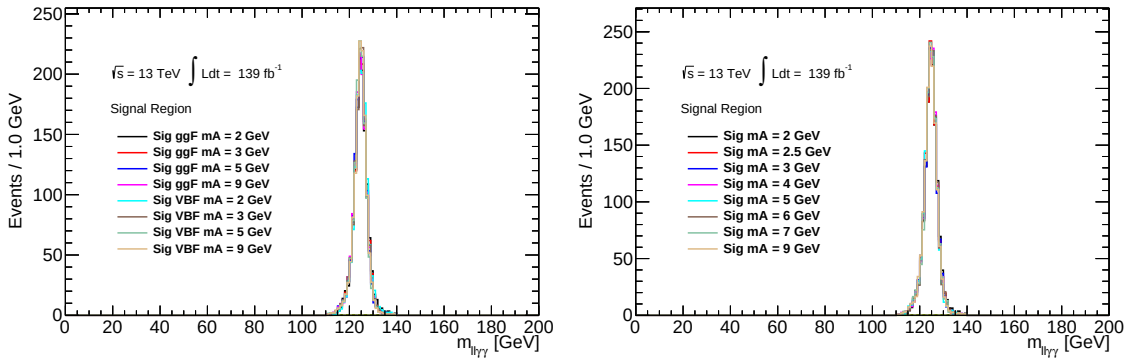

(a) Signal $m_{\ell\ell\gamma\gamma}$, split by process

(b) Signal $m_{\ell\ell\gamma\gamma}$

Figure 6.1: $m_{\ell\ell\gamma\gamma}$ distributions for the axion mass points considered for the resolved category selection before any region cuts. (a) shows the distributions split by ggF and VBF processes and (b) when both processes are added together. Each signal sample is normalised to the same number of events for shape comparison.

The data in the SB is used to perform an analytical template of the reconstructed mass of the diphoton system, described in Section 6.5.

6.2 Photon Identification and Isolation

Photon Identification

As with the merged category, resolved category events must have both photons satisfying the Loose identification criteria. Introduced already in Section 4.1.6, the Loose criteria cuts on two variables describing the shower shape in the middle layer of the calorimeter (R_η and $w_{\eta 2}$) and two variables that describe hadronic leakage (R_{had} and R_{had1}).

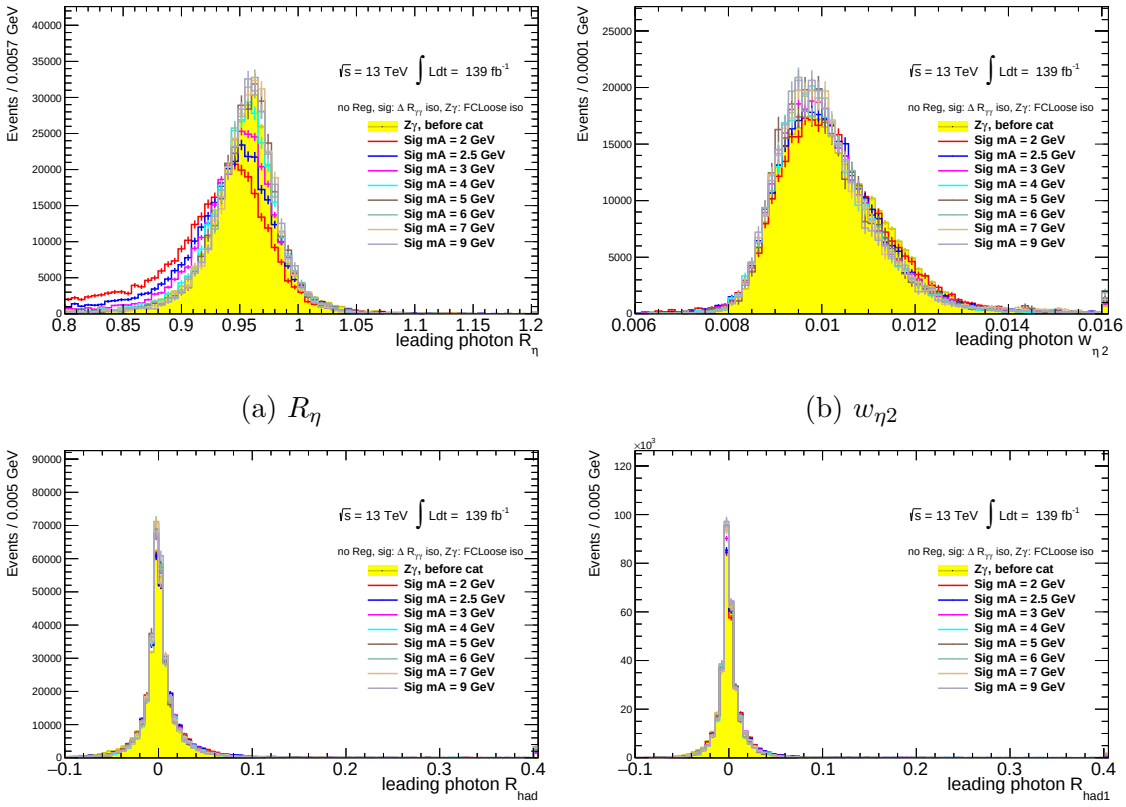

(a) R_η (b) $w_{\eta 2}$

(c) R_{had} (d) R_{had1}

Figure 6.2: Variables that are used in the definition of the loose identification criterion distributions for signal leading photon in the signal region comparison after the resolved category selection with the $Z\gamma$ photon before categorisation. $Z\gamma$ events are before the categorisation stage for better statistics. Isolation criteria applied to the photons. No photon identification cuts are applied. Distributions are normalised to the same number of events for shape comparison. Uncertainties shown are due to the finite number of generated events.

Figure 6.2 is a shape comparison of resolved category signal leading photon distri-

butions for the Loose identification variables with calibrated isolated photons from the $Z\gamma$ process passing pre-selection. Isolated photons from $Z\gamma$ are calibrated to Loose identification. Photons from signal variables are compared in this way to check whether the distribution widths are within those from calibrated photons when also taking into account the Loose identification cuts. The Loose identification cuts on the photon are defined as having a $w_{\eta 2}$ between 0.012 and 0.0015 depending on η and $R_\eta > 0.9$. Also depending on η, hadronic leakage variables R_{had} and R_{had1} must be between 0.04 and 0.065. These plots show that, other than R_η with a slightly longer tail for signal photons the shape of the signal distributions are similar to those from $Z\gamma$. As the signal photon distributions are similar to the calibrated $Z\gamma$ photon then the Loose identification selection criteria can be used for photon selection.

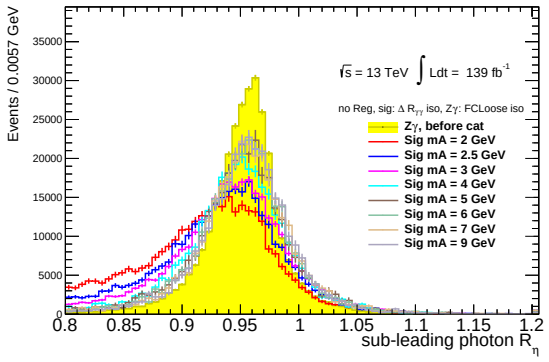

(a) R_η

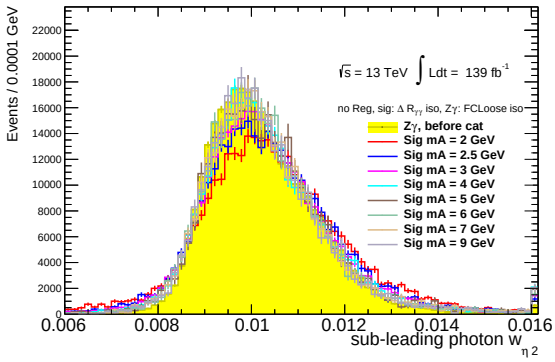

(b) $w_{\eta 2}$

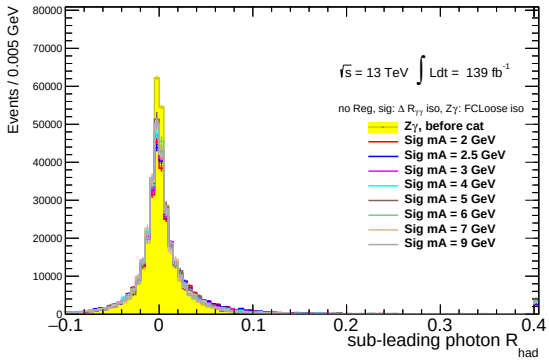

(c) R_{had}

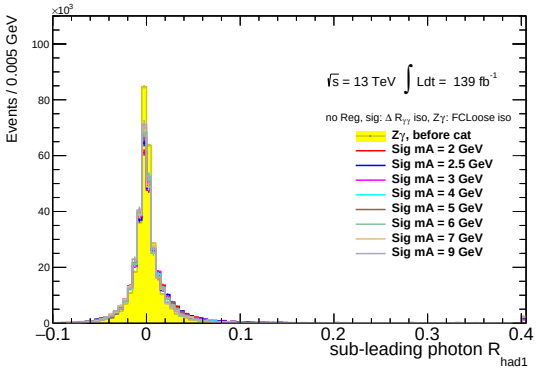

(d) R_{had1}

Figure 6.3: Same description as Figure 6.2 but comparing signal sub-leading photon to those from $Z\gamma$.

Tight identification was also considered as an option for photon selection in this category. Table D.1 in Section D.2 of Appendix D shows the comparison between

Loose and Tight identification efficiencies in the signal region for signal and background. The efficiency in signal reduced by half for some m_a values compared to Loose identification.

Photon Isolation

For photon isolation the Loose isolation common working point used for analysis with photon objects is applied. The Loose criteria, discussed already in Section 4.1.6, contain requirements on track isolation variable, p_T^{cone20}, and calorimeter isolation variable, E_T^{cone20}. For these variables the isolation cone has a ΔR of 0.2. For the resolved category, isolation is applied to events only with photon pairs that have a $\Delta R_{\gamma\gamma} > 0.22$ between them otherwise the photons will overlap isolation cones. For resolved category events that contain photons with $\Delta R_{\gamma\gamma} < 0.22$ then no isolation cuts are applied. The shape comparison of the $\Delta R_{\gamma\gamma}$ distributions for signal and background before any isolation cuts is shown in Figure 6.4. This shows that for the majority of events the isolation criteria is applied, especially for signal with axion mass greater then 3 GeV.

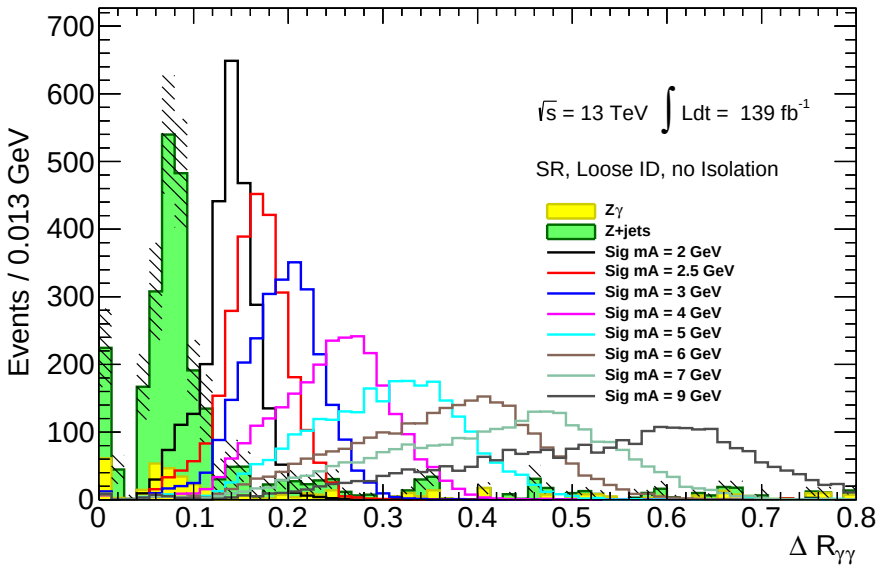

Figure 6.4: $\Delta R_{\gamma\gamma}$ between the two reconstructed photons in the resolved category signal region for photon selection where Loose photon identification is applied but isolation is not. Distributions normalised to the same number of events for shape comparison. Uncertainty bars shown are MC statistical errors.

6.3 Signal and Background properties

The reconstructed mass of the two photon system is used as the discriminating variable in the fit to extract the signal, which peaks at the mass of the axion. Figure 6.5 shows the distribution for signal separated by both Higgs boson production processes, the comparison with background in the signal region. Figure 6.6 shows this distribution for data in the sideband. The signal $m_{\gamma\gamma}$ distributions each contain a peak approximately the mass at which the MC samples were generated at and get broader with increasing mass. For example, at 2 GeV the FWHM is 0.12 GeV whereas at 9 GeV it is 0.48 GeV. Higgs boson production VBF contains approximately 10 % of the number of events compared to ggF. The width of the distributions for both processes are similar. In comparison, background events are almost entirely below signal $m_{\gamma\gamma}$ values, with a peak about 1 GeV which is also the case for data in the sideband. The fact that the distribution of the background is as such means it is difficult to distinguish signal any lower than 2 GeV although higher mass points appear over the tail.

Table 6.1 summarises the origin of the photons from the background processes. As expected, it was found that the majority of the leading and sub-leading photons from $Z\gamma$ are photons from ISR/FSR whereas for $Z+$jets, the dominate background process for this category, 80 % of photons originate from π^0 decays with just under 20 % from other low mass mesons. Combining this information means that approximately 90 % of the total background is due to photon pairs faked by jets.

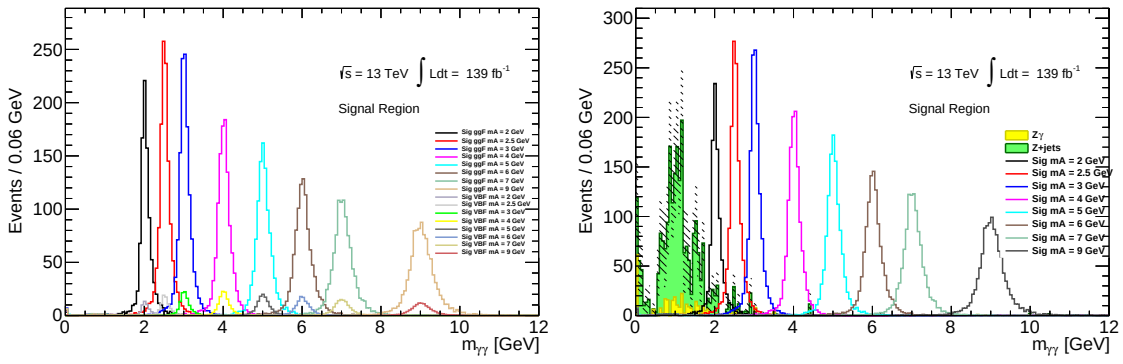

(a) $m_{\gamma\gamma}$, split by process, SR

(b) $m_{\gamma\gamma}$, SR

Figure 6.5: Multiple $m_{\gamma\gamma}$ distributions for (a) signal split by the ggF and VBF process, (b) signal and background comparisons in the signal region. The signal distributions in both plots assume a branching ratio for process $h \to Za = 10\,\%$.

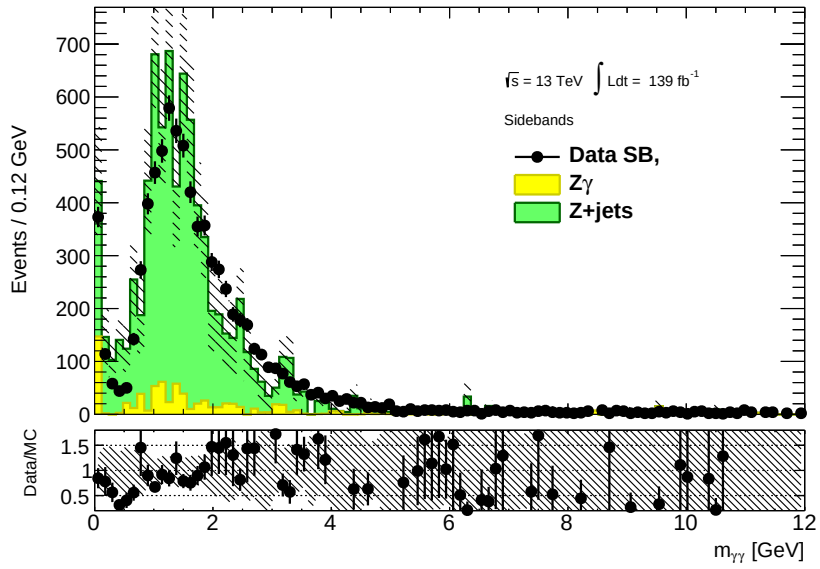

(a) $m_{\gamma\gamma}$, SB

Figure 6.6: The $m_{\gamma\gamma}$ distribution background data comparison in the sideband region. The $h \to Za = 10\,\%$. The $Z\gamma$ and $Z+$jets processes are scaled by 1.8 for plotting purposes only for clearer comparison with data in this region.

Resolved category Background photon truth origins fractions			
lead/sublead photon pairs	**Zγ (%)**	**Zjets (%)**	**Total Bkg (%)**
ISR or FSR/ISR or FSR	69.64	0.00	6.65
π^0/π^0	8.89	72.33	67.38
ISR or FSR/π^0	8.83	0.00	1.52
π^0/ISR or FSR	5.22	0.00	0.68
Light Meson/Light Meson	0.46	10.48	9.59
π^0/Light Meson	2.00	8.62	7.85
Light Meson/π^0	1.11	0.00	5.39
Other	3.85	8.57	0.94

Table 6.1: Table summarising the fraction of events and their truth origins for photons in the resolved category for different leading and sub-leading photon pairs. The term "Light Meson" refers to low mass meson decays that are not π^0.

6.4 Signal parametrisation

The $m_{\gamma\gamma}$ distributions are modelled using a double sided crystal ball function (DSCB) [137] for which the parameters are interpolated to model mass points that are not simulated by MC. The DSCB is defined as follows:

$$f_{\text{DSCB}}(m; m_0, \sigma, \alpha_1, \alpha_2, n_1, n_2) = \begin{cases} g(m; m_0, -\sigma, \alpha_1, n_1) \cdot \mathrm{e}^{-\frac{1}{2}\alpha_1^2} & \text{for } \frac{m-m_0}{\sigma} \leq -\alpha_1 \\ \mathrm{e}^{-\frac{1}{2}\left(\frac{m-m_0}{\sigma}\right)^2} & \text{for } -\alpha_1 < \frac{m-m_0}{\sigma} \leq \alpha_2 \\ g(m; m_0, \sigma, \alpha_2, n_2) \cdot \mathrm{e}^{\frac{1}{2}\alpha_2^2} & \text{for } \frac{m-m_0}{\sigma} > \alpha_2 \end{cases}$$

with

$$g(m; m_0, \sigma, \alpha, n) = \frac{|\alpha|}{n} \left(\frac{n}{|\alpha|} - |\alpha| + \frac{m - m_0}{\sigma} \right)^{-n}.$$

In this relation, m represents the mass of the two photon system. The Gaussian core of the distribution has a mean m_0 and variance σ^2, with the remaining parameters α and n describing the left and right side tails.

The parameters that model the signal distributions are interpreted using the average values and linear fits between all of the available simulated mass points. The signal yield is also interpolated, using a linear fit, and it's uncertainty of 4 % estimated by comparing the differences of the interpolated values to the existing points. The values of the fitted parameters and their interpolation functions are given in Table 6.2. Figure 6.7 shows the resulting signal $m_{\gamma\gamma}$ DSCB distributions for m_a 2 GeV to 9 GeV using the interpolated values. A comparison between the resulting DSCB with each of the simulated signal samples can be found in Appendix D.3.

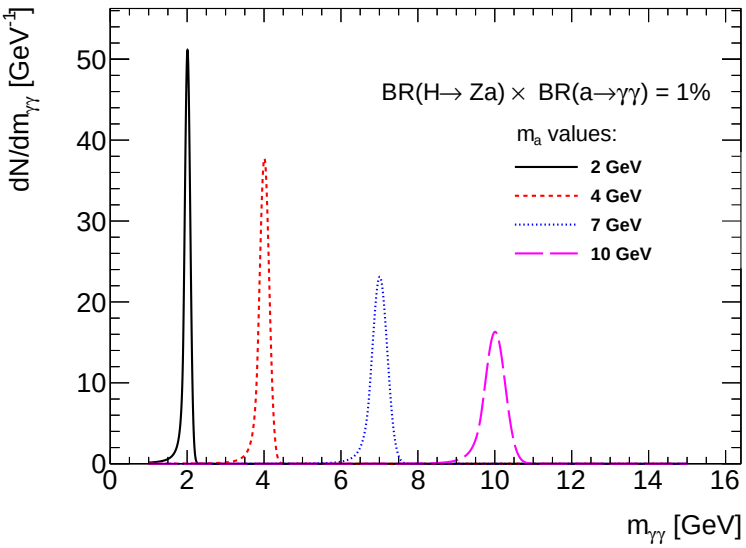

Figure 6.7: Resolved category signal $m_{\gamma\gamma}$ distributions for m_a points 2.0 GeV to 9.0 GeV using the DSCB function with interpolated parameters that are given in Table 6.2.

Table 6.2: The interpolation of the DSCB parameters that is used for the fit. The value of m_a is in GeV.

Parameter	Value
m_0	$-1.21 \times 10^{-5}\ m_a^2 + m_a + 0.00984$
σ	$-5.87 \times 10^{-7}\ m_a^4 + 3.61 \times 10^{-5}\ m_a^3 - 9.35 \times 10^{-4}\ m_a^2 + 0.031\ m_a + 0.0127$
α_1	$-0.0152\ m_a + 1.53$
α_2	0.98 for $m_a > 4$ GeV
	$0.80 - (0.80 - 0.98) \times (m_a - 2.5)/(4.0 - 2.5)$ for $m_a \leq 4$ GeV
n_1	$0.47\ m_a + 1.10$
n_2	$1.17\ m_a + 6.75$
yield interpolation	$-342 \times m_a + 14082$

6.5 Background shape parametrisation

The background $m_{\gamma\gamma}$ distribution is expected to correspond to a smooth and falling spectrum for the region starting from 1.5 GeV. The background estimation is performed with an analytical template method such as the method used in the $h \to \gamma\gamma$

analysis [138, 139]. Modelling the distribution around the $m_{\gamma\gamma}$ peak at $< 1.5\,\text{GeV}$ is not relevant as events in this region contain photons that are too boosted to be reconstructed as two separated photons and result in a loss of sensitivity.

The parametric form of the background used is the sum of a 2$^{\text{nd}}$ order exponential and a constant defined as:

$$f^{bkg}(m; a, b, c, d) = a \cdot \exp(-\frac{b}{m} - c \cdot m) \; + \; d \tag{6.5.1}$$

were m is the mass of the two photon system and a, b, c and d are free parameters fitted to the template.

This function was chosen as it presented the lowest χ^2 value when fitting the background and yielded the lowest outputs from the spurious signal test (described in Section 6.6) from the models that were tested. This means that this function is less susceptible to background mis-modelling. Testing polynomials of higher order did not improve the fit. The $m_{\gamma\gamma}$ distribution comparing data in the SB and the fit shown in Figure 6.8. The validity of the parametrisation is evaluated by comparing the fit to data in several $m_{\ell\ell\gamma\gamma}$ selections of the SB. These regions are $140\,\text{GeV} < m_{\ell\ell\gamma\gamma} < 160\,\text{GeV}$ and $m_{\ell\ell\gamma\gamma} > 160\,\text{GeV}$. The background fits well for all validation regions tested implying that it is robust.

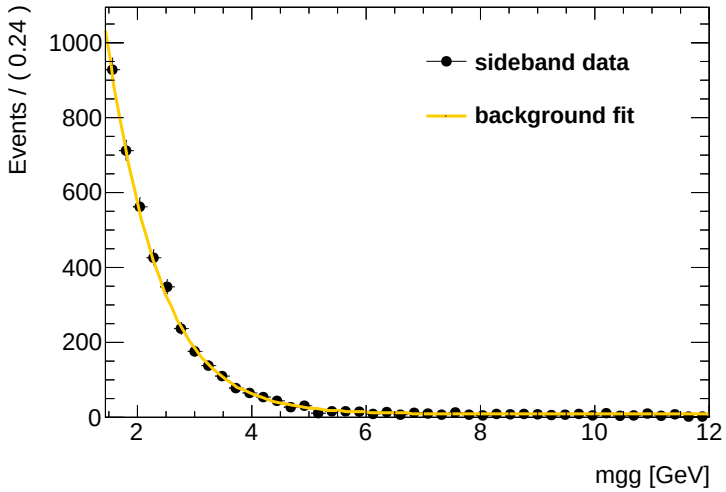

Figure 6.8: Data distribution of $m_{\gamma\gamma}$ in the SB. Yellow line represents the fitted function.

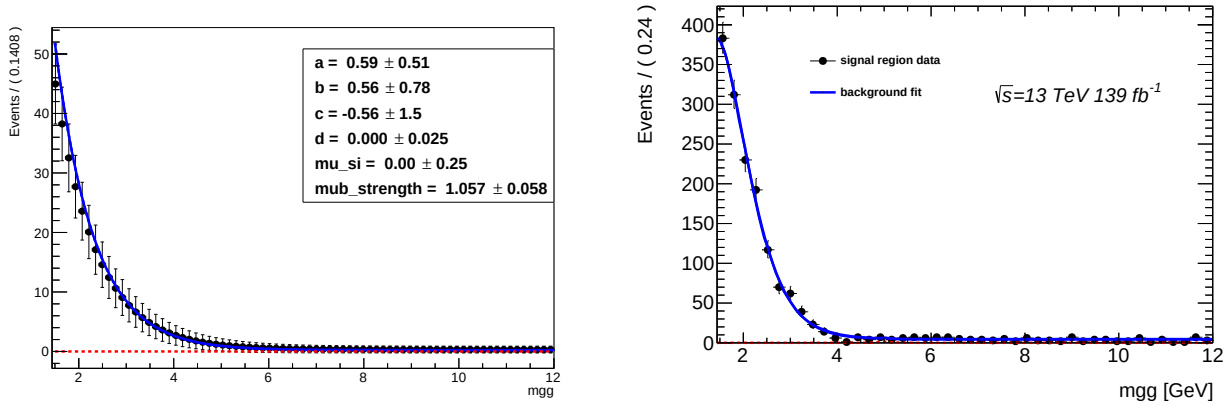

(a) Generated SR $m_{\gamma\gamma}$ (b) $m_{\gamma\gamma}$ fit in the SR

Figure 6.9: Signal region $m_{\gamma\gamma}$ distributions where (a) is the fit result with a Asimov data set generated SR and (b) the parametric function fit to data.

The expected background distribution in the SR is generated from Equation 6.5.1 and normalised to the expected background events in the SR obtained from scaling the MC to match data in the SB region by a factor of 1.8. Figure 6.9a shows the fit in the SR generated with an Asimov dataset for background only. An Asimov dataset is a binned dataset generated so that the event count in each bin is set to the chosen event yield for chosen parameters of a model [140]. Figure 6.9b confirms that the parametric function is able to fit correctly the data in the SR.

6.6 Spurious signal estimation

The validity of the parametric function from Section 6.5 used for the background estimation is tested by fitting the sum of the background model plus a signal template to data that is known to have a very low signal to background ratio. This is known as the spurious signal test and is a way of estimating the induced biases inherited in the template.

Two templates are fitted to data and MC in the SB in order to test this bias. This includes a combination of exponentials:

$$a \cdot \exp(-\frac{m}{b} - m^2 \cdot c) + f \cdot \exp(-m/g - m^2 \cdot k) \tag{6.6.1}$$

and an exponential plus polynomial

$$a \cdot \exp(-\frac{m}{b}) + c + f \cdot m + g \cdot m^2 \tag{6.6.2}$$

were m is the mass of the two photon system and a, b, c, f, g and k are free parameters. Both templates are fit to data and MC in the SB $m_{\gamma\gamma}$ distribution tail similarly to the background fit in Section 6.5 and an Asimov dataset is generated using said templates, S_{fit}. This is tested against the nominal background and S_{expected} by spurious signal test

$$S_{\text{spur}} = S_{\text{fit}} - S_{\text{expected}} \tag{6.6.3}$$

implemented in $m_{\gamma\gamma}$ intervals of 0.1 GeV, starting from 2 GeV to 10 GeV. The signal template is in the form of the DSCB described in Section 6.4. Figure 6.10a shows the spurious signal normalised by the variance of S_{fit} for each of the two templates both when they were fit to either data or MC in the SB.

An envelope from the two templates fitted by an exponential plus a constant is calculated for the final spurious signal systematic estimation approximating the bias. The green line in Figure 6.10b shows the envelope of S_{spur} covering all tested fits. The bias extracted from the signal estimated in this way is included as a systematic uncertainty. It is shown that for number of events relative to the statistical error on the background fit from the test is 0.28 for 2 GeV before plateauing at approximately 0.1 for the highest mass points in the range.

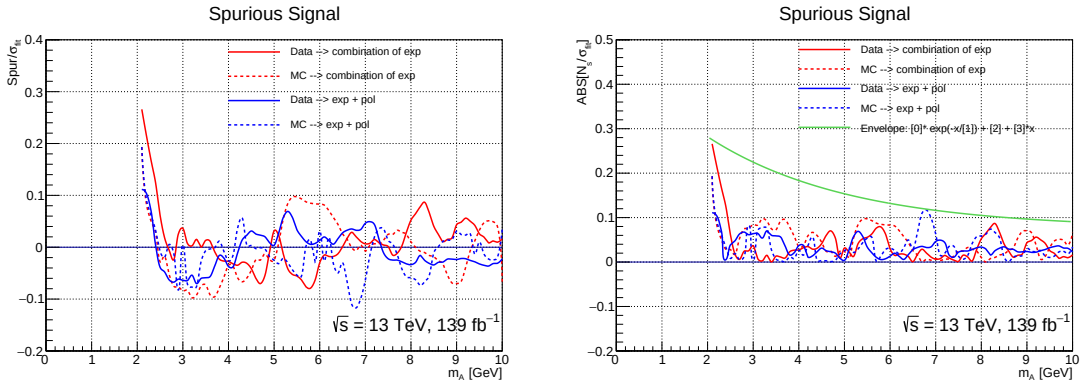

(a) Spurious signal test

(b) Number of entries

Figure 6.10: (a) Spurious signal test and (b) the number of expected entries. The green line represents the envelope of the spurious signal estimation for the two templates.

Object affected	Systematic uncertainty definition
Event	Pile-up re-weighting normalisation factors
Electron	Electron identification efficiency normalisation factors
Muon	Systematic component of the reconstruction and and identification efficiency for muons with pt >15 GeV
	Systematic component of the muon isolation efficiency
	Systematic component of the muon trigger efficiency
Photon	Photon isolation efficiency normalisation factors

Table 6.3: Table showing the descriptions of each of the dominant systematic variables evaluated in the final selection.

6.7 Systematic uncertainties

Uncertainties from both experimental and theoretical sources affect simulation of the background and signal. Approximately 20 sources of uncertainty were studied for both the resolved and merged categories. The majority of the sources had an impact of less than 0.5 % on the shape of the final discriminant and were considered negligible. Only the six dominant sources of experimental systematic uncertainty were included in the final fit for both categories. Each source is listed in Table 6.3.

Because of the use of an interpolated parametric function, a set of signal parameters were computed by following the same method described in Section 6.4 in order to evaluate the impact of each source of uncertainty. The largest impact for each fit parameter across all tested mass points is shown in Table 6.4. Parameter n_2 shows deviance greater than 100 %, though has little impact on distribution shape. These variations were included in the fit as a nuisance parameter. The most dominate source of systematic uncertainty was the event pile-up re-weighting that accounts for the difference between the predicted and measured inelastic cross-sections.

Systematic variations due to uncertainties in theory were also taken into account for signal distributions. These included PDF+α_s and scale uncertainties. There are numerous uncertainties that affect the determination of PDFs and determining the strong coupling constant, α_s, associated to pertubative QCD calculations. Scale uncertainties are variations of the re-normalisation and factorisation scales used in the estimations due to missing higher order corrections. After studying the effect of

Source of systematic uncertainty	Fit parameter					
	σ	n_1	n_2	a_1	a_2	m_0
Event pile-up	17.1 %	<(stat)	136.4 %	5.3 %	6.9 %	20.0 %
Electron identification efficiency	8.5 %	<(stat)	40.0 %	0.1 %	0.1 %	1.4 %
Muon reconstruction and identification efficiency	2.0 %	<(stat)	0.7 %	0.1 %	0.2 %	0.3 %
Muon isolation efficiency	2.1 %	<(stat)	9.0 %	0.1 %	0.1 %	0.5 %
Muon trigger efficiency	0.3 %	<(stat)	6.3 %	0.1 %	0.2 %	0.7 %
Photon isolation efficiency	5.9 %	<(stat)	83.9 %	0.8 %	0.3 %	3.3 %

Table 6.4: Table showing the largest systematic impact from all tested mass points for each fit parameter and source of systematic uncertainty.

these uncertainties on the resolved category signal samples for both the ggF and VBF Higgs boson production mechanisms, the variations were found to be relatively small but non-negligiable. In summary the effect due to these theoretical uncertainties for each were found to be:

- PDF+α_s :< 3 % ggF, < 2 % VBF
- Scale: < 10 % ggF, < 2 % VBF

Plots showing the effect of the scale uncertainties on the shape of the final discriminant for mass points 3 GeV to 9 GeV are shown in Appendix F. These show that for ggF both the up and down variations of the shape uncertainty look approximately symmetric with respect to one another.

The main systematic impact on the background is that from the the spurious signal. This indicates the number of signal events expected due to the fluctuation of the background fit when there is no signal. Two templates, a combination of exponentials and an exponential plus a polynomial, are fit to data and MC in the sideband for the test. The entire procedure is detailed in full in the previous section, Section 6.6. It is shown that for number of events relative to the statistical error on the background fit from the test is 0.28 for the lowest mass point 2 GeV and ranges to approximately 0.1 for 10 GeV.

6.8 Post-fit Distribution

Following the selection and fitting procedures detailed in Section 6.4 to Section 6.7, the $m_{\gamma\gamma}$ distribution after the fit and including all systematic uncertainties for background and signal is shown in Figure 6.11. The solid blue line is the background fit with the dashed representing the background component. For comparison, the signal distribution for $m_a = 5\,\text{GeV}$ is shown in red, assuming $\text{BR}(h \to Za) \times \text{BR}(a \to \gamma\gamma) = 5\,\%$. A discussion of the results including the interpretation is given in Section 8.

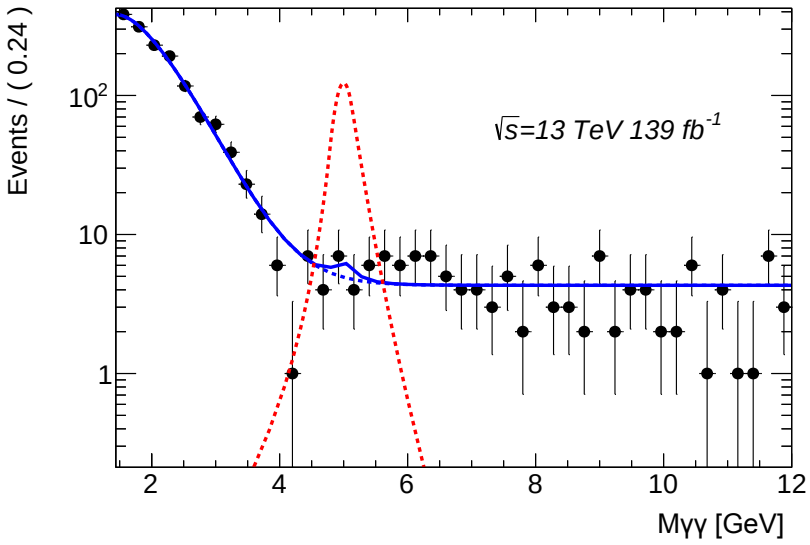

Figure 6.11: The $m_{\gamma\gamma}$ distribution after the fit. The blue solid line is the background fit and the dashed blue is the background component. The red dashed line is a signal distribution for $m_a = 5\,\text{GeV}$ assuming $\text{BR}(h \to Za) \times \text{BR}(a \to \gamma\gamma) = 5\,\%$ for comparison.

Chapter 7

Merged Category

Merged Category Selection

This chapter details the selection for events that fail the resolved category criteria but contain a photon object that is likely reconstructed as a result of both photons from $a \to \gamma\gamma$ decaying in close proximity to each other. This selection category is known as the merged category and the categorisation criteria and analysis method is summarised below:

Merged category selection: The event fails the resolved category selection and includes a photon with $p_T > 20\,\text{GeV}$.
Method: The angular distance between the two lepton system and photon, $\Delta R(\ell\ell, \gamma)$, and photon identification variable E_{ratio} in the sideband region is used for the background simulation normalisation and to model the uncertainties.

This chapter describes the signal and sideband regions for this category, the signal properties and also how photon identification variable E_{ratio} is used to define a Z + jets dominate region in order to calculate normalisation factors for the background simulation. The photon identification and isolation procedure is also described here. The background is estimated from simulation corrected using data in the sideband. This chapter finishes by discussing the uncertainty from systematic effects and describing the fit method to the final discriminant in order to extract the signal.

7.1 Selection regions, normalisation and shape correction

7.1.1 Selection Regions

Events categorised into the merged category will fall either into a signal region (SR) or a sideband region (SB). A signal region is chosen using the Higgs boson mass distribution window, $m_{\ell\ell\gamma}$, that contains signal. This distribution is shown in Figure 7.1 and the chosen window to be $110\,\text{GeV} < m_{\ell\ell\gamma} < 130\,\text{GeV}$. The chosen window for $m_{\ell\ell\gamma}$, which contains 94 % of signal events, is a result of an optimisation study described in Section E.1 of Appendix E. In Figure 7.1 the background sample normalisation is corrected using SB data. Normalisation factors for each background sample are estimated to be 1.18 ± 0.01 for $Z\gamma$ and 2.33 ± 0.05 for $Z+\text{jets}$. The calculation of these factors is explained in Section 7.1.4. Simulation is used as a template and corrected using data in the SB. As per the definition of the two regions, it is expected that any signal in the pre-sideband (pSB) area is low and has negligible effect in this region.

A further cut on photon identification variable E_{ratio} at $E_{\text{ratio}} > 0.8$ to define the final signal (SR) and sideband regions (SB). The definition of photon identification variable E_{ratio} has been introduced in Section 4.1.6. The reason for choosing $E_{\text{ratio}} > 0.8$ is twofold. Firstly, the majority of signal events for all mass points is above this threshold with an average signal efficiency of 67 % and secondly this cut reduces $Z+\text{jets}$ by two-thirds. Figure 7.7 shows the E_{ratio} variable for signal and background in the pSR and pSB regions that were used to define the cut (described in Section 7.1.2). Other variables were reviewed to reduce the background further but either had minimum effect or contained regions with relatively more signal events. This E_{ratio} cut in the pSB regions also creates a $Z+\text{jets}$ dominate region that is useful for calculating normalisation factors for the background MC samples and correction scaling to correct mis-modelling in the background. The role of the E_{ratio} variable for normalisation and MC corrections is explained in more detail in Section 7.1.4 and Section 7.1.5.

Table 7.1 summarises the various selection regions of the merged category and the purpose of each.

Merged category analysis regions			
Region	Selection	Blinded	Comments
pre-SR (pSR)	$m_{\ell\ell\gamma}$ window	Y	
pre-SB (pSB)	$m_{\ell\ell\gamma}$ sideband	N	fit E_{ratio} to obtain normalization for $Z+\text{jets}$ and $Z\gamma$
correction region A	pSB, $E_{\text{ratio}} > 0.8$	N	$Z\gamma$ dominate to obtain $\ell\ell$ p_T , $\ell\ell\gamma$ p_T , $\Delta R_{\ell,\gamma}$ corrections
correction region B	pSB, $E_{\text{ratio}} < 0.8$	N	$Z+\text{jets}$ dominate to obtain $\ell\ell$ p_T , $\ell\ell\gamma$ p_T , $\Delta R_{\ell,\gamma}$ corrections
SR	pre-SR, $E_{\text{ratio}} > 0.8$	Y	final signal region
SB	pre-SB, $E_{\text{ratio}} > 0.8$	N	validation region
Definitions:			
$m_{\ell\ell\gamma}$ window		$m_{\ell\ell\gamma}$: $110-130\,\text{GeV}$	
$m_{\ell\ell\gamma}$ sideband		$m_{\ell\ell\gamma}$ not in window	

Table 7.1: Regions used in the merged category event analysis. All events pass the merged category definition and all photons pass Loose photon identification and an isolation selection described in Section 7.1.2.

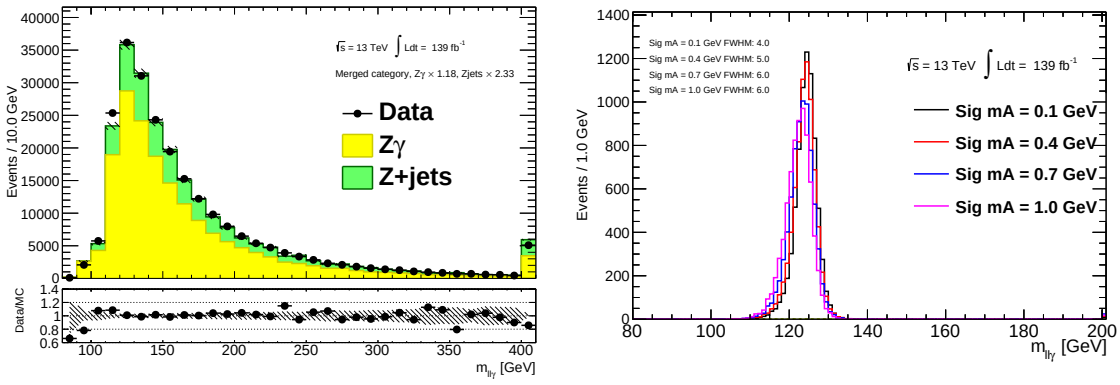

(a) $m_{\ell\ell\gamma}$ (b) $m_{\ell\ell\gamma}$, signal samples only

Figure 7.1: $m_{\ell\ell\gamma}$ plots for signal, background and data after the merged category selection. Signal has a full branching ratio for $h \to Za$; $a \to \gamma\gamma$ of 0.1. The background $Z\gamma$ and $Z+\text{jets}$ processes in (a) are scaled by 1.18 and 2.33 respectively and before any of the final shape corrections or fit is applied (Section 7.2.1). Distributions in (b) are normalised to the same number of events for shape comparison. Uncertainty bands shown are uncertainties due to the finite number of simulated events only.

7.1.2 Photon Identification and Isolation

As is the case for the resolved category, photons in events that are selected into the merged category must pass the Loose photon identification criteria. As introduced already in Section 4.1.6, the Loose criterion cuts on two variables describing the shower shape in the middle layer of the calorimeter (R_η and $w_{\eta 2}$) and two variables that describe hadronic leakage (R_{had} and R_{had1}). Figure 7.2 is a shape comparison of these variables for merged category photons from signal to that of the isolated

photons from the $Z\gamma$ process. These plots show that the signal distributions are not majorly different in shape, other than R_η which has a slightly longer tail in signal due to overlapping of the two energy deposits. The cuts on these variables are the same as detailed in the resolved category photon identification chapter, Section 6.2.

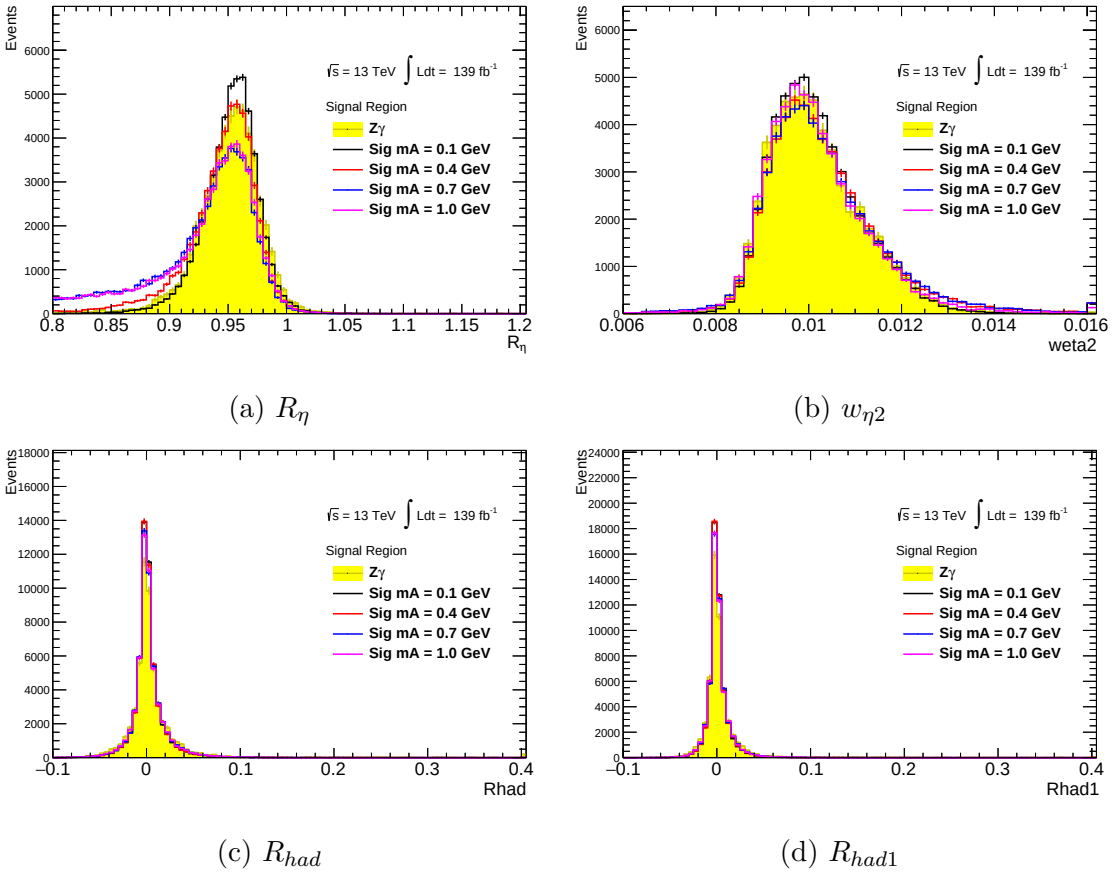

(a) R_η (b) $w_{\eta 2}$

(c) R_{had} (d) R_{had1}

Figure 7.2: Loose identification variables for signal and $Z\gamma$ photon comparisons after the merged category selection in the signal region. Loose isolation criteria applied to the photons. No photon identification cuts are applied. Distributions normalised to the same number of events for shape comparison. Uncertainty bars shown are MC statistical errors.

Isolated photons from $Z\gamma$ are calibrated to Loose identification therefore as the signal photon distributions are similar this means Loose can indeed be applied in the merged category selection.

Tight identification was also considered as an option for photon selection in this category. Although Tight identification did remove a higher proportion of $Z+$jets it was also shown that for signal this identification criteria had a much lower efficiency compared to Loose, especially for the lowest mass points. Given that the $Z+$ jets

background is sub-dominate in this event category, Loose identification was deemed more suitable. Table E.1 in Section E.2 of Appendix E shows the comparison between Loose and Tight identification efficiencies.

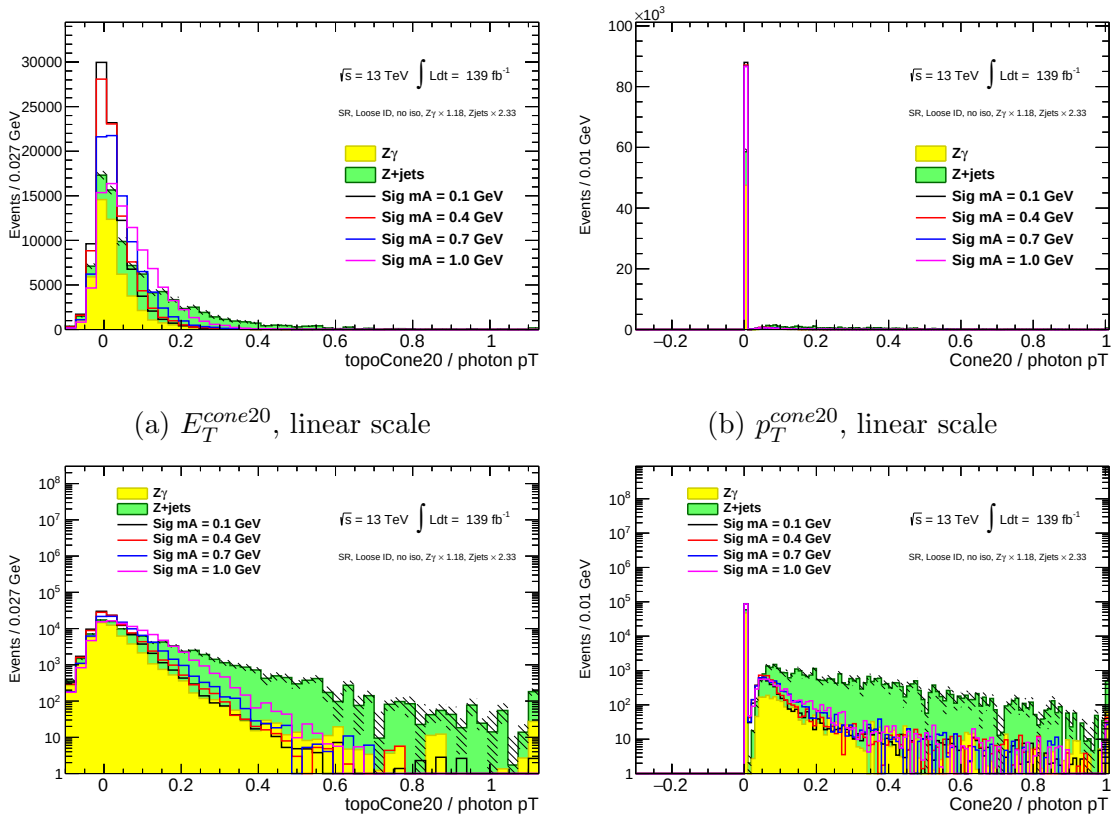

(a) E_T^{cone20}, linear scale

(b) p_T^{cone20}, linear scale

(c) E_T^{cone20}, log scale

(d) p_T^{cone20}, log scale

Figure 7.3: Calorimeter and track isolation variables E_T^{cone20} and p_T^{cone20} for an energy cluster cone defined as $\Delta R = 0.2$ for merged category events in the signal region. Loose photon identification is applied but no isolation cuts. The background normalisation factors and uncertainty bands follow the same convention as Figure 7.1. Bottom two plots show the same information as the top plots but on a log scale.

For photon isolation a unique working point was studied based on the isolation variables that make up the Loose criteria (defined in Section 4.1.4); track isolation variable, p_T^{cone20}, and calorimeter isolation variable, E_T^{cone20}. Figure 7.3 shows the isolation variable distribution shape comparison between the signal and background before any isolation cuts. As well as passing the Loose identification criteria, photons in merged category events must satisfy the Loose isolation track isolation variable condition of 0.05, as stated in Table 4.1 in Section 4.1.6. Unlike Loose isolation however, no condition is required for the calorimeter part of the criteria. Removing

only this calorimeter isolation cut means that there is still a relatively large signal efficiency while keeping it for the track isolation reduces $Z+$jets in the background by approximately 75 %. Variations on the cuts applied to the p_T^{cone20} and E_T^{cone20} variables were studied and the chosen criteria described resulted in a better comparative sensitivity.

7.1.3 Signal Properties

As mentioned previously, photons from the axion decay are more likely to be collimated at lower m_a values. Figure 7.4 shows this by comparing the $\Delta R_{\gamma\gamma}$ distributions of the two truth particle level photons for both low and high mass points passing the merged category selection. "Truth particle level", a term introduced in Section 5.3, is the MC generator output quantities before detector simulation. Truth-level photons in signal events with $m_a \leq 1\,\text{GeV}$ have $\Delta R_{\gamma\gamma}$ distributions with peaks approximately at 0.1 which is half that of the ΔR cone used for photon reconstruction. Mass points above this range have on average much larger ΔR values inferring that signal with $m_a > 1\,\text{GeV}$ are much less likely to have merged photons.

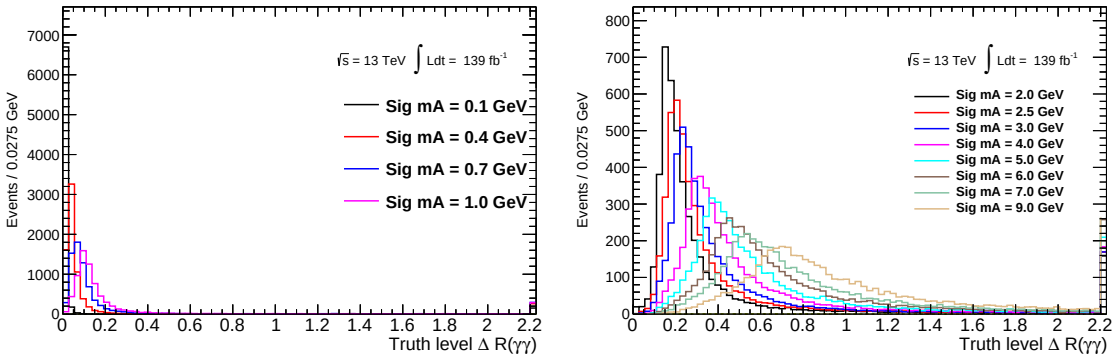

(a) $\Delta R_{\gamma\gamma}$, 0.1 - 1.0 GeV

(b) $\Delta R_{\gamma\gamma}$, 2.0 - 9.0 GeV

Figure 7.4: Merged category photon truth-level $\Delta R_{\gamma\gamma}$ distribution in the signal region. Loose photon identification and isolation selection applied.

The photon p_T distribution comparisons between the leading and sub-leading truth-level photons and the reconstructed photon in Figure 7.5 show that the reconstructed photon distributions at higher mass points match closely to the shape from the leading photon at truth-level. This is in contrast to lower signal a particle mass values where the reconstructed photon energy is larger than the generated en-

ergy. This confirms that the reconstructed photon in lower mass points after being selected for the merged category is a result of the energies from the collimated photons whereas the reconstructed photon in higher mass points is entirely due to the truth-level leading photon and does not include any sub-leading photon information. This, and the shape of the ΔR distributions, implies that signal of higher m_a values are only categorised into the merged category when they contain a leading photon with p_T greater than 20 GeV but also a sub-leading photon with p_T less than the 10 GeV threshold. This evaluation furthers the evidence that the merged category selection focuses only in the case of lower m_a values.

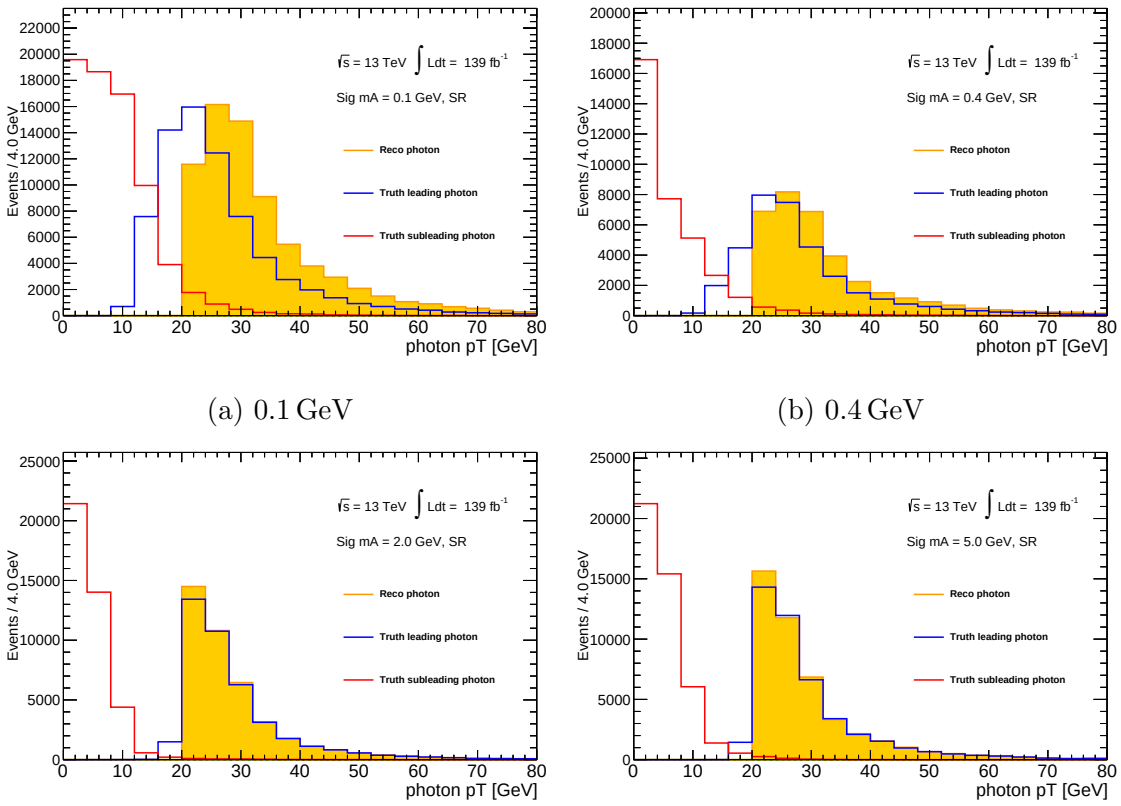

(a) 0.1 GeV (b) 0.4 GeV

(c) 2.0 GeV (d) 5.0 GeV

Figure 7.5: Merged category signal region truth-level photon p_T distributions compared to the photon p_T of the reconstructed photon, for selected signal mass points. Loose photon identification and isolation selection applied.

More signal kinematic variable shape distribution comparisons for ggF and VBF are shown in Figure 7.6. The mass of the dilepton and photon system which defines the signal and sideband regions shows that both Higgs boson production processes

are well within the $100\,\text{GeV} < m_{\ell\ell\gamma} < 130\,\text{GeV}$ window. Also, the overwhelming majority of signal events are within the E_{ratio} cut required for the background normalisation discussed in the next subsection, Section 7.1.4. The major difference between the two production processes is the p_T of the $\ell\ell\gamma$ system, Figure 7.6d. Signal from ggF peak at a p_T of approximately 20 GeV and drops off rapidly compared to the signal from VBF of which generally has larger p_T . This results in the dilepton and photon to decay closer together, shown in Figure 7.6c, which is important for the chosen final discriminant discussed in Section 7.2.

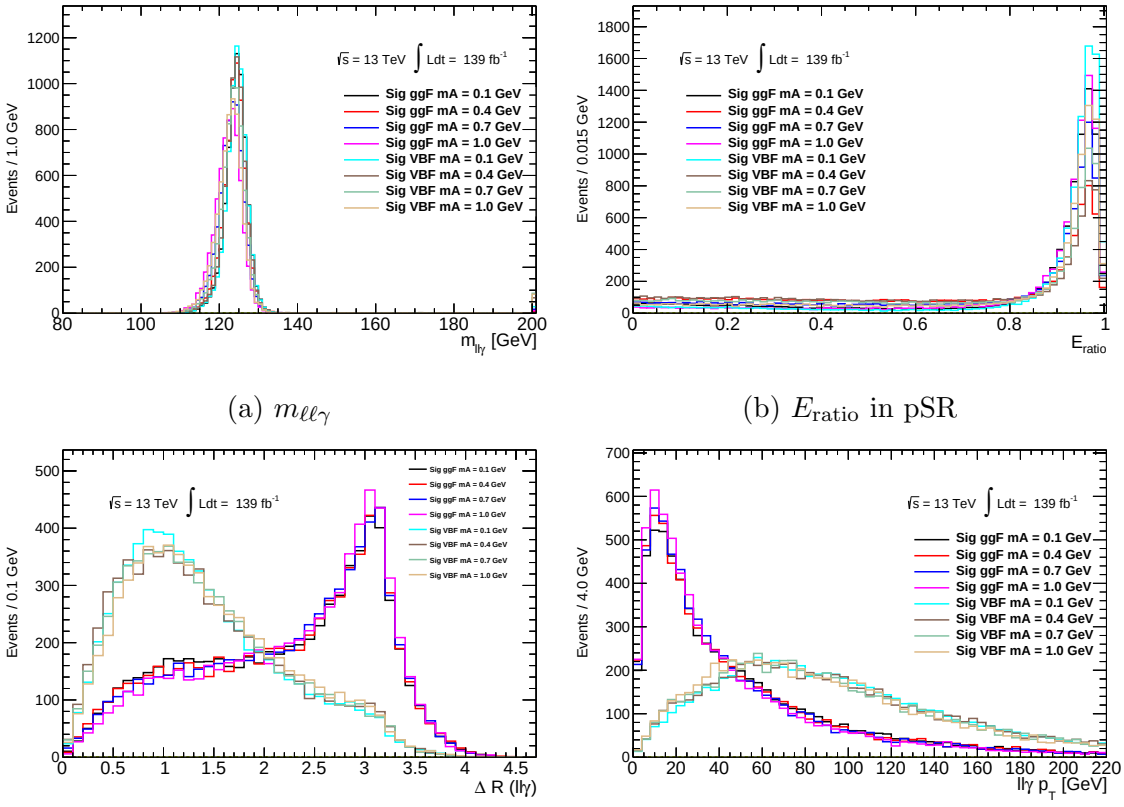

(a) $m_{\ell\ell\gamma}$

(b) E_{ratio} in pSR

(c) $\Delta R_{\ell\ell\gamma}$ in SR

(d) $p_T(\ell\ell, \gamma)$ in SR

Figure 7.6: Various kinematic variables in different selection regions for merged category signal samples, split by the ggF and VBF processes. Signal has a full branching ratio for $h \to Za$; $a \to \gamma\gamma$ of 0.1. All distributions are normalised to the same number of events for shape comparison.

7.1.4 Background Normalisation

The merged category uses data corrected simulations therefore the background MC samples must both be scaled to match data in the sideband. Figure 7.7 shows that

for the pre-sideband region and $E_{\text{ratio}} < 0.8$ a sample pure in Z + jets is obtained. Using this region, and also the region enriched with $Z\gamma$ events when inverting the cut, a fit is done to derive the normalisation factors of the background samples. The sideband fit results with normalisation factors 1.18 ± 0.01 and 2.33 ± 0.05 estimated for the $Z\gamma$ and Z + jets samples respectively. The error quoted on each value is the statistical uncertainty of the data and MC combined in quadrature. Figure 7.7 shows some E_{ratio} signal distributions in the pSB and pSR regions confirming, firstly, that the low abundance of signal in the pSB does not interrupt the background fit and, secondly, a negligible amount of signal is removed by the E_{ratio} cut at 0.8 in the pSR.

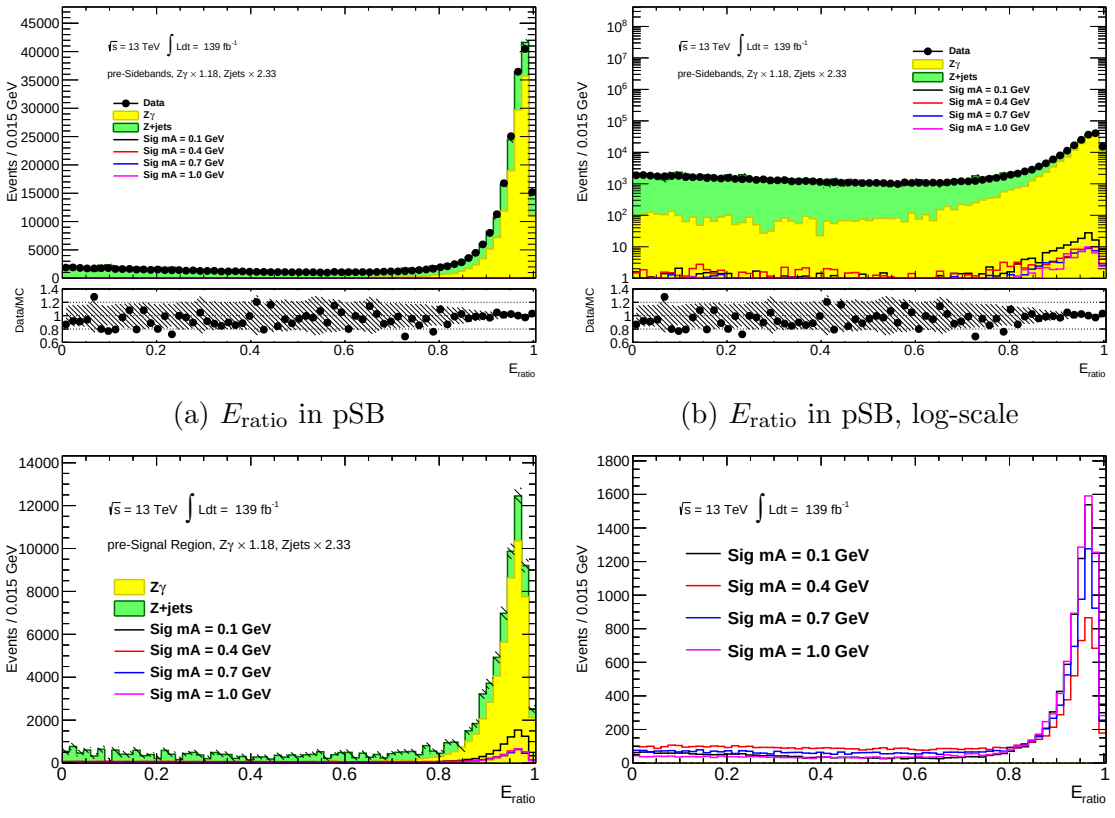

(a) E_{ratio} in pSB

(b) E_{ratio} in pSB, log-scale

(c) E_{ratio} in pSR

(d) E_{ratio} in pSR, signal samples only

Figure 7.7: E_{ratio} plots for signal, background and data in different selection regions. The background normalisation factors, signal branching ratio and uncertainty bands follow the same convention as Figure 7.1. Distributions in plot (d) showing signal only are normalised to the same number of events for shape comparison.

7.1.5 Background shape correction and properties

The $Z\gamma$ and $Z+$jets modelling is tested using the sideband control region. In particular, shape corrections are applied to the p_T of the $\ell\ell$ system ($\ell\ell$ p_T), p_T of the $\ell\ell\gamma$ system ($\ell\ell\gamma$ p_T) and the angular distance between the photon and the closest lepton ($\Delta R_{\ell\gamma}$) for both background samples. The reason for applying these corrections is to take into account mis-modelling in initial state radiation (ISR), final state radiation (FSR) and soft hadronic recoil.

For ISR, the $\ell\ell$ p_T was corrected. The two regions in pre-sideband either side of the E_{ratio} cut at 0.8 discussed in Section 7.1.4 was also used to derive the correction normalisation factors. These regions are referenced as correction regions A and B for the $Z\gamma$ and $Z+$ jets enriched regions respectively (see Table 7.1). Figure 7.8 shows correction regions A and B for the sideband photon p_T before the correction is applied.

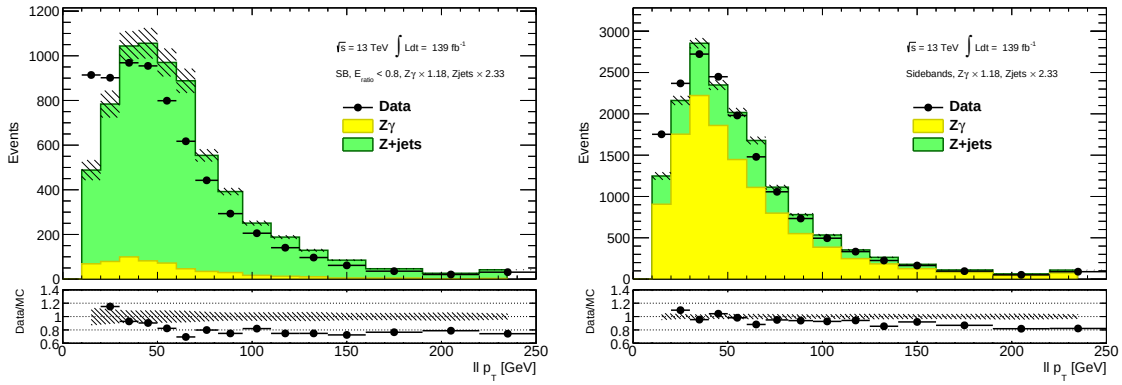

(a) $p_T(\ell\ell)$ in pSB, $E_{\text{ratio}} < 0.8$ (b) $p_T(\ell\ell)$ in pSB, $E_{\text{ratio}} > 0.8$

Figure 7.8: $\ell\ell$ p_T distributions for background and data in the pSB region either side of the E_{ratio} cut at 0.8. (a) shows the pSB region at $E_{\text{ratio}} < 0.8$ whereas (b) shows this for $E_{\text{ratio}} > 0.8$. The background normalisation factors and uncertainty bands follow the same convention as Figure 7.1.

The correction itself is applied to each bin individually following the conditions

$$c_{Z\gamma}\eta_{Z\gamma}^{(A)} + c_{Zj}\eta_{Zj}^{(A)} = \eta_D^{(A)} \tag{7.1.1}$$

and

$$c_{Z\gamma}\eta_{Z\gamma}^{(B)} + c_{Zj}\eta_{Zj}^{(B)} = \eta_D^{(B)}. \tag{7.1.2}$$

The correction values $c_{Z\gamma}$ and c_{Zj} were calculated by scaling each bin contents, $\eta_{Z\gamma}$ and η_{Zj}, to the data in the sideband, η_D, and minimising the χ^2 for both backgrounds in correction regions A and B.

For events that fall within the decided binning, the correction values are applied to simulation. Once the $\ell\ell$ p_T variable is corrected, using the same method an additional correction on $\ell\ell\gamma$ p_T is applied to account for soft hadronic recoil which is followed by a correction in $\Delta R_{\ell\gamma}$ due to FSR.

The shape uncertainty for each correction was calculated by ($\mathrm{MC_{corr}}$ - MC)/$\mathrm{MC_{corr}}$ with $\mathrm{MC_{corr}}$ being the $Z\gamma$ or $Z+$jets simulation output after a particular correction and MC is the simulation from before the correction was applied. As this is a shape uncertainty, the $\mathrm{MC_{corr}}$ histograms are re-normalised to the integral prior to the correction. This calculation is regarded as the up variation with the down variation being calculated by the same method but inverted about where the uncertainty equals 0. Figure 7.9 shows the $c_{Z\gamma}$ and c_{Zj} values for each correction variable and Figure 7.10 shows the equivalent up and down shape variation. The error bars on Figure 7.9 are statistical and indicate the number of events in each bin. To summarise the effect of the three corrections thus far, Figure 7.11 displays each correction variable after each set of shape correction values are applied and the effect that they have on each.

As a cross-check, the shape of the $m_{\ell\ell\gamma}$ distribution, the variable that defines the signal and sideband regions, and also the shape of the photon p_T distribution in the SB were checked before and after the corrections were applied. It was found that there were no changes in shape. The photon p_T distribution however still contained a slope in the ratio comparing simulation to data. The cause of this was found to be due to the fact that the collective p_T of the jet system is corrected however the allocation of the p_T among the jets, including the p_T of the jet that fakes the photon, is not covered. Therefore a further correction to only $Z+$jets simulation is required to correct the photon p_T of the jets that fake photons which are not corrected by the previous three corrections. The correction values and shape uncertainty is calculated by the same method. Figure 7.12 shows the c_{Zj} values and shape uncertainty for this correction and also the photon p_T in the SB region before and after the final correction is applied.

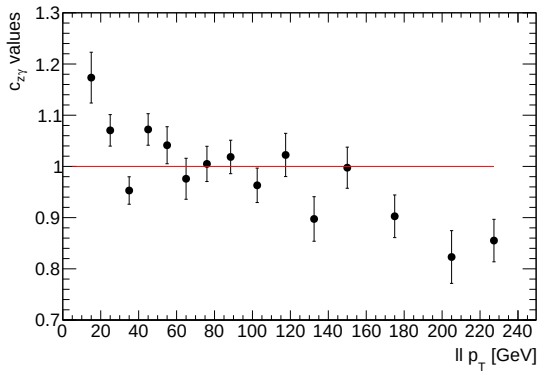

(a) $p_T(\ell\ell)$, $c_{z\gamma}$

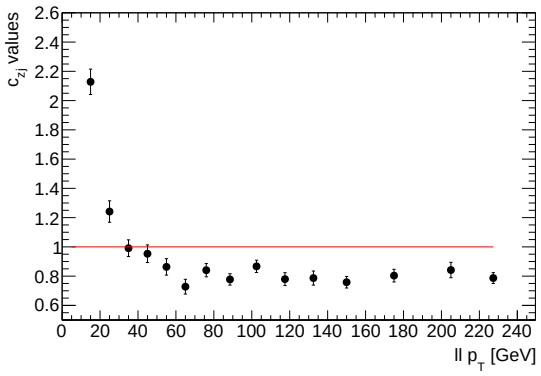

(b) $p_T(\ell\ell)$, c_{zj}

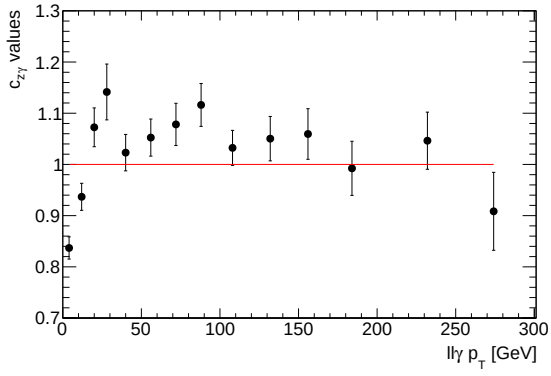

(c) $p_T(\ell\ell\gamma)$, $c_{z\gamma}$

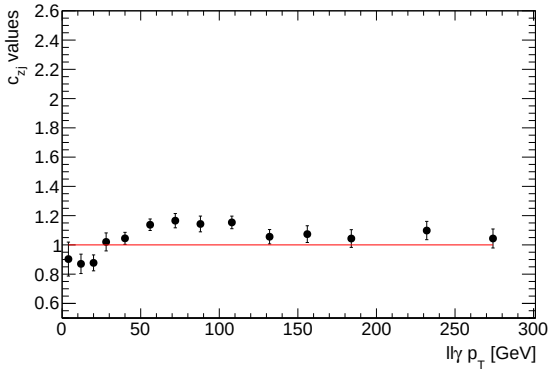

(d) $p_T(\ell\ell\gamma)$, c_{zj}

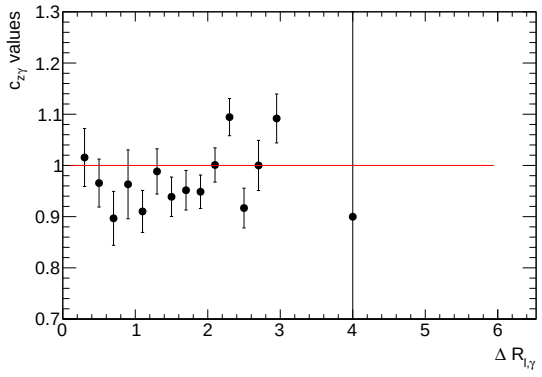

(e) $\Delta R(\ell\gamma)$, $c_{z\gamma}$

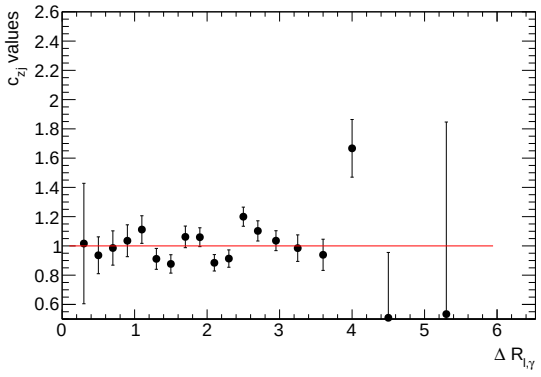

(f) $\Delta R(\ell\gamma)$, c_{zj}

Figure 7.9: Bin shape correction values for $Z\gamma$, $c_{z\gamma}$, and $Z+\mathrm{jets}$, c_{zj}, for correction variables ℓ p_T , $\ell\ell\gamma$ p_T and $\Delta R(\ell\gamma)$.

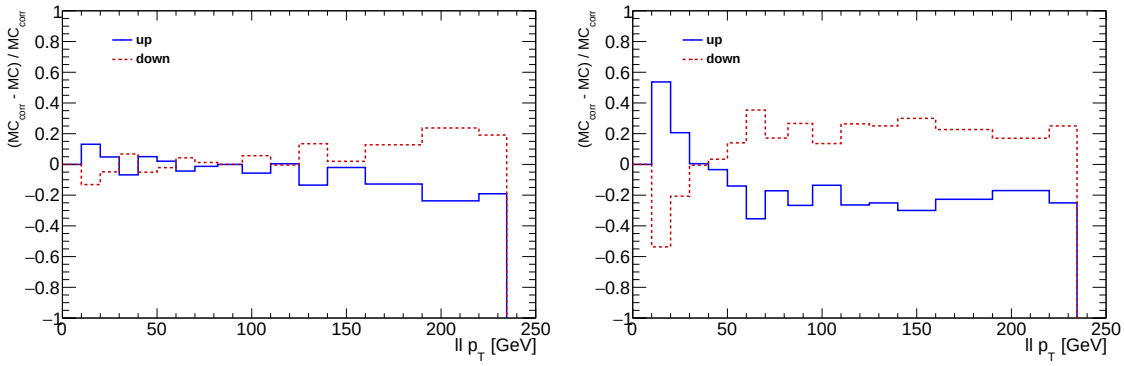

(a) $p_T(\ell\ell)$, $c_{z\gamma}$ uncertainty

(b) $p_T(\ell\ell)$, c_{zj} uncertainty

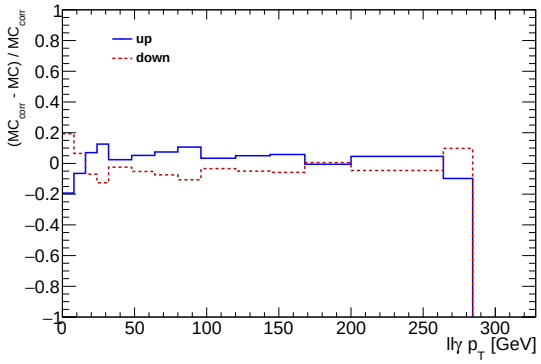

(c) $p_T(\ell\ell\gamma)$, $c_{z\gamma}$ uncertainty

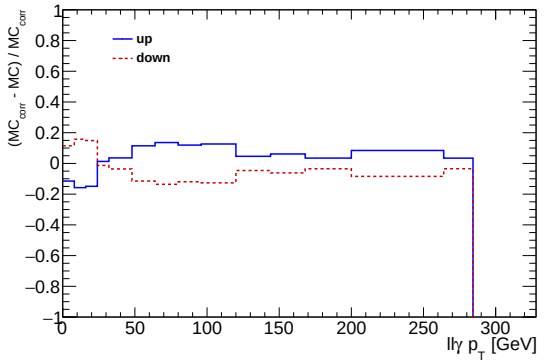

(d) $p_T(\ell\ell\gamma)$, c_{zj} uncertainty

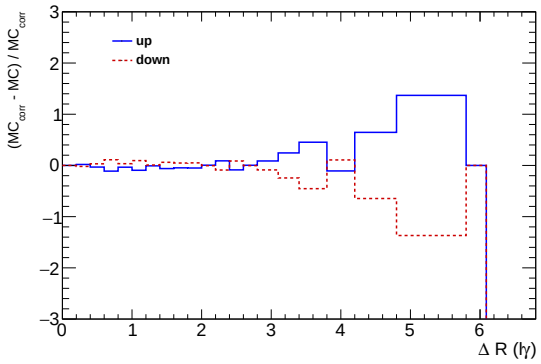

(e) $\Delta R(\ell\gamma)$, $c_{z\gamma}$ uncertainty

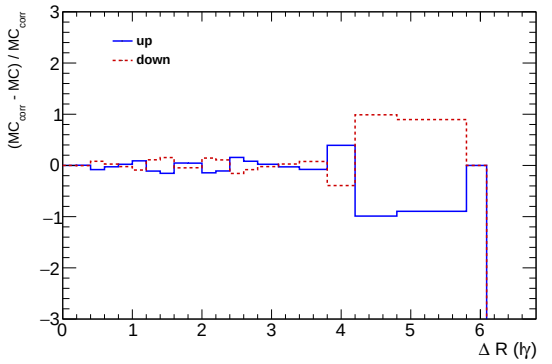

(f) $\Delta R(\ell\gamma)$, c_{zj} uncertainty

Figure 7.10: Bin shape uncertainty values for correction variables $\ell\ell$ p_T , $\ell\ell\gamma$ p_T and $\Delta R(\ell\gamma)$. Blue line represents the up variation and the red dotted line the down variation.

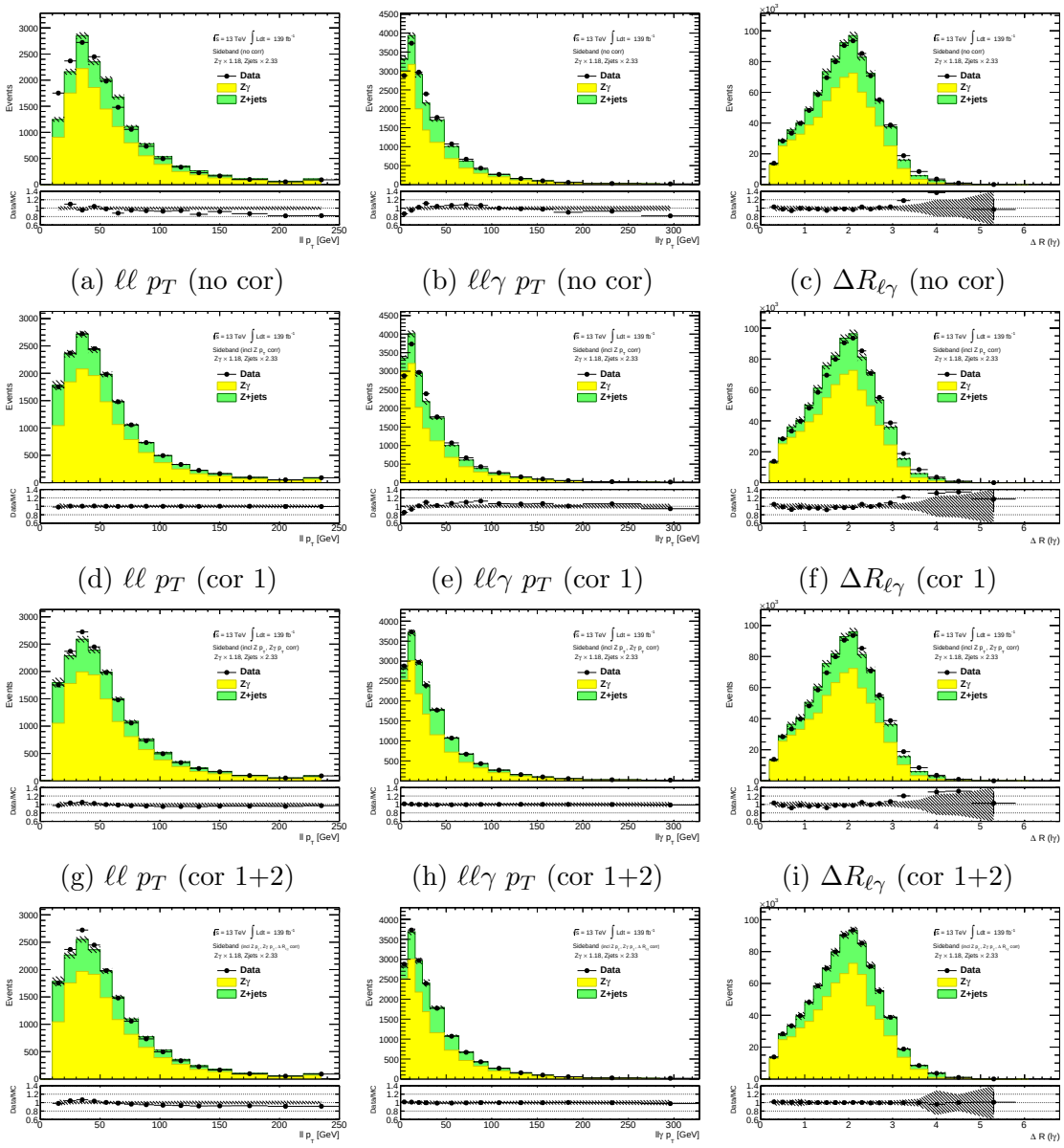

(a) $\ell\ell$ p_T (no cor) (b) $\ell\ell\gamma$ p_T (no cor) (c) $\Delta R_{\ell\gamma}$ (no cor)

(d) $\ell\ell$ p_T (cor 1) (e) $\ell\ell\gamma$ p_T (cor 1) (f) $\Delta R_{\ell\gamma}$ (cor 1)

(g) $\ell\ell$ p_T (cor 1+2) (h) $\ell\ell\gamma$ p_T (cor 1+2) (i) $\Delta R_{\ell\gamma}$ (cor 1+2)

(j) $\ell\ell$ p_T (cor 1+2+3) (k) $\ell\ell\gamma$ p_T (cor 1+2+3) (l) $\Delta R_{\ell\gamma}$ (cor 1+2+3)

Figure 7.11: Sideband MC and data comparisons for correction variables $\ell\ell$ p_T , $\ell\ell\gamma$ p_T and $\Delta R(\ell\gamma)$ with different levels of correction combinations applied. Correction 1=$\ell\ell$ p_T correction, 2=$\ell\ell\gamma$ p_T correction and 3=$\Delta R(\ell\gamma)$ correction. The background normalisation factors and uncertainty bands follow the same convention as Figure 7.1.

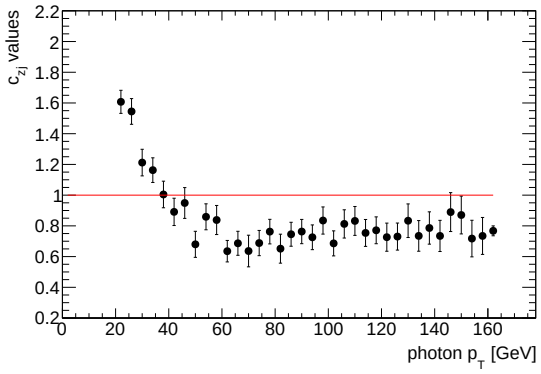

(a) $Z+$jets $p_T(\gamma)$, c_{zj}

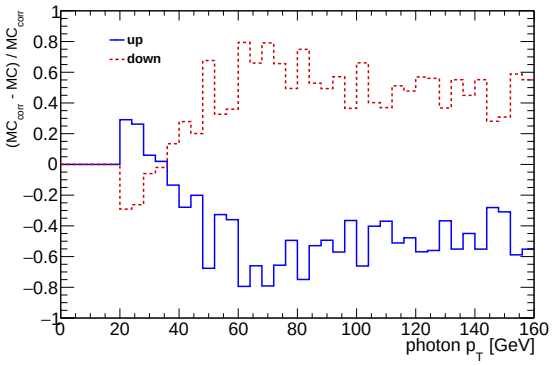

(b) $Z+$jets $p_T(\gamma)$, c_{zj} uncertainty

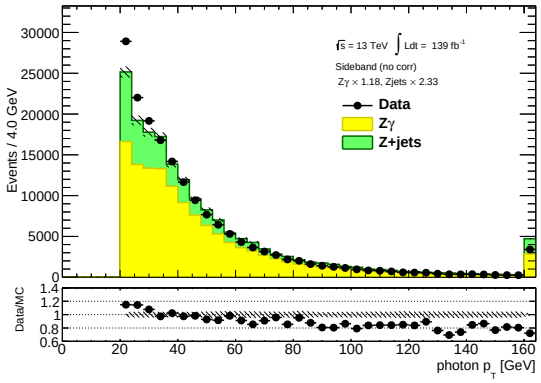

(c) photon p_T SB before corrections

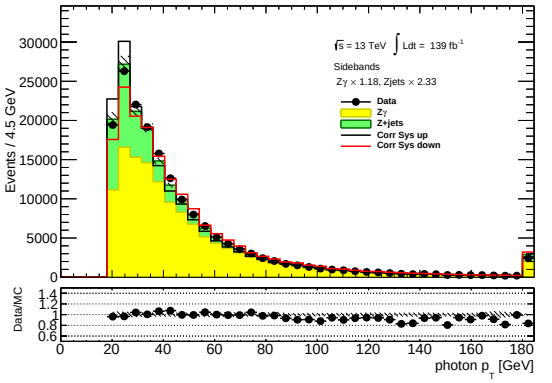

(d) photon p_T SB, all corr incl $Z+$jets $p_T(\gamma)$ applied

Figure 7.12: The $Z+$jets photon p_T (a) correction and (b) shape uncertainty values. Figure (c) is the photon p_T in the sideband before any of the corrections are applied. Figure (d) shows the sideband photon p_T distribution after all corrections, including the $Z+$jets photon p_T correction, is applied. The blue and red lines in (d) represent the up and down uncertainty due to the latter correction. The background normalisation factors and uncertainty bands follow the same convention as Figure 7.1.

The origins of the photon in the merged category background processes was also studied. Table 7.2 summarises the origins of the selected reconstructed photon using truth-level information. For the $Z\gamma$ process over 99 % of the photons are from ISR or FSR. For $Z+$jets, the majority of photons originate from $\pi^0 \to \gamma\gamma$ and other light meson decays meaning that although $Z\gamma$ is the dominate background, approximately 30 % of the total merged category background is faked by jets. The SB data and simulation agree well with respect to each other. This, as well as the fact that the $Z+$jets fraction to total background compositions are similar in both SR and SB (22 % vs 24 % respectively) implies that this information can be extrapolated to the SR and in data.

Merged category Background photon truth origins fractions			
	Zγ (%)	**Zjets (%)**	**Total Bkg (%)**
ISR/FSR	99.67	0.00	71.58
Light Meson	0.07	23.53	6.69
π^0	0.25	75.81	21.55
Other	0.01	0.66	0.18

Table 7.2: Table summarising the fraction of events and the origins for photons in the merged category. The term "Light Meson" refers to low mass meson decays that are not π^0.

Table 7.3 shows a complete cutflow for the number of events starting from when they are categorised up to the final selections and the respective different regions. In this table, normalisation and correction factors calculated using the sideband validation region are applied. The 'ID' and 'Iso' labels refer to the number of events after Loose identification and isolation cuts have been applied respectively. Regions SB and SR are the sideband and signal regions respectively with the 'p' before them representing the selection before the E_{ratio} cut at 0.8. Each row assumes the cut of the previous row is applied up to pSB.

Merged category Cutflow								
	Data $\times 10^3$	**Total Bkg** $\times 10^3$	**Zγ** $\times 10^3$	**Zjets** $\times 10^3$	**Signal mA = 0.1 GeV**	**Signal mA = 0.4 GeV**	**Signal mA = 0.7 GeV**	**Signal mA = 1.0 GeV**
AfterCat	1890 ± 1.38	3580 ± 4.08	190 ± 0.890	3390 ± 3.98	678 ± 10.5	647 ± 10.2	607 ± 9.91	612 ± 9.97
ID	603 ± 0.776	870 ± 2.68	201 ± 0.904	668 ± 2.52	10100 ± 42.3	7710 ± 36.7	5060 ± 29.6	4300 ± 27.3
Iso	337 ± 0.581	370 ± 1.77	189 ± 0.867	180 ± 1.54	9750 ± 41.4	7370 ± 35.8	4790 ± 28.8	4030 ± 26.4
pSB	247 ± 0.497	267 ± 1.39	139 ± 0.726	128 ± 1.18	192 ± 5.71	137 ± 4.85	91.2 ± 3.89	72.3 ± 3.38
SB	176 ± 0.420	184 ± 1.04	132 ± 0.704	51.9 ± 0.767	135 ± 4.76	66.0 ± 3.33	54.5 ± 3.03	48.5 ± 2.78
pSR	90.5 ± 0.300	103 ± 1.10	50.1 ± 0.475	52.7 ± 0.993	9560 ± 41.0	7230 ± 35.5	4700 ± 28.5	3960 ± 26.2
SR	61.5 ± 0.248	67.6 ± 0.777	47.1 ± 0.459	20.4 ± 0.627	7290 ± 35.7	3510 ± 24.8	2990 ± 22.9	3100 ± 23.3

Table 7.3: Merged category cutflow table after the initial categorisation. Each row assumes the cut of the previous row is applied up to pSB.

7.2 Final Discriminant, Fit Strategy and Systematic Uncertainties

Final Discriminant

To extract signal from background the angular distance between the two lepton system and photon, $\Delta R_{\ell\ell\gamma}$, is fit. Already discussed in Section 7.1.3, there is a peak in the signal VBF process at lower $\Delta R_{\ell\ell\gamma}$ values and an extended tail for ggF shape compared to that of the background. Figure 7.13 shows various signal, background and sideband data comparisons in the SB and SR regions. Figure 7.13c in particular demonstrates the difference in distribution shape between the signal samples and background. Other variables were examined to test whether there are better discriminants, including using multivariate techniques but were found to not improve the signal extraction.

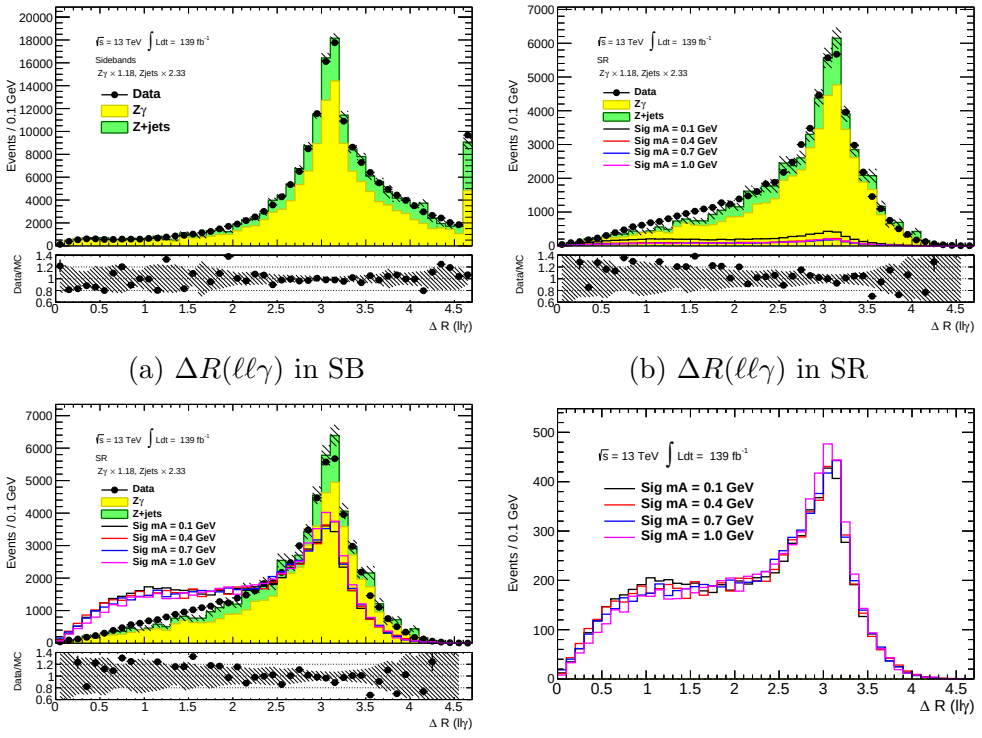

(a) $\Delta R(\ell\ell\gamma)$ in SB

(b) $\Delta R(\ell\ell\gamma)$ in SR

(c) $\Delta R(\ell\ell\gamma)$ in SR, shape comparison

(d) $\Delta R(\ell\ell\gamma)$ in SB, signal samples only

Figure 7.13: $\Delta R(\ell\ell\gamma)$ plots for data, signal, background for different regions. Plot (c) and (d) normalises all histograms to the same number of events to better see the distribution shape. The background normalisation factors, signal branching ratio and uncertainty bands follow the same convention as Figure 7.1 and all shape corrections are applied.

7.2.1 Fit Strategy

A simultaneous likelihood fit is applied to obtain the normalisation of the backgrounds from the SB, using E_{ratio} as described, and to extract the signal interpretation from the SR using variable $\Delta R_{\ell\ell\gamma}$. The normalisation in the SB and SR regions is treated as a random variable with a Poisson distribution function that has an expectation value given by the nominal MC prediction of each background corrected by global normalisation factors κ^{Zjets} and $\kappa^{Z\gamma}$. The values of κ^{Zjets} and $\kappa^{Z\gamma}$ are the normalisation of $Z+\text{jets}$ and $Z\gamma$ respectively and are free parameters in the fit. By doing this, the information from the background enriched SB is used to determine the normalisation of the background events in the SR.

Minimising the log-likelihood ratio method is done on each bin were the likelihood function is defined as

$$\begin{aligned}\mathcal{L}(\mu,\kappa,\theta) = \text{Possion}(N_{SR}^{obs} \mid \mu N_{SR}^{sig}(\theta) \ + \ N_{SR}^{bkg}(\kappa,\theta)) f_{constr}(\theta) \\ \cdot \text{Possion}(N_{SB}^{obs} \mid \mu N_{SB}^{sig}(\theta) \ + \ N_{SB}^{bkg}(\kappa,\theta)) f'_{constr}(\theta),\end{aligned} \tag{7.2.1}$$

where

$$N_i^{bkg} = \kappa^{Zjets} N_i^{Zjets} + \kappa^{Z\gamma} N_i^{Z\gamma}. \tag{7.2.2}$$

Free parameter μ is the signal strength and fits the signal in the background. Parameter θ allows for fluctuations with respect to the nominal prediction of the yield in each process, such as the systematic uncertainty values. This is omitted when showing its dependence on N_i^X, with X being the process, to simplify the notation. The term f_{constr} represents the product of a Gaussian distribution with each nuisance parameter with σ of the Gaussian being determined by the up and down variation of the systematic uncertainties, which are described in the next section.

7.2.2 Systematic Uncertainties

As described in the resolved category discussion, Section 6.7, uncertainties from both experimental and theoretical sources affect simulation of the background and signal. Six dominant sources of experimental systematic uncertainty were included in the final fit. The sources are the same those chosen for the resolved category and are summarised in Table 6.3 in Section 6.7. For $Z\gamma$ and $Z+\text{jets}$, the normalisation uncertainty and also the uncertainties of each correction described in Section 7.1.5

Source	1σ Uncertainty total background
Total statistical	0.40 %
Total background systematic	0.47 %
Pileup reweight	1.10 %
Electron identification	1.04 %
Photon isolation	1.02 %
Muon trigger	0.85 %
Muon reconstruction	0.85 %
Muon isolation	0.85 %
Z+γ - $\Delta R(l,\gamma)$ correction	0.82 %
Z+jets - $\Delta R(l,\gamma)$ correction	0.81 %
Z+γ - p_T^{ll} correction	0.38 %
Z+jets normalisation	0.24 %
Z+γ - $p_T^{ll,\gamma}$ correction	0.21 %
Z+γ normalisation	0.19 %
Z+jets - $p_T^{ll,\gamma}$ correction	0.17 %
Z+jets - p_T^{ll} correction	0.15 %
Z+jets - p_T^{γ} correction	0.14 %

Table 7.4: The impact from each source of systematic uncertainty to the background only fit. The percentages show the size of the 1σ uncertainty relative to each parameter. There is some correlation between individual uncertainties and as such summing in quadrature will not equal the total uncertainty.

are also included. The contributions from each source were implemented as nuisance parameters in the likehood function, Eq. 7.2.1. Their contribution to the background only fit was performed by fixing the parameters of each source to the best-fit value and repeating the fit with the other parameters floating. Table 7.4 summarises the impact of each systematic source on the selection results. The impact was obtained by the quadratic difference between the initial fit with the parameter fixed model.

For signal, systematic variations due to uncertainties in theory, also described in resolved category analysis Section 6.7, were also taken into account. The effect due to these theoretical uncertainties on the signal ggF and VBF processes were:

- PDF+α_s :< 4 % ggF, < 3 % VBF
- Scale: < 10 % ggF, < 2 % VBF

Plots showing the effect of the scale uncertainties on the shape of the final discriminant are shown in Appendix F.

7.2.3 Post-fit Distributions

The signal region and control region plots for variables E_{ratio} and $\Delta R_{\ell\ell\gamma}$ before and after the fit, following the procedures detailed in Section 7.1.4 to Section 7.2.2 are shown in Figure 7.14. A discussion of the results is given in Section 8.

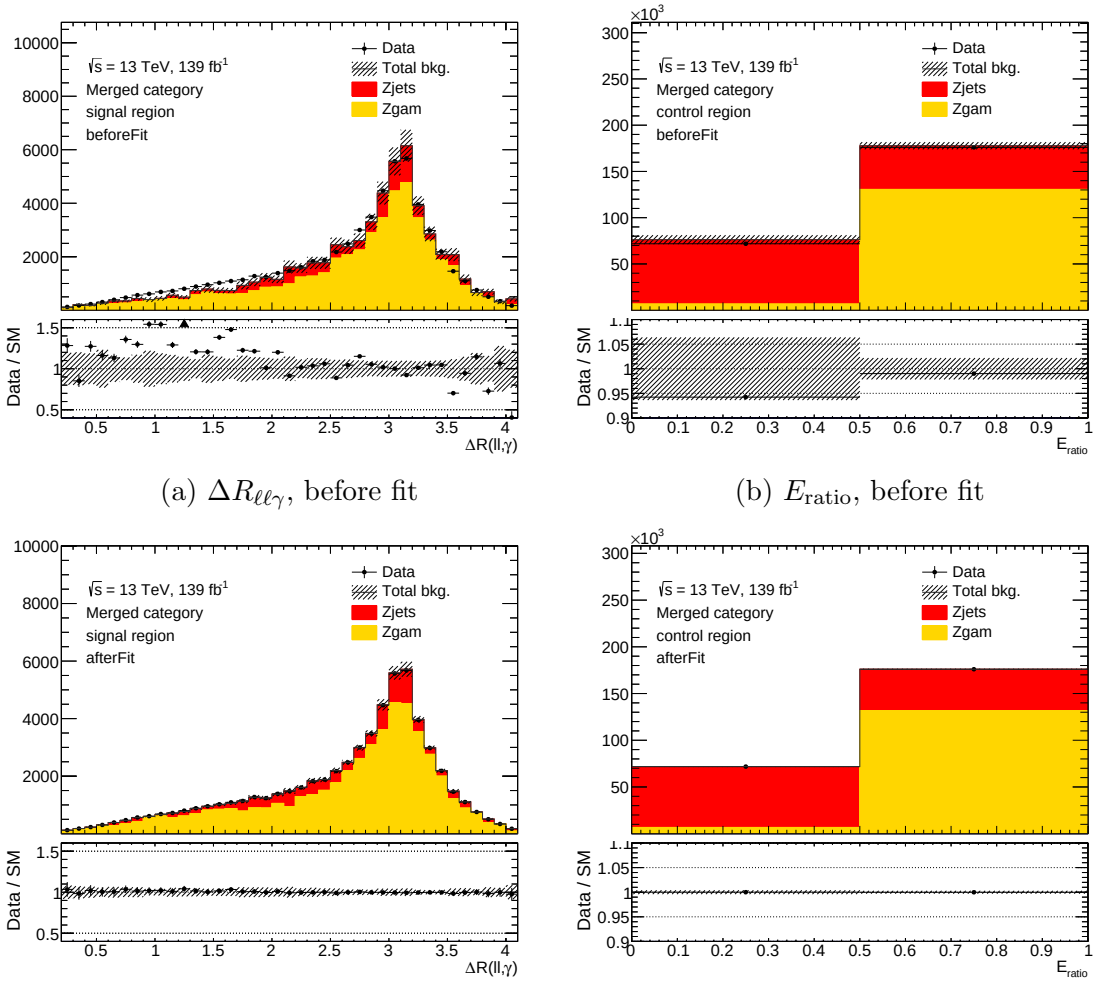

(a) $\Delta R_{\ell\ell\gamma}$, before fit

(b) E_{ratio}, before fit

(c) $\Delta R_{\ell\ell\gamma}$, after fit

(d) E_{ratio}, after fit

Figure 7.14: Final discriminant $\Delta R_{\ell\ell\gamma}$ in the signal region and E_{ratio} in the control region before (top) and after (bottom) the simultaneous likelihood fit is applied.

Chapter 8

Final Result, Interpretation and Conclusion

Final Result, Interpretation and Conclusion

This chapter shows the final results of both event selections and discusses the implications of these results. Expected and observed upper limits on $h \to Za$ branching ratios at 95 % confidence level are compared. The interpretation is also shown as a function of ALP mass and $a \to \gamma\gamma$ photon coupling for prompt axion decays. A conclusion is given which summarises this and the thesis in its entirety.

8.1 Final result

The statistical analysis of the data for both search categories uses binned maximum-likelihood fits of their respective final discriminate variables. The reconstructed mass of the two photon system is fit for the resolved category, as described in Section 6, whereas $\Delta R_{\ell\ell\gamma}$ is fit for the merged, Section 7. In particular for the merged category, $\Delta R_{\ell\ell\gamma}$ is fit also with the sideband E_{ratio} distribution. This was done so that the background normalisation is determined by the data. This corresponds to overall post-fit normalisation scale factors of 1.15 ± 0.03 for $Z\gamma$ and 2.30 ± 0.05 for Z+jets. The systematic uncertainties stated at the end of the selection chapters are accounted for in the fit by being included as nuisance parameters that are parameterised with Gaussian probability density functions that multiply the fit likelihood. The merged category also includes the shape errors due to the $Z\gamma$ and Z+jets corrections as

additional systematic uncertainties.

The expected and observed upper limits at the 95 % confidence level on the $h \to Za$ branching ratio where the axion decays into a pair of photons are compiled as a function of m_a using a modified frequentist approach known as the CL_S method [141]. The merged category has an abundance of events and as such the asymptotic approximation [142] was computed for the exclusion limits of this selection.

The upper limits between the two analysis channels are presented in Figure 8.1. The value of m_a that separates the two categories is at 2 GeV. It is concluded that no significant excess was observed in this search. The branching ratio $\mathrm{BR}(h \to Za) \times \mathrm{BR}(a \to \gamma\gamma)$ range of 0.1 % and 4.0 % is excluded depending on the mass of the ALP, with mass points within the resolved category window achieving the lower values of this range. The merged category shows a peak in the limit which is due to the size of the photon isolation cone (explained in more detail in Section E.4).

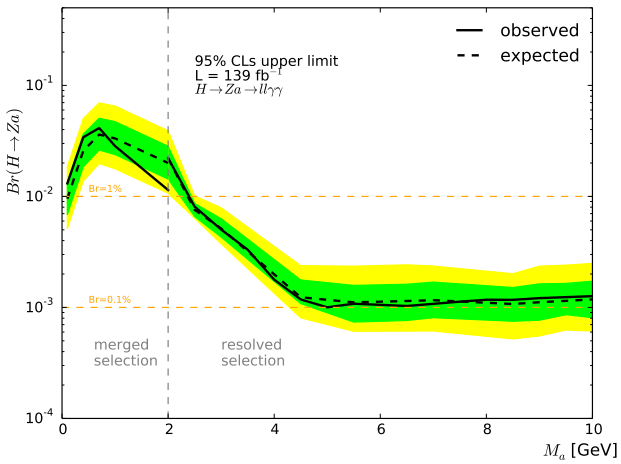

Figure 8.1: The 95 % confidence level upper limits on the branching ratio for the process $h \to Za$ branching ratio where the axion decays into a pair of photons with $\mathrm{BR}(a \to \gamma\gamma) = 100\,\%$. Values below $m_a = 2\,\mathrm{GeV}$ were obtained by the merged category selection with values over this threshold were obtained by the resolved category.

8.2 Interpretation

The observed and expected upper limits on the branching ratio shown in Figure 8.1 are interpreted as a function of ALP mass and $a \to \gamma\gamma$ photon coupling values for prompt ALP decays. ALP decays for given m_a and $C_{\gamma\gamma}$ value pairs were considered prompt if at least 95 % of the ALPs decayed before the pixel layer of the tracking system (corresponding to a displacement, L_{xy}, of 50 mm). Upper limits excluded for various C_{Zh} values for axions decaying within this region are shown on Figure 8.2. The four values of C_{Zh} shown in the plot are 0.4 TeV^{-1}, 0.25 TeV^{-1}, 0.1 TeV^{-1} and 0.07 TeV^{-1} with each corresponding to different branching ratios following the relation shown in Equation 1.2.4. This plot shows a number of features such as lower $C_{\gamma\gamma}$ values associate with more prompt decays. Prompt decays as we have defined them stretch to approximately 10^{-2} TeV^{-1} for the largest shown m_a at 9 GeV. The area shown covers space uncovered by past experiment results. Larger C_{Zh}/Λ values correspond to larger cross-sections. C_{Zh}/Λ at 0.4 TeV^{-1} constrains the entirety of the region whereas the smallest coupling value tested at 0.07 TeV^{-1} only constrains on resolved category focused axion mass points greater than 3 GeV. The C_{Zh}/Λ values at 0.1 and 0.25 were chosen to show the effect caused by the merged category upper limits peak at approximately $m_a = 1$ GeV shown in Figure 8.1. The space covered by the observed and expected limits are comparable to one another, with the only difference being the size of the area covered by the largest C_{Zh}/Λ value due to how each behave close to said peak.

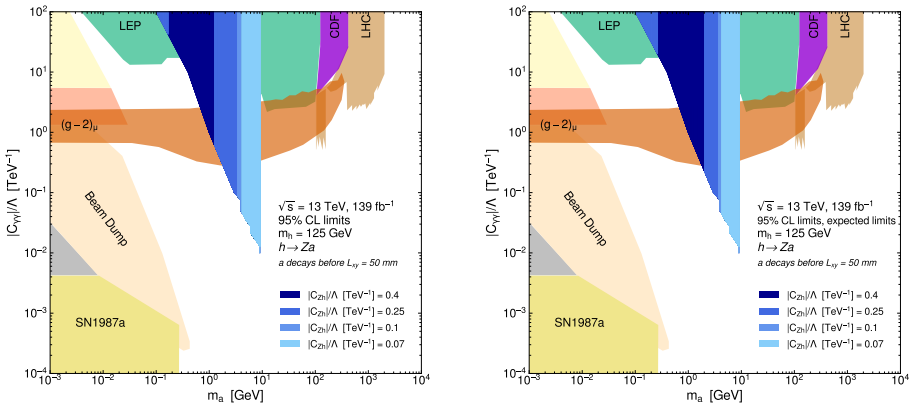

(a) Observed limit (b) Expected limit

Figure 8.2: The observed and expected $h \to Za$ upper limits interpreted onto the m_a and photon coupling parameter space.

8.3 Conclusion

Although axion searches at the LHC are nothing new, theoretical research has shown that Run-II data collected at the LHC could potentially probe unexplored parameter space. The analysis in this thesis looks at data recorded by the ATLAS experiment for proton-proton collisions with center of mass energy at 13 TeV and an integrated luminosity of $139\,\mathrm{fb}^{-1}$ to search for rare axion-like particle, a, in association with a Standard Model Higgs boson, h, with mass at 125 GeV, and a Z boson. The Z boson is considered to decay leptonically into either a pair of muons or electrons and the a particle into a pair of photons. Two selection categories were analysed according to how close the photon pair decay relative to one another. The resolved category selects events were both photons could separately be reconstructed whereas the merged category selects those for which the photons are close enough that they are reconstructed only as one. The background estimation of the resolved category was performed with an analytical template method of the reconstructed mass of the diphoton system using data in the control region. A double-sided crystal ball function was chosen to model the a particle mass between 2 GeV and 10 GeV. For the merged category, the background was estimated using a Monte Carlo template with corrections derived using data in the control region. The angular distance between the dilepton and the photon was fit as the final discriminant. Both experimental and theoretical systematic uncertainties were included in the final fit. No significant discrepancies are observed and the data is in agreement with Standard Model predictions. Upper limits on the branching ratio $\mathrm{BR}(h \to Za) \times \mathrm{BR}(a \to \gamma\gamma)$ at 95 % confidence level were found to range from 0.1 % to 4 % depending on the mass value of the a particle.

With the number of strip and pixel hybrids being produced in the thousands for the HL-LHC upgrade, this thesis also explores whether a software based tool for the semi-automation of the visual part of the hybrid quality control process was possible. It is shown that such a software can be made, with the results shown on a user interface, however only performs best if certain parameters (e.g scan quality) are specific to the method. Work is undergoing to improve the generalisability, such as using neural networks to classify the features of the hybrid, although the software as it stands provides a framework for future work.

Appendix A

Di-photon pair as a jet

A.1 Di-photon pair as a jet

Figure A.1 shows anti-kt jets with radius parameter 0.4 for a single signal event and gives an example when the truth-level di-photon pair is matched to a jet. Table A.1 shows the fraction of events with jets that are matched to the truth-level di-photon pair from the $a \to \gamma\gamma$ decay for various p_T constraints and JVT score conditions on the jets. The table shows that for the recommended JVT score set at > 0.59, introduced in Section 4.1.3, reduces the number of events post pre-selection that have jets containing the di-photon pair. For a jet p_T threshold of 20 GeV passing pre-selection and the JVT score condition, only 30 % of events had jets linked to the di-photon pair as opposed to approximately 85 % for events without the JVT score constraint applied.

all events (xAOD generated)	12901	-
pass preselection	11345	-
$a \to \gamma\gamma$ matched to a jet		
jet $p_T > 20$ GeV	3331	29.36% ± 0.43%
jet $p_T > 20$ GeV and without JVT cut	9555	84.22% ± 0.34%
jet $p_T > 10$ GeV and without JVT cut	9921	87.45% ± 0.31%

Table A.1: Efficiencies for matching the a particle di-photon pair to a jet with binomial errors for events passing pre-selection, for signal mass $m_a = 1$ GeV. Note: Results in this table are from a version/selection much earlier than version finally used, but the conclusions remain unchanged.

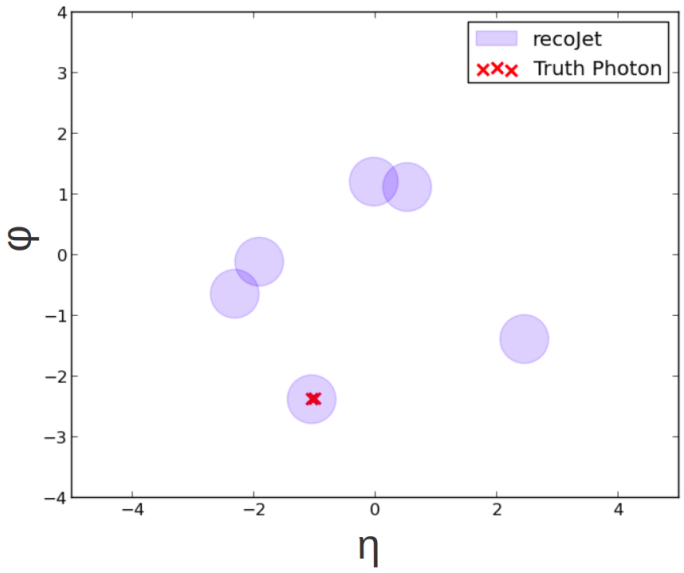

Figure A.1: Example of an event when the truth-level di-photon pair is matched with an anti-kt jet. Shaded blue dots represent a reconstructed jet with radius parameter 0.4 and red crosses represent a truth-level photon from the di-photon pair in the $\eta - \phi$ coordinate space.

Appendix B

Z boson mass window optimisation

The di-lepton mass cut chosen at 81 GeV to 101 GeV was chosen after an optimisation study, briefly detailed here. This optimisation study is as follows. Figure B.1 shows the significance curves, $\sigma = \frac{s}{\sqrt{b}}$, as a function of chosen mass window for each of the signal samples. Figure B.2 shows the ROC curve for the same windows. The signal efficiency is $\frac{s_i}{s}$ for particular mass window i and signal events s. The background rejection is $1 - (\frac{b_i}{b})$ for background events b. Taking into account both the significance and ROC curves it was decided to choose an $m_{\ell\ell}$ interval between 81 GeV and 101 GeV.

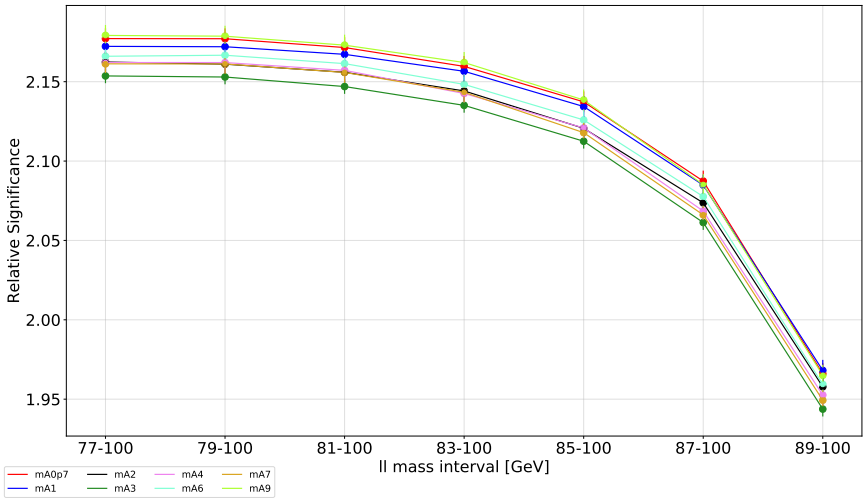

(a) Relative significance

Figure B.1: The relative significance for each signal samples for various chosen $\ell\ell$ windows around the Z boson peak.

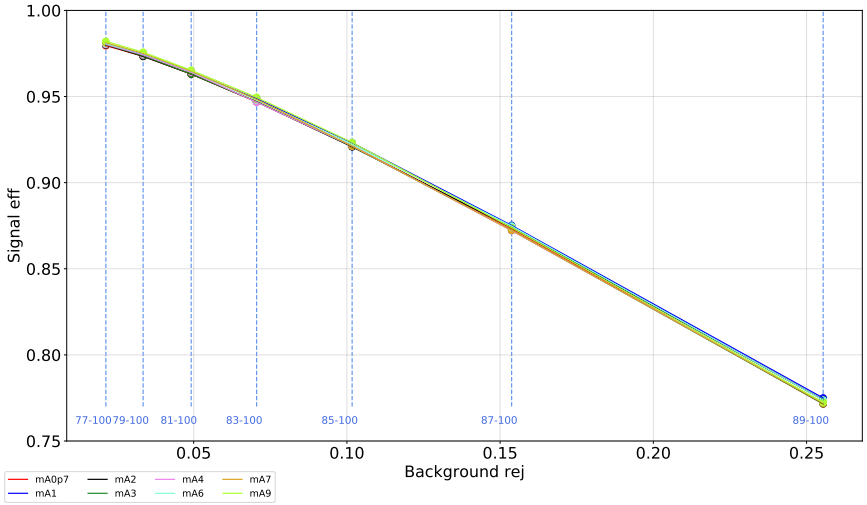

(a) ROC

Figure B.2: The ROC curve for the signal points for the same set of windows as Figure B.1.

Appendix C

Signal properties additional plots

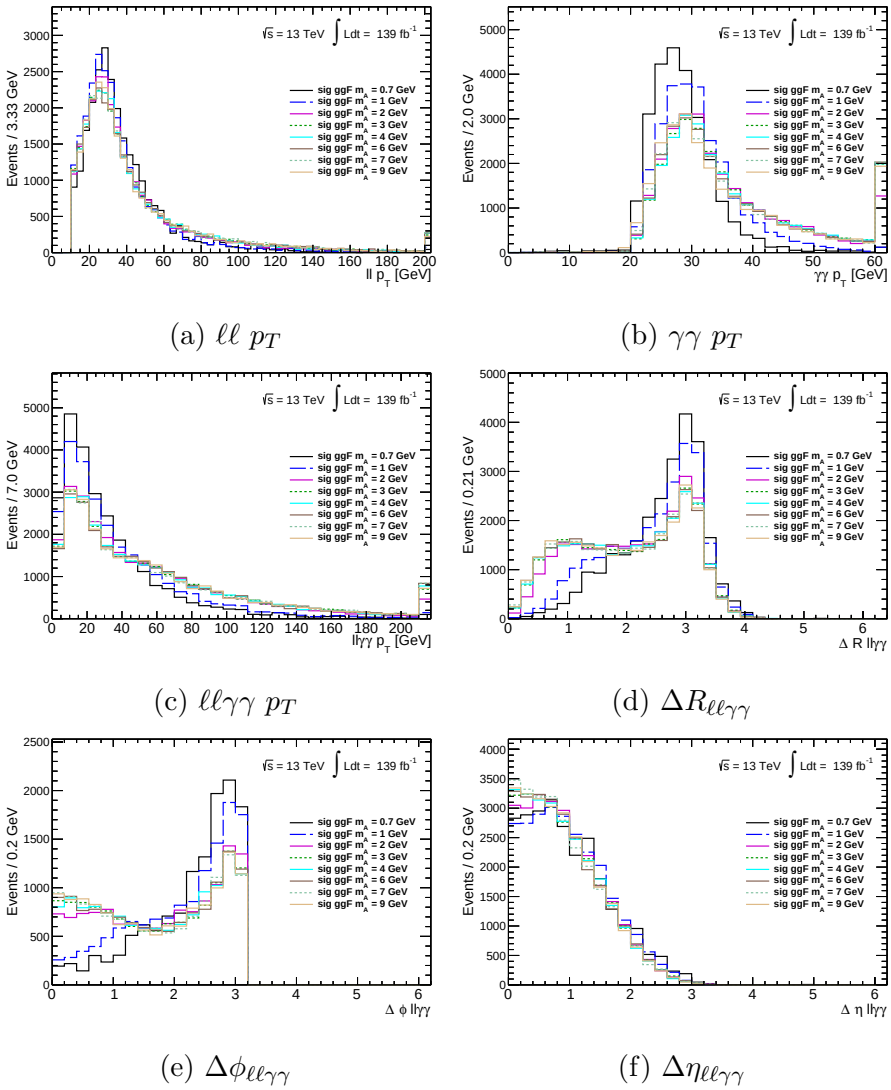

(a) $\ell\ell$ p_T (b) $\gamma\gamma$ p_T

(c) $\ell\ell\gamma\gamma$ p_T (d) $\Delta R_{\ell\ell\gamma\gamma}$

(e) $\Delta\phi_{\ell\ell\gamma\gamma}$ (f) $\Delta\eta_{\ell\ell\gamma\gamma}$

Figure C.1: Various kinematic distributions for different signal sample events passing the pre-selection criteria, for Higgs boson production mechanism ggF only. Histograms normalised to the same integral for shape comparison. Reconstructed photon objects are matched to truth-level photons.

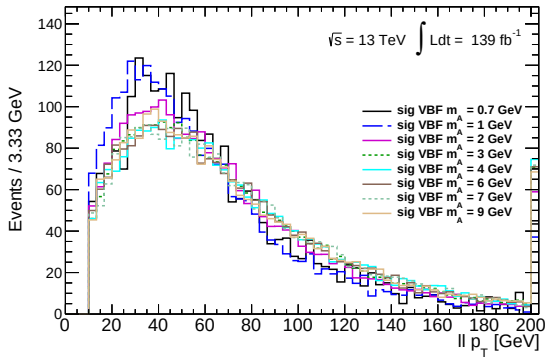

(a) $\ell\ell$ p_T

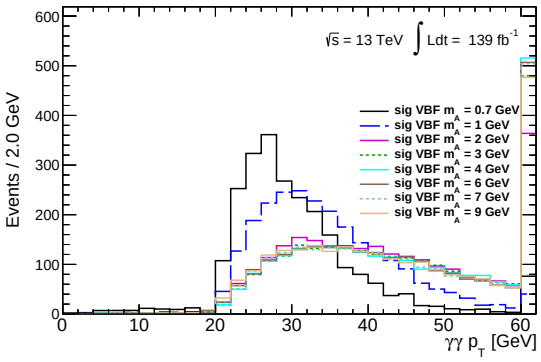

(b) $\gamma\gamma$ p_T

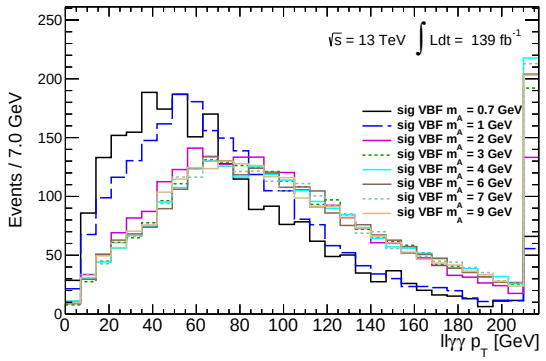

(c) $\ell\ell\gamma\gamma$ p_T

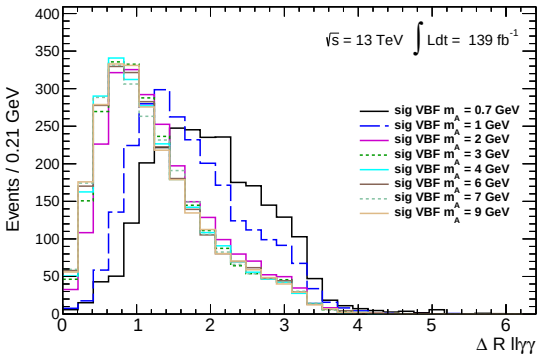

(d) $\Delta R_{\ell\ell\gamma\gamma}$

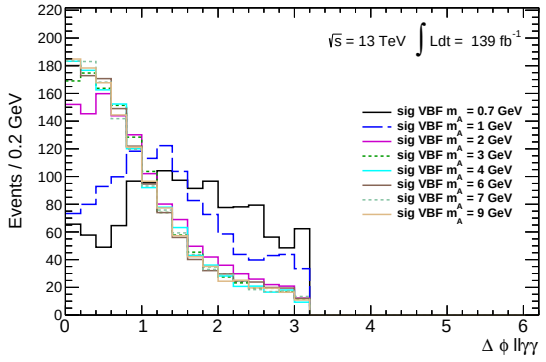

(e) $\Delta\phi_{\ell\ell\gamma\gamma}$

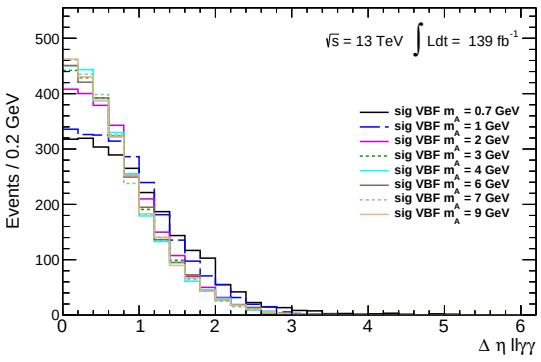

(f) $\Delta\eta_{\ell\ell\gamma\gamma}$

Figure C.2: Various kinematic distributions for different signal sample events passing the pre-selection criteria, for Higgs boson production mechanism VBF only. Histograms normalised to the same integral for shape comparison. Reconstructed photon objects are matched to truth-level photons.

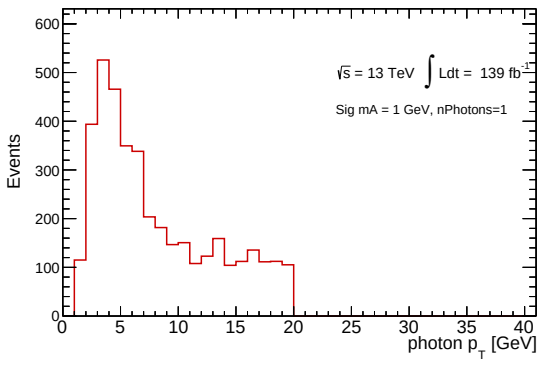

(a) $m_A = 1.0\,\text{GeV}$, nPhoton $= 1$

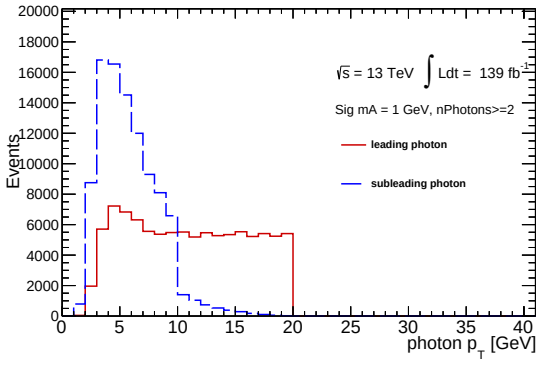

(b) $m_A = 1.0\,\text{GeV}$, nPhoton ≥ 2

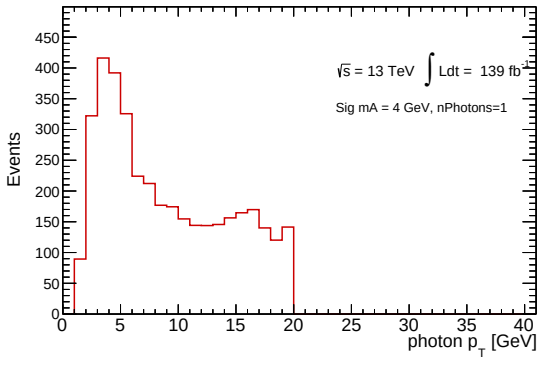

(c) $m_A = 4.0\,\text{GeV}$, nPhoton $= 1$

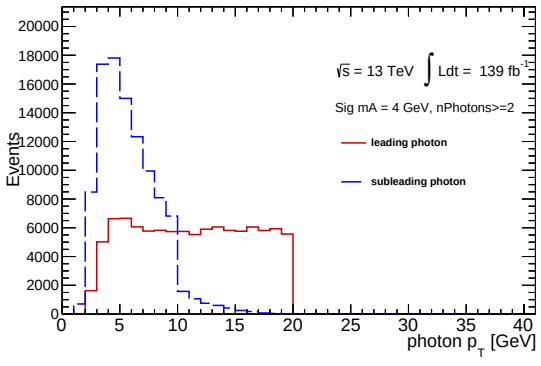

(d) $m_A = 4.0\,\text{GeV}$, nPhoton ≥ 2

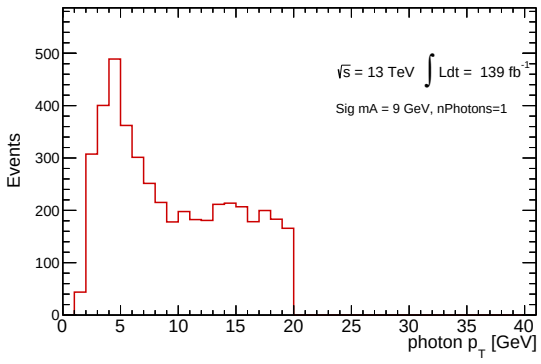

(e) $m_A = 9.0\,\text{GeV}$, nPhoton $= 1$

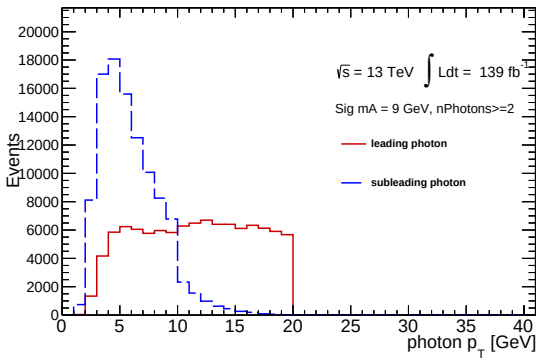

(f) $m_A = 9.0\,\text{GeV}$, nPhoton ≥ 2

Figure C.3: Reconstructed photon p_T distributions for signal mass points 1.0 GeV, 4.0 GeV and 9.0 GeV events passing pre-selection but failing both category selections. Left-side plots show the photon p_T for events where there is only one reconstructed photon present and the right-side plots shows the leading and sub-leading photon p_T for events where there are two or more reconstructed photons.

Appendix D

Resolved category appendix

D.1 Higgs Boson mass window optimisation

This section details the short optimisation study regarding choosing the signal and sideband regions for the resolved category. For each signal MC sample the significance and ROC curves were computed for a range of different windows. The window which had the better results in terms of signal relative to background was chosen.

Four different Higgs boson mass $m_{\ell\ell\gamma\gamma}$ windows were evaluated for signal region optimisation, these were 100-140 GeV, 114-136 GeV, 118-132 GeV and 122-128 GeV. The significance and ROC curves for each signal MC mass points > 3 GeV were compared, shown in Figure D.1. Significance was calculated by $\frac{S}{\sqrt{S+B}}$ where S is MC signal events and B is MC total background events for a particular Higgs boson mass window. Note in this category MC background events are limited. The three loosest cuts had comparable significance and high signal efficiencies. Because a tighter signal window made little improvement it was decided to use the signal region $m_{\ell\ell\gamma\gamma}$ at 110 GeV to 140 GeV.

D.2 Loose vs Tight Identification

Table D.1 shows the comparison between Loose and Tight identification efficiencies.

Sample	ID efficiency	
	Loose ID	**Tight ID**
sig 2.0 GeV	36.2 ±0.6	16.5 ±0.4
sig 2.5 GeV	51.2 ±0.7	27.4 ±0.5
sig 3.0 GeV	60.8 ±0.6	35.4 ±0.4
sig 4.0 GeV	78.5 ±1.7	50.6 ±1.3
sig 5.0 GeV	72.0 ±1.1	44.2 ±0.8
sig 6.0 GeV	80 ±1.3	51.1 ±1.0
sig 7.0 GeV	81.4 ±1.3	52.8 ±1.0
sig 9.0 GeV	82.6 ±1.4	52.7 ±1.0
$Z\gamma$	15.6 ±2.3	2.7 ±0.8
Z + jets	3.8 ±0.3	0.1 ±0.1
Total Background	4.2 ±0.3	0.2 ±0.1

Table D.1: Table comparing the efficiencies of Loose and Tight photon identification on the relevant samples for the resolved category relative to no identification being set. Photon isolation criteria described in Section 6.2 has been applied. Error values are statistical due to the number of MC events.

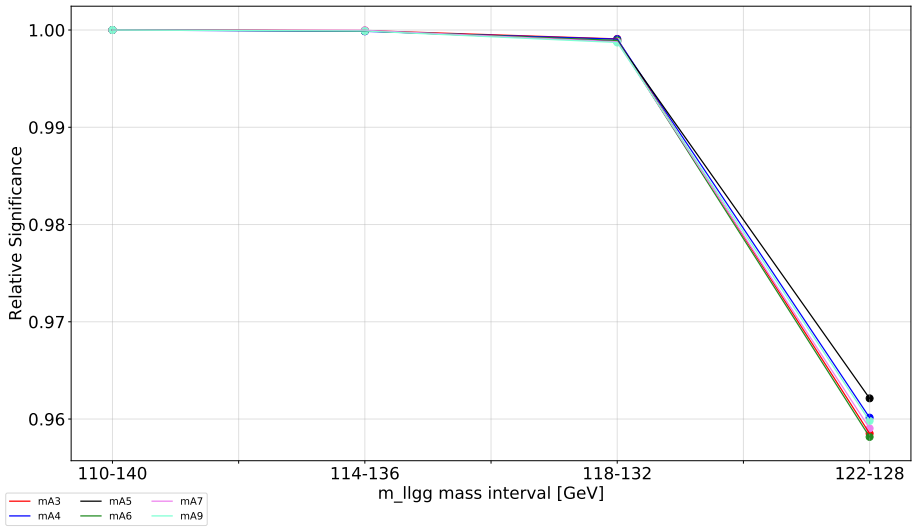

(a) Significance

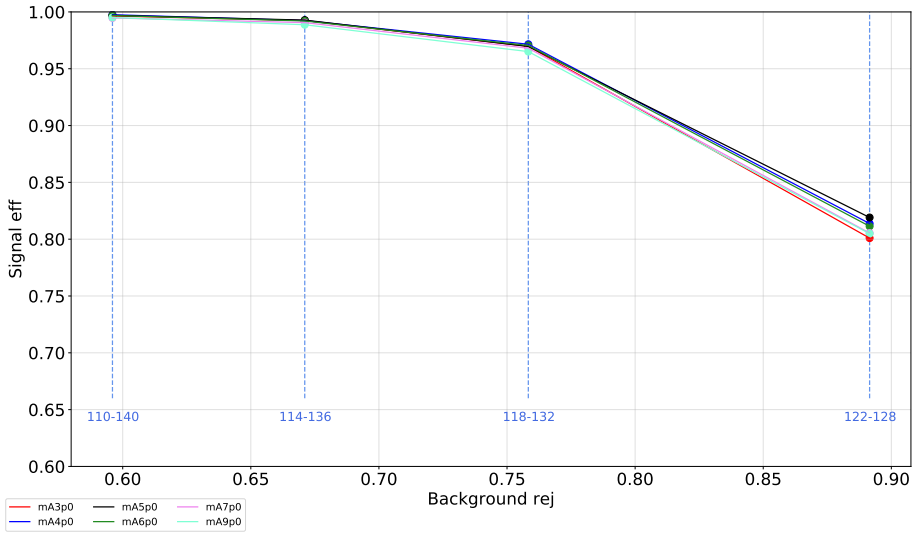

(b) ROC

Figure D.1: Resolved category significance and ROC curve comparing signal region mass windows; 100-140 GeV, 114-136 GeV, 118-132 GeV and 122-128 GeV. Top plot is relative significance and bottom plot is ROC curve.

D.3 Signal Parameterisation DSCB plots

Figure D.2 shows the reconstructed signal $m_{\gamma\gamma}$ distributions for $m_a \geq 2\,\text{GeV}$ compared to the DSCB fit (red line) and also the DSCB using the interpolated parameters given in Table 6.2 of Section 6.4. The plots show good agreement between the in-

terpolated DSCB function with monte carlo samples for the mass points of this range.

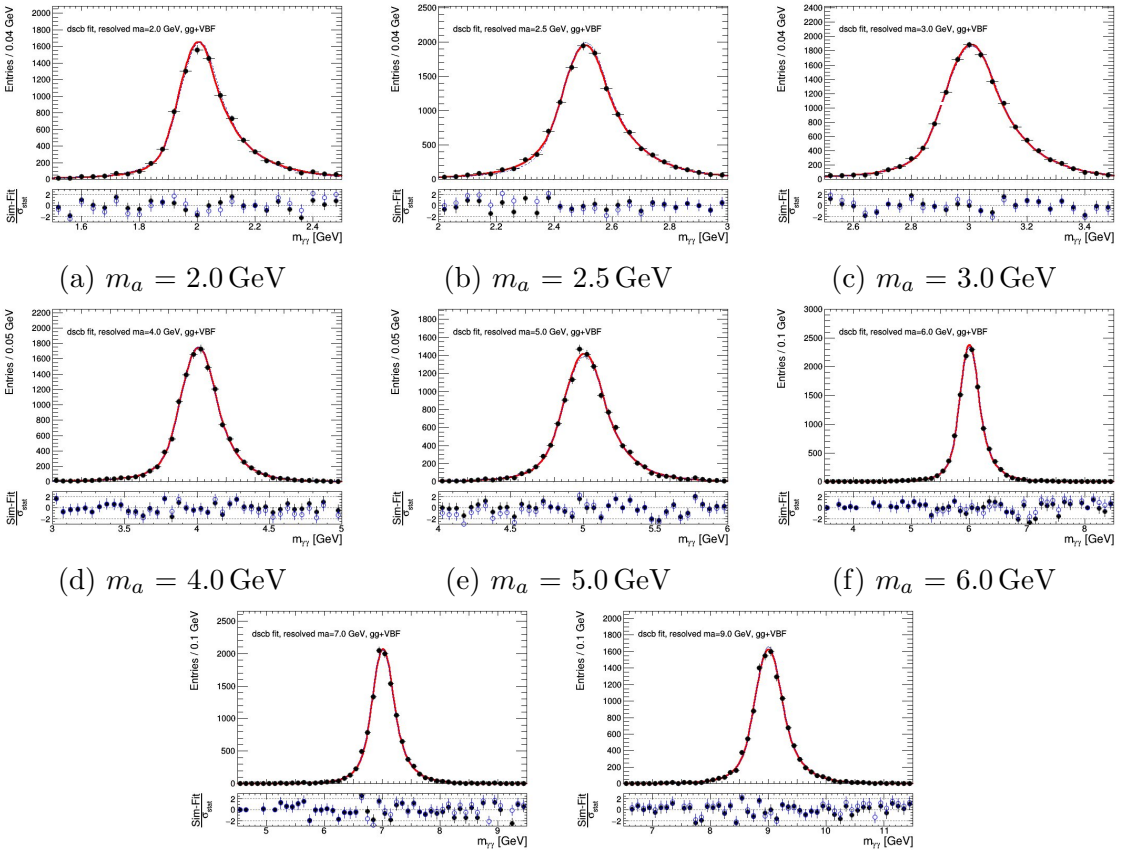

(a) $m_a = 2.0\,\text{GeV}$ (b) $m_a = 2.5\,\text{GeV}$ (c) $m_a = 3.0\,\text{GeV}$

(d) $m_a = 4.0\,\text{GeV}$ (e) $m_a = 5.0\,\text{GeV}$ (f) $m_a = 6.0\,\text{GeV}$

(g) $m_a = 7.0\,\text{GeV}$ (h) $m_a = 9.0\,\text{GeV}$

Figure D.2: Resolved category reconstructed signal $m_{\gamma\gamma}$ distributions for $m_a \geq 2\,\text{GeV}$ fitted with the DSCB function. The black points are simulation for each signal mass point, the red line is the DSCB fit for that particular mass point and the blue-dashed line is the DSCB using the fitted parameters.

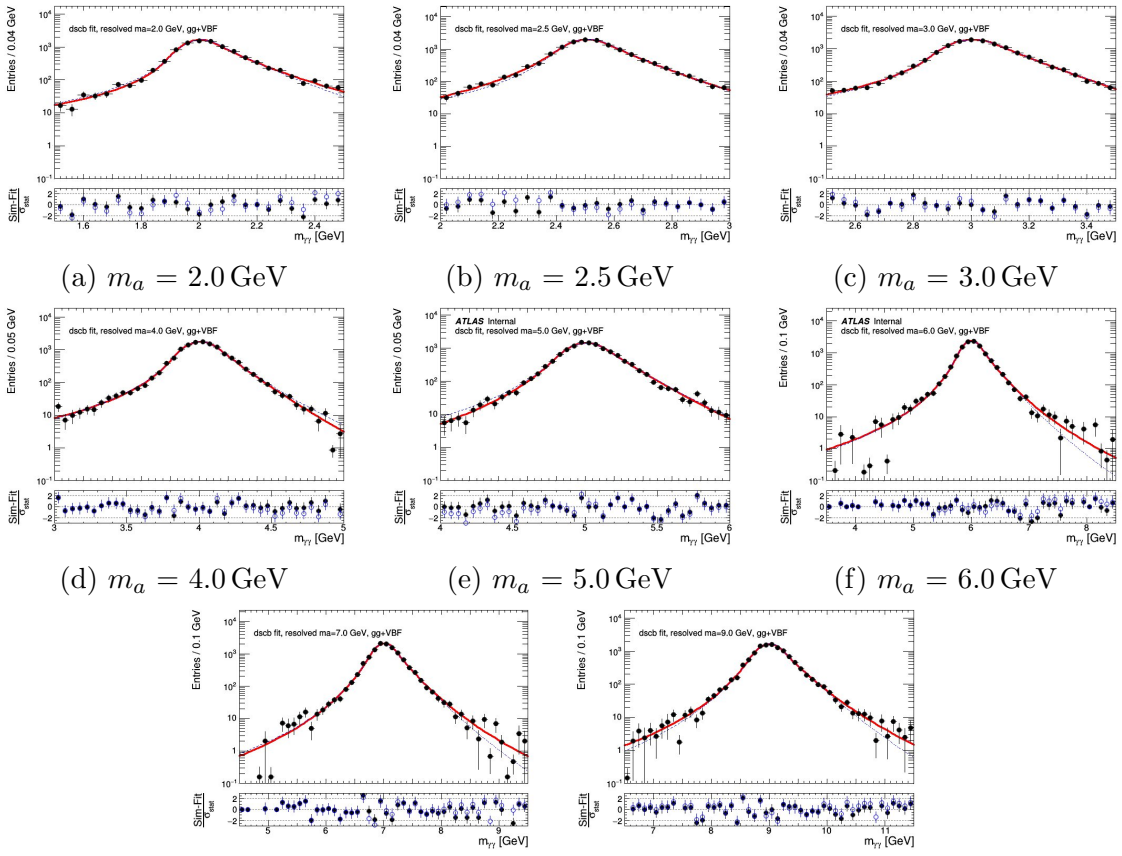

(a) $m_a = 2.0\,\text{GeV}$ (b) $m_a = 2.5\,\text{GeV}$ (c) $m_a = 3.0\,\text{GeV}$

(d) $m_a = 4.0\,\text{GeV}$ (e) $m_a = 5.0\,\text{GeV}$ (f) $m_a = 6.0\,\text{GeV}$

(g) $m_a = 7.0\,\text{GeV}$ (h) $m_a = 9.0\,\text{GeV}$

Figure D.3: Same figure description as Figure D.2 but log-scale to better compare the fit and interpolated DSCB function.

Appendix E

Merged category appendix

E.1 Higgs Boson mass window optimisation

For each of the signal samples in the merged category the significance and ROC curves were tested against different Higgs boson mass window ranges. The window which shows better results was chosen as the signal region.

Five different $m_{\ell\ell\gamma}$ windows were evaluated. These were 107-133 GeV, 110-130 GeV, 116-124 GeV, 119-121 GeV. The significance and ROC curves for MC signal samples with mass between 0.1 GeV and 2.5 GeV are compared in Figure E.1. The window that shows a relatively high significance and ROC output, and chosen to be the signal region, was 110-130 GeV. Note also the resolved category mass window 110-140 GeV was also tested but performed less well compared to the chosen window.

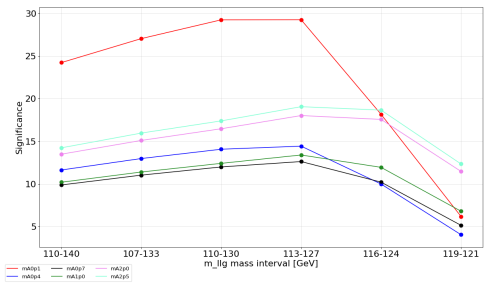

(a) Signal significance

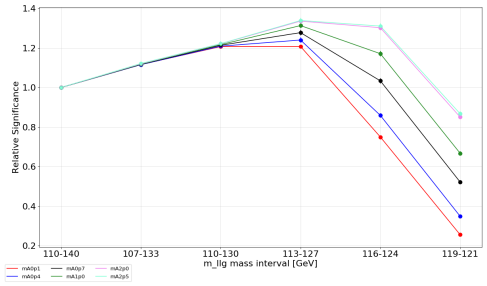

(b) Relative signal significance

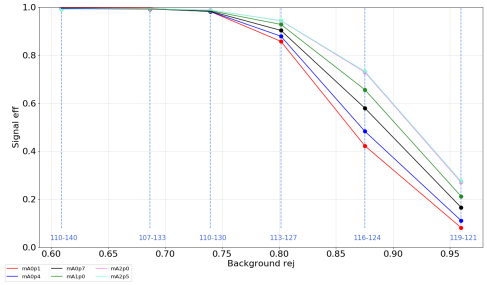

(c) ROC

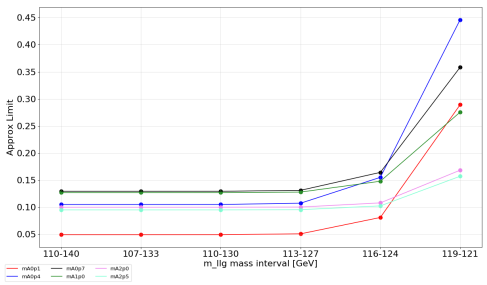

(d) Approximate limit

Figure E.1: Plots used for the optimisation study of the merged category Higgs boson mass window, $m_{\ell\ell\gamma}$. Figure (a) and (b) show the significance and relative significance of the relevant mass points as a function of different $m_{\ell\ell\gamma}$ windows. Figure (c) shows the ROC curve and (d) the approximate calculated limit using the significance.

E.2 Loose vs Tight Identification

Table E.1 shows the comparison between Loose and Tight identification efficiencies.

Sample	ID efficiency (%)	
	Loose ID	Tight ID
sig 0.1 GeV	95.2 ± 0.7	60.5 ± 0.5
sig 0.4 GeV	86.0 ± 0.8	54.4 ± 0.6
sig 0.7 GeV	69.2 ± 0.7	46.6 ± 0.5
sig 1.0 GeV	69.3 ± 0.7	52.9 ± 0.6
Zγ	94.2 ± 1.3	84.1 ± 1.2
Zjets	44.5 ± 1.6	23.6 ± 1.1
Total Background	70.4 ± 1.1	55.1 ± 0.6

Table E.1: Table comparing the efficiencies of Loose and Tight photon identification on the relevant samples for the merged category relative to no identification being set. Photon isolation criteria described in Section 7.1.2 has been applied. Error values are statistical due to the number of MC events.

E.3 Photon p_T correction plots

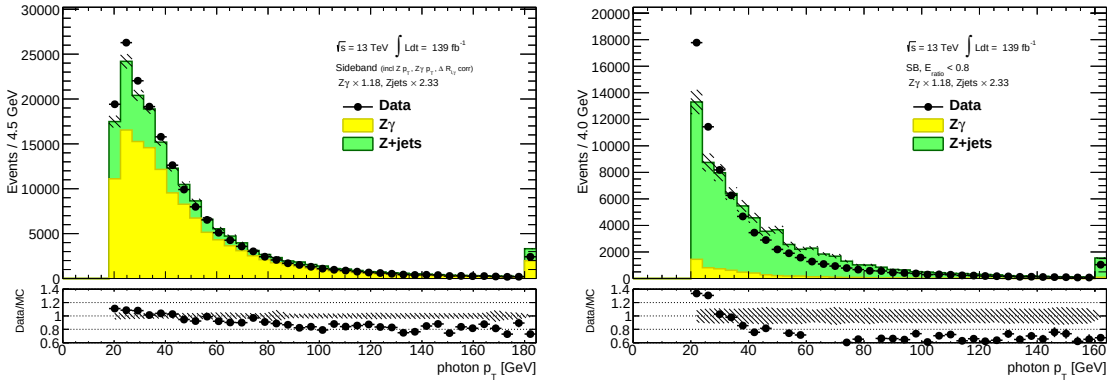

(a) photon p_T SB, corrections applied

(b) photon p_T SB, $E_{\text{ratio}} < 0.8$, corrections applied

Figure E.2: Photon p_T distributions for (a) sideband and (b) sideband in the Z+jets dominated region (i.e $E_{ratio} < 0.8$ region) after the $\ell\ell$ p_T , $\ell\ell\gamma$ p_T and $\Delta R(\ell\gamma)$ corrections are applied. The background $Z\gamma$ and Z + jets processes are scaled by 1.18 and 2.33 respectively. Uncertainty bands shown are MC statistical errors.

E.4 Photon Isolation on Signal

Figure E.3 shows the merged category signal region for various signal samples with no isolation or photon identification cuts applied. The plots show that the topocone20

cut in FCLoose isolation criteria would affect m_a 2 GeV more so than other low mass points. Figure E.3a shows proxy for ΔR between 2 photons from the axion for merged signal events. Based on size of the cone, either 0.4 or 0.2, Figure E.3a can be used to explain that the effect of the topocone variable varies based on whether signal generally sits within the chosen cone or not. For isolation cone 0.1-0.2 it should show topocone distributions for m_a at 1 GeV, 4 GeV and 6 GeV to be similar. For an isolation cone at 0.1-0.4 it should instead show distributions of 1 GeV and 6 GeV being similar with 2 GeV and 4 GeV similar also. Plots Figure E.3b and Figure E.3c show that this is indeed what is observed. It is the size of the cone that affects the efficiency for merged category events in which the isolation cone splits the two photons. It is for this reason there is a peak at approximately 1 GeV in the results shown in Figure 8.1.

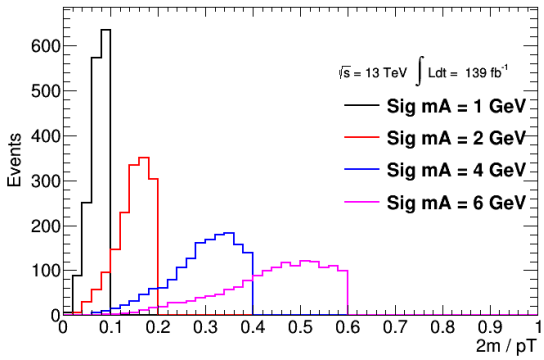

(a) $2m_a$ / photon p_T

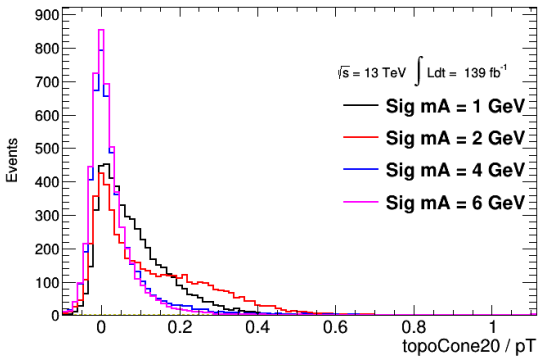

(b) topoCone20 / photon p_T

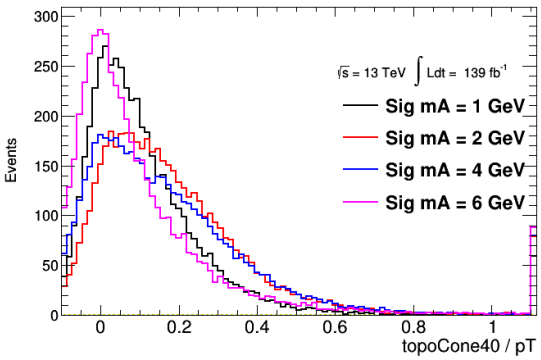

(c) topoCone40 / photon p_T

Figure E.3: Isolation plots for different signals passing the merged category signal region. Top plot, (a), is approximate cone using the sample m_a value and photon p_T . Bottom two plots are calorimeter-based isolation variables topoCone20 and topoCone40 where the numbers on variable name represent the size of the cone, i.e $\Delta R = 0.2$ for topocone20 and $\Delta R = 0.4$ for topocone40. No isolation or photon identification cuts are applied for these plots. Branching Ratio $BR(h \to Za) = 0.1$.

Appendix F

Scale Uncertainty Plots

The following pages show the signal scale uncertainty plots for both Higgs boson production processes ggF and VBF. These are higher order correction uncertainties that are calculated by varying renormalisation and factorisation scales μ_r,μ_f. The pairwise variation of this is:

$\{\mu_r, \mu_f\} \times \{0.5, 0.5\}, \{1, 0.5\}, \{0.5, 1\}, \{1, 1\}, \{2, 1\}, \{1, 2\}, \{2, 2\}$

are applied and scale uncertainty for each sample is calculated by finding the maximum and minimum variation from the nominal as described in Equation F.0.1 where $\sigma_{(\mu_{R,i},\mu_{F,i})}$ is the uncertainty on the variation and σ_{nom} the uncertainty on the nominal.

$$\max\left[\frac{\sigma_{(\mu_{R,i},\mu_{F,i})} - \sigma_{nom}}{\sigma_{nom}}\right], \min\left[\frac{\sigma_{(\mu_{R,i},\mu_{F,i})} - \sigma_{nom}}{\sigma_{nom}}\right] \tag{F.0.1}$$

The scale uncertainties are up and down systematics that are applied to the bins of the final variables. These are the $m_{\ell\ell\gamma\gamma}$ for the resolved category and $\Delta R_{\ell\ell\gamma}$ for the merged category.

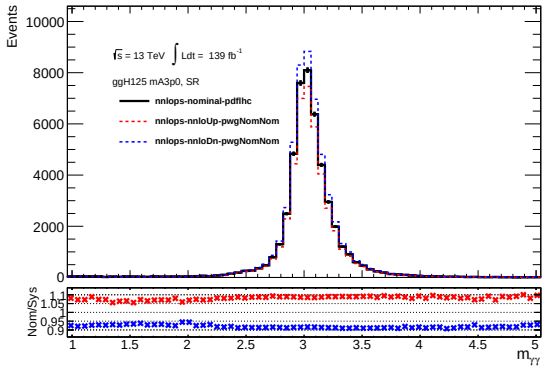

(a) $m_a = 3.0\,\text{GeV}$, ggF

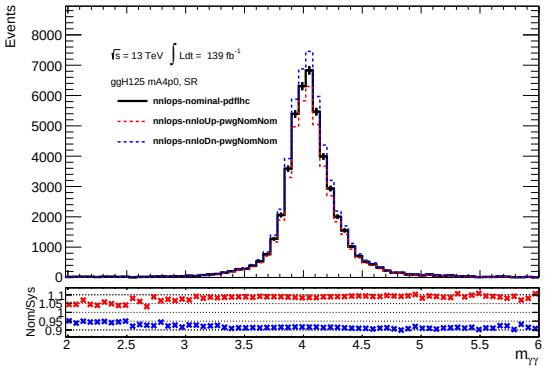

(b) $m_a = 4.0\,\text{GeV}$, ggF

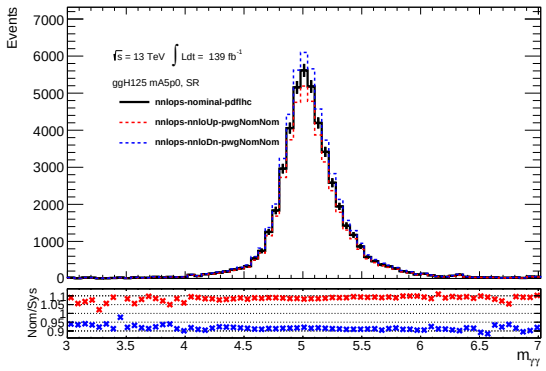

(c) $m_a = 5.0\,\text{GeV}$, ggF

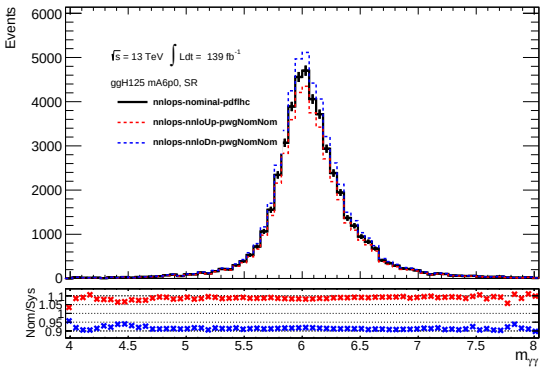

(d) $m_a = 6.0\,\text{GeV}$, ggF

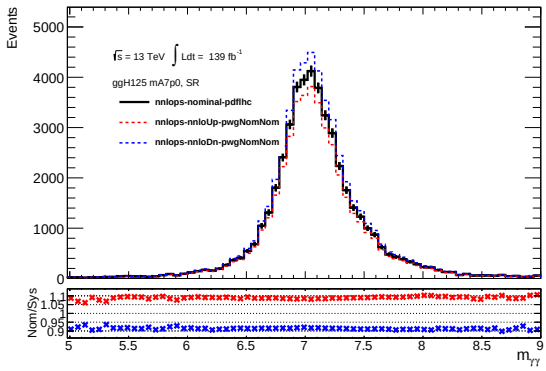

(e) $m_a = 7.0\,\text{GeV}$, ggF

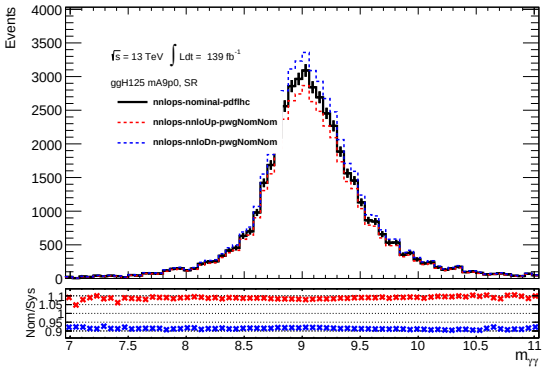

(f) $m_a = 9.0\,\text{GeV}$, ggF

Figure F.1: Nominal distributions for resolved category fit variable $m_{\gamma\gamma}$ compared with the up and down scale uncertainties for ggF signal samples with m_a values relevant to the resolved category.

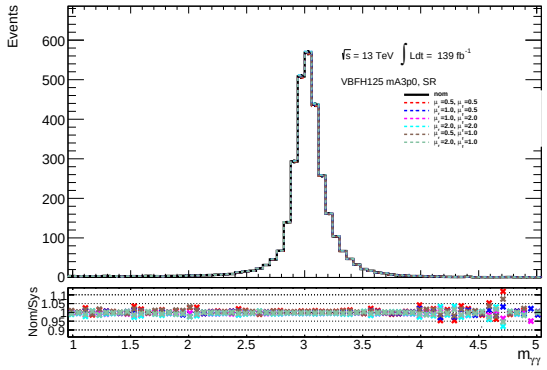

(a) $m_a = 3.0\,\text{GeV}$, VBF

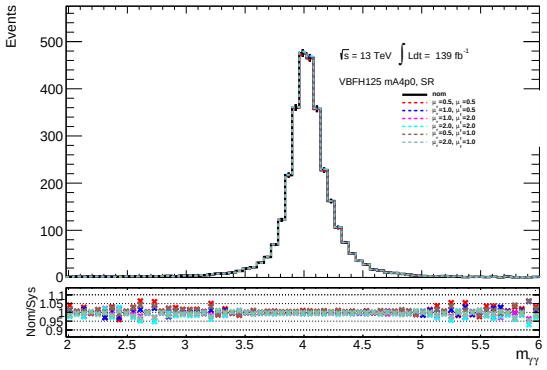

(b) $m_a = 4.0\,\text{GeV}$, VBF

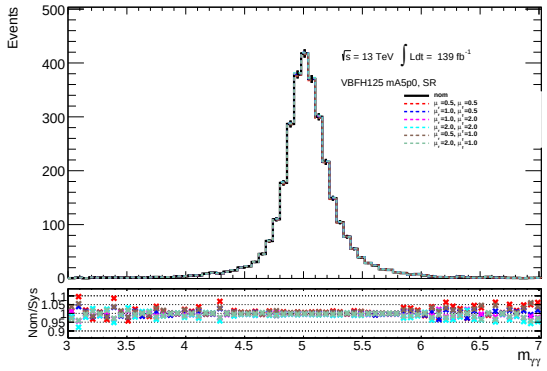

(c) $m_a = 5.0\,\text{GeV}$, VBF

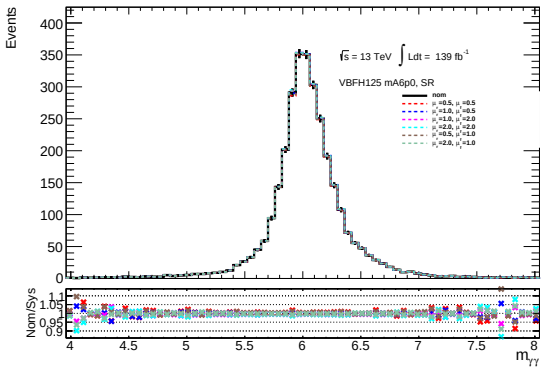

(d) $m_a = 6.0\,\text{GeV}$, VBF

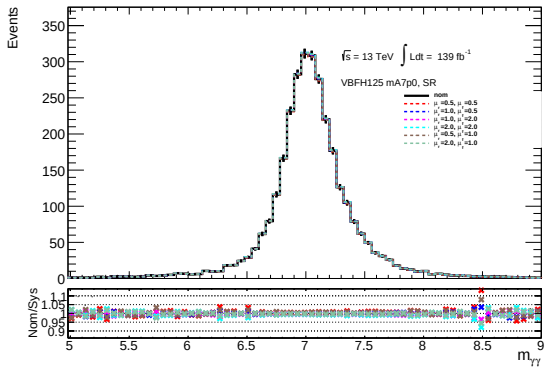

(e) $m_a = 7.0\,\text{GeV}$, VBF

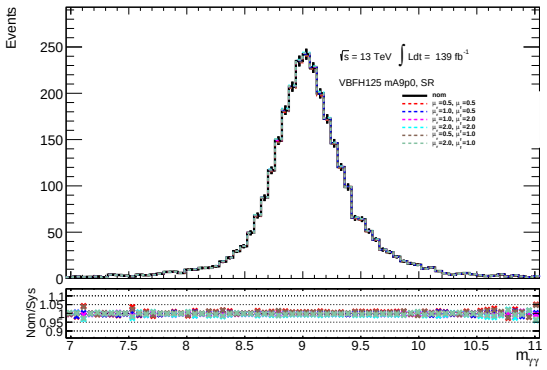

(f) $m_a = 9.0\,\text{GeV}$, VBF

Figure F.2: Nominal distributions for resolved category fit variable $m_{\gamma\gamma}$ compared with the up and down scale uncertainties for VBF signal samples with m_a values relevant to the resolved category.

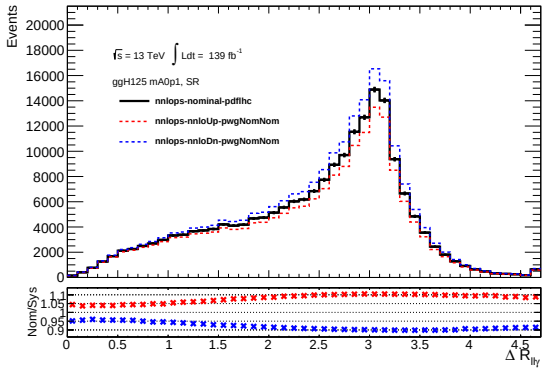

(a) $m_a = 0.1\,\text{GeV}$, ggF

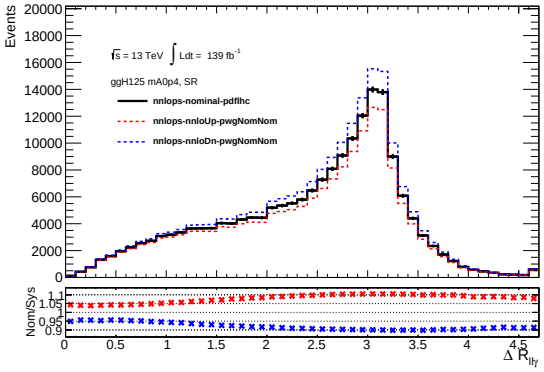

(b) $m_a = 0.4\,\text{GeV}$, ggF

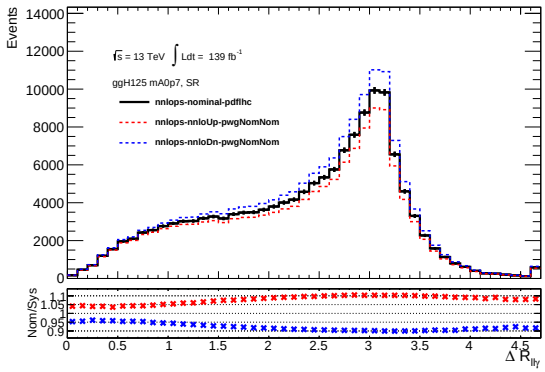

(c) $m_a = 0.7\,\text{GeV}$, ggF

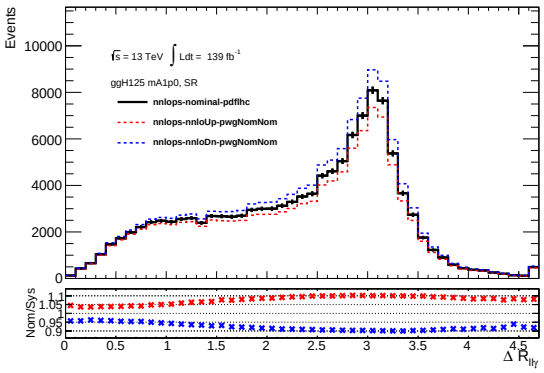

(d) $m_a = 1.0\,\text{GeV}$, ggF

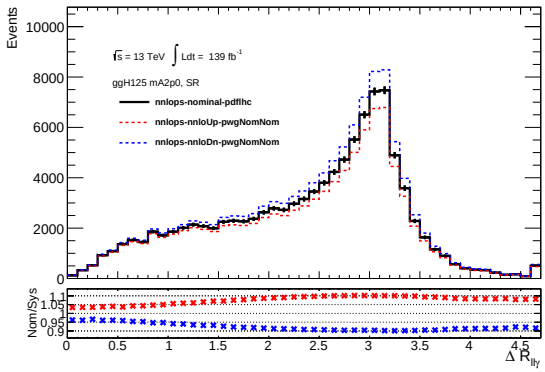

(e) $m_a = 2.0\,\text{GeV}$, ggF

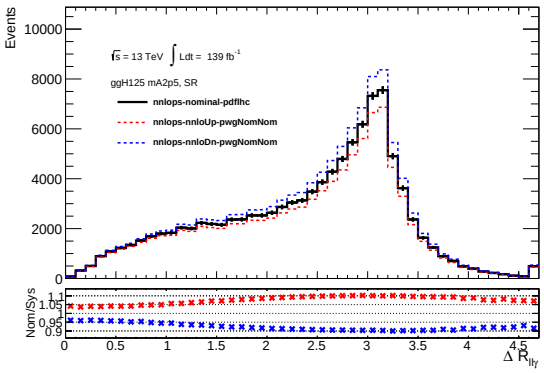

(f) $m_a = 2.5\,\text{GeV}$, ggF

Figure F.3: Nominal distributions for merged category fit variable $\Delta R_{\gamma\gamma}$ compared with the up and down scale uncertainties for ggF signal samples with m_a values relevant to the merged category.

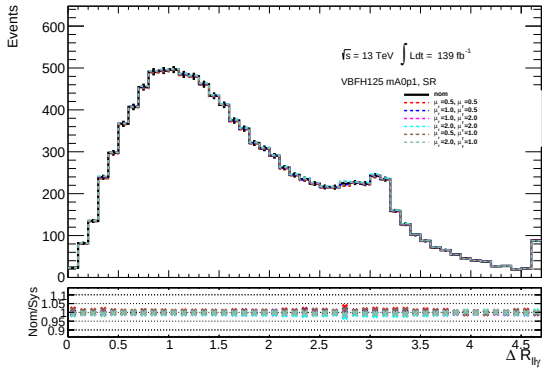

(a) $m_a = 0.1\,\text{GeV}$, VBF

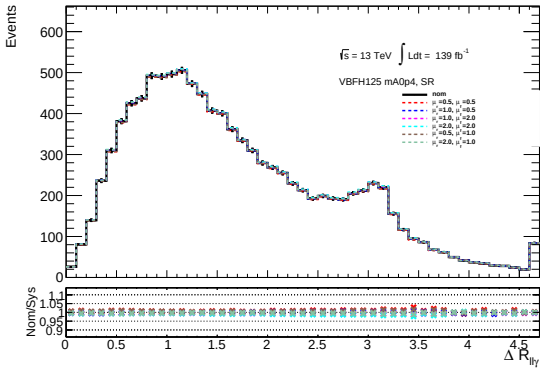

(b) $m_a = 0.4\,\text{GeV}$, VBF

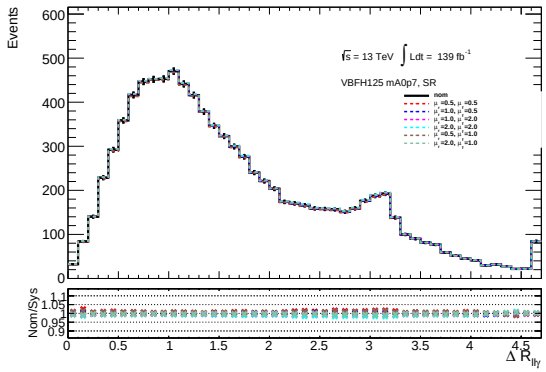

(c) $m_a = 0.7\,\text{GeV}$, VBF

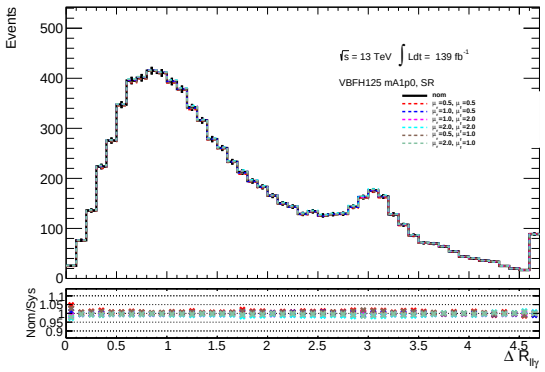

(d) $m_a = 1.0\,\text{GeV}$, VBF

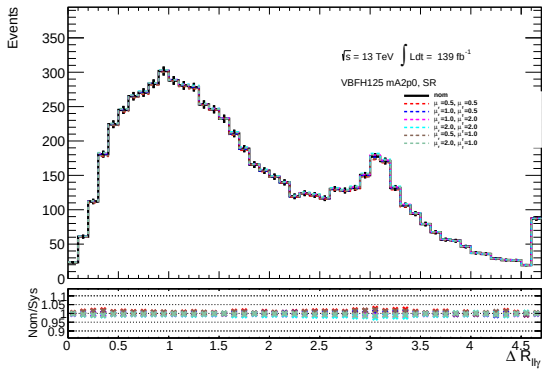

(e) $m_a = 2.0\,\text{GeV}$, VBF

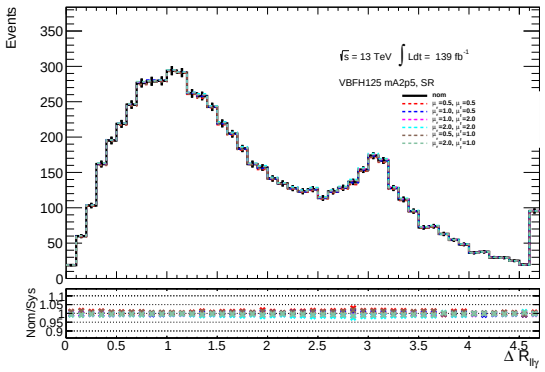

(f) $m_a = 2.5\,\text{GeV}$, VBF

Figure F.4: Nominal distributions for merged category fit variable $\Delta R_{\gamma\gamma}$ compared with the up and down scale uncertainties for VBF signal samples with m_a values relevant to the merged category.

Bibliography

[1] S. L. Glashow, J. Iliopoulos and L. Maiani, *Weak interactions with lepton-hadron symmetry*, *Phys. Rev. D* **2** (1970) 1285.

[2] S. Weinberg, *A model of leptons*, *Phys. Rev. Lett.* **19** (1967) 1264.

[3] ATLAS collaboration, *Observation of a new particle in the search for the standard model higgs boson with the atlas detector at the lhc*, *Physics Letters B* **716** (2012) 1.

[4] CMS collaboration, *Observation of a New Boson at a Mass of 125 GeV with the CMS Experiment at the LHC*, *Phys. Lett. B* **716** (2012) 30 [1207.7235].

[5] M. Bauer, M. Neubert and A. Thamm, *LHC as an Axion Factory: Probing an Axion Explanation for $(g-2)_\mu$ with Exotic Higgs Decays*, *Phys. Rev. Lett.* **119** (2017) 031802 [1704.08207].

[6] M. Thomson, *Modern particle physics*. Cambridge University Press, New York, 2013, 10.1017/CBO9781139525367.

[7] P. Langacker, *The standard model and beyond*. 2010.

[8] M. Gell-Mann, *The interpretation of the new particles as displaced charge multiplets*, *Nuovo Cim.* **4** (1956) 848.

[9] T. Nakano and K. Nishijima, *Charge Independence for V-particles**, *Progress of Theoretical Physics* **10** (1953) 581 [https://academic.oup.com/ptp/article-pdf/10/5/581/5364926/10-5-581.pdf].

[10] A. Purcell, *Go on a particle quest at the first cern webfest. le premier webfest du cern se lance à la conquête des particules*, *https://cds.cern.ch/record/1473657* (2012) 10.

[11] S. L. Glashow, *Partial-symmetries of weak interactions*, *Nuclear Physics* **22** (1961) 579.

[12] S. Weinberg, *A model of leptons*, *Phys. Rev. Lett.* **19** (1967) 1264.

[13] A. Salam, *Weak and Electromagnetic Interactions*, *Conf. Proc. C* **680519** (1968) 367.

[14] PDG, *Review of Particle Physics*, *Progress of Theoretical and Experimental Physics* **2020** (2020) [https://academic.oup.com/ptep/article-pdf/2020/8/083C01/34673722/ptaa104.pdf].

[15] P. Higgs, *Broken symmetries, massless particles and gauge fields*, *Physics Letters* **12** (1964) 132.

[16] F. Englert and R. Brout, *Broken symmetry and the mass of gauge vector mesons*, *Phys. Rev. Lett.* **13** (1964) 321.

[17] G. S. Guralnik, C. R. Hagen and T. W. B. Kibble, *Global conservation laws and massless particles*, *Phys. Rev. Lett.* **13** (1964) 585.

[18] J. Ellis, *Higgs Physics*, 1312.5672.

[19] J. Goldstone, A. Salam and S. Weinberg, *Broken symmetries*, *Phys. Rev.* **127** (1962) 965.

[20] UA2 collaboration, *Observation of single isolated electrons of high transverse momentum in events with missing transverse energy at the cern pp collider*, *Physics Letters B* **122** (1983) 476.

[21] UA2 collaboration, *Evidence for z0→e+e at the cern pp collider*, *Physics Letters B* **129** (1983) 130.

[22] ATLAS collaboration, *Observation of h→bb¯ decays and vh production with the atlas detector*, *Physics Letters B* **786** (2018) 59.

[23] CMS collaboration, *Observation of* $\mathrm{t\bar{t}}H$ *production*, *Phys. Rev. Lett.* **120** (2018) 231801 [1804.02610].

[24] C. Grojean, *Higgs Physics*, 1708.00794.

[25] CMS collaboration, *Precise determination of the mass of the Higgs boson and tests of compatibility of its couplings with the standard model predictions using proton collisions at 7 and 8 TeV*, *Eur. Phys. J. C* **75** (2015) 212 [1412.8662].

[26] ATLAS collaboration, *Measurement of the Higgs boson mass from the $H \to \gamma\gamma$ and $H \to ZZ^* \to 4\ell$ channels with the ATLAS detector using 25 fb^{-1} of pp collision data*, *Phys. Rev. D* **90** (2014) 052004 [1406.3827].

[27] LHC Higgs Cross Section Working Group collaboration, *Handbook of LHC Higgs Cross Sections: 4. Deciphering the Nature of the Higgs Sector*, 1610.07922.

[28] ATLAS collaboration, *Cross-section measurements of the higgs boson decaying into a pair of τ-leptons in proton-proton collisions at $\sqrt{s} = 13$ TeV with the atlas detector*, *Phys. Rev. D* **99** (2019) 072001.

[29] CMS collaboration, *Observation of the higgs boson decay to a pair of leptons with the cms detector*, *Physics Letters B* **779** (2018) 283.

[30] CMS collaboration, *Observation of higgs boson decay to bottom quarks*, *Phys. Rev. Lett.* **121** (2018) 121801.

[31] ATLAS collaboration, *Higgs search at ATLAS*, tech. rep., CERN, Geneva, May, 2013. https://cds.cern.ch/record/1546765.

[32] ATLAS collaboration, *Combined measurements of Higgs boson production and decay using up to 80 fb^{-1} of proton-proton collision data at $\sqrt{s} = 13$ TeV collected with the ATLAS experiment*, *Phys. Rev. D* **101** (2020) 012002 [1909.02845].

[33] About Fermilab, https://www.fnal.gov/pub/about/index.html, Date accessed Feb 2022.

[34] About SLAC, https://www6.slac.stanford.edu/about, Date accessed Feb 2022.

[35] T. Taylor and D. Treille, *The Large Electron Positron Collider (LEP): Probing the Standard Model*, *Adv. Ser. Direct. High Energy Phys.* **27** (2017) 217.

[36] F. J. Gilman, K. Kleinknecht and B. Renk, *The Cabibbo-Kobayashi-Maskawa quark mixing matrix: in Review of Particle Physics (RPP 2000)*, *Eur. Phys. J. C* **15** (2000) 110.

[37] The nobel prize in physics 2004, Date accessed Jan 2023, https://www.nobelprize.org/prizes/physics/2004/popular-information/.

[38] R. D. Peccei and H. R. Quinn, CP *conservation in the presence of pseudoparticles*, *Phys. Rev. Lett.* **38** (1977) 1440.

[39] Muon g-2 (E989) collaboration, *Status of the Fermilab Muon g – 2 Experiment*, *EPJ Web Conf.* **262** (2022) 01003 [2202.11391].

[40] Muon g-2 collaboration, *Final Report of the Muon E821 Anomalous Magnetic Moment Measurement at BNL*, *Phys. Rev. D* **73** (2006) 072003 [hep-ex/0602035].

[41] K. G. Begeman, A. H. Broeils and R. H. Sanders, *Extended rotation curves of spiral galaxies: dark haloes and modified dynamics*, *Monthly Notices of the Royal Astronomical Society* **249** (1991) 523 [https://academic.oup.com/mnras/article-pdf/249/3/523/18160929/mnras249-0523.pdf].

[42] A. Pich, *CP violation*, *ICTP Ser. Theor. Phys.* **10** (1994) 14 [hep-ph/9312297].

[43] G. Senjanovic and V. Tello, *Strong CP violation: problem or blessing?*, 2004.04036.

[44] M. Kawasaki, M. Yamada and T. T. Yanagida, *Cosmologically safe qcd axion as a present from extra dimension*, *Physics Letters B* **750** (2015) 12.

[45] J. E. Kim, *Light pseudoscalars, particle physics and cosmology.*, *physrep* **150** (1987) 1.

[46] A. Ringwald, *Exploring the Role of Axions and Other WISPs in the Dark Universe*, *Phys. Dark Univ.* **1** (2012) 116 [1210.5081].

[47] W. J. Marciano, A. Masiero, P. Paradisi and M. Passera, *Contributions of axionlike particles to lepton dipole moments*, *Phys. Rev. D* **94** (2016) 115033.

[48] D. Cadamuro and J. Redondo, *Cosmological bounds on pseudo Nambu-Goldstone bosons*, *JCAP* **02** (2012) 032 [1110.2895].

[49] A. Payez, C. Evoli, T. Fischer, M. Giannotti, A. Mirizzi and A. Ringwald, *Revisiting the SN1987A gamma-ray limit on ultralight axion-like particles*, *JCAP* **02** (2015) 006 [1410.3747].

[50] CAST collaboration, *Probing eV-scale axions with CAST*, *JCAP* **02** (2009) 008 [0810.4482].

[51] K. A. Beyer, G. Marocco, R. Bingham and G. Gregori, *Light-shining-through-wall axion detection experiments with a stimulating laser*, *Phys. Rev. D* **105** (2022) 035031.

[52] ATLAS collaboration, *Search for Higgs boson decays into two new low-mass spin-0 particles in the 4b channel with the ATLAS detector using pp collisions at* $\sqrt{s} = 13$ *TeV*, *Phys. Rev. D* **102** (2020) 112006 [2005.12236].

[53] CMS collaboration, *Search for light pseudoscalar boson pairs produced from decays of the 125 GeV Higgs boson in final states with two muons and two nearby tracks in pp collisions at* $\sqrt{s} = 13$ *TeV*, *Phys. Lett. B* **800** (2020) 135087 [1907.07235].

[54] CMS collaboration, *Search for a light pseudoscalar Higgs boson in the boosted* $\mu\mu\tau\tau$ *final state in proton-proton collisions at* $\sqrt{s} = 13$ *TeV*, *JHEP* **08** (2020) 139 [2005.08694].

[55] ATLAS collaboration, *Search for Higgs boson decays into two spin-0 particles in the* $bb\mu\mu$ *final state with the ATLAS detector in pp collisions at* $\sqrt{s} = 13$ *TeV*, tech. rep., CERN, Geneva, 2021. http://cds.cern.ch/record/2759283.

[56] ATLAS collaboration, *Measurement of light-by-light scattering and search for axion-like particles with 2.2* nb^{-1} *of Pb+Pb data with the ATLAS detector*, *JHEP* **03** (2021) 243 [2008.05355].

[57] CMS collaboration, *Evidence for light-by-light scattering and searches for axion-like particles in ultraperipheral PbPb collisions at* $\sqrt{s}$ *NN = 5.02 TeV*, *Phys. Lett. B* **797** (2019) 134826 [1810.04602].

[58] ATLAS collaboration, *Search for new phenomena in events with an energetic jet and missing transverse momentum in pp collisions at* $\sqrt{s}$ *=13 TeV with the ATLAS detector*, *Phys. Rev. D* **103** (2021) 112006 [2102.10874].

[59] CMS collaboration, *Search for dark matter produced in association with a leptonically decaying Z boson in proton-proton collisions at $\sqrt{s}$ = 13 TeV*, *Eur. Phys. J. C* **81** (2021) 13 [2008.04735].

[60] ATLAS collaboration, *Search for dark matter in association with an energetic photon in pp collisions at $\sqrt{s}$ = 13 TeV with the ATLAS detector*, *JHEP* **02** (2021) 226 [2011.05259].

[61] ATLAS, CMS, TOTEM collaboration, *Searches for Axion Like Particles at the LHC*, *PoS* **LHCP2021** (2021) 005.

[62] ATLAS collaboration, *A search for the z decay mode of the higgs boson in pp collisions at s=13 tev with the atlas detector*, *Physics Letters B* **809** (2020) 135754.

[63] L. Evans and P. Bryant, *LHC machine*, *Journal of Instrumentation* **3** (2008) S08001.

[64] S. Myers, *The LEP Collider, from design to approval and commissioning*, John Adams' memorial lecture. CERN, Geneva, 1991, 10.5170/CERN-1991-008.

[65] The tale of a billion-trillion protons, Date accessed Mar, 2022. https://cerncourier.com/a/the-tale-of-a-billion-trillion-protons/.

[66] ATLAS collaboration, *The ATLAS experiment at the CERN large hadron collider*, *Journal of Instrumentation* **3** (2008) S08003.

[67] CMS collaboration, *The CMS experiment at the CERN LHC*, *Journal of Instrumentation* **3** (2008) S08004.

[68] LHCb collaboration, *The LHCb Detector at the LHC*, *JINST* **3** (2008) S08005.

[69] ALICE collaboration, *Performance of the ALICE Experiment at the CERN LHC*, *Int. J. Mod. Phys. A* **29** (2014) 1430044. 120 p [1402.4476].

[70] CERN, *High-Luminosity Large Hadron Collider (HL-LHC): Technical design report*, CERN Yellow Reports: Monographs. CERN, Geneva, 2020, 10.23731/CYRM-2020-0010.

[71] E. Mobs, *The CERN accelerator complex - 2019. Complexe des accélérateurs du CERN - 2019*, *https://cds.cern.ch/record/2684277* (2019) .

[72] L. Evans and P. Bryant, *LHC machine*, *Journal of Instrumentation* **3** (2008) S08001.

[73] ATLAS collaboration, *ATLAS data quality operations and performance for 2015-2018 data-taking*, *JINST* **15** (2019) P04003. 43 p [1911.04632].

[74] G. Soyez, *Pileup mitigation at the lhc a theorist's view*, *Physics Reports* **803** (2018) .

[75] J. T. Boyd, *LHC Run-2 and Future Prospects*, in *2019 European School of High-Energy Physics*, 1, 2020, 2001.04370.

[76] ATLAS collaboration, *Observation of a new particle in the search for the Standard Model Higgs boson with the ATLAS detector at the LHC*, *Phys. Lett. B* **716** (2012) 1 [1207.7214].

[77] CMS collaboration, *Observation of a New Boson at a Mass of 125 GeV with the CMS Experiment at the LHC*, *Phys. Lett. B* **716** (2012) 30 [1207.7235].

[78] N. Ky and N. Vân, *Latest results on the higgs boson discovery and investigation at the atlas-lhc*, *Journal of Physics: Conference Series* **627** (2015) .

[79] ATLAS collaboration, *ATLAS Insertable B-Layer Technical Design Report*, tech. rep., Sep, 2010. https://cds.cern.ch/record/1291633.

[80] J. Jentzsch, *Performance tests during the ATLAS IBL Stave Integration*, tech. rep., CERN, Geneva, Nov, 2014. 10.1088/1748-0221/10/04/C04036, https://cds.cern.ch/record/1969020.

[81] S.Haywood, *ATLAS SCT End-cap*, http://www.ep.ph.bham.ac.uk/general/seminars/slides/stephen-haywood-210109.pdf, Seminar given 2009.

[82] ATLAS collaboration, *Particle Identification Performance of the ATLAS Transition Radiation Tracker*, tech. rep., CERN, Geneva, Sep, 2011. https://cds.cern.ch/record/1383793.

[83] ATLAS collaboration, *Electron and photon performance measurements with the ATLAS detector using the 2015–2017 LHC proton-proton collision data*, *JINST* **14** (2019) P12006 [1908.00005].

[84] F. Cavallari, *Performance of calorimeters at the LHC*, *Journal of Physics: Conference Series* **293** (2011) 012001.

[85] ATLAS collaboration, *Muon reconstruction performance of the ATLAS detector in proton–proton collision data at* $\sqrt{s}$ *=13 TeV*, *Eur. Phys. J. C* **76** (2016) 292 [1603.05598].

[86] Worldwide LHC Computing Grid [Online], https://wlcg-public.web.cern.ch/, Date accessed Feb, 2022.

[87] TRIUMF Grid Information [Online], http://grid.triumf.ca/, Date accessed Feb, 2022.

[88] GridPP [Online], https://www.gridpp.ac.uk/, Date accessed Feb, 2022.

[89] RC Site List [Online], http://wlcg-cric.cern.ch/wlcg/fedrcsite/list/, Date accessed Feb, 2022.

[90] The Grid: A system of tiers [Online], https://home.cern/science/computing/grid-system-tiers, Date accessed Feb, 2022.

[91] ATLAS collaboration, *ATLAS Computing: technical design report*, Technical design report. ATLAS. CERN, Geneva, 2005.

[92] G. Barrand et al., *GAUDI - A software architecture and framework for building HEP data processing applications*, *Comput. Phys. Commun.* **140** (2001) 45.

[93] ATLAS collaboration, *High-Luminosity Large Hadron Collider (HL-LHC): Technical design report*, CERN Yellow Reports: Monographs. CERN, Geneva, 2020, 10.23731/CYRM-2020-0010.

[94] ATLAS collaboration, *ATLAS ITk Pixel Detector Overview*, in *International Workshop on Future Linear Colliders*, 5, 2021, 2105.10367.

[95] ATLAS collaboration, *Expected Tracking Performance of the ATLAS Inner Tracker at the HL-LHC*, tech. rep., CERN, Geneva, Mar, 2019. https://cds.cern.ch/record/2669540.

[96] ATLAS collaboration, *Technical Design Report for the ATLAS Inner Tracker Pixel Detector*, tech. rep., CERN, Geneva, Sep, 2017. https://cds.cern.ch/record/2285585.

[97] G. Bradski, *The OpenCV Library*, *Dr. Dobb's Journal of Software Tools* (2000) .

[98] ATLAS collaboration, ATLAS Luminosity Public Results Run-2, https://twiki.cern.ch/twiki/bin/view/AtlasPublic/LuminosityPublicResultsRun2, 2022.

[99] P. Nason, *A New method for combining NLO QCD with shower Monte Carlo algorithms*, *JHEP* **11** (2004) 040 [hep-ph/0409146].

[100] S. Frixione, P. Nason and C. Oleari, *Matching NLO QCD computations with Parton Shower simulations: the POWHEG method*, *JHEP* **11** (2007) 070 [0709.2092].

[101] S. Alioli, P. Nason, C. Oleari and E. Re, *A general framework for implementing NLO calculations in shower Monte Carlo programs: the POWHEG BOX*, *JHEP* **06** (2010) 043 [1002.2581].

[102] J. Alwall, R. Frederix, S. Frixione, V. Hirschi, F. Maltoni, O. Mattelaer et al., *The automated computation of tree-level and next-to-leading order differential cross sections, and their matching to parton shower simulations*, *JHEP* **07** (2014) 079 [1405.0301].

[103] T. Sjöstrand, S. Ask, J. R. Christiansen, R. Corke, N. Desai, P. Ilten et al., *An introduction to PYTHIA 8.2*, *Comput. Phys. Commun.* **191** (2015) 159 [1410.3012].

[104] M. Bahr et al., *Herwig++ Physics and Manual*, *Eur. Phys. J. C* **58** (2008) 639 [0803.0883].

[105] J. Bellm et al., *Herwig 7.0/Herwig++ 3.0 release note*, *Eur. Phys. J. C* **76** (2016) 196 [1512.01178].

[106] *Example ATLAS tunes of Pythia8, Pythia6 and Powheg to an observable sensitive to Z boson transverse momentum*, tech. rep., CERN, Geneva, Nov, 2013. https://cds.cern.ch/record/1629317.

[107] H.-L. Lai, M. Guzzi, J. Huston, Z. Li, P. M. Nadolsky, J. Pumplin et al., *New parton distributions for collider physics*, *Phys. Rev. D* **82** (2010) 074024 [1007.2241].

[108] J. Pumplin, D. R. Stump, J. Huston, H. L. Lai, P. M. Nadolsky and W. K. Tung, *New generation of parton distributions with uncertainties from global QCD analysis*, *JHEP* **07** (2002) 012 [hep-ph/0201195].

[109] NNPDF collaboration, *Parton distributions for the LHC Run II*, *JHEP* **04** (2015) 040 [1410.8849].

[110] P. Z. Skands, *Tuning Monte Carlo Generators: The Perugia Tunes*, *Phys. Rev. D* **82** (2010) 074018 [1005.3457].

[111] ATLAS collaboration, *Performance of the ATLAS Track Reconstruction Algorithms in Dense Environments in LHC Run 2*, *Eur. Phys. J. C* **77** (2017) 673 [1704.07983].

[112] R. Frühwirth, *Application of kalman filtering to track and vertex fitting*, *Nuclear Instruments and Methods in Physics Research Section A: Accelerators, Spectrometers, Detectors and Associated Equipment* **262** (1987) 444.

[113] ATLAS collaboration, *A neural network clustering algorithm for the ATLAS silicon pixel detector*, *Journal of Instrumentation* **9** (2014) P09009.

[114] *Vertex Reconstruction Performance of the ATLAS Detector at* $\sqrt{s} = 13$ *TeV"*, tech. rep., CERN, Geneva, Jul, 2015. https://cds.cern.ch/record/2037717.

[115] ATLAS collaboration, *Topological cell clustering in the ATLAS calorimeters and its performance in LHC Run 1*, *Eur. Phys. J. C* **77** (2017) 490 [1603.02934].

[116] M. Cacciari, G. P. Salam and G. Soyez, *The anti-k_t jet clustering algorithm*, *JHEP* **04** (2008) 063 [0802.1189].

[117] *Tagging and suppression of pileup jets with the ATLAS detector*, tech. rep., CERN, Geneva, May, 2014. https://cds.cern.ch/record/1700870.

[118] ATLAS collaboration, *High Precision Electron and Muon Reconstruction Performance with ATLAS at LHC Run-2*, *PoS* **ICHEP2022** (2022) 675.

[119] ATLAS collaboration, *Electron reconstruction and identification in the ATLAS experiment using the 2015 and 2016 LHC proton-proton collision data at* $\sqrt{s} = 13$ *TeV*, *Eur. Phys. J. C* **79** (2019) 639. 40 p [1902.04655].

[120] ATLAS collaboration, *Muon identification and performance in the atlas experiment*, tech. rep., CERN, Geneva, Jul, 2018. 10.22323/1.326.0068, http://cds.cern.ch/record/2631716.

[121] ATLAS collaboration, *Muon reconstruction performance of the ATLAS detector in proton–proton collision data at* $\sqrt{s}$ *=13 TeV*, *Eur. Phys. J. C* **76** (2016) 292 [1603.05598].

[122] H. Abreu, M. Aharrouche, M. Aleksa, L. Aperio-Bella and e. a. J P Archambault, *Performance of the electronic readout of the ATLAS liquid argon calorimeters*, *Journal of Instrumentation* **5** (2010) P09003.

[123] ATLAS collaboration, *Electron and photon performance measurements with the atlas detector using the 2015–2017 lhc proton-proton collision data*, *Journal of Instrumentation* **14** (2019) P12006.

[124] ATLAS collaboration, *Electron and photon reconstruction and performance in ATLAS using a dynamical, topological cell clustering-based approach*, *ATL-PHYS-PUB-2017-022* (2017) .

[125] ATLAS collaboration, *Electron and photon performance measurements with the ATLAS detector using the 2015–2017 LHC proton-proton collision data*, *JINST* **14** (2019) P12006 [1908.00005].

[126] ATLAS collaboration, *Measurement of the photon identification efficiencies with the ATLAS detector using LHC Run 2 data collected in 2015 and 2016*, *Eur. Phys. J. C* **79** (2018) 205. 55 p [1810.05087].

[127] ATLAS collaboration, *Photon identification in 2015 ATLAS data*, *ATL-PHYS-PUB-2016-014* (2016) .

[128] J. Therhaag, *TMVA Toolkit for multivariate data analysis in ROOT*, *PoS* **ICHEP2010** (2010) 510.

[129] A. Tarek Abouelfadl Mohamed, *The LHC and the ATLAS Experiment*. Springer International Publishing, Cham, 2020, 10.1007/978-3-030-59516-6˙4.

[130] ATLAS collaboration, *Operation of the ATLAS trigger system in run 2*, *Journal of Instrumentation* **15** (2020) P10004.

[131] *2015 start-up trigger menu and initial performance assessment of the ATLAS trigger using Run-2 data*, tech. rep., CERN, Geneva, Mar, 2016. https://cds.cern.ch/record/2136007.

[132] ATLAS collaboration, *Trigger Menu in 2016*, tech. rep., CERN, Geneva, Jan, 2017. https://cds.cern.ch/record/2242069.

[133] ATLAS collaboration, *Trigger Menu in 2017*, tech. rep., CERN, Geneva, Jun, 2018. https://cds.cern.ch/record/2625986.

[134] ATLAS collaboration, *Trigger menu in 2018*, tech. rep., CERN, Geneva, Oct, 2019. https://cds.cern.ch/record/2693402.

[135] Particle physics: Deep inelastic scattering, https://www.hep.phy.cam.ac.uk/~thomson/partIIIparticles/handouts/Handout_6_2011.pdf, 2011.

[136] A. D. Martin, W. J. Stirling, R. S. Thorne and G. Watt, *Parton distributions for the LHC*, *Eur. Phys. J. C* **63** (2009) 189 [0901.0002].

[137] M. Oreglia, *A Study of the Reactions* $\psi' \to \gamma\gamma\psi$, thesis, 12, 1980.

[138] ATLAS collaboration, *Recommendations for the Modeling of Smooth Backgrounds*, tech. rep., CERN, Geneva, Nov, 2020. https://cds.cern.ch/record/2743717.

[139] ATLAS collaboration, *Observation of a new particle in the search for the Standard Model Higgs boson with the ATLAS detector at the LHC*, *Phys. Lett. B* **716** (2012) 1 [1207.7214].

[140] Hands-on Statistics, https://indico.stfc.ac.uk/event/119/contributions/1344/attachments/290/430/stats_lecture.pdf.

[141] A. L. Read, *Presentation of Search Results: The CL(s) Technique*, *J. Phys. G* **28** (2002) 2693.

[142] G. Cowan, K. Cranmer, E. Gross and O. Vitells, *Asymptotic formulae for likelihood-based tests of new physics*, *Eur. Phys. J. C* **71** (2011) 1554 [1007.1727].